TECHNISCHE UNIVERSITÄT MÜNCHEN
Max-Planck-Institut für Plasmaphysik

Wasserstoffrückhaltung und Erosionsverhalten von wolframdotierten Kohlenstofffilmen (a-C:W)

Philipp André Sauter

Vollständiger Abdruck der von der Fakultät für Maschinenwesen der Technischen Universität München zur Erlangung des akademischen Grades eines

Doktor-Ingenieurs (Dr.-Ing.)

genehmigten Dissertation.

Vorsitzender: Univ.-Prof. Dr.-Ing. Horst Baier

Prüfer der Dissertation:

1. Hon.-Prof. Dr.-Ing., Dr. Eng. (Univ. Nagoya/Japan) Hans-Harald Bolt
2. Univ.-Prof. Dr. mont. habil. Dr. h.c. Ewald Werner

Die Dissertation wurde am 10.11.2011 bei der Technischen Universität München eingereicht und durch die Fakultät für Maschinenwesen am 13.06.2012 angenommen.

Zusammenfassung

Für die Stabilität des Fusionsplasmas von ITER, das zeigen soll, dass die Kernreaktion von Deuterium (D) und Tritium (T) durch magnetischen Einschluss nach dem Tokamak Prinzip nutzbar ist, besteht die Notwendigkeit, Fusionsasche und -energie kontinuierlich abzuführen. Die durch das Divertorkonzept realisierte Magnetfeldanordnung leitet die Heliumasche und damit auch andere Partikel aus dem Plasma, insbesondere D und T, auf die Divertorprallplatten. Zu Beginn des ITER Betriebs wird vor allem an den vertikalen Prallplatten ein enormer Energieeintrag erwartet, was die Verwendung von faserverstärktem Kohlenstoff nahe legt. In diesem Fall kommt es - durch die hohe Reaktivität von D mit Kohlenstoff (C) - zu einer starken Erosion des C, welcher zusammen mit anderen zerstäubten Wandmaterialien, v.a. Wolfram (W), in einer Mischschicht auf benachbarten Wandflächen deponiert wird. Die so unter einem D Plasma deponierten Mischschichten stellen bei T Betrieb ein Reservoir dar, das einen beträchtlichen Beitrag zur Ausbildung des Gesamtinventars an T leisten kann. Eine Anhäufung von T in Mischschichten kann zum einen durch Diffusion des eingefangenen T in die Tiefe statt finden (Wasserstoffrückhaltung), zum anderen durch ein erneutes Erodieren des aufgewachsenen C, der sich zusammen mit T an Stellen ohne Plasmabelastung ungestört in Form T-haltiger Kohlenwasserstoffe abscheiden kann.

In dieser Arbeit wurden Wasserstoffrückhaltung und Erosionsverhalten eines Modellsystems von Mischschichten, Wolfram dotierter C Film (a-C:W), charakterisiert, besonders im Hinblick auf den Einfluss der Präsenz von W. Dazu wurde ein Vergleich zum reinen C Film (a-C) gezogen. Die Verwendung eines wohl definierten Modellsystems und der Beschuss mit einem massenseparierten, monoenergetischen D Strahl (200 eV/D; $1.2{\cdot}10^{15}$ D$\cdot$cm$^{-2}\cdot$s^{-1}) ermöglichten quantitative Untersuchungen. Dabei wurden Parameter variiert, die eine Extrapolation der Ergebnisse zu ITER relevanten Maßstäben erlauben: Die W Konzentration (1 - 18.5 at%), die Probentemperatur bei D Beschuss (300 - 1300 K) und die Fluenz des einfallenden D (10^{15} - 10^{20} D/cm^2).

Die Anreicherung von W nahe der Oberfläche wurde nach Implantation bei einer Fluenz von 10^{20} D/cm^2 analysiert. Bei 300 K ist für hohe Dotierkonzentrationen ein stationärer Zustand erreicht; die Weite der Anreicherungszone entspricht der Ionenreichweite und die W Konzentration beträgt 100%. Für niedrige Dotierkonzentrationen ist kein stationärer Zustand erreicht. Darüber hinaus nimmt mit zunehmender Temperatur die W Konzentration in der Anreicherungszone stark ab und ihre Weite nimmt stark zu.

Das Erosionsverhalten wurde bei einer Fluenz von 10^{20} D/cm^2 analysiert. Das Erosionsverhalten von a-C resultiert in einer starken Temperaturabhängigkeit der totalen Ausbeute an C (Y_{tot}). Dem gegenüber ist Y_{tot} von a-C:W nur schwach von der Probentemperatur

bei D Beschuss abhängig. Generell ist Y_{tot} von a-C:W deutlich niedriger als Y_{tot} von a-C; Y_{tot} hängt nur schwach von der Dotierkonzentration ab. Die Herabsetzung von Y_{tot} von a-C:W ist jedoch nur im Falle hoher Dotierkonzentrationen und niedriger Temperaturen auf die Anreicherung von W zurückzuführen.

Das Rückhaltevermögen von a-C ist bei 300 K und bei 900 K über den gesamten betrachteten Fluenzbereich kein Verschiedenes zu pyrolytischen Graphits. Nach Sättigung der oberflächennahen Implantationszone zeigt das D Inventar einen schwachen, monotonen Anstieg mit der Fluenz (Φ). Dieser Anstieg wird durch die Diffusion von D in die Tiefe verursacht und kann mit dem Ausdruck Φ^X beschrieben werden. Insgesamt unterscheidet sich das Rückhaltevermögen von a-C:W nur in zwei Aspekten von dem des a-C: Der leicht erhöhte Exponent X für a-C:W, im mittleren Temperaturbereich um 900 K, und das nicht-monotone Anwachsen des D Inventars mit der Fluenz, bei Fluenzen oberhalb 10^{19} D/cm^2.

Der leicht erhöhte Exponent X für a-C:W beruht auf einer Herabsetzung der Bindungsenergie zwischen D und C durch W. Dadurch nimmt die Diffusion von D in die Tiefe mit zunehmender Temperatur stärker zu als in a-C. Eine zunehmende Diffusion in die Tiefe macht sich allerdings erst bei Temperaturen oberhalb 500 K bemerkbar.

Das nicht-monotone Anwachsen des D Inventars mit der Fluenz beruht bei 300 K auf der Anreicherung von W bei Fluenzen oberhalb 10^{19} D/cm^2. Allerdings ist zu vermuten, dass der Einfluss der Anreicherung auf einen Fluenzbereich um 10^{20} D/cm^2 beschränkt ist, d.h. auf jenen Fluenzbereich, in dem sich die Anreicherungszone ausprägt. Weil das Anwachsen des D Inventars auf einer Diffusion von D in die Tiefe beruht, wird bei hohen Fluenzen das Rückhaltevermögen vom Trappingverhalten der C Matrix in der Tiefe dominiert. Dieses wird selbst bei hohen Temperaturen nur schwach durch die Präsenz von W beeinflusst.

In Konsequenz ist es möglich, den Anstieg des D Inventars mit der Fluenz zu hohen, ITER-relevanten Fluenzbereichen zu extrapolieren, ohne den Einfluss der Anreicherung zu berücksichtigen. Dies sollte auch für hohe Temperaturen gelten, falls das nicht-monotone Anwachsen des D Inventars mit der Fluenz durch Anreicherung verursacht ist. Dann unterscheidet sich das Rückhaltevermögen von a-C:W, bis auf einen kleinen Fluenzbereich um 10^{20} D/cm^2 und bis auf einen kleinen Temperaturbereich um 900 K, nicht vom Rückhaltevermögen des wohl bekannten pyrolytischen Graphits.

Abstract

For the stability of the fusion plasma of ITER, which shall demonstrate the possibility to harness the nuclear reaction between deuterium (D) and tritium (T) through magnetic confinement based on the Tokamak concept, the necessity is given to continuously remove ash and energy obtained from fusion. For the divertor concept, the magnetic field lines are distorted in such a way that the helium ash and thus other plasma particles, specifically D and T, are guided to the divertor target plates. During the beginning of the ITER operation an enormous entry of energy is expected, especially at the vertical target, which suggests the use of carbon-fibre-reinforced carbon. This choice results - through the reactivity between D and carbon (C) - in a considerable erosion of C, which will be deposited in the form of mixed layers on neighbouring areas of the inner vessel wall, together with other sputtered wall materials, e.g. tungsten (W). Under the operation with T, mixed layers deposited under a D plasma will act as a reservoir, which can significantly contribute to the build-up of the total T inventory. T can be accumulated in mixed layers by implantation, trapping and diffusion into depth (hydrogen retention), and, on the other hand, through subsequent erosion of the deposited C, which leads to an undisturbed deposition of C and T, forming T-containing hydrocarbons at areas without direct plasma contact.

In this study retention and erosion behaviour of a model system of mixed layers, the tungsten-containing carbon film (a-C:W), were characterized, especially with regard to the influence of the presence of W inclusions. Thus, a comparison was drawn to the pure C film (a-C). The use of a well defined model system and the exposure to a mass-separated, mono-energetic D beam (200 eV/D; $1.2{\cdot}10^{15}$ D$\cdot$cm$^{-2}\cdot$s^{-1}) made quantitative investigations possible. Thereby, parameters were varied, which allow extrapolation to ITER relevant scales: The W concentration (1 - 18.5 at%), the specimen temperature during D beam exposure (300 - 1300 K) and the fluence of incident D (10^{15} - 10^{20} D/cm^2).

The enrichment of W near the surface was analysed after implantation at a fluence of 10^{20} D/cm^2. At 300 K steady-state is reached for high dopant concentrations; the width of the enrichment zone matches the width of the ion range and the W concentration is 100%. For low W concentrations steady-state is not reached. Furthermore, with increasing temperature the W concentration in the enrichment zone decreases and its width increases.

The erosion behaviour was analysed at a fluence of 10^{20} D/cm^2. The erosion behaviour of a-C results in a strong temperature dependence of the total yield of C (Y_{tot}). In contrast, Y_{tot} of a-C:W depends only slightly on the specimen temperature during D beam exposure. In general, Y_{tot} of a-C:W is significantly lower than Y_{tot} of a-C; Y_{tot} only slightly depends on the dopant concentration. However, the reduction of Y_{tot} of a-C:W is only in case of high dopant concentrations and low temperatures caused by the enrichment of W.

The retention behaviour of a-C is at 300 K and at 900 K no different to pyrolytic graphite, along the whole analysed range of fluences (Φ). After saturation of the shallow implantation zone the D inventory exhibits a weak, monotonic increase with fluence. This increase is caused by the diffusion of D into depth and can be described by the expression Φ^X. Altogether, only two aspects distinguish the retention behaviour of a-C:W and of a-C from one another: The slightly increased exponent X for a-C:W, in the medium temperature range around 900 K, and the non-monotonic accumulation of the D inventory with fluence, at fluences above 10^{19} D/cm^2.

The slightly increased exponent X for a-C:W is caused by a lowering of the bonding energy between D and C by W. Thus, the diffusion of D into depth more strongly increases with increasing temperature than in a-C. An increase of the diffusion of D into depth is at first observable for temperatures above 500 K.

The non-monotonic accumulation of the D inventory with fluence is based on the enrichment of W, for fluences above 10^{19} D/cm^2. However, it is suggested that the influence of enrichment is limited to a range of fluences around 10^{20} D/cm^2, i.e. limited to that range of fluences, in which the enrichment zone builds up. Since the accumulation of the D inventory is caused by a diffusion of D into depth, the retention behaviour at high fluences is dominated by the trapping behaviour of the C matrix in the depth. This is even at elevated temperatures only slightly affected by the presence of W.

Consequently, it is possible to extrapolate the increase of the D inventory with fluence to large, ITER-relevant fluence ranges, neglecting the influence of enrichment. This should be valid for elevated temperatures as well, if the non-monotonic accumulation of the D inventory with fluence is caused by enrichment. In this case, the retention behaviour of a-C:W is not different to the retention behaviour of the well known pyrolytic graphite, but for a small range of fluences around 10^{20} D/cm^2 and for a small range of temperatures around 900 K.

Contents

List of Figures

List of Tables

Chapter 1

Introduction

1.1 Nuclear fusion in ITER: Energy and particle exhaust

Nuclear fusion is the most sophisticated attempt to address the issues of limited resources and global warming [1, 2], besides rational use of energy, renewable energy sources and nuclear fission. The nuclear reaction between tritium (T) and deuterium (D), the T(D,n)^{4}He nuclear reaction, has the largest average cross section ($\sim 10^{-16}$ cm^3/s) at the lowest temperature ($\sim 10^8$ K), i.e. the temperature necessary to overcome the Coulomb-barrier [1, 3]. The kinetic energy set free is shared by the 3.5 MeV alpha particle (^{4}He) and the 14.1 MeV neutron (n). The energy of the ^{4}He is suitable to maintain the fusion process after ignition and the energy of the n will produce heat in the blankets, which can drive turbines over a cooling circuit. The main advantages of nuclear fusion are the availability of fuel, low radioactive half times and its climate protection potential [1, 2].

A plasma heated to temperature contains energy, which is directly proportional to the volume density n of the plasma and the thermal energy [1]. In a plasma, the energy set free out of the T(D,n)^{4}He nuclear reaction is directly proportional to the square of the plasma density, to the reaction cross section (averaged over the distribution of thermal velocities), to the reaction heat and to the energy confinement time t_E (the time span, in which the energy is confined) [1]. The scientific break even will be reached, if the energy in the plasma out of the T(D,n)^{4}He nuclear reaction is equal or larger than the energy consumed to heat the plasma to temperature [1]. This results in the Lawson-criterion [4]: $n \cdot t_E \geq 2 \cdot 10^{14}$ s/cm^3, at 10^8 K ($\sim$12 keV). Therefore, it is necessary to compensate the plasma pressure at temperature and thus to keep the plasma density inside the range claimed by the Lawson-criterion [1]. The most promising confinement technique is the magnetic confinement. The Tokamak concept is the most tried and tested [5, 6] and the Stellerator is the version, which allows a stationary plasma confinement [7].

Besides the Lawson criterion, an ash removal criterion exists [9, 10, 11, 12, 13]: $n \cdot t_p \leq 2 \cdot 10^{15}$ s/cm^3, with the particle confinement time t_p (the time span, in which the fuel is confined). A necessary condition for the plasma performance is the removal of the ^{4}He ash from the plasma, at the same rate that it is produced and introduced [12, 13]. In addition to the bending magnets, which produce the toroidal field, a divertor magnet is used [14]. The divertor distorts the plasma magnetic field lines (a superposition of polidal and toroidal magnetic field lines) in such a way that the ionised ^{4}He ash is guided from the separatix towards the strike point of the divertor where it is pumped outwards [14].

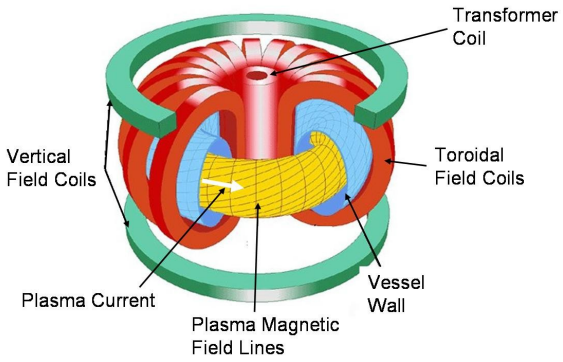

Figure 1.1: Schematic illustrating the Tokamak concept. Picture taken from [8].

The next-step fusion device, the International Thermonuclear Experimental Reactor (ITER), is currently under construction in France [15]. ITER is based on the Tokamak concept. "The primary aim of the ITER device is to demonstrate the scientific and technological feasibility of fusion power for peaceful purposes. An important programmatic goal is the achievement of sustained (300 - 500 s) burning plasma operation with $Q_{DT} \geq 10$, where Q_{DT} is the ratio of fusion power to auxiliary input power [16]." Plasma facing components of ITER will be exposed to an extreme environment, including neutron irradiation, high particle fluxes (helium, hydrogen and impurity ions, neutrals) and heat loads (radiation from the plasma, electrons, magnetic energy) [17]. For the initial phase of ITER and during normal operation, calculations predict particle fluxes to range from 10^{11} to $10^{20}/\mathrm{cm}^2\mathrm{s}$ and to carry energies in the eV to keV range [18]. At the vertical target of the divertor D fluxes will be largest, i.e. $10^{20}/\mathrm{cm}^2\mathrm{s}$ at the strike point ($3\,\mathrm{m}^2$) and $10^{19}/\mathrm{cm}^2\mathrm{s}$ around ($47\,\mathrm{m}^2$) [18]. Low D fluxes around $10^{16}/\mathrm{cm}^2\mathrm{s}$ are expected at baffle and dome of the divertor ($100\,\mathrm{m}^2$) and at the first wall ($700\,\mathrm{m}^2$) [18]. The D impact energy is expected to reach $\sim$15 eV at the divertor and $\sim$200 eV at the first wall [18]. Predicted heat loads for normal operation range between $5\,\mathrm{MW/m}^2$ at the divertor region and up to $20\,\mathrm{MW/m}^2$ at the strike point of the divertor [9, 12].

Besides these normal operation conditions, high transient heat loads and off-normal events are expected. High transient heat loads such as type I ELMs are expected to impose an energy density of $<1\,\mathrm{MJ/m}^2$ onto the divertor target, with a duration of 0.2 ms and a frequency of 1 - 10 Hz [19]. For off-normal events such as disruptions at the divertor and vertical displacement events (VDEs) at the first wall larger peak energy densities are expected [19]. The peak energy density of disruptions would be $30\,\mathrm{MJ/m}^2$ ($<$10% of 1-10 ms duration) and of VDEs $60\,\mathrm{MJ/m}^2$ (1% of 300 ms duration) [19].

1.2 Plasma-facing materials in ITER

The choice of plasma-facing materials (PFMs) for ITER depends strongly on the power and particle exhaust onto the individual parts of the wall and thus on the plasma performance. While plasma facing components, e.g. the vertical target of the divertor, will be faced with an extreme environment during the initial phase, a rather quiescent plasma operation, a tolerable impact by transient heat loads (e.g. type II ELMs) and a negligible amount of off-normal events (e.g. disruptions), is envisaged for the T burning phase [20]. Furthermore, Ne- or Ar-gas seeding under detached conditions is suggested, in order to reduce power loads to the divertor ($\leq$10 - 15 MW/m^2) [20].

For the initial phase, the material choice is determined by the extreme power and particle loads mentioned above. In [20] a "rationale for the selection of PFMs in ITER (Be, W, carbon fibre reinforced carbon) is described with regard to the critical issues concerning PFMs, esp. erosion during transient heat loads and the T-inventory in connection with the redeposition of carbon." Issues regarding the selection of PFMs are [20]:

- Preference for low-Z first wall material: Particle bombardment leads to sputtering of wall atoms, which can enter the plasma and cause serious problems to the plasma performance. Low-Z materials such as carbon (C) and beryllium (Be) show a low ability in plasma cooling via radiation loss and thus can be tolerated up to a dilution limit of the ITER plasma of 1%. At low electron temperatures, on the other hand, e.g. at the low plasma temperature divertor zone, low-Z materials increase the radiation of the plasma edge. This spreads the peaked power loads and thus helps to reduce the power load onto plasma facing materials.

- Erosion during edge localized mode activity and during off-normal events: Transient heat loads at the divertor have the ability to considerably ablate PFMs. For a type I ELM of 0.3 ms duration, Be has the lowest energy deposition limit of $\sim$0.2 MJ/m^2 (melting limit). For C the evaporation limit is 0.4 MJ/m^2 and for tungsten (W) the melting limit is 0.6 MJ/m^2. Therefore, Be cannot be used as a divertor material. Further to this, under the impact of disruptions, e.g. at the strike point of the divertor, the ablation of PFMs is even more severe. While for CFC the ablation loss during a disruption is in the order of 10 μm, W suffers a loss of material in the order of 0.1 mm through melt layer ejection. Therefore, it is necessary - under such conditions - to use CFC at the strike point of the divertor, i.e. for the vertical target plates, during the initial phase.

- T inventory: For the in-vessel T inventory of ITER a safety limit of 330 g was imposed. The build-up of T inventory is a concern for the T burning phase. Nevertheless, the build-up of T inventory during the T burning phase is affected by the material choice for the initial phase. During the initial phase, processes occur which will affect the extent of the build-up of T inventory during the activated phase. Especially erosion processes at the CFC vertical target and thus the deposition of C on low temperature surfaces will lead to a build-up of a C reservoir during the initial phase. This will serve as source for the accumulation of T-containing co-deposited layers in remote areas during the T burning phase. Co-deposition of T and C is a critical source for

the T inventory build-up. In order to keep the amount of eroded C as low as possible, the use of C during the initial phase is restricted to the region at and around the strike point of the divertor. T retention through co-deposition in the T burning phase is also dominated by co-deposition of T with Be, which is caused by the same mechanisms of deposition during the initial phase as described afore for the case of C. Besides co-deposition, the accumulation of T in W is a critical source for the T inventory build-up during the T burning phase. Considerable amounts of T implanted into W will diffuse into depth of bulk W, which critically contributes to the build-up of T inventory with increasing numbers of 400 s ITER discharges during the activated phase.

Each component located at an individual part of the vessel wall must sustain an individual demand [20, 21, 22]. Experience about plasma wall interaction gained in different experimental devices was compared and resulted in a suggestion for the initial material choice of the plasma facing components in ITER [5]. For different components of the vessel wall the use of a specific plasma facing material is expected to exhibit optimized properties. Major parts of the main wall (700 m^2), which will be exposed to moderate heat loads, will be covered by Be tiles. Be is a low-Z material and serves as an oxygen getter. 100 m^2 of the divertor, which will be exposed to heat loads up to 5 MW/m^2, will be covered by W tiles. W is a high-Z material and has the highest melting point of all metals (~3500 K). W does not build hydrides and shows a low sputtering yield. For the hydrogen phase, tiles made of C fiber composites (CFC) are planned to be used at the strike point of the divertor (50 m^2) to withstand heat loads up to 20 MW/m^2.

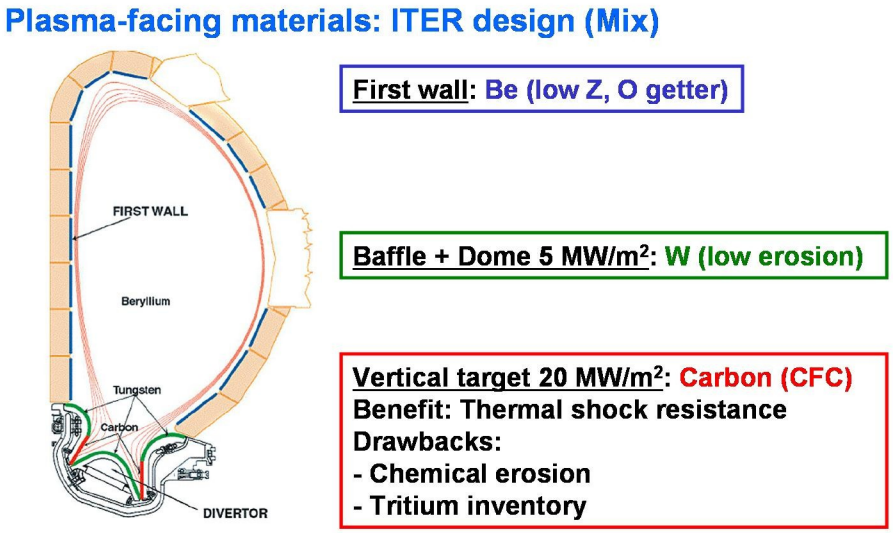

Figure 1.2: Schematic of ITER cross section illustrating the divertor configuration as well as showing the locations and choice of plasma facing materials Be, W, CFC for the initial phase. Picture taken from [23].

For the T burning phase the use of CFC at the vertical target is excluded through the safety limit for the T inventory [20, 24]. Additionally, neutron damage would lead to an amorphisation of the CFC structure and thus to a degradation of its desired thermo-mechanical properties [20]. Therefore, the achievement of a quiescent plasma operation and an effective cooling are necessary conditions for the use of W as vertical target

[20]. This means, the ablation of W must be kept as low as possible, in order to ensure impurity concentrations of W below 10^{-5} and a sufficient component life time [20, 24, 25]. Nevertheless, it must be kept in mind that the neutron irradiation will cause activation of each used material, especially a high-Z material like W [26, 27]. Neutron irradiation will also produce radiation damage and thus increase the accumulation of D in W [24].

1.3 Co-deposition and build-up of T inventory

From the issues regarding the selection of PFMs for ITER mentioned above, the main interest for the study presented in this thesis is the build-up of T inventory in such kind of deposited layers during the T burning phase, which contain major portions of C and minor portions of metal (e.g. W) impurities. Experience with the origin of hydrogen-containing co-deposited layers, which was gained from the present Tokamaks, and the expected consequences for ITER are described in the following.

Most of the present day Tokamaks are composed of C and of other metallic wall components, which are used at different locations inside the vessel wall. For each of these Tokamaks a common scenario was observed [18, 19, 28, 29, 30, 31, 32, 33, 34]. At normal plasma conditions C was chemically eroded under hydrogen impact leading to the formation of volatile hydrocarbons. Through the presence of type I ELMs and under off-normal plasma operation (e.g. arcs, plasma disruptions) large amounts of particles were ejected from metallic components, too [31]. Ionized C and metal atoms were migrating along the magnetic field lines and were co-deposited with hydrogen at other parts of the plasma facing components, leading to the formation of hydrogen-containing mixed materials (hydrogen-containing co-deposited layers) [31]. Co-deposited layers were growing linearly with time up to a thickness of several microns. This resulted in changes in the desired material properties and in the accumulation of considerable amounts of hydrogen. The Joint European Torus (JET), for instance, operates with a D+T - plasma under reactor-like conditions [28, 35]. After the JET DTE1 campaign 40% of the T input were retained in T-containing co-deposited layers [28]. After the application of various detritiation techniques, about 10% of T was still left inside the vessel [28]. In a post mortem analysis, major portions of co-deposited layers were found at the inner divertor and at remote areas of the inner divertor, such as shadowed portions of the tiles, louvres and the divertor support structure [28].

Similar mechanisms of material mixing are expected for ITER as well [24, 36, 37]. For the T burning phase C will be replaced by W. Therefore, the main source of deposited layers will be reduced. For the deposited layers, building up already during the initial phase, several mitigation and recovery techniques are envisaged, which were already applied in present Tokamaks and laboratory experiments. In [23] an overview is given. Some of these techniques will be applied already during a campaign of the initial phase (during the shot, inter-shot, daily, weekly and quarterly). While techniques applied intermediately, e.g. nitrogen seeding and low pressure discharges in D, are non-invasive, their removal efficiency is not better than a factor of 2-3. For the periods after the campaigns more invasive recovery approaches exist, e.g. baking in oxygen at high pressure ($\geq 10^4$ Pa) and laser ablation. These techniques, however, require a shut down of the plasma operation,

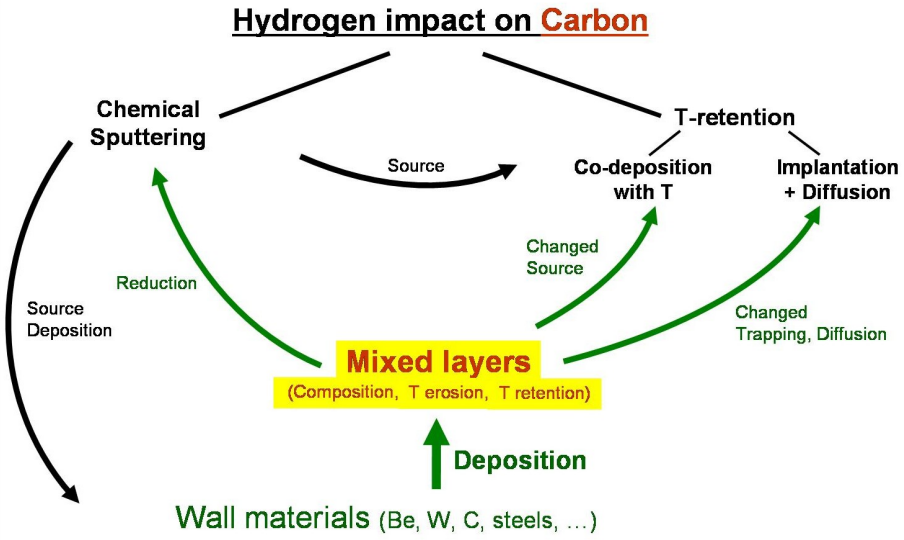

Figure 1.3: Sketch illustrating the mechanisms leading to a build-up of T inventory in deposited layers.

followed by recovery of the plasma after maintenance [23]. Further more, concerning the removal techniques of deposited layers such as baking in oxygen [38, 39, 40, 41] and glow discharge cleaning [42] at elevated surface temperatures and under the presence of oxygen, rather more experience in laboratory experiments exists than for the application to Tokamaks [16]. Therefore, the application of removal techniques to ITER is expected to be complicated by several operational (accessing the required temperatures in the bake out system) and - concerning the activated phase - safety issues (handling tritiated, volatile hydrocarbons and tritiated water) and thus remains challenging [16, 43, 44]. Deposited layers are expected to be left in the machine at the beginning of the T burning phase. T leaving the plasma will be implanted into the deposited layers. If T diffuses into deeper layers, especially beyond the thickness of the deposited layer, it will accumulate and thus exhibit a considerable contribution to the T inventory [45]. Besides the retention process, deposited layers may face re-erosion - forming T-containing ionized hydrocarbons - and subsequently co-deposition in remote areas accumulating undisturbed in tile gaps shadowed from the plasma. The T safety limit will be reached within a few hundred discharges [46, 47]. Note that considerable outgassing of T co-deposited with C will not be achieved by the foreseen baking temperatures, neither for the ITER first wall blanket modules (513 K) nor for the divertor (623 K) [16]. Additional mitigation and recovery techniques would, of course, suffer from the same draw backs as mentioned afore. Consequently, there would be a need to interrupt reactor operation after a relatively short period, in order to recover the T inventory and thus to avoid a serious safety hazard in the case of T release to the atmosphere. This is, of course, a matter of the economic feasibility of ITER.

Several attempts at estimating the hydrogen content and the erosion behaviour of co-deposited layers exist [48, 49, 50, 51, 52, 53, 54]. For instance, tiles removed from locations where net deposition occurs are investigated with regard to their inventory and tiles removed from locations where net erosion occurs are investigated with respect to their erosion behaviour [55, 56, 57, 58]. However, the formation of co-deposited layers is difficult

to predict under the influence of a fusion reactor like plasma that exhibits a parameter set (e.g. ranges of flux, temperature, energy, incident angle) varying strongly with time and location [16, 59, 60]. In general, effects leading to different compositions of co-deposited layers, i.e. plasma performance, particle impact and material migration, are not well known and thus difficult to predict. Investigations of removed tiles show to have a large variety in structure and composition.

1.4 Method: Laboratory experiments under defined conditions

Besides the experience gained from present day Tokamaks, attempts are made in order to establish a closer connection between cause and effect. Experimental setups were developed to allow specimen exposure under defined conditions (e.g. flux, temperature, energy, incident angle) and thus to explore a parameter space [61, 62, 63, 64, 65]. Firstly, these experiments are embedded in investigations, which try to understand basic mechanisms governing the plasma-wall-interaction. Further to this, results from such measurements have the potential to serve as input for simulation codes like EDDY and ERO, which allow modelling of mixed material formation [51, 66, 67].

For the study presented in this thesis, the attempt was made to assess the build-up of T inventory in deposited layers during the T burning phase of ITER. This was performed by taking the results of investigations on the retention and erosion behaviour of deposited layers into account. In investigating the retention and erosion behaviour of deposited layers, laboratory experiments were performed under defined conditions. At the Garching high current ion source [61] specimens were exposed to a D beam under defined conditions (flux, energy and specimen temperature), which allows characterisation of the retention and erosion behaviour under parameter variation. Results were upscaled to ITER relevant parameter ranges (see section 1.5 *Purpose: Assessment of the T inventory build-up* and chapter 7 *Assessment of the ITER T inventory build-up*). The Garching high current ion source facility produces a D beam, which has a flux of $10^{15}\,\mathrm{D\,cm^{-2}\,s^{-1}}$. The energy of the D beam can be adapted by the choice of the acceleration voltage and the voltage of the bias at the target. The specimen temperature (implantation temperature) can be controlled by electron bombardment from the rear side. For the investigation of the retention and erosion behaviour, the implantation temperature was introduced as a parameter and the energy of the D beam was fixed at 200 eV/D.

Besides defined experiments, a material is given, which is similar to deposited layers on one hand and has an adaptable structure on the other hand. Metal-containing amorphous carbon films (a-C:Me) are a possibility to define a model system for deposited layers [68]. They are produced by dual magnetron sputter deposition with argon working gas. The cathode material is sputtered by the impacting argon ions accelerated towards the cathode by a bias. Sputtered atoms, from two different cathodes, are deposited on the substrate holder. For this production process a possibility is given - by choosing the same parameters of the production process given in [68] and under the assumption that the production process is reproducible - to introduce a set of parameters, which changes the structure and the composition of a-C:Me. These parameters are the Me concentration and the temperature of the heat

treatment before the D beam exposure (pre-heating temperature). The study presented in this thesis is restricted to W-C mixtures with W concentration below 20 at%, since C and W are located next to each other at the divertor; small amounts of impurity atoms ($\leq$2 at% of Al, Ar, O) are present in these films as well.

In investigating the D retention and the C erosion behaviour parameter studies were performed. On one hand, the specimen temperature under the D beam exposure was varied between 300 K and 1300 K. With rising temperature, diffusivity of D increases and the contribution of thermal chemical erosion is changed, in contrast to the contribution of physical sputtering. On the other hand, the structure of the films was varied, by producing a-C:W with different W concentrations below 18.5 at% and by applying a different temperature for the heat treatment before the D beam exposure (pre-heating at 700 K and at 1300 K). While varying the temperature of the D beam exposure, the structure was held fixed (dopant concentration: 7.5 at% W, pre-heating temperature: 1300 K). While varying the structure, the implantation temperature was held fixed at 300 K. For both investigations (influence of film structure and influence of implantation temperature) specimens were exposed to the D beam at different fluences between $\sim 10^{15}$ D/cm^2 and $\sim 10^{20}$ D/cm^2. The fluence of incident D was obtained out of a calibration factor for the accumulated charge during the D beam exposure, which was evaluated from the investigation of the profile of the D beam (see appendix A *Characterization of the D beam profile*).

The investigation of the retention and erosion behaviour of a-C:W was carried out by comparing pure carbon films (a-C) and a-C:W. Since a-C and a-C:W have the same porosity, it was possible to focus on investigations with regard to the influence of nano structure. Pyrolytic graphite was used as reference material. A changed erosion behaviour results in a changed accumulation of re-eroded, T-containing hydrocarbons with time. This is of major concern in the context of T accumulation and safety limits. The erosion behaviour of a-C:W is an important aspect in assessing the accumulation of T through the co-deposition of T-containing hydrocarbons in remote areas. Another concern is the accumulation of T in deposited layers through implantation and diffusion into depth, i.e. the retention behaviour. This topic was already investigated for pure graphites, e.g. pyrolytic graphite, and for metal carbide-containing fine grain graphites [69, 70, 71, 72] exposed to a D beam. The amount of retained D increased with the amount of incident D, even after saturation of the implantation zone [69, 70, 71, 72]. Under a T plasma, the T safety limit would be reached after a limited time. In this context, the number of ITER discharges, necessary to reach the safety limit, is determined by the increase of the inventory with fluence. This topic has not been investigated yet for a-C:W. Therefore, the main topic of the studies presented in this thesis is the D retention behaviour of a-C:W. The increase of the D inventory with fluence depends on the porosity [69, 73]. Pore surfaces and grain boundaries act as diffusion channels [73]. a-C:W exhibits a lower porosity than metal carbide-containing fine grain graphites. Another influence is given by the W inclusions. Compared to pyrolytic graphite and to a-C, trapping and diffusion behaviour may be changed intrinsically through the impact of atomically dispersed W inclusions, which change bondings inside the C matrix and in the near vicinity of W inclusions. The evolution of a surface enriched with W, which exhibits an altered reflection coefficient and an altered trapping and diffusion behaviour, may lead to a changed D retention behaviour as well. In this context, the evolution of a W enrichment zone is of major interest. W enrichment originates from the changed erosion

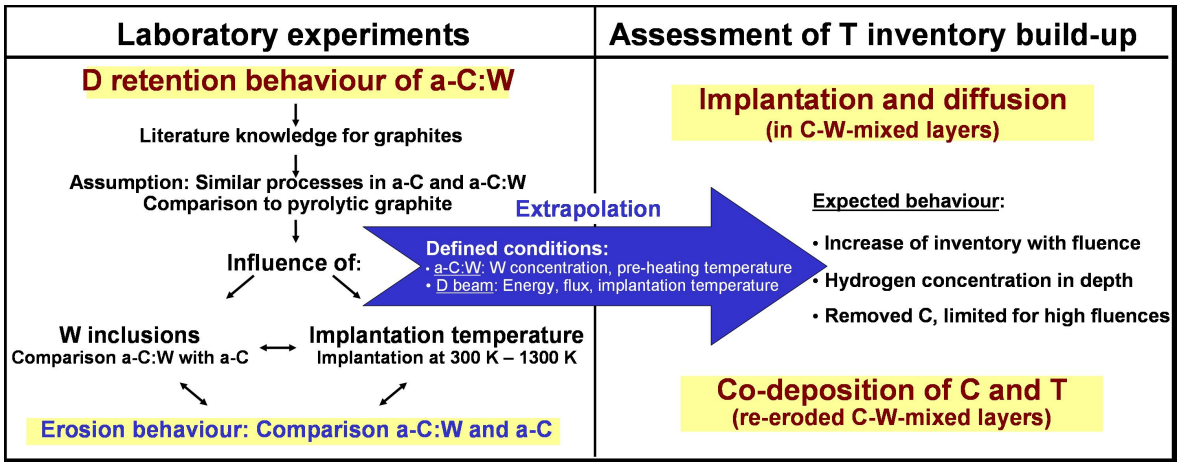

Figure 1.4: Illustration of the purpose of the thesis: Assessment of T inventory build-up, using results obtained from investigations under defined conditions, on the retention and erosion behaviour of a-C:W.

behaviour in a-C:W. The influence of W concentration and of implantation temperature on the enrichment of W has not yet been investigated.

In characterising the retention and erosion behaviour of a-C:W a set of methods was used. The retention behaviour was characterized by the increase of the amount of retained D (D inventory) with fluence of incident D for different fluences between 10^{15} D/cm^2 and 10^{20} D/cm^2. This method is already known to be suitable for characterising the retention behaviour of graphites [74]. Since a-C:W is expected to exhibit a retention behaviour, which is governed by the same processes as already observed in graphites, this methods was expected to be suitable for characterising the retention behaviour of a-C:W, too. The erosion behaviour was characterised by measuring the amount of eroded C atoms after implantations at a fixed fluence of 10^{20} D/cm^2. This leads to a total yield of C. This method was already applied successfully in literature for a-C:Me [75]. In order to find explanations for the retention and erosion behaviour, underlying processes were analysed, in most cases on specimens implanted at a fluence of 10^{20} D/cm^2. Concerning the retention behaviour, trapping and diffusion were analysed by measuring bonding energies and depth profiles of retained D. Concerning the erosion behaviour, the shielding effect was investigated analysing the width and the composition of the W enrichment zone (depth profiles of W).

1.5 Purpose: Assessment of the T inventory build-up

For the study presented in this thesis the assessment of the T inventory build-up during the T burning phase of ITER is performed, by focusing on the following two aspects: First, the deposition of eroded C and sputtered W during the initial phase, which results in the formation of C-W-mixed layers. During the T burning phase, these C-W-mixed layers serve as reservoir for the accumulation of T through implantation, trapping and diffusion into depth. Second, the co-deposition of re-eroded C together with T during the T burning phase, whereby the C originates from the C-W-mixed layers. Both aspects originate from the use

of CFC at the vertical target of the divertor during the initial phase of ITER.

The assessment of the T inventory build-up is based on those investigations under defined conditions, which were explained afore. For the assessment of the T inventory build-up through implantation and diffusion into depth two aspects need to be considered: The T inventory within the saturated implantation zone and the increase of the inventory with fluence above the saturation level of the implantation zone. For pyrolytic graphite, for instance, the saturation level of the implantation zone is largest at 300 K ($\sim 10^{17}$ D/cm^2) [69, 70, 71, 72]. This value leads to a maximum inventory of $\sim$1 g T over an area of 10^3 m^2, which is slightly above the total area of the inner vessel walls. Therefore, the saturation level of the implantation zone can be neglected for all implantation temperatures and the increase of the inventory with fluence, above saturation of the implantation zone, is of major interest, in assessing the T inventory build-up through implantation and diffusion into depth. In this context, the concentration of T at depths beyond the implantation zone and the enrichment zone, i.e. in the unaffected layer, is of major interest, too. This value determines the fluence necessary to reach penetration of deposited layers so that T reaches the underlying W tiles, where the diffusion into depth and thus the accumulation of T is drastically increased. The concentration of T in the depth for different temperatures can be obtained from the temperature series of the depth profiles of D. Up scaling was finally performed by combining these results with energy and flux dependences of the retention behaviour of C, known in literature [70, 76]. The energy is known to affect the width of the implantation zone [61] and thus the saturation level of the implantation zone [76]. The saturation level is directly proportional to the D beam energy [76]. Since the saturation level of the implantation zone can be neglected, the energy of the D beam does not have to be taken into account. This conclusion also allows to neglect the type of isotope species used for the experiments, since the isotope species only affects the width of the ion range and thus the saturation level. In [70] it was shown that inventory in C does not depend on the hydrogen flux, for fluxes of 10^{16}/cm^{2}s and below.

The assessment of T inventory build-up by re-erosion of C and subsequent co-deposition is performed for the case of normal operation conditions. Without the presence of off-normal events, and for energies of 200 eV/T and below, which is below the threshold energy of physical sputtering of W, a W enrichment zone will be formed. Therefore, it needs to be figured out whether enrichment of W will bring chemical sputtering of C to stop, in the range of large fluences. In this case, the amount of re-eroded C and thus the amount of co-deposited C will be limited. Thus, a maximum T inventory can be estimated by taking the amount of eroded C atoms after implantations at a fixed fluence of 10^{20} D/cm^2 into account. Thereby, it is assumed that each re-eroded C will be co-deposited on a surface, shadowed from the plasma; the ratio T/C between T and C, co-deposited in remote areas, does no exceed 1. For the flux dependence of the total yield of removed C literature knowledge exists, for pure C [36]. The total yield is nearly constant at fluxes around 10^{16} D/cm^{2}s and decreases with increasing flux. At a flux of 10^{18} D/cm^{2}s, the total yield is reduced to 1/2, and at a flux of 10^{20} D/cm^{2}s, the total yield is reduced to 1/10. Concerning the energy dependence of the total yield of removed C in a-C:W, less data exist in literature. For instance, the ratio between the yield at 30 eV and the yield at 200 eV is 0.5 at 300 K and 0.25 at 700 K [75]. Since the accumulation of T through co-deposition of re-eroded C with T increases with increasing total yield of removed C, the values obtained within the framework of the study presented in this thesis, i.e. under a 200 eV D beam of a flux of 10^{15}/cm^{2}s, serve as an upper limit. The influence of the angle of incidence on the erosion behaviour of a-C:W may be considered

in the following manner: Erosion processes, which contribute to chemical sputtering, are affected, firstly, by the amount of broken bonds inside the implantation zone, imposed by energetic hydrogen [77]. This behaviour does not depend on the angle of incidence. Concerning physical sputtering, which also contributes to chemical sputtering of C, the angular dependence of the yield of physical sputtering is known quite well in literature [78]. For C the yield of physical sputtering shows a clear increase with angle of incidence, between 0° and 55°. On the other hand, the yield of physical sputtering of W is weak for angles of incidence between 0° and 55°. Especially, the threshold energy for physical sputtering of W is not affected by the angle of incidence. Therefore, preferential sputtering of C must be present at larger angles of incidence as well. So, at large angles of incidence the enrichment zone must reach steady state for lower fluences, than observed at an angle of incidence of 0°. This changes the fluence dependence of the total yield of removed C, but it does not affect the total yield of removed C, if the erosion process is brought to stop by enrichment. For these considerations physical sputtering of W due to the impact of impurity species, e.g. Ar, N, C, He, which might affect W enrichment, is just neglected. In general, physical sputtering of C due to the impact of impurities is neglected compared to the contribution of chemical sputtering of C.

Chapter 2

Background knowledge

This chapter introduces literature knowledge relevant for the studies presented in this thesis. Section 2.1 *Structure of metal-containing amorphous carbon films* describes production and structure of metal-containing carbon films. Tungsten-containing carbon films belong to the group of metal-containing carbon films and show similar properties. Section 2.2 *Interaction between energetic D and C* describes those processes, which occur while exposing C to energetic D and affect the erosion and retention behaviour of C. The influence of doping is described as well. Section 2.3 *Ion beam analysis* describes the analysing techniques used: Rutherford backscattering spectrometry (RBS) and nuclear reaction analysis (NRA).

2.1 Structure of metal-containing amorphous carbon films

Metal-containing amorphous carbon films are an intensively studied material, e.g. with respect to the structure of the C matrix and metal carbide inclusions, since structural features can be controlled and manipulated for a wide variety of applications, by selecting a specific composition and adjusting the production parameters [79]. Many investigations try to find a correlation between parameters used in specific production processes and the structure of the films, and between the structure and thermo-mechanical, tribological, electrical properties as well [80, 81, 82, 83, 84].

Beyond the scope of its relevance for industrial research, this knowledge can also be used to learn something about deposited layers within the framework of fusion research. Since structural properties can be changed, relying on all of these known results, by selecting different compositions and different parameters for the production process, e.g. for the heat treatment of films produced by dual magnetron sputtering deposition, the possibility is given to study the influence of structural parameters on the retention and erosion behaviour. In this context, amorphous carbon films, containing less than 20 at% metal atoms, are of great interest, since deposited layers are, in principal, a C-based mixed material, due to the high erosion rate of C. These films exhibit a sp^2-containing C matrix and nm-sized metal carbide inclusions [85]. Since C and W are planned to be used at the divertor plates of ITER [24], the place with the largest particle impact, tungsten-containing amorphous carbon films exhibit a model system for deposited layers.

C matrix

Amorphous carbon films have been investigated with regard to chemical bondings inside the C matrix. In [86, 87] a review is given on the micro structure of amorphous carbon films. Three different bond hybridisations are available for the four valence electrons of C, i.e. sp^3 -, sp^2 -, sp^1 hybridisation. The index denotes the number of hybridised p orbitals. In a C network, hybridised p orbitals build up π bonds and non-hybridised build up σ bonds. Both bonds are built up between C and impurity atoms as well. Diamond is fully composed of sp^3 hybridised C and graphite is fully composed of sp^2 hybridised C. Amorphous C, however, can be composed of a mixture of bonds, hybridised in any of the three forms, in which the content of sp^1 bonds is low. Amorphous C with sp^3 contents between 40% and 60% is denoted as diamond like amorphous C and can be produced by applying a DC bias on the substrate during the magnetron sputtering process - the highest sp^3 content is achieved for a bias of $\sim$100 V. Another form is the graphite-like amorphous C. It is deposited without bias voltage, and thus contains less than 30% of sp^3 bonds. sp^2 bonds, on the other hand, can be arranged in clusters of aromatic rings and in oliferic chains. In [68] clustering of aromatic rings was investigated after heat treatment by means of Raman spectroscopy for pure and metal-containing amorphous carbon films. Titanium (Ti), vanadium (V), zirconium (Zr) and W were used as metal inclusions. They were produced by dual magnetron sputter deposition without bias voltage. After deposition, the pure films contained mainly oliferic chains and the metal-doped films contained larger portions of aromatic clusters. Heating up to 1300 K vanished differences. Pure and doped films showed the same structure. Besides pure amorphous C, hydrogen-containing amorphous C exist. Production processes and their influence on the structure are described in [88].

Carbide phases

C builds up bondings to impurity atoms. In recent years several groups studied the structure of metal-containing C layers - mainly containing Ti or W as dopant - with a focus on the bonding environment of the metal [81, 89, 90, 91, 92, 93]. "Generally, the formation of a nanocomposite is observed, with nm-sized carbide crystals embedded in a matrix of amorphous C. The near vicinity of metal inclusions (Ti, V, Zr, W) and metal carbide (TiC, VC, ZrC, WC, W_2C) formation, in carbon films, containing less than 20 at% metal additions, was investigated in [68] after heat treatment. Combining the X-ray diffraction (XRD) and extended X-ray absorption fine structure (EXAFS) results, it appears that the metal distribution of metal-containing carbon films without heat treatment is similar for all four metals. No significant carbide particle formation has occurred (except 19 at% V), and the majority of the metal atoms is distributed atomically disperse in the C matrix, surrounded by a C shell. With annealing, carbide particle formation occurred, in all samples. After annealing to 1300 K, the largest crystallites were observed for V-doping ($\sim$10 nm), the smallest particles ($\sim$3 nm) were observed in Zr and W-doped films [85]."

Producing tungsten-containing carbon films, containing less than 25 at% W inclusions, by magnetron sputter deposition, carbide phases are achieved forbidden in thermodynamic equilibrium. In tungsten-containing carbon films with high amounts of C, three carbide phases were identified, e.g. WC, W_2C and WC_{1-x} [80, 94]. In [85] the formation of the carbide phases of W and crystallite growth were investigated in tungsten-containing carbon

films, with W concentrations below 15 at% and after heat treatment at temperatures up to 1700 K. X-ray diffraction was applied analysing carbide phases and crystallite growth. Additionally, near edge X-ray absorption fine structure spectroscopy (NEXAFS) was applied, in order to analyse the atomic environment of W inclusions. In the diffractogram of a 9.5 at% tungsten-containing carbon film, which was not heat treated, only a broad peak and a weak, broad hump is observable, at positions where reflexes of carbide standard materials are very close together. From the large widths of the peak and of the hump it is not possible to allocate any carbide phase in the as-deposited film. With increasing temperature, a slight shift of the maximum of the peak, a narrowing of the peak and an increase of the intensity suggests carbide formation and crystallite growth. At 1300 K the peak position can be allocated to the W_2C phase. From NEXAFS measurements on a 6.5 at% tungsten-containing carbon film, it was concluded that W inclusions are atomically dispersed inside the C matrix of the as-deposited films. At 1300 K the atomic environment of W was similar to the environment in W_2C standard material and at 1700 K to the environment in WC standard material.

Classification of amorphous C films

Amorphous carbon films are classified in the VDI guideline 2840 [95]. For each type of amorphous carbon film an acronym is given. For hydrogen-free carbon films with a high sp^2 content and prepared by PVD the acronym a-C is used. For metal-containing a-C the acronym a-C:Me is used. According to these guide lines tungsten-containing carbon films are denoted as a-C:W; a-C:W, containing, e.g. 7.5 at% of W, is denoted as 7.5 at% a-C:W. W concentrations are given in atomic per cent throughout this thesis.

2.2 Interaction between energetic D and C

The following chapter describes the effects, which occur while bombarding C with energetic D of several eV up to a few keV. First an overview in brief is given.

The kinematic between D and C leads to the following processes: A part of the incident D beam is reflected by backscattering processes at surface near layers. The reflection coefficient for the incoming D depends on its energy and incident angle, and on structure and surface roughness of the C material (see subsection 2.2.1 *Reflection*). The unreflected part of the incident beam penetrates into C, depositing its energy. Thus, it is thermalised inside a certain range according to its incident energy and to the stopping power. The energy transfer from the incident beam to C creates a primary recoil atom. C atoms with energies exceeding the surface binding energy are ejected at the surface. C is physically sputtered and bonds are broken (see subsection 2.2.2 *Sputtering -Physical sputtering*).

Further processes occur by the chemistry between C and D. D atoms depositing their energy are thermalised at the end of the ion range. Thermalised D is bound to broken C bonds and trapped locally. With an increasing number of incident D atoms, a subsurface zone is filled successively with D until a saturation ratio of $\sim$0.4 D atoms per C atom is reached [77]. This zone is called the implantation zone and its extent into depth is determined by the width of the ion range (see subsection 2.2.3 *Retention and reemission -Implantation*). With further increasing fluence a major portion of implanted D recombines forming D_2 molecules and a minor portion forms volatile hydrocarbons, both induced

by the entry of energy from the D beam [77]. D is re-emitted at the surface, in the form of molecules (see subsection 2.2.3 *Retention and reemission -Reemission*) and bound in hydrocarbons (see subsection 2.2.2 *Sputtering -Chemical sputtering*). The non-released part of the implanted D may diffuse into depth, along pore surfaces and grain boundaries, and through micro channels (see subsection 2.2.3 *Retention and reemission -Diffusion*).

In the following those underling mechanisms are described, which lead to basic dependences on the experimental conditions, such as specimen temperature, D energy, fluence of incident D, the type of the C material, and its structure and morphology.

2.2.1 Reflection

In [96] a review about status of knowledge of ion backscattering from solid surfaces is given:

Reflection is a kinetic process. Penetrating projectiles suffer an energy loss through collisions with electrons and nuclei of the target. A minority of the projectiles are scattered under an angle larger than 90°, i.e. the projectile is backscattered. Backscattered particles leave the target after their travel towards the surface, if their energy is sufficient to overcome the surface barrier. The projectile may suffer one backscattering process under an angle close to 180°, followed by multiple forward scattering processes. Multiple backscattering processes under scattering angles slightly larger or lower than 90° are possible, too. In both cases the energy loss is straggling. Reflected particles escape the target with different energies and angles. The angular distribution of reflected particles is cosine-shaped. The total number of reflected particles per incident particle is denoted as particle (number) reflection coefficient and the ratio between the total reflected energy and the energy of the projectile is denoted as energy reflection coefficient. Both reflection coefficients depend on the energy of the incident particle and the angle of incidence. In general, a decrease of reflection is observed with increasing projectile energy and decreasing angle of incidence. In both cases, projectiles reach larger depths normal to the surface and thus the energy loss during the travel to the surface is larger. The reflection coefficient may also depend on the structure of the material, since it influences the energy loss. For instance, in an amorphous structure the energy loss is larger than in a crystalline structure. Projectiles reach lower depths, and thus the reflection coefficient is enhanced compared to crystalline structures. A roughened surface may also exhibit a changed reflection coefficient. On one hand, projectiles may reach lower depths normal to a surface segment, leading to an enhanced reflection. On the other hand, particles reflected once may penetrate into a neighbouring hump again where, only a potion is reflected again, decreasing the overall number of reflected particles. Note that the reflection coefficient changes with temperature, if the structure, e.g. surface roughness and crystalinity, changes with temperature.

In [78] energy and angular dependence of the total particle and the total energy reflection coefficients are listed for a large number of elemental targets, and light (D and helium) and heavy (mainly noble gases and self-bombardment) bombarding atoms. This data base includes results from various measurements and computer simulations. In figure 2.1 calculated particle and energy reflection coefficients taken from [78] are given for C and for W, bombarded with D of energies between 10 eV and 1 keV and under various angles of incidence between 0° and 55°. Reflection coefficients taken from [97] are inserted. For C and for W bombarded with D of 200 eV and at 0° angle of incidence the total particle reflection

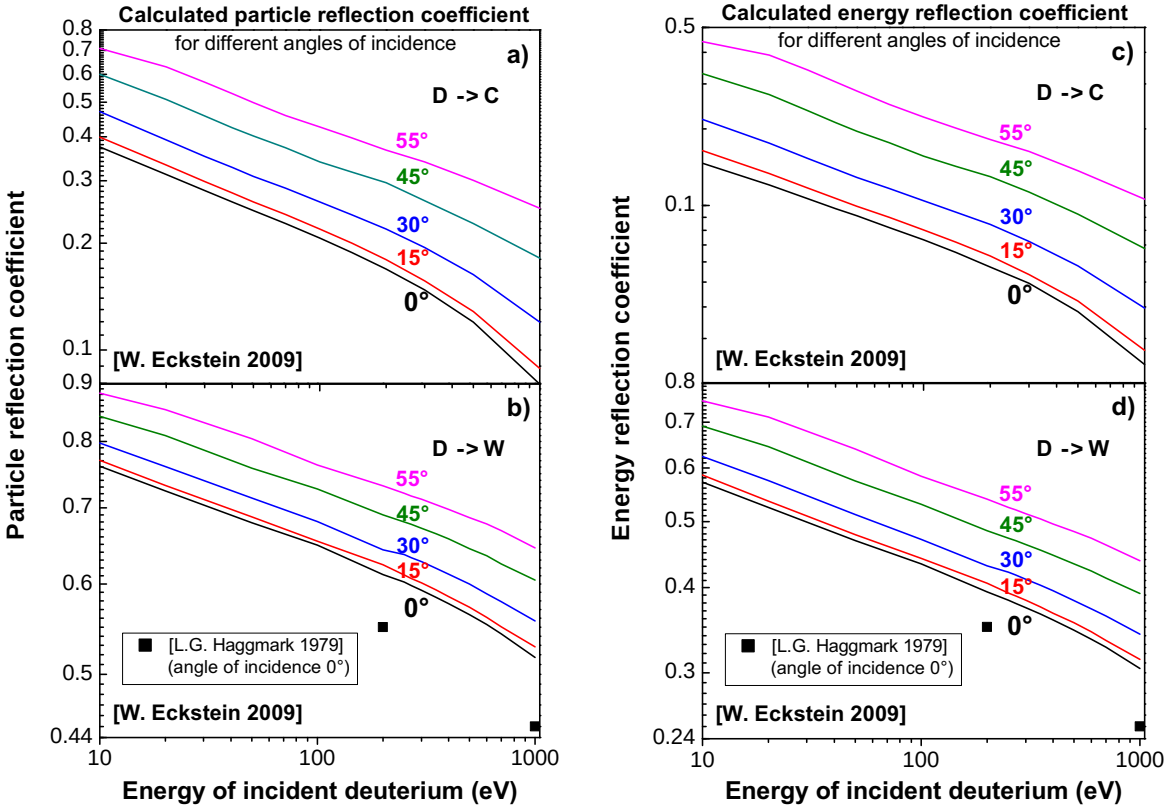

Figure 2.1: Calculated (a), (b) particle and (c), (d) energy reflection coefficients taken from [78] for C and for W, bombarded with D of energies between 10 eV and 1 keV and under various angles of incidence between 0° and 55°. For W reflection coefficients are given in [97] as well (symbols).

coefficient is about 0.17 and 0.6, respectively.

2.2.2 Sputtering

Sputtering leads to a removal of particles, due to energetic particle bombardment at the surface of the target material. This effect is observed for all materials and is of great interest in fusion research. Energetic particles that escape the magnetic cage in the fusion vessel have the ability to destruct each plasma facing material. Wall atoms are ejected into the scrape off layer (SOL). The extent of the destruction differs within different sorts of materials and depends on the sputtering yield. Materials with a low sputtering yield are thought to be suitable for use as plasma facing material.

The sputtering yield is defined as the ratio between the mean number of removed atoms per incident particle [98]. For C bombarded with D three categories exist:

- Physical sputtering [98]: A kinetic process, which exhibits a strong energy dependence with a threshold behaviour. Physical sputtering shows no temperature dependence.
- Chemical sputtering [77]: This process is caused by the chemistry between D and C. It depends on temperature, energy, particle flux, isotope species and on the type of C material.

- Radiation enhanced sublimation [77]: This process is observable in graphite for temperatures above 1200 K. By an additional entry of energy through the impacting D individual C atoms sublimate already at temperatures well below the sublimation temperature. These atoms are interstitials, removed from their site by the energetic D.

The sputtering yield of doped C is known to be different compared to pure C. This is due to the shielding effect and due to a changed chemistry between D and C, induced by the presence of the dopant [77].

Some experimental methods analysing the mean number of removed atoms exist. In many cases weight loss measurements are applied. Alternatively, the mean number of removed atoms can be identified with the change of the areal density of a thin layer, obtained from Rutherford backscattering spectrometry.

Physical sputtering

In [98] a review about status of knowledge of physical sputtering is given:

Physical sputtering can be explained by underlying physical mechanisms. The energy of the impacting projectile is transferred to the nuclei and to the electronic shell of the target atoms, while travelling through the target material. The relaxation of excited states will result in atomic motion, if the binding energy at the lattice is overcome in the same time scale as the relaxation processes (the rest will end up in heat and bulk radiation damage, i.e. ionisation, disordering, etc.) [98]. A primary recoil atom is created, being scattered during the travel through the target. The energy of the recoil atom depends on the extent of the energy transfer from the projectile and thus on the ratio of the masses of projectile and recoil atom. For light ions (H^+, D^+, He^+) with energies above 10 keV the energy is transferred to further target atoms producing secondary recoil atoms and subsequently a recoil cascade. Each recoil atom with a momentum directed towards the surface and a larger energy than the surface binding energy, i.e. the heat of sublimation (7.41 eV for graphite and 8.68 eV for W [99]), is ejected at the surface [98]. Therefore, the sputtering yield depends on the ratio of the masses of projectile and recoil atom. The angular distribution of sputtered particles is cosine-shaped, in the case of normal incidence, and the distribution of the energy of sputtered particles has a maximum around the half value of the surface binding energy.

Recoil atoms produced at surface near layers result in the highest sputtering yield. Their energy is usually larger than the surface binding energy, after a short pathway towards the surface. Surface near recoil cascades are created for low projectile energies and high angles of incidence, which exhibit low penetration depths normal to the surface, and for close packed target structures, which exhibit a large stopping power. Further properties of the sputtering yield are based on these elementary physical mechanisms. The sputtering yield changes with surface roughness, analogous to the dependence on the angle of incidence. Rough surfaces exhibit small penetration depth normal to the surface tangential. “Since sputtering is dominated by kinetic processes, the sputtering yield does not depend on the temperature, if the temperature is well below the melting temperature [77].”

Data bases for calculated and experimental sputtering yields exists, e.g. [78, 61]. These data bases give data for the energy and the angular dependence of the sputtering yield, for a large number of projectile-target combinations. In figure 2.2 calculated yields of physical sputtering taken from [78] are given for C and W, bombarded with D of energies between 10 eV and 1 keV and under various angles of incidence between 0° and 55°. Experimental

sputtering yields for W, taken from [61], are inserted, too. Curves show a common shape, i.e.

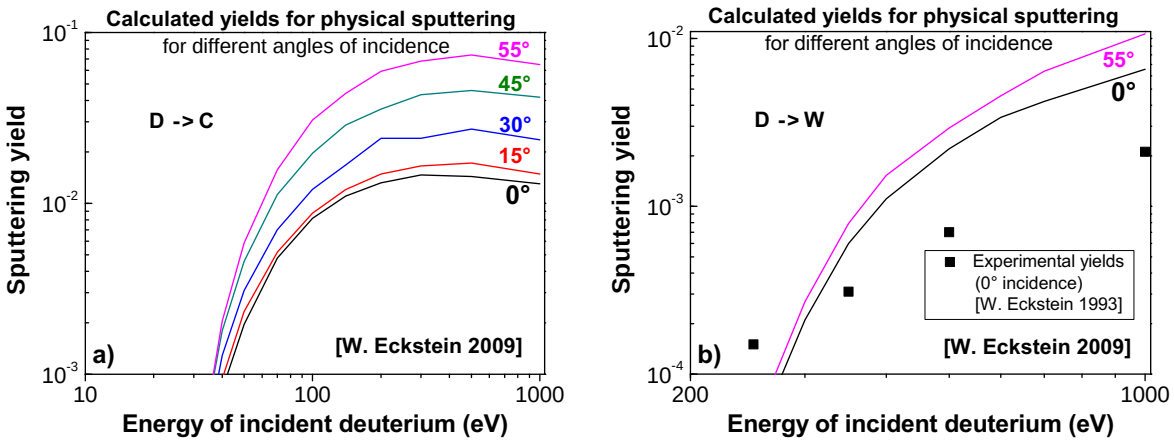

Figure 2.2: Calculated yields of physical sputtering taken from [78] for (a) C and for (b) W, bombarded with D of energies between 10 eV and 1 keV and under various angles of incidence between 0° and 55°. Experimental yields for W (symbols) are taken from [61].

a threshold energy and a maximum. Note that for W experimental yields under normal incidence do not match the calculated yields under normal incidence. Given data points suggest a lowered increase of the experimental sputtering yield compared to the calculated. Therefore, the experimental yields suggest a lowered threshold energy compared to the calculated yields. Especially at an energy of 1 keV the experimental yield is decreased by a factor of five. This discrepancy between experimental and calculated yields of physical sputtering of W is suggested to be due to the presence of oxides at the surface of W [61].

Calculated yields for C have a strong dependence on the angle of incidence. For instance, the yield around the maximum increases by a factor of ten by increasing the angle of incidence from 0° to 55°. This suggests a strong effect of roughening for pure C exposed to 200 eV as well as to 1 keV D. The influence of the angle of incidence on the calculated yields of W is however gentle, i.e. it leads to an increase of a factor of two around the maximum. For a pure W enrichment zone at the surface of a-C:W roughening would change the sputtering yield only slightly by a factor of two, even at an energy of 1 keV.

Furthermore, for a D beam, containing simultaneously 200 eV and 1200 eV particles, for instance, the threshold energy is of interest. Especially for energies below about 100 eV, no analytical description of the energy dependence of the sputtering yield exists [98]. In this energy range the binary collision approximation is not valid, due to partial screening of the nucleus [98]. For W experimental data are difficult to produce, since error bars are in the order of the measured size [98]. Several attempts at fitting experimental data exist, e.g. [100, 101]. From the Bohdansky formula, the threshold energy is 30 eV and 211 eV for C and for W, respectively [100]. By a 200 eV D beam, W is not sputtered considerably. At 1 keV and under an angle of incidence of 0°, however, the calculated sputtering yield of W is increased to about the half value of C. For C, on the other hand, yields were observed for energies below 30 eV. This is attributed to chemical sputtering.

Chemical sputtering

For C bombarded with energetic D, additional processes are observed that enhance the amount of C atoms removed from the material compared to physical sputtering. This is illustrated in figure 2.3. At energies below 10^2 eV, the experimental sputtering yield is clearly

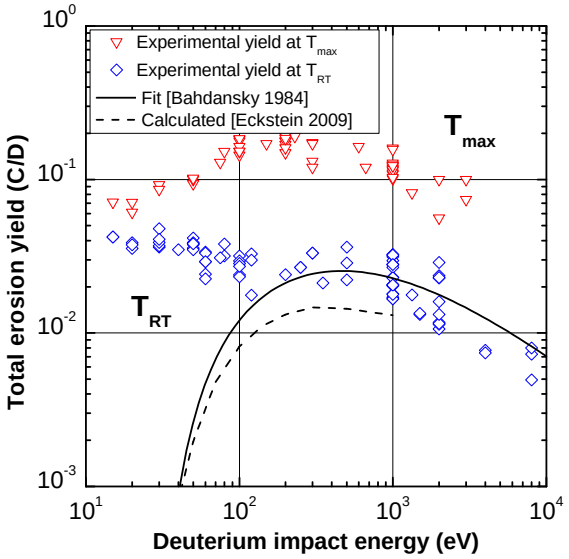

Figure 2.3: Experimental and calculated sputtering yields for C, taken from [102] and from [78], respectively, bombarded with D of energies between 10 eV and 10 keV. Experimental yields (symbols) were obtained by weight loss at fluxes of 1-8·10^{19} m^{-2} s^{-1}. T_{max} is the temperature maximum of the sputtering yield (550-850 K).

enhanced compared to the calculated sputtering yield, which has a threshold behaviour. At energies above 10^2 eV, the given experimental sputtering yields of C are increased by a factor of two at 300 K and by a factor of ten at the temperature maximum of the sputtering yield (550-850 K) compared to the calculated yields for physical sputtering. Since hydrogen is a chemically reactive species, the chemistry between hydrogen and C needs to be taken into account.

In [77] a review about status of knowledge of chemical sputtering of C is given: In the presence of energetic hydrogen, reaction cycles at the end of the ion range lead, if thermally activated, to the formation of hydrocarbons, which are emitted after diffusion towards the surface. The spectrum of volatile hydrocarbons depends on experimental parameters and is dominated by CH_3. CH_4, C_2H_x and C_3H_y species are formed in lower portions. At the surface, loosely bound hydrocarbons, i.e. sp^3-CH_n groups, are easily sputtered as well, even by low energetic hydrogen. In contrast to the energy dependence of physical sputtering, the chemical sputtering yield remains high at low energies, even below the threshold for physical sputtering. Furthermore, this process is characterized by a pronounced temperature dependence significantly below the sublimation temperature of C.

Besides physical sputtering of loosely bound hydrocarbons, which dominates at low energies and temperatures, one of the main underlying processes of chemical sputtering is the thermal chemical erosion. In this context, the terms chemical sputtering and chemical erosion are used according to the definitions given in [77]. Chemical erosion is a thermally

activated process which does not require energetic species, but is pronounced by the presence of defects. Elementary processes of the thermal chemical erosion were investigated by means of the interaction of thermal atomic hydrogen with a thin hydrogenated amorphous C layer on platinum [103], resulting in a reaction cycle that quantitatively describes the individual reaction steps by cross sections and activation energies (see figure 2.4) [77]. During

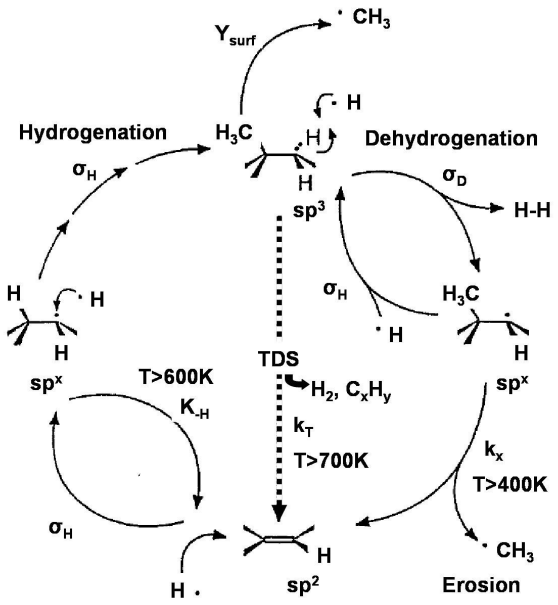

Figure 2.4: Illustration of the elementary reaction steps contributing to the thermal chemical erosion (interaction of thermal atomic hydrogen with a thin hydrogenated amorphous C layer on platinum [103]). σ_i denote cross sections for hydrogenation ($i=h$) and desorption ($i=d$) and k_i denote temperature dependent rate constants ($i=x$: desorption of CH_3; $i=h$: recombination of incoming H with adsorbed H), including activation energies. Picture taken from [77].

irradiation sp^3 bonds are formed by successive hydrogen uptake, at the edges of crystallite planes and at broken sp^2 bonds. At temperatures below 400 K, a steady state is built up (upper right reaction step in figure 2.4). A dehydrogenation process forms hydrogen molecules and leaves a sp^x radical that is converted back to a sp^3 bond by hydrogen uptake. Above 400 K, sp^x sites return to the basic sp^2 configuration, since the desorption of hydrocarbon complexes is thermally activated. Without the presence of thermal atomic hydrogen, however, heating to temperatures above $\sim$700 K leads to a release of hydrogen molecules and hydrocarbons. This is accompanied by a conversion of sp^3 bonds to sp^2 bonds.

These reaction steps explain the temperature dependence of the erosion yield and gives a hint at the influence of structure and energetic species. Two opposing trends lead to a maximum in the temperature dependence of the erosion yield. Above 400 K, hydrocarbon complexes are desorped, i.e. the thermal chemical erosion is initiated. The yield of this thermal process depends strongly on the amount of broken sp^2 bonds, which determines the sp^x formation. Above 600 K, bound hydrogen recombines with the incoming hydrogen beam, forms hydrogen molecules and diffuses towards the surface. For both processes thermally activated rate coefficients exist, determined by activation energies.

The influence of energetic particles was investigated using two independent particle

beams, namely thermal hydrogen atoms, causing the thermal chemical erosion, and argon ions, causing physical sputtering. The erosion rate of simultaneously bombardment with thermal hydrogen atoms and argon ions clearly exceeded the sum of physical sputtering and the thermal chemical erosion. Therefore, it was concluded that chemical sputtering is based on a synergistic effect of physical sputtering and the thermal chemical erosion. Nuclear stopping of energetic hydrogen leads to displacement of target atoms and physical sputtering. The number of broken sp^2 bonds increases and a larger portion of the incoming hydrogen beam is finally bound at sp^x sites. In the reaction cycle, a larger portion of hydrocarbon complexes is desorped from the sp^x sites above 400 K and the thermal chemical erosion is enhanced.

The influence of structure on the erosion yield depends on the energy of the impacting hydrogen. In principle, the degree of hydrogenation changes with the amount of open sp^2 sites, acting as bonds for the uptake of thermalised hydrogen. The edges of graphite planes, for instance, easily react with hydrogen. Therefore, the mosaic spread of the graphite influences the reactivity. Diamond-like C, however, shows a high intrinsic amount of sp^3 sites, and thus exhibits the most reactive C structure in the low energy range. However, at higher energies and with increasing fluence, each C structure is getting amorphous and hydrogenated by the impact of energetic hydrogen. Therefore, the erosion yield is not affected by C structure in steady-state.

Furthermore, the erosion yield is influenced by particle flux and isotope species. In general, chemical sputtering depends on a variety of experimental parameters such as type of C material, sample temperature, ion energy and ion flux [77]. These various parameters show strong, non linear interdependences [77].

Influence of metal-doping

In compound materials a change of the composition of the surface is observed with an increasing amount of impacting D, until steady state is reached. In steady state, atoms are removed stoichiometrically. The change of the surface composition is accompanied by a changing sputtering yield. In most cases preferential sputtering of the lighter component, i.e. C, leads to an enrichment of the heavier component, i.e. the metal [98]. Furthermore, for some compound materials additional processes exist, which influence the enrichment of metal by preferential sputtering, e.g. radiation enhanced segregation or radiation induced solid state reactions [104]. In [104] a study is presented, which investigates the erosion behaviour of Si carbide, Ti carbide and W carbide, i.e. sputtering yields and changes in surface composition due to preferential sputtering, under D bombardment at room temperature in the energy range between 20 eV and 1.5 keV. Thereby, the contribution of different factors to compositional changes, such as physical sputtering, chemical erosion and radiation induced solid state reactions, were studied [104]. The influence of each of these factors varied among the three materials and showed an energy dependence. It is found that the dominant erosion mechanism for carbides is physical sputtering at ion energies above about 5 times the threshold energy [104]. A surface layer depleted of C is formed at lower ion energies, due to preferential erosion of C [104]. In Si carbide, this is due to chemical erosion of C [104]. The surface concentration of Si in steady state decreases with increasing energy, from $\sim$90% at 10 eV to $\sim$60% at 1 keV. In Ti carbide, evidence is given that, at lower ion energies, the surface composition is governed by bombardment induced solid state reactions between

titanium and C [104]. The surface concentration of Ti in steady state obtains values around 70%, nearly constant with energy. In W carbide, the large mass ratio between W and C results in preferential erosion of C, due to threshold effects [104]. The surface concentration of W in steady state slightly increases with increasing energy, from ∼70% at 10 eV to ∼90% at 1 keV. At 200 eV the steady state surface concentration of W obtains values between 80% and 85%. Note that surface concentrations were measured by Auger electron spectroscopy. Values were averaged over the information depth of this analysing technique (up to 1 nm). TRIDYN simulations [105, 106] suggest a strong gradient of metal concentration over the width of the ion range (5-10 nm).

In literature [107, 108] studies exist, which investigate the influence of metal carbide inclusions on the fluence dependence of the sputtering yield (total erosion yield). The total erosion yield was investigated by weight loss measurements and optical emission spectroscopy. Each of these studies showed that the erosion yield is reduced significantly with an increasing total amount of the incoming D particles (fluence of incident D). This is valid for different exposure temperatures and for different energies of the impacting D. Furthermore, from the comparison of results given in [108] with results given in [107] it is evident that the lowering of the sputtering yield by doping is even more pronounced for decreasing grain sizes. The most pronounced reduction of the erosion yield was observed for a-C produced by dual magnetron sputtering deposition, containing finely dispersed metal atoms, e.g. Ti, V, Zr and W [68]. The reduction of the sputtering yield with increasing fluence is attributed to preferential sputtering, which leads metal enrichment at the surface. The depletion of C at surface near zones, which can be reached by energetic D, is assumed to reduce the sputtering yield. Furthermore, an enriched surface exhibits an altered reflection coefficient. Note that the surface may alter its roughness with changing composition. Surface roughness is known to influence kinetic processes leading to sputtering.

Furthermore, the chemistry between D and C can be changed by doping as well. For graphites containing boron (B), for instance, it was observed that the activation energy for hydrogen desorption is lower than the activation energy for hydrocarbon radical emission [109, 110, 111]. Hydrogen is desorped already at temperatures below 600 K. Thus, the reaction chain leading to erosion is interrupted, leading to a drastic reduction of the sputtering yield. This behaviour is attributed to the presence of individual boron atoms at the lattice sites of the graphite, within narrow zones surrounding the grain boundaries between the graphite grains and the boron-carbide grains. Similarly, other dopant materials, e.g. Fe, Ni, Ti, Mo and Si, were investigated [112, 113, 114]. A significant decrease of the erosion yield was observed. Special attention was paid to metal carbide-containing fine grain graphites [107] and to a-C:Me [115, 75, 116]. For the fine grain graphites different metal carbide additions, e.g. Si carbide, Ti carbide, V carbide and Zr carbide, and different grain sizes between 1 μm and 5 μm were analysed [117]. For a-C:Me different dopants, e.g. Ti, W, V and Zr were used, under variation of the dopant concentration. In many cases the temperature dependence of the methane production yield was investigated [115]. The yield of the methane production is lowered and the maximum shifted to lower temperatures compared to pure carbon. This is attributed to a lowered activation energy for the hydrogen desorption. At 300 K and an impact energy of 30 eV, the methane production yield is enhanced in a-C:Me [68]. This is due to changes in the composition of the spectrum of emitted hydrocarbons. In this context, it was also shown that the methane production yield does not represent the total yield of eroded C.

2.2.3 Retention and reemission

A wide variety of graphite materials, pure and doped, as well as C fiber reinforced C (CFC) have been investigated by different research groups with respect to their D retention behaviour. In [74] a summary is given. In many cases the D retention behaviour was characterised by the extent of the accumulation of a D inventory with increasing fluence of incident D. This was carried out under different parameters, e.g. energy, temperature and flux. For each graphite material the same processes influence the accumulation of the D inventory, i.e. implantation, reemission and diffusion. Therefore, the accumulation of the D inventory with increasing fluence is observable as a characteristic curve proceeding (see figure 2.5). For low

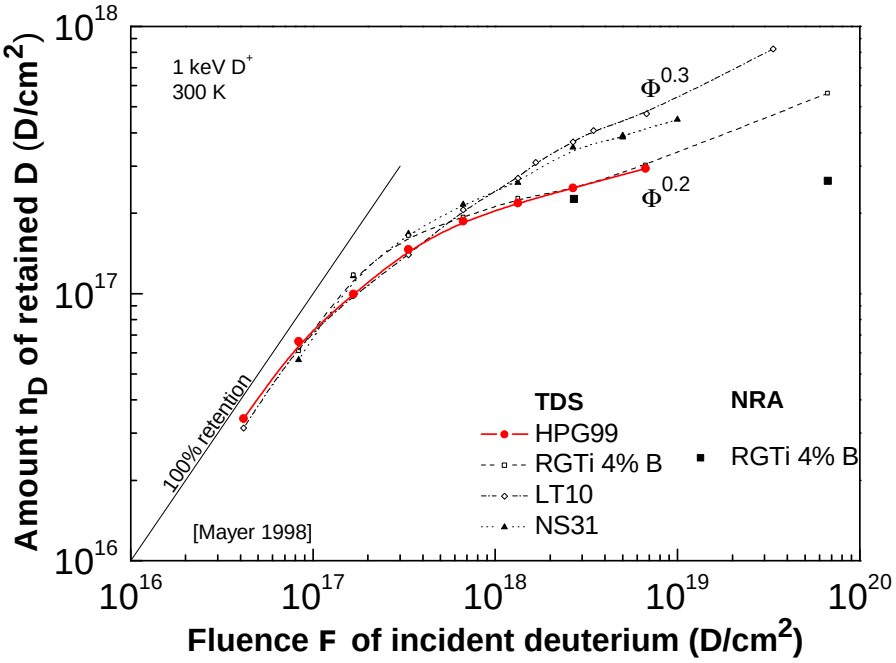

Figure 2.5: Amount of retained D implanted at 300 K versus the fluence of incident 1 keV D, for pyrolytic graphite and different MeC-containing fain grain graphites (Me = B, Si, Ti), at fluences between 10^{16} D/cm^2 and 10^{20} D/cm^2. Data were obtained by thermal desorption spectroscopy (TDS). For RGTi 4% B a comparison was drawn to nuclear reaction analysis (NRA). Data taken from [69].

fluences the D inventory equals the fluence of incident (unreflected) D. Data points follow a line through the origin. Above a certain fluence, which depends on the experimental conditions, the accumulation of the D inventory is slowed down, but a stationary inventory is usually not reached. Data points follow a line in double-logarithmic scale, which exhibits an increase with fluence. This increase of the D inventory with fluence depends on the C material and on the temperature, and is of major interest concerning the D retention behaviour.

Implantation

For low fluences 100% of the unreflected, incoming D is retained in the implantation zone, until saturation is reached over the whole width of the implantation zone. Through the production of radiation damage during the formation of the implantation zone sp^2 bonds are transferred to sp^3 bonds, which serve as trapping sites. After saturation of the implantation

zone a D-containing layer is present at the surface, which exhibits an amorphous structure [77]. The saturation concentration of D in the implantation zone (e.g. 30% at 300 K) decreases with increasing temperature [118] and the width of the implantation zone (e.g. 5.5 nm at 200 eV/D) increases with increasing energy of the isotope [99]. Thus, the amount of retained D in the saturated implantation zone (saturation level) is determined by the saturation concentration and by the width of the implantation zone. At 300 K and at energies between 30 eV/D and 1 keV/D the saturation level is between $\sim 10^{16}$ D/cm^2 and $\sim 10^{17}$ D/cm^2 [77].

As previously mentioned, 100% of the unreflected portion of the incoming D is retained during formation of the implantation zone. This fact gives the possibility to measure the reflection coefficient of a C material. The difference in the amount of incident particles and retained particles results in the amount of reflected particles. Relating the amount of reflected particles to the amount of incident particles gives the reflection coefficient.

Reemission

During the built up of the implantation zone an increasing portion of the incoming D is reemitted in molecular form and bound in hydrocarbons [119]. The latter process is also denoted as erosion, which was already described afore (see subsection 2.2.2 *Chemical sputtering*). In the following, the focus is on reemission of D in molecular form. Bound D is released by the momentum and energy transfer of further incoming D and diffuses locally until it recombines with another locally diffusing D atom. Thermal release in pure C, however, was at first observed at temperatures above $\sim$1000 K. Since the implantation zone exhibits broken bonds, bond angle distortions and thus channels created by the entry of energy, diffusion of molecules is preferentially directed towards the surface. After saturation of the implantation zone is reached, a portion close to 100% of the incoming D is reemitted.

In literature, models exist, which describe trapping and diffusion of hydrogen in C, e.g. [120, 121, 122, 76]. These models assume local saturation, ion induced detrapping and local formation of molecules. Trapping and diffusion can be described by means of experimental parameters, e.g. ion flux, energy and specimen temperature. Good agreement is found to experimental data, within the framework of the experimental accuracies. Besides these models, a model exists, which takes into account diffusion along internal surfaces beyond the width of the implantation zone into depth [123]. It takes the structure of the graphite into account, e.g. porosity and grain size.

Diffusion

In single crystal and dense pyrolytic graphite, implanted D does not diffuse from the implanted region into deeper layers of the bulk for temperatures below 1100 K [74]. After reaching a local concentration of D/C $\approx$ 0.4 at 300 K, further implanted D diffuses - after recombination with another locally diffusing D atom, through channels (broken bonds, bond angle distortions) created by the entry of energy - towards the surface, where it is reemitted [74]. This means, a diffusion of D perpendicular to graphite planes is not possible for temperatures below 1100 K. In fine grain graphite (typical density of $\sim$ 1850 kg/m^3), no saturation of the total amount of retained D occurs [74]. The inventory slowly increases with increasing fluence, even after saturation of the implantation zone is reached and even at temperatures below 1100 K [74]. The diffusion of D molecules over long distances along pore surfaces

and grain boundaries is not only directed towards the surface but also, in smaller portions, towards the depth. This kind of diffusion into depth is not a free diffusion of D, which is governed by the square root over the time, but it is a kind of diffusion, which is delayed by additional mechanisms of trapping and detrapping. In many cases, the increase of the D inventory with fluence along the line in double-logarithmic scale, illustrated in figure 2.5, is attributed to this kind of diffusion of D into depth. The same tendency, but more pronounced, is found in CFCs [74]. The D inventory in the depth exceeds the inventory in the implantation zone. In general, after saturation of the implantation zone is reached, the accumulation of D with further increasing fluence depends on material structure and on temperature [74].

Influence of metal-doping

In literature, only a few studies exist, which investigate the influence of metal-doping on the retention behaviour of C, e.g. [69, 124, 72]. In each of these studies the retention behaviour of doped graphites (with dopants: e.g. B, Si, Ti; concentrations $\leq$20%) was investigated. In [69] the carbides of B, Si and Ti were investigated, additionally. In each of these studies samples were exposed to a D beam with D energies in the keV range, at fluences above saturation of the implantation zone. The amount of retained D was analysed by thermal desorption spectroscopy.

In each of these studies it was found that most of the doped graphites exhibited a larger increase of the D inventory with fluence than the pure graphites. The increase of the D inventory with fluence after saturation of the implantation zone was attributed to a diffusion of D along internal surfaces into depth, beyond the width of the implantation zone. In TDS spectra of these studies, additional desorption peaks were found at lower temperatures for the doped graphites.

In [72] this behaviour was attributed to the presence of dopants. This behaviour was not attributed to differences in the structure, e.g. the porosity and the density, between pure and doped graphites. In [69, 124], however, it is suggested that the extent of diffusion into depth along internal surfaces is affected by the micro structure of the material and that the doped graphites have a larger porosity than the pure graphites. Additionally it was found in [69] that the carbide materials exhibited a changed saturation ratio of D/C in the implantation zone. In Ti carbide, for instance, the saturation ratio is lowered to 0.15 and the D inventory is lowered compared to the pure graphites. This would suggest a changed trapping behaviour at bonding sites in doped graphites.

Concluding, from these studies it can not be decided whether the observed increase of D accumulation in doped graphites is due to changes in the trapping behaviour caused by a changed porosity or whether it is due to the presence of the dopants, changing chemical bonds between D and C.

2.3 Ion beam analysis

The following section describes ion beam analysis, which is an analysing technique suitable to evaluate - based on its mass selectivity and on its depth resolution - the material composition of a specimen, averaged over the whole thickness of a specimen as well as by means of depth profiles. Therefore, ion beam analysis allows to characterize a-C:W by means of total amounts of C and of retained D, as well as by means of depth profiles of W and D.

For Rutherford backscattering spectrometry and nuclear reaction analysis performed in this study low fluxes (1-100 nA) of high energetic protons ($^{+}$H), ^{3}He and ^{4}He particles are used as projectiles, in the energy range between 0.5 MeV and 4 MeV. These experiments are focused on analysing the energy spectrum and on counting the number of backscattered or ejected particles, which are detected at a fixed solid detector angle and at a fixed scattering angle.

The shape of the energy spectrum is influenced by kinematics of scattering and nuclear reaction processes, as well as by stopping powers and energy loss straggling. This offers the possibility to convert energy spectra into depth profiles. The physics behind this is implemented in SIMNRA software [125]. In particular cases surface roughness influences the shape of the energy spectra, too.

The number N of backscattered or ejected particles reaching the detector depends on the areal density of the target material ρ_{areal} (at/cm^2), on the differential cross section dσ/dΩ (mbarn/sr), on geometrical factors of the target-detector-system (detector solid angle Ω (sr), angle of incidence α ($^\circ$)) and on the number of incident projectiles N_0 [126]:

$$N = N_0 \cdot \rho_{areal} \cdot \Omega \cdot d\sigma/d\Omega. \tag{2.1}$$

Rutherford backscattering spectrometry (RBS)

Scattering angle and energy of elastically scattered particles are determined by the binary collision model. The energy of the projectile after an elastic scattering process is defined by the kinematic factor, which is a function of the mass ratio between projectile and target and the scattering angle [126]. This results in the mass selectivity of RBS.

The ratio of the number of particles scattered into a differential solid angle and the number of particles incident on a differential area is defined as a differential scattering cross section [126]. For elastic scattering processes the Rutherford cross section is determined by the kinematics of the binary collision model. It depends on the mass ratio between projectile and target and on the nuclear charge of the scattering partners. It is indirectly proportional to the square of the initial energy of the projectile and, for low scattering angles, to the fourth power over the sine of the scattering angle. The scattering angle shows an anisotropy in its spacial distribution.

The Rutherford cross section applies for a certain range of the projectile energy. The energy range depends on target and projectile material and can be estimated by a formula given in [127]:

$$E_{NR}(MeV) = \frac{M_1 + M_2}{M_2} \frac{Z_2}{10}, \text{ for } Z_1 = 1, \tag{2.2}$$

$$E_{NR}(MeV) = \frac{M_1 + M_2}{M_2} \frac{Z_1 Z_2}{8}, \text{ for } Z_1 > 1. \quad (2.3)$$

E_{NR} is the energy at which the deviation from the Rutherford cross section gets larger than 4% [127]. M_1 and Z_1 are mass and nuclear charge of the projectile and M_2 and Z_2 are mass and nuclear charge of the target material, respectively.

For protons on W and on C E_{NR} is 2.01 MeV and 0.43 MeV, respectively. For alphas on W and on C E_{NR} is 5.11 MeV and 1.33 MeV, respectively. For instance, the cross section of 1 MeV protons and of 4 MeV alphas on C deviates from the Rutherford cross section, while the cross section of 1 MeV protons and of 4 MeV alphas on W does not deviate from the Rutherford cross section, respectively. For 1 MeV alphas both cross sections do not deviate from the Rutherford cross section. For the non-Rutherford cross sections data bases exist, which contain measured data and are tabulated in [127].

Nuclear reaction analysis (NRA)

The main advantage of nuclear reaction analysis compared to Rutherford backscattering spectrometry is its capability of detection of light particles with high sensitivity. It avoids peak overlap of heavy and light elements and especially for target elements, lighter that the projectile, forward scattering of the target atom [128].

In a nuclear reaction, energy (Q-value) is released during the relaxation of the excited nucleus. The sum of the initial energy of the projectile and the energy released is transfered to the reaction products. The emission angle and the energy of the light and the heavy product are determined by conservation laws of energy and momentum [128]. For instance, in the 800 keV D(^{3}He,^{4}He)p nuclear reaction, a collision of a 800 keV ^{3}He projectile with a D atom target at rest, the proton is emitted with an energy of about 14 MeV and the alpha particle with an energy of about 3 MeV. The Q-value of this reaction is about 18 MeV [128].

Usually there is no analytical theory of nuclear reaction cross sections and experimental data need to be used. For many reaction cross sections and their energy dependence data bases exist, e.g. [129]. The total cross section of the D(^{3}He,^{4}He)p nuclear reaction is given in figure 2.6 for different energies of the ^{3}He projectile, up to 2500 keV [129]. In the inlet a magnification is given, in the energy range between 500 keV and 800 keV. The cross section shows a maximum at about 640 keV of about 830 mbarn. Comparing the energy range between 0 and 640 keV to the energy range between 640 keV and 2 500 keV, the curve shows a steep slope at energies below 640 keV and above the descent levels out for increasing energies.

For the study presented in this thesis, an energy of 800 keV was chosen for the ^{3}He projectile. In a-C:W of 1μm thickness the energy loss for the ^{3}He projectile over the whole film thickness is not larger than 300 keV. So the cross section of the D(^{3}He,^{4}He)p nuclear reaction is close to the maximum at each depth of a-C:W, which is reached by the ^{3}He projectile, i.e. the variation of the cross section is less than 15%. This is illustrated in the inlet of figure 2.6. This leads to a high signal-to-noise ratio in the detected signal and thus small amounts of retained D are detectable.

Stopping power and energy loss

The following characteristics make depth profiling possible [127]. The incident projectile (e.g. ^{4}He, ^{3}He) travels through layers of material while it penetrates into deeper layers of the

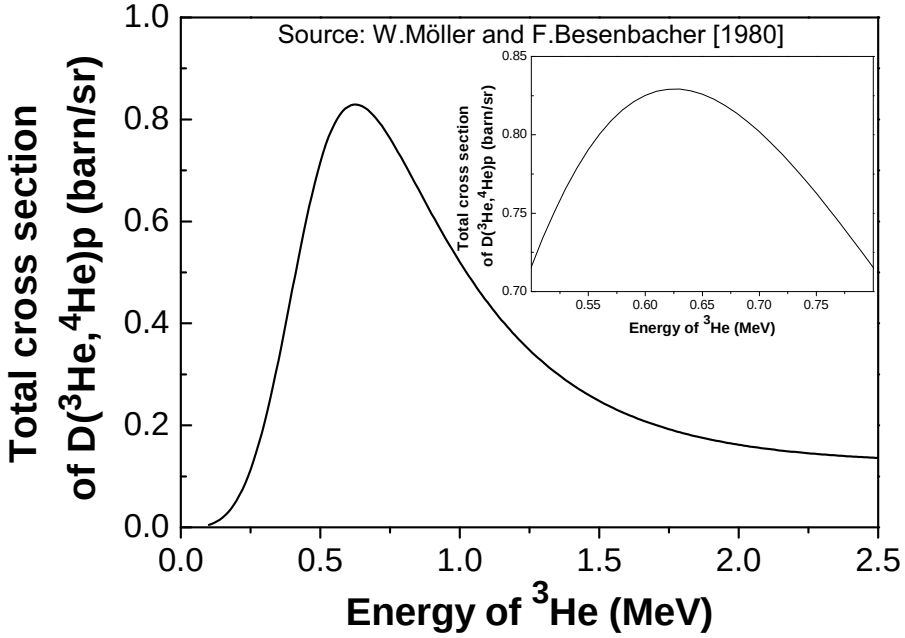

Figure 2.6: Total cross section of the D(^{3}He,^{4}He)p nuclear reaction for different energies of the ^{3}He projectile, up to 2500 keV. In the inlet a magnification is given, in the energy range between 500 keV and 800 keV. Data taken from [129].

bulk, until it suffers a backscattering process (e.g. W(^{4}He,^{4}He)W) or a nuclear reaction (e.g. D(^{3}He,^{4}He)p) at a depth. While passing through layers of material the projectile and the ejectile continuously loose energy. The amount of the energy loss per unit length is denoted as stopping power. The stopping power depends on the composition of the bulk material, on the projectile and the ejectile species and on the energy of the projectile and of the ejectile. Nuclear and electronic stopping exist.

"Anderson-Ziegler stopping" and "Ziegler-Biersack stopping" are the most widely used data bases of energy dependent elemental stopping powers [130, 131, 132]. Elemental stopping powers can be used to describe stopping in compounds. Stopping in a compound is supposed to be a superposition of single interactions taking place with only one atom at a time. Since one interaction with a single atom in a compound and in an elemental target are supposed to lead to the same loss of energy, elemental stopping powers are weighted, in "Bragg′s rule", with the atomic concentration of each compound before superposition [126].

Depth profiling and depth resolution

The following considerations are valid for elastic scattering and for nuclear reactions. The ratio of particles ejected from a unit depth interval to incident particles depends on the reaction cross section (assumed to be constant over a unit depth interval) and on the number of target atoms per unit depth interval (i.e. the areal density of target atoms; see equation 2.1). The energy of particles ejected from the target depends on reaction kinematics and on the extent of the energy loss during their travel from a certain depth to the surface, i.e. the length of its track. This results in an energy spectrum that can be converted into a depth profile of the target atoms. An energy spectrum usually contains peaks, superposing a continuum in some cases. The position of the high energy edge of a peak and of a continuum is determined

by the kinematic factor, i.e. by the projectile-target combination. This enables identification of all target elements, which contribute to the energy spectrum. The peak intensity is determined by the cross section and by the areal density of the corresponding element. The width of the peak is determined by the energetic loss and thus by width (affecting the path lengths) and composition (affecting the stopping power) of the target. Energy spectra are converted into depth profiles using SIMNRA software [125]. SIMNRA software describes depth profiles by a target, which consists of a number of layers with different thickness and composition. The thickness and the composition of each target layer and the number of different target layers are fit parameters. With these fit parameters SIMNRA calculates energy spectra.

In practice the influence of surface roughness needs to be considered. A rough surface consists of humps and valleys, which exhibit variations in layer thickness and the surface normal with position. A particle incident and ejected through a hump would have a different path length than a particle incident and ejected through a valley, assuming both particles were being backscattered at the same position. Since the energy loss for particles with longer path lengths is enlarged, the shape of the energy spectrum of detected particles is affected. SIMNRA approximates the spectrum of a rough film by a superposition of a number of spectra with different layer thicknesses (thickness distribution) [127]. Another approximation is a tilt angle distribution of surface segments (distribution of the local tilt angles) [127]. Both approximations are weighted by a distribution function, i.e. a Gamma function for the layer thicknesses and a Lorentz function for the tilt angles. Both the thickness distribution and the distribution of the local tilt angles have a full width at half maximum (FWHM), i.e. a FWHM of the surface roughness and a FWHM of the distribution of the local tilt angles, respectively. For the thickness distribution the mean value is identified with the thickness of the target layer. With an increasing FWHM of the thickness distribution (FWHM of the surface roughness), the low energy edge is broadened and its height decreases. If the FWHM of the surface roughness exceeds $\sim$60% of the mean thickness, the height of the high energy edge decreases. With an increasing FWHM of the distribution of the local tilt angles, the low energy edge gets a tail. However, both approximations do not take into account correlation effects, such as incidence through a hump and emergence through a valley or multiple surface crossings [127]. Incidence through a hump and emergence through a valley would require two different thickness values. This effect is pronounced for normal incidence. Under gracing incidence, the analysing beam crosses several humps of the rough surface. This process is denoted as multiple surface crossings (see figure 2.7). Multiple surface crossings lead to multiple scattering, energy loss straggling and thus a larger FWHM in the thickness distribution. In the energy spectrum of alpha particles from the D(^{3}He,^{4}He)p nuclear reaction, which are detected at an angle of 102°, multiple surface crossings result in a tail towards lower energies.

Depth resolution and mass separation are two important aspects analysing an energy spectrum [127]. The depth resolution of the energy spectrum is strongly influenced by energy loss straggling. Electronic and nuclear energy loss straggling exist. The latter is also denoted as energy broadening due to multiple scattering (multiple small angle scattering processes). Straggling imposes a spread on the energy of the backscattered projectile after leaving the target. The positions of target atoms that are located at different depths are undistinguishable, if the full width at half maximum in the spread of the projectile energy is larger than the difference in their energetic loss. This effect is especially pronounced for high energetic

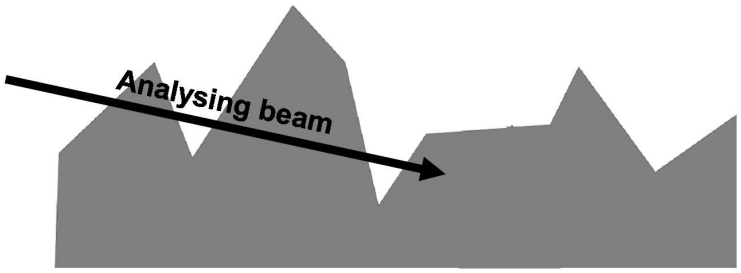

Figure 2.7: Sketch illustrating multiple surface crossings. Under gracing incidence, the analysing beam crosses several humps of the rough surface. Multiple surface crossings lead to multiple scattering, energy loss straggling and thus a larger FWHM in the thickness distribution. Picture taken from [127].

projectiles travelling through a thin layer of target material with a low stopping power and through a rough surface. Straggling reduces mass separation in a spectrum of backscattered particles in a similar manner, if target atoms exhibit only a slight different kinematic factor from each other. Masses can be separated well fixing the detector at a scattering angle close to 180°, e.g. 165°. At scattering angles close to 180°, a small change of the mass of the target atom leads to large changes of the kinematic factor [126]. This produces a large differences in the projectile energy for collisions at different target atoms.

The depth resolution is not only determined by processes, which occur in the target, but also by the detecting system [127]. The detector geometry affects the depth resolution, besides the resolution of the detector. This means, another form of straggling is due to the detector geometry and thus called geometrical straggling. Since the detector aperture and the incident beam have a finite width, particles with different exit angles are allowed to enter the detector. A spread in the exit angle is caused by a spread in the scattering angle and by a multiple scattering. A spread in the scattering angle results in an energy spread, since the energy of the backscattered particle depends on the scattering angle. Multiple scattering results in an energy spread due to path length differences, which are caused by the geometry between the incident beam, the ejected beam and the detecting system. A spread in the path length causes an energy spread, because the extent of energy loss and energy loss straggling depend on the particles path length. Path length differences are especially pronounced in case of a rough surface and its correlation effects.

In converting an energy spectrum into a depth profile of target atoms, the surface roughness and the depth resolution need to be taken into account.

If multiple surface crossings smear out an energy spectrum considerably, the depth, from which an ejectile originates, appears to be increased so that the energy spectrum does not reflect the depth profile of the target atoms. In order to convert an energy spectrum into a depth profile of target atoms, in needs to be checked whether it is considerably affected by multiple surface crossings.

In order to distinguish two different depths of a depth profile of target atoms from one another by means of the energy spectrum, the distance of these depths must be larger than the depth resolution. It is not possible to quantify the thickness and the composition of a target layer by means of the energy spectrum, if the thickness is lower than the depth

resolution. This means, in case of a layer thickness, lower than the depth resolution, the fitting of the energy spectrum with SIMNRA software, which calculates the energy spectrum by means of the thickness and the composition of this target layer, must be possible with an arbitrary combination of thickness and composition, since layer thicknesses lower than the resolvable depth can not be distinguished from one another. The depth resolution depends on the thickness and on the composition of a target layer (i.e. on the energy loss straggling), on surface roughness and on the resolution of the detection system (i.e. on the detector resolution and on the geometrical straggling). The depth resolution of a target layer can be estimated by RESOLNRA software [133].

Without the understanding of the influence of surface roughness and of the depth resolution on the shape of an energy spectrum, it is not possible to convert an energy spectrum into a depth profile of target atoms.

Chapter 3

Investigations under defined conditions

The following sections introduce the experimental setups and the methods used for film production and characterization, specimen exposure and beam profile characterisation, and for analysis of retention and erosion behaviour.

3.1 Film deposition

Pure carbon films (a-C) and tungsten-containing carbon films (a-C:W) were deposited at temperatures near room temperature, without biasing the substrate holder. At these temperatures the mobility of C and W atoms is low. An additional entry of energy (a few hundred eV) may only be created by argon ions, reflected at the cathodes. Phases are formed, which appear to be forbidden in the thermodynamic equilibrium (see appendix F *Analysis of carbide phases*).

For deuterium (D) beam exposure, which was performed for specimen temperatures up to 1300 K, Si (100) wafer fragments were used as substrate material. It was shown that the silicon substrate has no influence on the structure of the C matrix and on the W-C-chemistry inside the film for temperatures of 1300 K and below [68]. For the analysis of the carbide phases (see appendix F *Analysis of carbide phases*) pyrolytic graphite platelets (polished with diamond paste) were used to sustain temperatures up to 2800 K. Silicon wafer fragments and pyrolytic graphite platelets were of 12x15 mm^2 size. Before the deposition process, both silicon and graphite substrates were cleaned in an ultrasonic bath.

Two commercial multi magnetron sputter devices were used (Denton Vacuum Discovery 18, Leybold Unnex 450 C). Both are equipped with a rotating substrate holder. Specimens were arranged on the substrate holder in a manner, which ensures a homogeneous film thickness among the different specimens of one batch. The film thickness varied less than $\sim$3.8 nm along the 15 mm edge of any specimen. This is between 1% and 2% of the removed film thickness after the 200 eV D beam exposure at a fluence of 10^{20} D/cm^2 (see section 4 *Erosion behaviour of a-C:W under D beam exposure*).

Between different deposition runs, the deposition chamber was cleaned by blast air and a vacuum cleaner, and in addition the chamber walls were covered with aluminium foil, in order to minimize the influence of impurities on film growth. A cooling trap was applied, after the chamber was pumped, until a pressure of $\sim 5 \cdot 10^{-5}$ Pa was reached. Substrate cleaning, cathode pre-sputtering and deposition were performed under argon working gas (purity

of 99.999%; Ar flow of 25 sccm in the Denton device and 90 sccm in the Leybold device) at a pressure of $\sim 3 \cdot 10^{-1}$ Pa. For the deposition process W (purity of 99.95%) and graphite (purity of 99.999%) were used as targets. The power at the graphite cathode was supplied by a RF generator (fixed at 500 W in the Denton device and at 600 W in the Leybold device). The W concentration was adjusted by selecting a low power between 2 W and 20 W for the DC discharge at the W cathode. Films with W concentrations between 1% and 22% were produced. After four hours of film deposition, a film thickness of $\sim 1 \mu$m was reached. During the deposition process, the substrate temperature did not exceed 350 K.

The areal density of films and the W concentration was determined by Rutherford backscattering spectrometry with ^{4}He at 4 MeV (angle of incidence 0°, scattering angle 165°). The areal densities and the W concentrations were averaged over the whole specimen area with an accuracy of 10% and 5%, respectively. The particle number density of the films (unit at/cm^3) was obtained by relating the areal density (unit 10^{18} at/cm^2) to the film thickness (unit centimetre). The particle number density for a-C as well as for a-C:W varies between $9 \cdot 10^{22}$ at/cm^3 and $10 \cdot 10^{22}$ at/cm^3, without respect to the W concentration. These values are between the value for a-C:D ($9 \cdot 10^{22}$ at/cm^3) and for the theoretical particle number density of graphite ($11 \cdot 10^{22}$ at/cm^3). The concentration of impurities, such as oxygen, aluminium and argon, was below 2%.

a-C:W was heat treated in a high vacuum furnace to 700 K or 1300 K for 15 min. This is also denoted as a pre-heating at temperature, or as a heat treatment before the D beam exposure; by comparing heat treated a-C:W and non heat treated a-C:W, a-C:W, heat treated at temperature, is denoted by a-C:W, pre-heated at temperature, and non heat treated a-C:W is denoted by as-deposited a-C:W. a-C was produced and analysed in the same manner.

As reference material, pyrolytic graphite was used (Grade HPG, Union Carbide). The graphite planes show a mosaic spread of 20° [122]. Depending on the special process of fabrication, pyrolytic graphite contains micro- and macropores so that the density varies between 0.8 and 2.2 g/cm^3 (the ideal density of graphite is 2.26 g/cm^3) [122]; the density of pyrolytic graphite (Grade HPG, Union Carbide) is $\sim$2.2 g/cm^3. Plates of 12x15 mm^2 size with 1 mm in thickness were cut with their surface aligned parallel to the graphite planes. The surface was polished with a diamond paste and cleaned in ultrasonic bath.

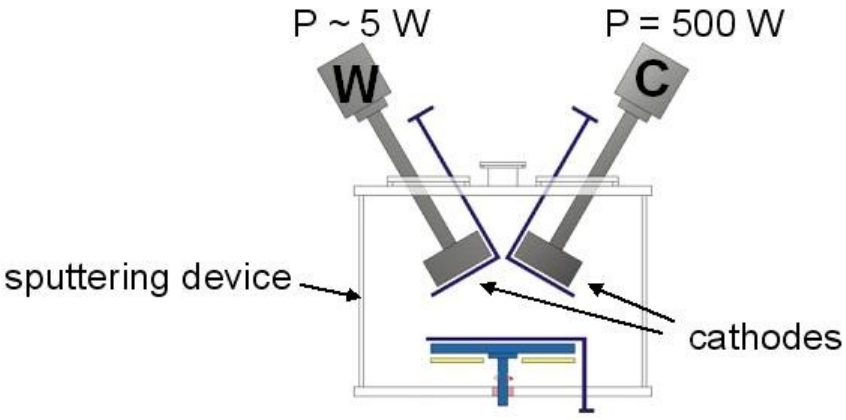

Figure 3.1: Schematic of a sputtering device. Picture taken from [134].

3.2 Specimen exposure

The D beam is provided by the Garching high current ion source (see figure 3.2). It produces

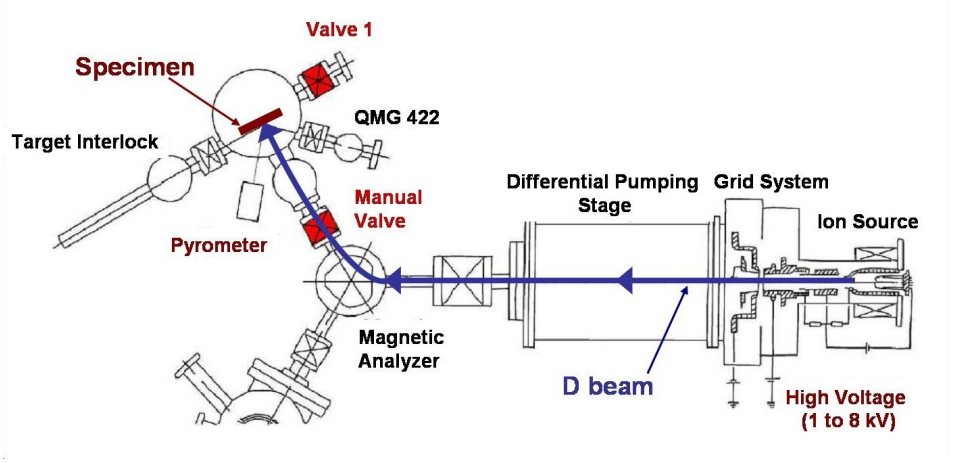

Figure 3.2: Sketch of the Garching high current ion source for light ions. Picture taken from [61].

a high flux of D_3^+ ions, i.e. in the order of 10^{15} D/cm^{2}s. D_3^+ ions are produced in the ion source (Oak Ridge type high current injector). Thereby, D_2 gas is ionized at the cathode. The ion source is working under a high pressure ($\sim 5 \cdot 10^{-3}$ Pa) and under a low discharge voltage (120 V - 150 V), leading preferentially to the formation of D_3^+ ions [135]. Since D_3^+ ions exhibit a lower plasma pressure than D_2^+ ions and D^+ ions, a better focusing of the D_3^+ ion beam is achieved. This avoids collisions with the wall and the rest gas and thus leads to a higher current density.

The D_3^+ ion beam is produced by extracting and accelerating the D_3^+ ions. Through the application of a high acceleration voltage, e.g. 3600 V, the current density is further increased. On its way to the target the ion beam passes several grid systems, which serve as focusing. Between source and magnetic analyser a differential pumping stage prevents major portions of the ion beam becoming neutralized. The magnetic analyser deflects ions with a certain ratio between mass and charge, i.e. 6, into the target chamber towards the target. Species, which were neutralized before entering the magnetic analyser, do not enter the target chamber. Inside the target chamber the ion beam is focused onto the target by two apertures, which serve as ion optic. Finally, the ion beam is decelerated again by a positive bias of 3000 V applied at the target. The D_3^+ ion beam is neutralized by an electron cloud at the specimens surface. Thereby, it splits off into three D atoms. In [136] it was shown that each of the atoms carries one third of the total energy for energies larger than 60 eV/D. For a D_3^+ ion beam accelerated to 3600 eV and decelerated by 3000 V this results in an energy of 200 eV per D atom. Therefore, the experiment is denoted as the 200 eV D beam exposure. Nevertheless, before the D_3^+ ion beam hits the specimen, portions of the beam are neutralized, e.g. at the two apertures in the target chamber. In the incident D beam two particle species simultaneously exist, D_3^+ ions (about 90%) and neutrals (about 10%; see subsection *Beam profile characterization*). In contrast to the D_3^+ ions, the neutrals are not decelerated by the bias voltage. This leads to an implantation energy of 1200 eV/D for the neutrals. In this context, the term "200 eV D beam exposure" always implicates a coaction of 200 eV particles and 1200 eV neutrals.

The experimental setup gives the possibility to count the total number of impacting D atoms during the D beam exposure, i.e. the charge accumulated by the D_3^+ ions. An electronic charge integrator, which is connected to the target, measures the current through the target, which is induced by the charge accumulated by the D_3^+ ions, and integrates the accumulated charge. Secondary electrons, which are produced by the impacting ion, are collected by a Faraday cup. This cup surrounds the target and is grounded. Thus, the integrated charge is adjusted downwards by the charge from the secondary electrons. The entrance of additional secondary electrons into the target chamber, produced at the apertures, is hindered by a second Faraday cup, which surrounds the first Faraday cup and is biased at -50 V below target potential. From the accumulated charge Q (Cb) the total number of impacting D atoms can be calculated, taking into account that an elementary charge e ($1.602 \cdot 10^{-19}$ Cb) is shared by three D atoms. By referring the total number of impacting D atoms to an unit area A (cm^2), a fluence Φ (D/cm^2) of incident D can be calculated:

$$\Phi = \frac{3 \cdot Q}{e \cdot A}. \tag{3.1}$$

The evaluation of the unit area is described in appendix A *Characterization of the D beam profile*. Comparison of equation (3.1) and equation (A.1) results in a value of 0.57 cm^2 for the unit area. This unit area can be identified with an effective area of the erosion spot.

The specimen can be heated by electron bombardment from the rear. The electrons are emitted from a W filament, which is grounded, and accelerated towards the rear side of the specimen, by the positive bias of 3000 V applied at the target. The current through the filament can be increased up to 25 mA. This leads to an increased amount of emitted electrons. For a-C and a-C:W deposited on a silicon substrate temperatures up to 1300 K are possible. The temperature was estimated by optical pyrometry. Two pyrometers were used for that purpose. One pyrometer, a filament pyrometer (Mikro Pyrometer 3725, Pyro-Werk GmbH) is standardized in such a way that it gives a temperature by means of a filament current. Thereby, the brightness of the glowing filament and of the glowing specimen are adapted to each other. The other pyrometer, an infrared pyrometer (TMSR 95/105, Dr. Georg Maurer GmbH), is standardized in such a way that it gives a temperature by means of the intensity of the emitted infrared radiation and the emissivity of the specimen, which can be set by a counter mechanism. The infrared pyrometer was calibrated against the filament pyrometer by changing its counter mechanism. The accuracy of this procedure is ± 50 K. This kind of calibration also gives the possibility to pre-anneal specimens (at $\sim$1300 K, for 15 min). The infrared pyrometer was used to monitor the temperature.

3.3 Characterization technique: Ion beam analysis

After exposing specimens to the D beam ion beam analysis (IBA) was performed, at the IPP tandem accelerator facility [137, 138]. Nuclear reaction analysis (NRA) with ^{3}He at 800 keV (angle of incidence 0°) was performed by analysing the total amount of retained D per unit area (D inventory) and depth profiles of retained D. Rutherford backscattering spectrometry (RBS) under a scattering angle of 165° was performed by analysing the total amount of eroded C atoms per unit area and the depth profiles of W.

The evaluation of the data obtained by IBA was performed with the help of the results from the analysis of the D beam profile. Through the analysis of the D beam profile in each campaign (see appendix A *Characterization of the D beam profile*) it was possible to define a reference zone, which exhibits a calibration factor for the accumulated charge in each D beam exposure. At this reference zone all data was obtained by IBA and related to the fluence of incident D. Details of this method are described in appendix B *Generation of IBA data*.

The analysis of the depth profiles of W and D was performed at a fixed position at the reference zone, since for energy spectra the necessity was given to obtain good statistics through the accumulation of sufficiently high charges, i.e. 20 μCb for the depth profiles of D and 2 μCb for the depth profiles of W. This means, the depth profile of W and of D was obtained from a single measurement, respectively. Analysing total amounts of retained D and of removed C per unit area, however, the number of ejected and backscattered particles was counted by the detecting system. Thereby, an accumulated charge of 1 μCb was sufficient and therefore it was possible to obtain data from a scan across the reference zone, by moving the manipulator one-dimensionally. This resulted in a series of measurements of single values.

3.3.1 Total amount of retained D and removed C

The total amount of retained D per unit area (D inventory) was evaluated by integration of the sharp proton peak in the energy spectrum of protons from the D(^{3}He,p)^{4}He nuclear reaction under an exit angle of 135° (see equation 2.1).

The total number of eroded C atoms per unit area was obtained from the difference between the total amounts of C atoms per unit area, before and after the D beam exposure. Both values were evaluated by integration of the C peak (see equation 2.1) in the energy spectrum of the backscattered particles (i.e. alphas from the 4 MeV C(^{4}He,^{4}He)C Rutherford backscattering process for the initial specimens and protons from the 1 MeV C(p,p)C Rutherford backscattering process for the eroded specimens, both under an angle of incidence of 0°). Note that total amounts of W atoms per unit area, for the initial as well as for the eroded specimens, were recorded by these analysing techniques as well.

The information depth of both analysing techniques is $\sim$1 μm. Since this value exceeds the thickness of the films, the films are probed over their whole thickness.

To determine the total amount of retained D per unit area and of C atoms per unit area in a-C and in a-C:W, in each analysing experiment a one-dimensional scan was performed parallel to the 12 mm edge of the specimen with the rectangular analysing beam spot of 1 x 1 mm^2 size, crossing the reference zone (see figure B.1). Data points generated on a part of the scan overlapping with the reference zone were averaged, resulting in an

averaged amount of retained D per unit area and of C atoms per unit area, respectively. In this context, each averaged value was understood as a mean value from a series of measurements of single values, i.e. of the single data points along the scan. Therefore, each averaged value a standard derivation and thus a relative error was assigned. The relative error was defined as accuracy. The accuracy of the total amount of retained D per unit area and of C atoms per unit area was 10% and 16%, respectively.

In this study, the erosion behaviour was analysed ex situ, after the D beam exposure at a fluence of 10^{20} D/cm^2. The total erosion yield was obtained from the ratio between the total amount of eroded C atoms per unit area and the total amount of incident D particles per unit area. In this context the total erosion yield is defined as an average value over a fluence of 10^{20} D/cm^2, evaluated over the reference zone. The total amount of incident D particles per unit area is defined as fluence of incident D atoms. The fluence is obtained with an accuracy of 16%. Therefore, the accuracy of the total erosion yield is $\sim$20%.

3.3.2 Analysis of depth profiles of W and D

During the D beam exposure, sputtering processes lead to a loss of C atoms near the surface. With increasing fluence, a subsurface layer enriched with W builds up due to preferential sputtering of C. This layer is denoted as the W enrichment zone. However, after the implantation zone is saturated with D, portions of additional D diffuse into depth. Two depth profiles can be found for a specimen, one for the D content and one for the W content. The depth profile of D is gained out of the energy spectrum of the alpha particles originating from the 800 keV D(^{3}He,^{4}He)p nuclear reaction (scattering angle 102°; angle of incidence 0°). The depth profile of W is gained out of the energy spectrum of the alpha particles originating from the 1 MeV W(^{4}He,^{4}He)W Rutherford backscattering process (scattering angle 165°; angle of incidence 70°). Both energy spectra were converted into depth profiles using SIMNRA software [125]. SIMNRA software describes depth profiles by a target, which consists of a number of layers with different thicknesses and compositions. The attempt is to find one target, which describes both depth profiles of a specimen.

Note that NRA and RBS are already well known in literature [126, 127, 128]. Nevertheless, a lack of experience exists in performing depth profiling of W and D on a-C:W. One of the main challenges concerning the analysing techniques used for the studies presented in this thesis was to figure out whether it is possible to perform depth profiling of W and D on a-C:W. Thereby, the most critical issues were the influence of depth resolution and of surface roughness on the shape of depth profiles. For the evaluation of the depth profiles of W and D surface roughness was taken into account by applying atomic force microscopy (AFM). Since the influence of parameters such as W concentration, implantation temperature and fluence on the evolution of surface roughness is not known, it was necessary to figure out, for each specimen, whether it is possible to convert the energy spectrum into a depth profile. Cross-checking was performed once by visualizing the W enrichment zone using cross section scanning electron microscopy (cross section SEM).

Depth profiles of retained D and of W enriched at the surface were analysed for the specimens implanted at different temperatures (300 K - 1300 K) and at a fluence of $\sim 10^{20}$ D/cm^2. At this fluence, depth scales of the profiles are expected to be sufficiently large, so that good prospects were offered avoiding problems with the depth resolution of each utilized analysing method. Thus, a temperature dependences of the width and the composition of

the enrichment zone and a temperature dependences of the diffusion depth and the depth distribution of the D concentration were evaluated.

In the following, the energy spectrum of alpha particles originating from the 800 keV D(^{3}He,^{4}He)p nuclear reaction (scattering angle 102°; angle of incidence 0°) will be denoted by NRA spectrum and the energy spectrum of alpha particles originating from the 1 MeV W(^{4}He,^{4}He)W Rutherford backscattering process (scattering angle 165°; angle of incidence 70°) will be denoted by RBS spectrum.

The conversion of RBS and NRA spectra into depths profiles of W and D is described in detail in appendix C *Evaluation of RBS and NRA spectra*.

Chapter 4

Erosion behaviour of a-C:W under D beam exposure

One important aspect concerning the build-up of T inventory during the activated phase of ITER is the re-erosion of deposited layers, which may lead to an accumulation of T-containing co-deposited layers at remote areas. The time scale relevant for the formation of co-deposited layers certainly depends on the time evolution of re-erosion, i.e. on the fluence dependence of the total yield of removed C. Pure carbon is known to exhibit a constant yield of removed C with fluence, leading to a linear growth of co-deposited layers with time. For tungsten-containing carbon the total yield of removed C deceases with increasing fluence. This would lead to a different time evolution for the formation of co-deposited layers. Here the question is raised whether the erosion of C even can be brought to a stop through the enrichment of tungsten (W) with increasing fluence. Enrichment certainly depends on several parameters. Therefore, tungsten-containing carbon films (a-C:W) were compared to pure carbon films (a-C), by varying the W concentration, the pre-heating temperature and the implantation temperature.

4.1 Enrichment of W: Depth profiles

Results of investigations on the changes of width and the composition of the W enrichment zone with temperature are presented and discussed in the following. W enrichment is expected to affect the erosion as well as the retention behaviour.

Temperature series of RBS spectra

Qualitative discussion: Change of peak width and intensity with temperature

In the following, those RBS spectra are discussed, obtained from the specimens exposed to the 200 eV D beam at a fluence of $\sim 10^{20}$ D/cm^2 and at different temperatures between 300 K and 1100 K. Figure 4.1 shows a temperature series of the RBS spectra of 7.5% a-C:W. The total number of detected alpha particles was normalized on the accumulated charge

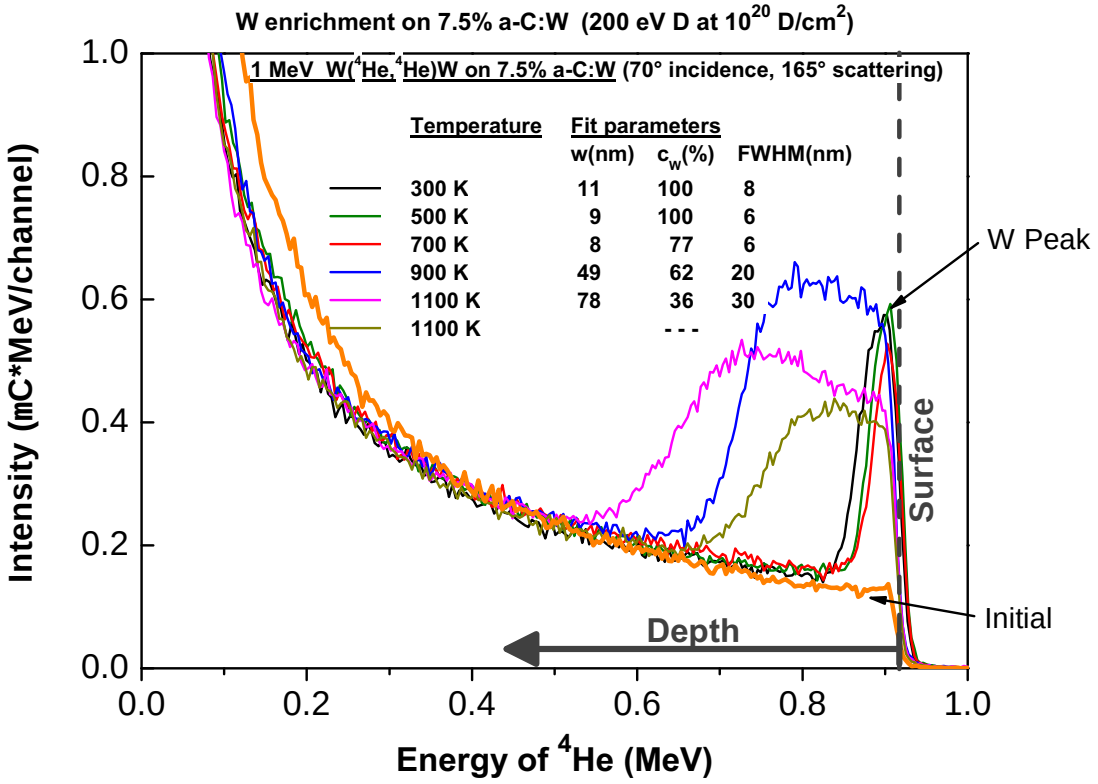

Figure 4.1: The RBS spectra of 7.5% a-C:W, exposed to a 200 eV D beam between 300 K and 1100 K and at 10^{20} D/cm^2. The high energy peak describes the W enrichment zone. For those spectra, which are not affected by multiple surface crossings (see figure E.3; colours corresponding), values for the width w, the W concentration c_W and the FWHM of roughness of the enrichment zone are given, neglecting resolution.

and on the channel width. This normalized value is plotted as intensity over the energy of backscattered alpha particles, in a range between 0 MeV and 1 MeV. All spectra of the temperature series show common characteristics. The intensity in the spectrum is dominated by the W content in a-C:W, since W has a larger Rutherford cross section at any energy than C [127]. A continuum is superposed by a peak at high energies. This means that among the high energetic alpha particles a larger portion was scattered from W than among

the low energetic alpha particles. The continuum exhibits an increase of the intensity with decreasing energy, due to an energy dependent scattering cross section, and for energies below 0.2 MeV due to multiple scattering effects [127]. The peak intensity drops to zero at the high energy side of the peak, i.e. at an energy of ∼0.92 MeV. This value matches the energy of scattered ions from the 1 MeV W(^{4}He,^{4}He)W RBS process, under a scattering angle of 165° [127]. Alpha particles with an energy of 0.92 MeV were scattered from W at the tips of the rough surface and contribute to the high energy edge of the peak [127]. Note, alpha particles scattered from C at the surface have an energy of 0.26 MeV and alpha particles scattered from the silicon substrate reach the detector with energies of 0.15 MeV, for eroded 7.5% a-C:W of 600 nm thickness [127]. Since the intensity in the spectrum is dominated by the W content and since alpha particles with an energy of 0.92 MeV were scattered from W at the tips of the rough surface, the peak is due to an enhanced W content at regions, which are close to the surface, and describes the W enrichment zone. The composition of the W enrichment zone determines the intensity of the peak, since the intensity depends on the Rutherford cross section [127]. The width of the peak, however, is determined by both the width and the composition of the enrichment zone (neglecting multiple surface crossings), since the peak width is determined by the energetic loss, which is affected by the stopping power (i.e. the composition) and by path lengths of alphas (i.e. the width of the enrichment zone) [127]. Furthermore, the peak smears out at its low energy edge. This energy spread is caused by surface roughness and increases with increasing surface roughness, i.e. with increasing FWHM of the surface roughness [127]. The intensity of the continuum is determined by the W content beyond the enrichment zone [127].

Comparing the RBS spectra, obtained at different temperatures, with each other reveals changes of width and intensity of the peak and in the degree of the energy spread at the low energy edge. These changes are small below 900 K. The intensity is nearly constant between 300 K and 500 K. At 700 K, the intensity slightly decreases and the energy spread at the low energy edge slightly increases compared to the energy spread at 300 K and at 500 K. It appears that the W content in the enrichment zone slightly decreases between 500 K and 700 K, from a nearly constant level between 300 K and 500 K. The FWHM of the surface roughness also seems to increase at temperatures above 500 K. The peak width slightly decreases by increasing the temperature from 300 K to 700 K. Since the peak width is caused by the width of the enrichment zone and by the W content, which is already changed at 700 K, no conclusion can be drawn, due to changes of the width of the enrichment zone between 500 K and 700 K. Above 700 K, the width of the peak clearly increases. At 900 K the intensity of the peak is not significantly changed compared to the intensity at lower temperatures. It appears that the W content in the enrichment zone is roughly comparable to the content at lower temperatures, i.e. the enrichment zone seems still to consist of predominantly W. Since the W content is about nearly constant, it appears that the increase of the width of the peak at 900 K is predominantly caused by an increase of the width of the enrichment zone. The energy spread at the low energy edge of the peak increased compared to lower temperatures, which indicates a further increase of the FWHM of the surface roughness.

At 1100 K, two spectra were obtained from different specimens. The width of the peak strongly varies among the two spectra. As discussed in appendix E *Surface morphology: Roughening*, for one of these two specimens multiple surface crossings need to be taken

into account. This specimen exhibits the narrow peak in the RBS spectrum. The width of the enrichment zone can not be quantified for this specimen. (Of course, this looks like a contradiction, since multiple surface crossings result in an energy spread and thus in a larger width of the W peak. Note, it can not be excluded that the width of the W enrichment zone is different among these two specimens, since they exhibit slightly different erosion yields (3.6% for the specimens affected by multiple surface crossings compared to 4.6% for the specimens not affected by multiple surface crossings; see section 4.2 *Influence of W and of pre-heating on total yields of C*). Since the W content is nearly constant among the specimens implanted at 1100 K, it appears that an increased width of the peak can be identified with an increase of the width of the enrichment zone. For a constant W content in the enrichment zone the width of the enrichment zone and erosion yield are proportional to each other.) For the specimen, which is not affected by multiple surface crossings, the intensity of the peak clearly decreased compared to the peak intensity at 900 K. Therefore, the W content in the enrichment zone appears to be decreased. The energy spread at the low energy edge also increased compared to the energy spread at 900 K, which indicates a further increase of the FWHM of the surface roughness at 1100 K. The width of the peak increases compared to the width at 900 K. This indicates an increase of the width of the W enrichment zone.

Looking at the temperature series of the RBS spectra points to a decrease of the W concentration in the enrichment zone with increasing temperature, to an increase of the width of the enrichment zone and to an increase of the FWHM of the surface roughness.

Quantitative discussion: Influence of temperature on width and composition of the W enrichment zone

For those RBS spectra, which are not predominantly affected by multiple surface crossings (see appendix E *Surface morphology: Roughening*), fits were performed by applying SIMNRA software. Thereby, the sum of the minimum resolvable depth (5 nm) and half value of the FWHM of the surface roughness, which was obtained from AFM, were chosen as start value for the thickness of the enrichment zone, and a W content of 100% for the composition. In adapting the fit curve on the RBS spectrum, it was kept in mind that the final value for the width of the enrichment zone must be larger than the sum of the resolvable depth and the half value of the FWHM of the surface roughness. Results of the fits, the width of the enrichment zone, the W concentration and the FWHM of the surface roughness, are given in the inlet of figure 4.1 for each specimen of the temperature series. The resolvable depth was estimated for each RBS spectrum of the analysed specimens by applying RESOLNRA software [133] for the same target composition, which is defined by the results of the fits (see appendix D *Depth resolution of RBS and NRA spectra*). This value was compared to the width of the W enrichment zone.

In performing this comparison it needs to be kept in mind that an uncertainty remains for the thickness of the W enrichment zone, which emerges from the analysing method. This uncertainty is imposed by the depth resolution at the depth, which matches the width of the W enrichment zone, and by the FWHM of the surface roughness; the sum of the squares of the half of the depth resolution and the half of the FWHM of the surface roughness was defined as measure for the uncertainty of the width of the W enrichment zone. Figure 4.2 gives an overview of all length scales relevant for this comparison. The left hand ordinate gives a depth scale and the abscissa gives the implantation temperature. Width of the enrichment

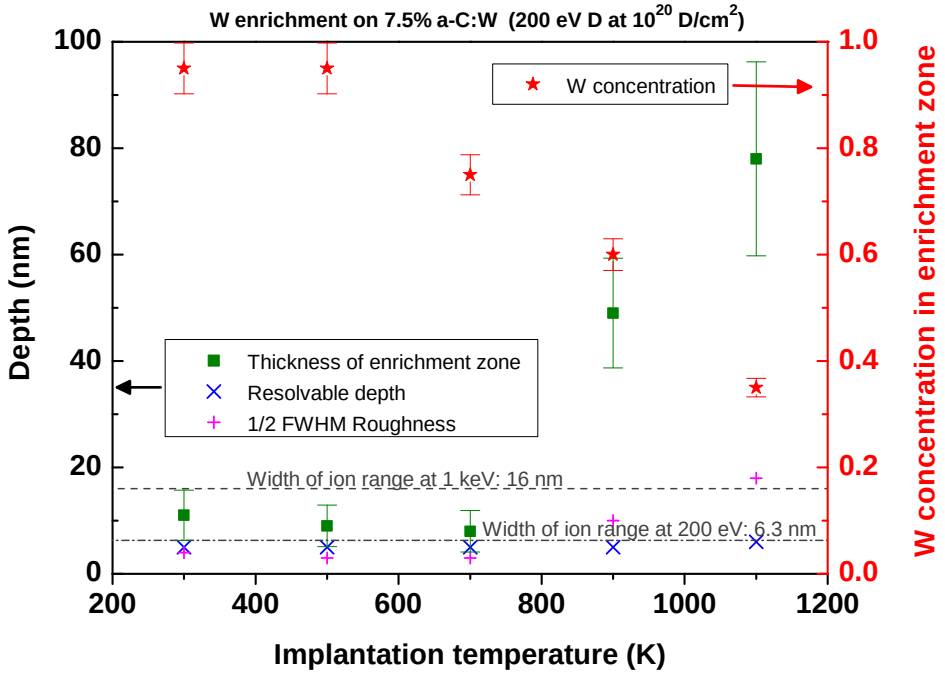

Figure 4.2: Comparison of the width of the enrichment zone with the resolvable depth and the half value of the FWHM of the surface roughness in 7.5% a-C:W, exposed to a 200 eV D beam between 300 K and 1300 K and at 10^{20} D/cm^2.

zone (green square), resolvable depth (blue X) and half value of the FWHM (red plus) refer to the ordinate and thus these length scales are plotted over the implantation temperature, in a range between 200 K and 1200 K. For of each value of the width of the W enrichment zone the uncertainty is marked by an error bar. Additionally, at the right hand ordinate the W concentration (red starlet) is plotted over the implantation temperature. For each value of the W concentration in the enrichment zone the accuracy is marked by an error bar, too. In this case again, only the accuracy of the analysis method is taken into account. The accuracy of the W concentration in the enrichment zone is higher than the accuracy of the width of the W enrichment zone. The accuracy of the W concentration is determined by the accuracy of the integration of the W peak in the RBS spectrum (see equation 2.1). The accuracy of the peak integration is dominated by the accuracy of the charge integration in the RBS experiment, which gives the number of incident projectiles in equation 2.1 and obtains a value of 5%. The W concentration slightly influences the resolvable depth. The influence of the accuracy of the W concentration on the resolvable depth and thus on the accuracy of the width of the W enrichment zone, however, was neglected. (The W concentration is, of course, of interest beyond the framework of the pure comparison of length scales.)

In figure 4.2, two horizontal lines are inserted along the whole temperature range. The dash-dotted line marks the width of the ion range of a 200 eV D beam in pure W (6.3 nm) and the dashed line marks the width of the ion range of a 1.2 keV D beam in pure W (16 nm). At 700 K and below, all length scales are close together. The width of the enrichment zone slightly decrease between 300 K (11 nm) and 700 K (8 nm). The half value of the FWHM of the surface roughness is nearly constant at 3 nm. So the “lowest width” of the enrichment zone (the width of the enrichment zone minus the half value of the FWHM of the surface

roughness) decreases from 8 nm at 300 K to 5 nm at 700 K. Since the resolvable depth is nearly constant at 5 nm, the lowest width of the enrichment zone is just above the resolvable depth at 300 K and just falls together with the resolvable depth at 700 K. Consequently, for 700 K it is not possible to give a final decision whether the width of the W enrichment zone is just resolvable or just unresolvable. Furthermore, taking the error of ± 5 nm into account, it is not possible to decide for any of the data points between 300 K and 700 K whether the width of the W enrichment zone is just resolvable or just unresolvable. Note that at 700 K and below, the width of the error bar (10 nm) matches the difference between the width of the ion range of a 200 eV D beam in pure W (6.3 nm) and the width of the ion range of a 1.2 keV D beam in pure W (16 nm). Therefore, a range must be given for the width of the W enrichment zone for temperatures at 700 K and below, which seems to be valid within the framework of the physical background. This range is given by the width of the ion range at 1.2 keV as the upper limit and at 200 eV as the lower limit. In fitting the W peak at 300 K and at 500 K for different widths of the W enrichment zone within this range, the W concentration must obtain values above 90%. The W concentration is very close to 100% at 300 K and at 500 K so that the W enrichment zone appears to be in steady state at 500 K and below. However, in fitting the W peak at 700 K for different widths of the W enrichment zone within 6.3 nm - 16 nm, the W concentration must obtain values between 70% and 80%. At 700 K the W concentration appears to be decreased to 75%. Above 700 K, the width of the enrichment zone drastically increases with temperature above the width of the ion range at 1.2 keV, above the resolvable depth and above the half value of the FWHM, while the latter value also shows a clear increase with temperature. It is obvious that the width of the W enrichment zone is resolvable at 900 K as well as at 1100 K. The W concentration decreases monotonically to 60% at 900 K and finally to 35% at 1100 K.

Cross-check by cross-section SEM

For the specimens implanted at 300 K and at 900 K the width of the enrichment zone was cross-checked by applying cross section SEM with focused ion beam (figure 4.3). In the

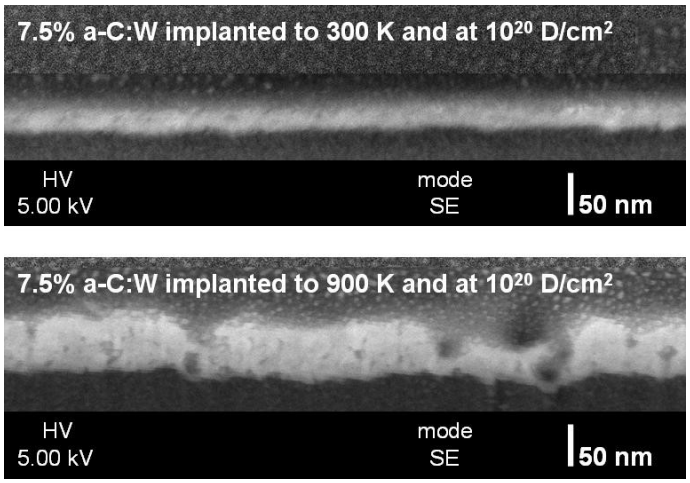

Figure 4.3: Cross section SEM images of 7.5% a-C:W implanted at a fluence of 10^{20} D/cm^2 and at 300 K (top) /900 K (bottom). Light grey area (W enrichment zone) on dark grey area (unaffected 7.5% a-C:W); covered by Pt-C. For the scale a tilt angle of 38° between surface and electron beam is already taken into account.

upper part of figure 4.3 a cross section SEM image of the specimen implanted at 300 K is shown. The light grey area is the W enrichment zone. The W enrichment zone is covered by a Pt-C layer, which is necessary for performing cross sections. The topmost part of this layer was scanned with a higher speed and thus is statistically noisy. This part of the image, however, is not important for analysis. Below the W-enrichment zone a dark grey area is visible. This area of the 7.5% a-C:W is not affected by enrichment. From the width of the light grey area one would estimate a value of $\sim$25 nm for the width of the W enrichment zone at 300 K. This value is hard at the limit of the achievable resolution on these specimens with the applied technique, due to charging of the specimen and drift of the device (Helios Nanolab 600, FEI), so that the grey area appears slightly smeared out. In the lower part of figure 4.3 a cross section SEM image of the specimen implanted at 900 K is shown. This image is composed of the same features as mentioned above; the topmost part of the image is noisy as well. At 900 K, a value of $\sim$65 nm can be read off for the width of the W enrichment zone. Note the dark zones extending partially into the light grey area. These are vacuities filled with the Pt-C layer. The areal coverage of these vacuities is about 5% so that the width of the W enrichment zone does not vary significantly across the reference zone.

4.2 Influence of W and of pre-heating on total yields of C

Within the framework of the analysis of the erosion behaviour at 300 K, results already published [115, 75, 108] were extended, in order to study the influence of the film structure (the structure of C matrix, variations of the W concentration) on the erosion behaviour. Specifically in [108], it was shown that the total yield of C decreases with increasing metal concentration of the metal-containing carbon films, e.g. titanium- and vanadium-containing carbon films exposed to a 30 eV D plasma. The data base of a-C:W, however, is less profound. Furthermore, the erosion behaviour was analysed, in order to identify those changes in a-C:W, which were caused by erosion and influenced the D retention behaviour.

The erosion behaviour at 300 K was analysed by comparing the total yield of C of a-C and a-C:W exposed to a 200 eV D beam at a fluence close to 10^{20} D/cm^2. It was ensured that yields, which were compared with each other, were obtained from specimens implanted in a fluence range, in which the change in the total yield of C with fluence is small [108]. The total yield of C was obtained from the amount of removed C, which was obtained ex situ using ion beam analysis.

Investigations of the influence of film structure on erosion were carried out by varying two parameters, which are known to influence the film structure [68], i.e. the W concentration ($\leq$15%) and the annealing temperature ($\leq$1300 K).

Figure 4.4 shows the total yield of C for a-C and a-C:W, which were heat treated at different temperatures (prior exposure) and contain different W concentrations up to 15%.

Firstly, some considerations are made with regard to units used in context with the results discussed here. The total yield of carbon - averaged over a fluence range of $\sim 10^{20}$ D/cm^2 - is given as a percentage and can be read off from the prefix of the ordinate in figure 4.4, for comparison with the literature data given in [115, 75]. On the other hand, the amount of removed C is suitable for discussion of the results obtained for a-C:W. Since the total yield of C of a-C:W was obtained at a fluence close to 10^{20} D/cm^2, the amount of removed C

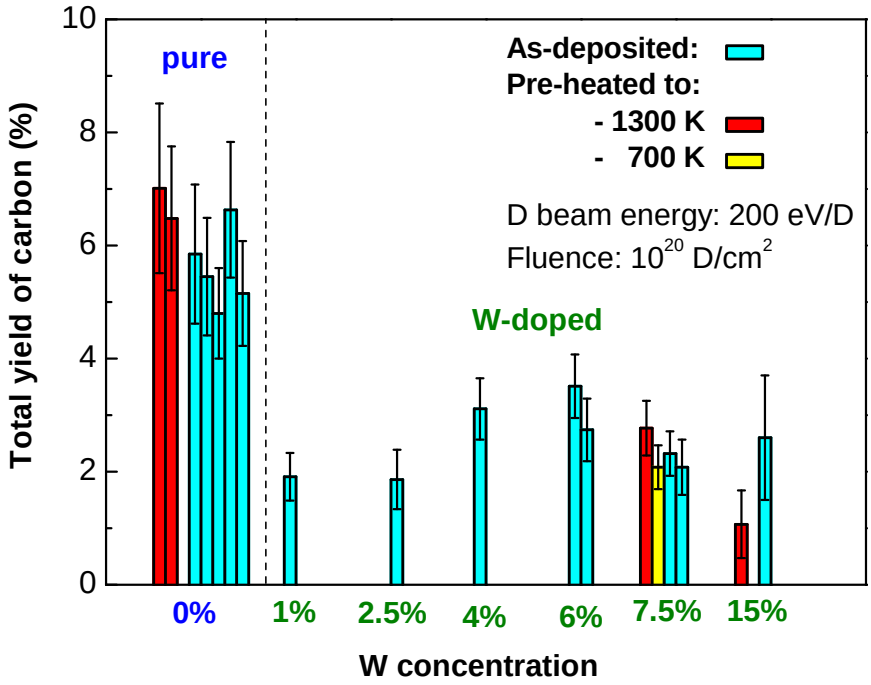

Figure 4.4: Total yield of C analysed by RBS with $^{+}$H at 1.5 MeV on a-C and a-C:W, implanted at 300 K with a D beam of 200 eV/D up to a fluence of $\sim 10^{20}$ D/cm^2. The accuracy of the data is about 20%.

can be - given in units 10^{18} at/cm^2 - read off from the prefix of the ordinate, too. This value does not differ from the value of the measured amount of removed C, within the accuracy of 20%. Note, the unit 10^{18} at/cm^2 describes a length scale and can be converted into the unit nanometre, using the literature data ($1 \cdot 10^{18}$ at/cm^2 equals 88 nm for C and 158.3 nm for W; assuming a dense material.) [127].

For W atoms the signal-to-noise ratio in the RBS experiment was too small, since the ratio between the amount of removed W atoms and the amount of removed C atoms is roughly 1%. Data and thus yields obtained for W are fluctuating by an order of magnitude. Therefore, yields of W can not be taken into account with regard to these results.

For the first step, the influence of pre-heating and thus of the structure of the C matrix on the erosion behaviour is figured out by means of the data points for a-C, for 7.5% a-C:W and for 15% a-C:W. In the second step, the influence of W on the erosion behaviour of a-C:W as well as the influence of changes of the W concentration are evaluated. Thereby, additional data points for 1%, 2.5%, 4% and 6% a-C:W are included.

For a-C, which was pre-heated at 1300 K, two data points are given. The difference of the total yield of C is about 0.005 and thus smaller than the error of each data point. The total yield of C may be averaged to 0.068. For a-C, which was not heat treated, five data points are given. The largest value and the lowest value of the total yield of C differ by about 0.02 from each other. Nevertheless, error bars are still overlapping. This means, the total yield of C does not vary significantly among these five specimens, within the accuracy of 20%. The average is 0.055 and the standard deviation is 0.007. This gives a relative deviation of 13% and thus an accuracy of 13% for the average value of the five data points. Even within this accuracy, it is not possible to distinguish the total yield of C between the non heated and the

pre-heated specimens. This leads to the conclusion that heat treatment and thus the structure of the C matrix does not influence the erosion behaviour of a-C. Therefore, it is possible to give one average value for the total yield of C of a-C: 0.059. The standard deviation is 0.008. This leads to an accuracy of 14%.

For 7.5% a-C:W and for 15% a-C:W the situation is similar. For 7.5% a-C:W, which were not heat treated, two data points are given. The total yield of C differs by 0.003, which is smaller than the error of each data point. Therefore, an average can bee given (0.022), which is between the values of the heat treated films (0.021 at 700 K, 0.028 at 1300 K). Among these three values, the largest and the lowest value differ from each other by 0.007. This difference is smaller than the error of each of 7.5% a-C:W, which is 20%. This means that it is not possible to distinguish the total yield of C between the non heated and the pre-heated 7.5% a-C:W. For the total yield of C of 7.5% a-C:W an average can be given: 0.023. The standard deviation is 0.003. This leads to an accuracy of 13%. For 15% a-C:W, which was not heat treated, the error bar is 43%, since data were scattering along the scan through the reference zone. The total yield of C of the non heated and the pre-heated 15% a-C:W differs from each other by 0.015. Nevertheless, no difference can be found, within the accuracy of 43%. For 15% a-C:W heat treatment does not influence the total yield of C. For the total yield of C of 15% a-C:W an average can be given: 0.018. Among the two data points the larger error bar dominates. So the relative error is 43%. For 15% a-C:W as well as for 7.5% a-C:W comparison of the total yields of C of the heat treated and the non heated specimens shows that heat treatment and thus the structure of the C matrix does not influence the erosion behaviour.

With the average values for the total yield of C of a-C, of 7.5% a-C:W and of 15% a-C:W, the influence of W on the erosion behaviour of a-C:W as well as the influence of the changes of the W concentration can be evaluated. Additional data points for 1%, 2.5%, 4% and 6% W are included. Within the accuracy of 20%, it is obvious that the total yield of C is lower for a-C:W compared to a-C. For a-C:W the total yield of C varies slightly with the W concentration (0.019 for 1% and 2.5%, 0.031 for 4% and 6%) so that W inclusions reduce the total yield of C of a-C:W to the half value, or even to one third of the total yield of C of a-C. This reduction agrees well with the literature data given in [75]. (The total yield of C obtained in this study can be identified with the total erosion yield given in [75]). Furthermore, in order to compare total yields of C for different W concentrations, the data points of a-C:W are arranged into three groups. In each of these three groups, films with different W concentrations exhibit values of the total yield of C, which are close together. For the first group, 1% a-C:W and 2.5% a-C:W, the total yield of C is 0.019. For the second group, 4% a-C:W and 6% a-C:W, the total yield of C is 0.031. This value is larger than the value of the first group, within the accuracy of 20%. For the third group, 7.5% and 15% a-C:W, the yield of 7.5% a-C:W (0.023) is not significantly below the yield of 4% a-C:W and of 6% a-C:W, within the accuracy of 0.13. Nevertheless, since 15% a-C:W exhibits a total yield of C, which is slightly lower than that of 7.5% a-C:W, it appears that a slight decrease can be observed for the total yield of C increasing the W concentration above 6%. In fact, the total yield of C shows a weak maximum between 4% and 6% of W.

4.3 Influence of implantation temperature on total yields of C

The thermal chemical erosion sets in at elevated temperatures. In this context, investigations were performed on the influence of W inclusions on the thermal chemical erosion. Therefore, changes of the total yield of C with temperature in 7.5% a-C:W and in a-C were compared with each other.

Figure 4.5 shows the total yield of C, given as a percentage, after the 200 eV D beam exposure at a fluence of $\sim 10^{20}$ D/cm^2 and at different temperatures between 300 K and 1300 K. The logarithmic scale facilitates reading off small values.

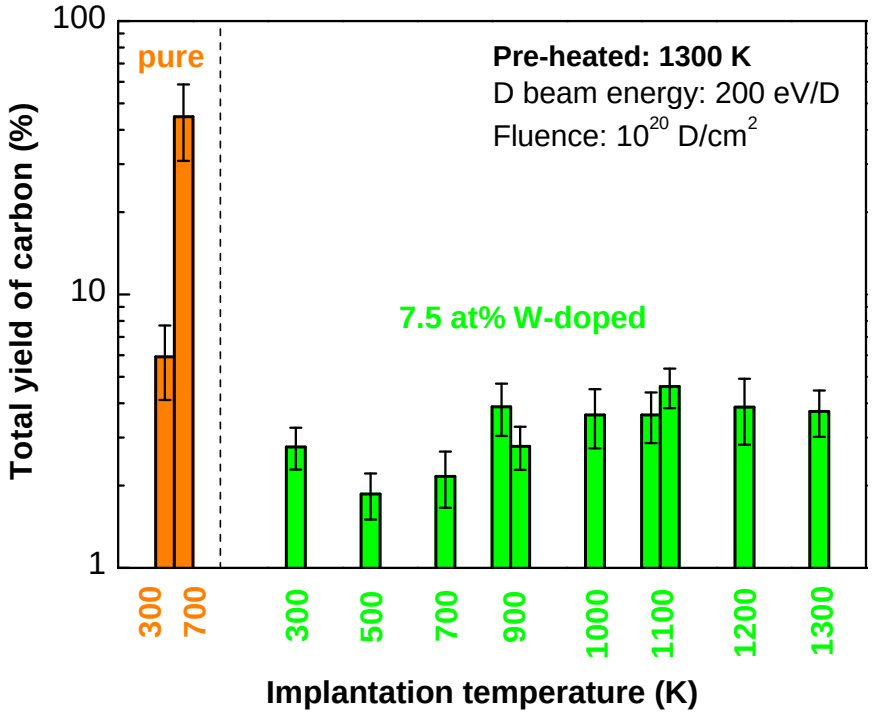

Figure 4.5: Total yield of C analysed by RBS with $^+$H at 1.5 MeV on a-C and a-C:W, implanted at different temperatures (300 K - 1300 K) with a D beam of 200 eV/D, at fluence of $\sim 10^{20}$ D/cm^2. The W concentration and the pre-heating temperature were fixed at 7.5% and 1300 K, respectively. The accuracy of the data is about 20%.

Regarding these results, yields of W are not taken into account. Left hand of the vertical dashed line a-C implanted at 300 K is compared to another one implanted at 700 K. A strong increase of the total yield of C was observed (about a factor of 10) increasing the temperature from 300 K to 700 K. This shows that the thermal chemical erosion is active in a-C implanted at 700 K. Right hand of the vertical dashed line the temperature series of 7.5% a-C:W is shown. Comparing a-C and 7.5% a-C:W implanted at 700 K shows that the total yield of C is significantly reduced for 7.5% a-C:W (to about 1/20). The temperature dependence of the total yield of C of 7.5% a-C:W shows no significant change between 300 K and 700 K, within the accuracy of 20%. At 900 K the total yield of C is increased to the 2-fold (from $\sim$2.3% to $\sim$3.7%). The total yield of C is roughly constant above 900 K, within the accuracy

of 20%. In general, the temperature dependence of the total yield of C is less pronounced for 7.5% a-C:W compared to a-C.

4.4 Summary: Erosion behaviour

The influence of temperature on the enrichment of W was investigated, since enrichment is expected to affect the erosion as well as the retention behaviour. In order to study the influence of temperature on the enrichment of W, depth profiles of W of the specimens exposed to a 200 eV D beam at a fluence of 10^{20} D/cm^2 and at temperatures between 300 K and 1100 K were analysed by RBS with ^{4}He at 1 MeV (scattering angle 165°; angle of incidence 70°). The RBS spectra were converted into depth profiles of W by taking surface roughness and depth resolution into account. At 700 K and below no fixed values for the width and the composition of the W enrichment zone can be given, since the surface roughness is in the same order of magnitude as the width of the enrichment zone and the resolvable depth. For the width of the W enrichment zone a range must be given, which is determined by the width of the ion range in W at 1.2 keV (16 nm) as the upper limit and at 200 eV (6.3 nm) as the lower limit. At 300 K and at 500 K the enrichment zone is in steady state and consists of nearly 100% of W. At 700 K the W concentration is decreased to 75%. At 900 K and at 1100 K, the width of the enrichment zone drastically increases with temperature to 50 nm and to 80 nm, respectively, which is clearly above the width of the ion range at 1.2 keV and the resolvable depth. The W concentration decreases monotonically to 60% at 900 K and finally to 35% at 1100 K.

The erosion behaviour of a-C:W was investigated, in order to assess the accumulation of T through the re-deposition of T-containing hydrocarbons in remote areas. The total yield of removed C was measured by RBS with $^+$H at 1 MeV (scattering angle 165°; angle of incidence 0°), for the specimens exposed to a 200 eV D beam at a fluence of 10^{20} D/cm^2 and at temperatures between 300 K and 1300 K. For implantations at 300 K the W concentration was varied below 20%, since W, which is located next to C at the divertor, is only sputtered under off-normal operation. This leads to lower amounts of sputtered W compared to sputtered C, which originates from the chemistry between C and hydrogen and thus is present under normal operation. For the doped films the total erosion yield is reduced between a half and two thirds compared to a-C. Varying the W concentration does not affect the total erosion yield significantly; at 6% of W the total erosion yield is slightly enhanced. Pre-heating was applied, since co-deposited layers are heat treated during various detritiation techniques. The specimens, pre-heated to 700 K and to 1300 K, were compared to the as-deposited specimens. The total erosion yield is insensitive to pre-heating for a-C, 7.5% a-C:W and 15% a-C:W, i.e. insensitive to changes in chemical bondings inside the C matrix. In order to observe the temperature dependence of the erosion mechanisms in a-C:W, the film structure was fixed. Each film was pre-heated at a temperature of 1300 K. The W concentration was fixed at 7.5%. At an implantation temperature of 700 K, doping with 7.5% W significantly reduces the total yield of eroded C compared to a-C (about a factor of 20). The temperature dependence of the total yield of eroded C of 7.5% a-C:W shows no significant change between 300 K and 700 K. At 900 K the total yield of eroded C is increased to the 2-fold. The total yield of eroded C is roughly constant above 900 K. In general, the temperature dependence of the erosion behaviour is less pronounced for the doped films compared to the a-C.

Chapter 5

Retention of a-C:W under D beam exposure

Another important aspect with regard to the build-up of T inventory during the activated phase of ITER lies in the implantation of T ejected from the plasma. T implanted in deposited layers diffuses into depth with increasing fluence, leading to an accumulation of T in deposited layers. For deposited layers of sufficient thickness the D retention behaviour is of major interest. In this case, the time span, which is necessary to reach the T safety limit, is determined by the increase of the D inventory with fluence. For thin deposited layers the diffusion of T into depth is of major interest. T diffusing through the entire thickness of deposited layers with increasing fluence will accumulate in the underlying W tiles. In this context, the increase of the D inventory with fluence as well as the T concentration at the depth determine the time span, which is necessary to reach the T safety limit.

5.1 Diffusion of D: Depth profiles

In the subsection *Diffusion and Trapping* the influence of temperature on the saturation ratio inside the implantation zone and on the diffusion depth is investigated qualitatively. The influence of temperature on the diffusion depth is quantified in the subsection *Temperature series of NRA spectra*.

Diffusion and Trapping

As previously mentioned in section 2.3 *Ion beam analysis*, the energy spectrum of alpha particles, emerging from the 800 keV D(^{3}He,^{4}He)p nuclear reaction (angle of incidence 0°), is influenced by the depth distribution of D as well as by the correlation effects of surface roughness, e.g. multiple surface crossings. During the D beam exposure, the change in surface roughness with the amount of incident D as well as the diffusion of D in C may depend on the specimen temperature. Therefore, a special investigation was performed in order to figure out whether it is, in principle, possible to see a depth profile of D in a NRA spectrum, which was obtained from a-C:W implanted with D. Thereby, main issue was to figure out whether the shape of the NRA spectrum is dominated by the influence of surface roughness or by the influence of depth profile of D. Within the framework of this investigation, a set

of specimens was exposed to the D beam in two steps. For the first step, fixed parameters (e.g. fluence, temperature) were chosen for each specimen exposed to the D beam, so that each of the specimens would exhibit the same roughness and the same D depth profile just at the beginning of the second step. In the second step, each of the specimens was exposed to the D beam at its own set of parameters (e.g. fluence, temperature), so that the D depth profile and/or the roughness produced in the first step was varied among the specimens. Note, roughness leads to a tail towards lower energies in the NRA spectrum. With increasing fluence this tail must change its extent to lower energies, if roughness changes. If roughness remains constant, the intensity of the tail must increase in equal portions along the whole energy spectrum. This means, the shape of the whole NRA spectrum must change in a certain characteristic, if roughness dominates the shape of the NRA spectrum. On the other hand, if the D depth profile dominates the shape of the NRA spectrum, different characteristics of changes of the NRA spectra would be expected with increasing fluence. The NRA spectrum would be changed in a certain energy range. This energy range represents a depth range, which exhibits a changed D content. By means of the observed changes of the shape of the NRA spectrum with fluence and temperature, it was estimated whether these changes were predominately caused by surface roughness or by diffusion of D.

a-C:W, containing 7.5% W, were implanted at a temperature of 900 K and at a fluence of 10^{18} D/cm^2. At this fluence either the heat treatment or the D beam exposure was stopped. If the heat treatment was stopped, D was implanted at additional fluences up to $\sim 10^{17}$ D/cm^2, while the temperature was decreasing exponentially (relaxation time $\sim$90 s). If the the D beam exposure was stopped, the heat treatment was continued for different time spans up to 36 s. Alternatively the time span was held constant at 300 s and the temperature was increased once to 1100 K and in another exposure to 1300 K. For a comparison the heat treatment and the D beam exposure were stopped, simultaneously, once.

Figure 5.1 depicts the NRA spectra of all 7.5% a-C:W used for this specific investigation. The intensity of detected alpha particles is plotted over the energy of ejected alpha particles, in a sufficiently large range between 1.75 MeV and 3.25 MeV. For the specimens implanted at 900 K and at a fluence of 10^{18} D/cm^2 a continuum is visible between $\sim$2.0 MeV and $\sim$3.0 MeV. For the specimens implanted at different fluences above 10^{18} D/cm^2 (figure 5.1 (a)) this continuum is superposed by a peak at high energies, just below 3.0 MeV. The intensity of the peak increases with increasing fluence and decreasing temperature, while the extent of the continuum into depth and the intensity of the continuum are constant with changing fluence and temperature. This means, the shape of the NRA spectrum changed over a small energy range below 3.0 MeV, of less than 0.25 MeV. As previously mentioned, this kind of change of the NRA spectrum is expected to be due to a changed D depth profile. Changes, which may originate from the influence of surface roughness were not observed. For the specimens heat treated at 900 K after exposure (figure 5.1 (b)) the shape of the NRA spectrum did not change with time. Heat treatment above 900 K (figure 5.1 (c)) led to a decrease of the intensity of the continuum with increasing temperature, not in equal portions along the whole NRA spectrum but pronounced at high energies. The extent of the continuum to lower energies did not change. This kind of change of the NRA spectrum is also expected to be due to a changed D depth profile. Changes, which may originate from the influence of surface roughness were not observed in this case as well.

The following conclusion can be drawn:

For the specimens in this particular investigation the NRA spectra were not predominantly influenced by surface roughness. Therefore, the correlation effects of surface roughness, e.g. multiple surface crossings, can be neglected here and thus it is possible to convert these NRA spectra into depth profiles of retained D.

Furthermore, these results suggest the following interpretations:

1. The peak near the surface ($<$70 nm) in figure 5.1 (a), which was increasing with decreasing temperature, is caused by an accumulation of D at surface near zones, which can be reached by energetic D. Bonding states with a lower binding energy than the thermal energy at 900 K, which were unoccupied before the decrease of the temperature, were becoming occupied during the decrease of the temperature. It is obvious that the saturation level of the implantation zone is lowered at 900 K compared to 300 K.

2. Before the decrease of the temperature, D was able to reach depths, which are beyond the peak near the surface and thus can not be reached by energetic D (i.e. $\leq$600 nm; figure 5.1 (a)). Consequently, it can be concluded that the tail to lower energies in the NRA spectrum is caused by a diffusion of D into depth ($\sim$90% of the total inventory). In a-C:W, D is able to diffuse into depths beyond the implantation zone.

3. Bonding states occupied at 900 K during beam exposure are not depleted after the exposure is stopped (figure 5.1 (b)). This interpretation is confirmed by the release of D towards the surface after the heat treatment at 1300 K (figure 5.1 (c)). Additional bonding states, which were occupied at 1100 K, were depleted raising the temperature above 1100 K.

4. Heat treatment at 1100 K and at 1300 K (figure 5.1 (c)) showed a clear trend of diffusion, which is directed towards the surface without the presence of an impacting D beam. In other words, the presence of a D beam is a necessary condition for the diffusion of D into depth.

The most important message is that the diffusion of D into depth and the number of available bonding states are in convolution with each other. With decreasing temperature the number of available bonding states was increasing. An enlarged number of bonding states enables thermalised D to be trapped inside the width of the ion range and slightly beyond. A low number of available bonding states forces thermalised D to diffuse - under the impact of the incoming D beam, which produces a concentration gradient - beyond the width of the implantation zone into depth (in this investigation: $\sim$90% of the total inventory). This leads to a reduced D/(C+W) saturation ratio inside the width of the ion range and to an enhanced diffusion depth.

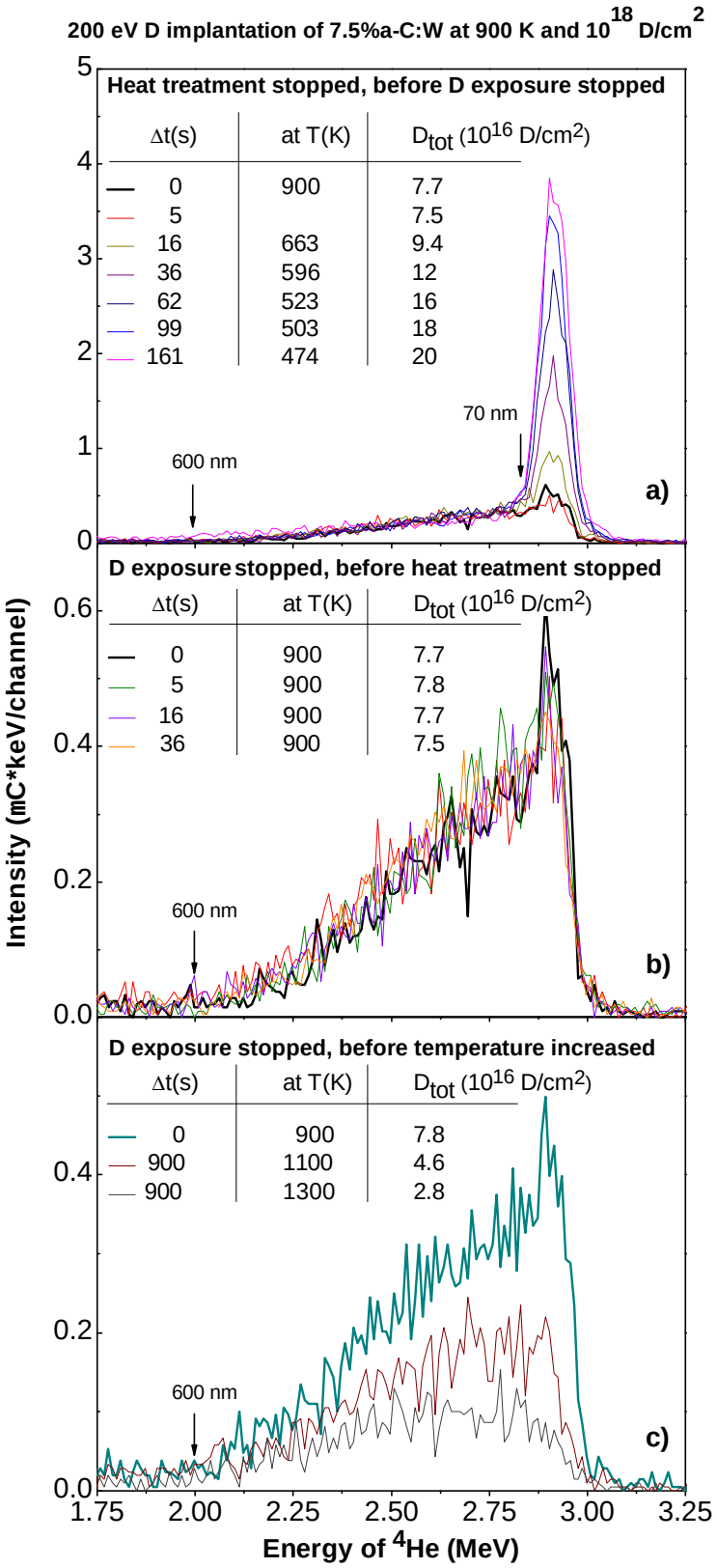

Figure 5.1: Energy spectra of the 800 keV D(^{3}He,^{4}He)p nuclear reaction on 7.5% a-C:W (thickness $\sim 1\mu$m). All specimens were implanted with a 200 eV D beam at 900 K and at a fluence of 10^{18} D/cm^2. At this fluence either the heat treatment or the D beam exposure was continued for different time spans: In (a) D was implanted at additional fluences up to 10^{17} D/cm^2 ($\tau(1/e) \approx 90$ s), in (b) the heat treatment at 900 K was continued for different time spans up to 36 s and in (c) the temperature was increased once to 1100 K and in another exposure to 1300 K, for 900 s each. The amount of retained D, D_{tot}, is listed in the inserted tables.

Temperature series of NRA spectra

In the previous section it was shown that temperature determines the number of available bonding states and thus the diffusion of D. Furthermore, an enhanced diffusion leads to an enlarged diffusion depth and to a lowered saturation ratio inside the implantation zone, which are therefore determined by temperature. Analysis of the D depth profiles aimed to quantify the influence of temperature on the diffusion depth.

Qualitative discussion: Change of peak width and intensity with temperature

In the following, the NRA spectra are discussed for the specimens exposed to a 200 eV D beam at a fluence of $\sim 10^{20}$ D/cm^2 and at different temperatures between 300 K and 1300 K. Figure 5.2 shows a temperature series of the NRA spectra of 7.5% a-C:W. The intensity

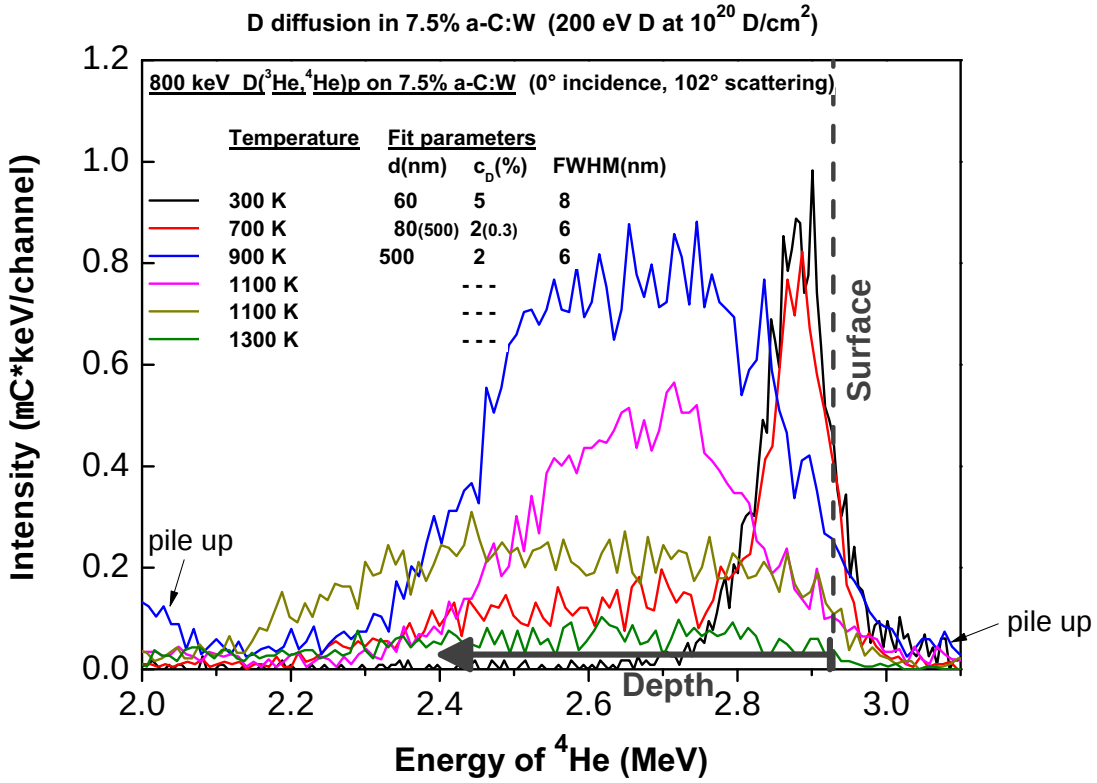

Figure 5.2: The NRA spectra of 7.5% a-C:W, exposed to a 200 eV D beam between 300 K and 1300 K and at 10^{20} D/cm^2. Peaks at 900 K and below describe D depth profiles. Above 900 K roughness influences the peak shape. For those spectra, which are not affected by multiple surface crossings (see figure E.3; colours corresponding), values for the diffusion depth d, the D concentration c_D and the FWHM of roughness of the enrichment zone are given, neglecting resolution (at 700 K additional values are given in brackets, due to the tail into depth).

of detected alpha particles is plotted over the energy of backscattered alpha particles, in a range between 2 MeV and 3 MeV. Each spectrum of the temperature series exhibits a Gaussian shaped peak. (Note that the shape of this peak does not necessarily reflect the depth distribution of the D concentration.) This Gaussian shaped peak originates from alpha particles from the D(^{3}He,^{4}He)p nuclear reaction at 800 keV [128]. The high energy edge

of each of these peaks drops to zero at $\sim$ 3MeV (signals above 3 MeV are pile ups [128]). This value matches the energy of alpha particles from the 800 keV D(^{3}He,^{4}He)p nuclear reaction, under a scattering angle of 102° [128]. Alpha particles with an energy of 2.9 MeV were ejected at the tips of the rough surface and contribute to the high energy side of the peak [128]. The peak intensity depends on the D content and the peak width depends on the diffusion depth and on the depth distribution of the D concentration, similar as previously mentioned in the subsection *Temperature series of RBS spectra* in chapter 4.1 *Enrichment of W: Depth profiles*. The NRA spectra are superposed by a continuum below 0.8 MeV (not shown), which is caused by ^{3}He projectiles backscattered at W, C and the silicon substrate [128]. This part of the spectrum does not describe the D depth profile. In some cases a pile up (e.g. at 900 K; 0.8 MeV - 2.1 MeV) overlaps with the part of the NRA spectrum, which is caused by the alpha particle from the D(^{3}He,^{4}He)p nuclear reaction at 800 keV [128]. In this energy range it can not be distinguished between a D depth profile and a pile up.

From the investigation of surface roughness of each specimen from the temperature series (see subsection *Roughening between 300 K and 1300 K* in appendix E *Surface morphology: Roughening*) it is known that the NRA spectra of specimens, exposed to the D beam at 1100 K and above, are shaped by the D depth profile as well as by the surface roughness. Consequently, it is not possible to quantify these NRA spectra by means of a diffusion depth and a depth distribution of the D concentration at 1100 K and above.

By comparing the NRA spectra obtained at different temperatures with each other, changes of the width and the intensity of the peak are revealed. At 300 K and at 700 K a peak appears at high energies. The peak widths are close together. The peak intensity decreases slightly between 300 K and 700 K. At 700 K a tail into depth is visible. This may be due to multiple surface crossings or due to a diffusion of D into depth. Looking at the distribution of the local tilt angles of this specimen (see figure E.3) shows that about 10% among the local tilt angles are larger than $|12|^\circ$. Therefore, it appears that the influence of multiple surface crossings on the shape of the NRA spectrum at 700 K just can be neglected and thus the tail is due to small amounts of D in the depth. The diffusion of D into the depth appears to increase already at 700 K. Note, in section 5.3 *Influence of implantation temperature on accumulation of D* it will be shown that the increase of the D content with fluence is increased at 700 K (exponent over the fluence equals 0.14) compared to 500 K and 300 K (exponent over the fluence equals 0.10 in both cases). For the increase of the D inventory with fluence it is concluded that the influence of temperature becomes dominant between 500 K and 700 K. This conclusion agrees with the change of the D depth profile between 300 K and 700 K.

At 900 K the peak width increases strongly so that the peak extends over the same energy range, which is covered by the high energetic peak at 700 K and the tail into depth. The diffusion depths appear to correspond at 700 K and at 900 K. The intensity of the peak is larger over the energy range, which is covered by a tail at 700 K. So, the depth distribution of the D concentration at 700 K appears to differ from 900 K, i.e. at 900 K the amount of D trapped in the implantation zone is lower and the amount of D diffused into depth is larger.

Above 900 K multiple surface crossings dominate the shape of the NRA spectra. A look at the distribution of the local tilt angles of the specimens implanted at 1100 K and above (see figure E.3) shows that about 27% (magenta curve) and 30% (dark yellow curve) among the local tilt angles are larger than $|12|^\circ$ at 1100 K. At 1300 K this portion increases to 32%.

This means, the effect of multiple surface crossings increases with increasing temperature, which is observable as an increase of the width of the peak and as a decrease of the overall intensity of the peak.

Altogether, a change of the shape of the NRA spectrum is observable with increasing temperature, i.e. the peak maximum shifts to lower energies. Therefore, looking at the temperature series of the NRA spectra points to an increase of the diffusion depth and to a changed depth distribution of the D concentration; the saturation ratio in the implantation zone appears to be lowered. The influence of temperature becomes dominant between 300 K and 700 K, which is observable as a tail into depth at 700 K. This means, at 700 K the diffusion depth is larger than the resolvable depth, in contrast to the case at 300 K.

Quantitative discussion: Influence of temperature on diffusion depth and D concentration

In this context, there is need to quantify the diffusion depth and the depth distribution of the D concentration for the specimens implanted between 300 K and 900 K. This is figured out by taking the resolvable depth into account (see appendix D *Depth resolution of RBS and NRA spectra*). Fits were performed on the NRA spectra, by taking the width and the composition of the W enrichment zone into account, for each specimen, implanted between 300 K and 900 K. Results of the fits, the diffusion depth, the D concentration and the FWHM of the surface roughness, are given in the inlet of figure 5.2.

At 300 K and at 700 K the peak, which would correspond to the implantation zone, is smeared out to a depth of 50 nm and 60 nm, respectively. Portions of D, which diffused from the implantation zone into depths below this range, can not be distinguished from D trapped in the implantation zone. Therefore, high energetic peaks are Gaussian shaped and the D concentrations found by SIMNRA fits are averaged values over this depth range. The tail at 700 K, on the other hand, is due to diffusion into depths beyond the resolvable depth of 60 nm. This was already estimated by looking at the NRA spectrum at 700 K. Alphas with lower energies than the low energy edge of the peak at 700 K originate from depths beyond 60 nm. The tail extends to depths around 0.5 μm. This value is far beyond the resolvable depth and therefore slight differences of film thickness caused by surface roughness (FWHM of $\sim$5 nm) can be neglected, by comparing the diffusion depth and the resolvable depth at 700 K. It is possible to distinguish between D trapped below the resolvable depth (60 nm) and D trapped in a tail into depth (440 nm), i.e. 50% of the D inventory are trapped inside the first 60 nm and a portion of 50% is trapped in a further 440 nm. At 900 K the resolvable depth ($\sim$100 nm) is larger than the width of the enrichment zone ($\sim$50 nm). Consequently, it is not possible to distinguished between D trapped in the implantation zone or in the enrichment zone or beyond. Furthermore, it is not possible to distinguish between D trapped below the resolvable depth (100 nm) and D trapped at larger depths. Therefore, a Gaussian shaped peak was observed, which points to a rather homogeneous depth distribution of the D concentration. This peak extends to depths of $\sim$0.5 μm, i.e. to the same depth range as already observed at 700 K. The averaged D concentration is 2% and thus larger than the average D concentration of 0.3% in the tail at 700 K. About 80% of the D inventory are trapped beyond the resolvable depth at 900 K. Therefore, the saturation ratio in the implantation zone appears to be lower compared to 700 K.

Figure 5.3 gives an overview of these results. The left hand ordinate gives a depth scale

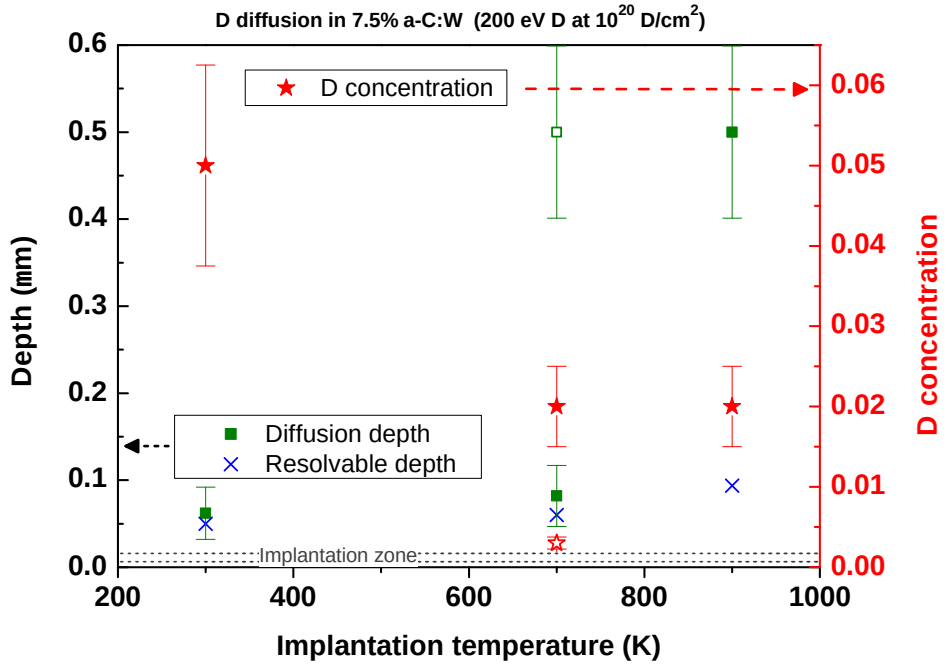

Figure 5.3: Diffusion depth and averaged D concentration in 7.5% a-C:W, exposed to a 200 eV D beam between 300 K and 900 K and at 10^{20} D/cm^2.

and the abscissa gives the implantation temperature. Diffusion depth (green square) and resolvable depth (blue X) refer to the ordinate and thus are plotted over the implantation temperature, in a range between 200 K and 1000 K. At the right hand ordinate the W concentration (red starlet) is plotted over the implantation temperature. The two horizontal, dotted lines inserted along the whole temperature range mark a range for the width of the implantation zone. At 700 K two data points are given for the diffusion depth and for the D concentration, respectively. While the points for the D concentration mark the values in the surface peak (2%) and in the tail (0.3%), respectively, the points for the diffusion depths mark a total depth. So the length of the tail would be the difference between the upper and the lower value.

For the diffusion depths and for the averaged D concentrations given in figure 5.3, of course, uncertainties exist, which rise from the uncertainty of the analysing method.

The estimation of the uncertainty of the averaged D concentration is rather straight forward. The uncertainty of the D concentration is given by the uncertainty of the integration of the D peak in the NRA spectrum (see equation 2.1). The uncertainty of the peak integration is dominated by the uncertainty of the differential cross section $d\sigma/d\Omega$ of the 800 keV D(^{3}He,^{4}He)p nuclear reaction. The uncertainty of this differential cross section is not larger than 25%.

Firstly, estimating accuracies for the diffusion depths, surface roughness can be neglected. For each temperature the half value of the FWHM of the surface roughness is small against the diffusion depth (<10%). So these values are not given in figure 5.3. For the uncertainty of the diffusion depth the depth resolution at depth can serve as first order approximation. Corresponding values can be read off from figure D.2 in appendix D *Depth resolution of*

RBS and NRA spectra. Nevertheless, it was shown in the appendix C *Evaluation of RBS and NRA spectra* that the depth resolution of the 800 keV D(^{3}He,^{4}He)p nuclear reaction on enriched a-C:W depends on the width and the composition of the W enrichment zone. For the width and the composition of the W enrichment zone uncertainties exist, which was already discussed in the subsection *Temperature series of RBS spectra* of section 4.1 *Enrichment of W: Depth profiles*. These uncertainties might affect the depth resolution at depth. Furthermore, it was shown in the appendix C *Evaluation of RBS and NRA spectra* that the influence of the width of the W enrichment zone on depth resolution dominates over the composition. Therefore, it seems to be possible to neglect the influence of the composition of the W enrichment zone on depth resolution for the estimations described in the following.

In the following, the effect of the uncertainty of the width of the W enrichment zone on the uncertainty of the depth resolution at depth is estimated. Thereby, the change of the depth resolution at depth with the change of the thickness of the W enrichment zone is of major interest (see estimations given in subsection *Influence of target composition on depth resolution* in appendix C *Evaluation of RBS and NRA spectra*). The change of the thickness of the W enrichment zone may be identified with the uncertainty of the width of the W enrichment zone. Thus, the uncertainty of the depth resolution at depth can be identified with the change of the depth resolution at depth with the magnitude of the uncertainty of the width of the W enrichment zone. Firstly, the change of the depth resolution at depth with the change of the width of the W enrichment zone is estimated, by taking results from estimations of the depth resolution at different implantation temperatures into account, i.e. at 300 K, at 700 K and at 900 K (see figure D.2 in appendix D *Depth resolution of RBS and NRA spectra*). For this temperature series the width of the W enrichment zone is analysed and well characterized. Figure D.2 plots the depth resolution at depth versus the depth for different widths of the W enrichment zone, obtained at different implantation temperatures (i.e. 6 nm at 300 K, 16 nm at 700 K and 49 nm at 900 K). While the depth resolution increases with depth, the influence of the width of the W enrichment zone on depth resolution decreases with increasing depth. This can be observed in a lowering of the ratio between two different curves with increasing depth (e.g. the ratio between the depth resolution at 300 K and at 900 K is 1.6 at a depth of $0.4{\cdot}10^{18}$ at/cm^2 and 1.15 at a depth of $6.5{\cdot}10^{18}$ at/cm^2). So the maximal change with thickness of the W enrichment zone is given at depths near the surface, e.g. at $0.4{\cdot}10^{18}$ at/cm^2. For each temperature, i.e. for each width of the W enrichment zone, values can be easily read off from the intersection of the respective curve with the ordinate. A linear curve fit reveals a maximal change of 1.05 for the change of the depth resolution at depth with the change of the thickness of the enrichment zone. As previously mentioned, the change of the thickness of the W enrichment zone may be identified with the uncertainty of the width of the W enrichment zone. The uncertainty of the width of the W enrichment zone is $\pm$5 nm at 300 K and at 700 K, and $\pm$10 nm at 900 K. So the maximal uncertainty of the depth resolution at depth is $\pm$5.25 nm at 300 K and at 700 K, and $\pm$10.5 nm at 900 K.

Attention must be paid to the positive value of the uncertainty of the depth resolution at depth, because this value leads to an increase of the depth resolution at depth and thus to an increase of the uncertainty of the diffusion depth. So the maximum uncertainty of the diffusion depth can be identified with the maximum depth resolution at depth. The maximum depth resolution at depth is the sum of the positive value of the uncertainty of the depth resolution at depth and the depth resolution at depth. Corresponding values are marked by means of error bars in figure 5.3.

In conclusion, analysis of the NRA spectra aimed to quantify changes of the saturation ratio in the implantation zone (the depth distribution of the D concentration) and changes of the diffusion depth with temperature, in a range between 300 K and 1300 K. This temperature range, however, is limited towards low temperatures as well as towards high temperatures. At temperatures above 900 K, surface roughness influences the shape of the NRA spectra so that it is not possible to convert the NRA spectra into D depth profiles. At 300 K, on the other hand, the NRA spectrum is not resolvable. It can not be distinguished between D trapped in the implantation zone and D trapped at depths blow the resolvable depth. For the maximal diffusion depth at 300 K (60 nm), which is only slightly above the resolvable depth, an average D concentration of 0.05 is given. If the total amount of the retained D was trapped within the implantation zone (within $\sim$10 nm), the D concentration within the implantation zone would be the six-fold of the D concentration within the diffusion depth, i.e. 0.3. This corresponds to a value of 0.43 for the ratio of D/C, which is slightly above the value of 0.4 for the saturation ratio of D/C inside the implantation zone well known in literature [77]. This suggests that portions of the D inventory are trapped in depths beyond the implantation zone at 300 K. In the medium temperature range between 700 K and 900 K, the NRA spectra are quantifiable with restrictions. It is not possible to quantify the saturation ratio in the implantation zone from the analysis of the NRA spectra, i.e. only a qualitative observation is possible, regarding a decrease of the saturation ratio in the implantation zone with increasing temperature. But it is possible to distinguish between D trapped below the resolvable depth and D trapped at depths larger than the resolvable depth. For the diffusion depth a maximum value can be given and for the D concentration averaged values can be given, within the resolvable depth and within depths beyond the resolvable depth. In both cases the diffusion depth is not larger than 0.5 μm. At 700 K, 50% of the D inventory is trapped within 60 nm below the surface and obtains a concentration of 0.02. If this D inventory was trapped inside the implantation zone, one would obtain a value of 0.2 for the ratio of D/C. This suggests that the saturation ration of D/C in the implantation zone is lowered at 700 K compared to 300 K. Such a kind of estimation for the saturation ratio inside the implantation zone is impossible at 900 K, since the resolvable depth is significantly increased to 100 nm.

5.2 Influence of W and pre-heating on accumulation of D

The total amount of retained D was evaluated by ion beam analysis, which has an information depth of about one micron. Film thicknesses, however, were between $\sim$0.6 μm and $\sim$1 μm. In order to ensure that the information depth is sufficient and to ensure that the detected amount of retained D does not depend on film thickness (i.e. to ensure that D does not diffuse into the substrate and films contain the total D inventory), a cross check with the D depth profiles was performed, for a-C:W, exposed to the D beam at 300 K (see chapter 5.1 *Diffusion of D: Depth profiles*).

For a-C as well as for a-C:W each D depth profile shows that more than 95% of the retained D is located within 50 nm below the surface at 300 K. Inside this subsurface layer, the shape of the depth profile and thus the total amount of retained D depends on the properties of a-C:W.

The following two subsections describe the influence of the film structure on the fluence dependence of the D inventory. Investigations of the influence of film structure on retention were carried out by varying two parameters, which are known to influence the film structure [68], i.e. the W concentration ($\leq$15%) and the annealing temperature ($\leq$1300 K).

Fluence dependence of the D inventory

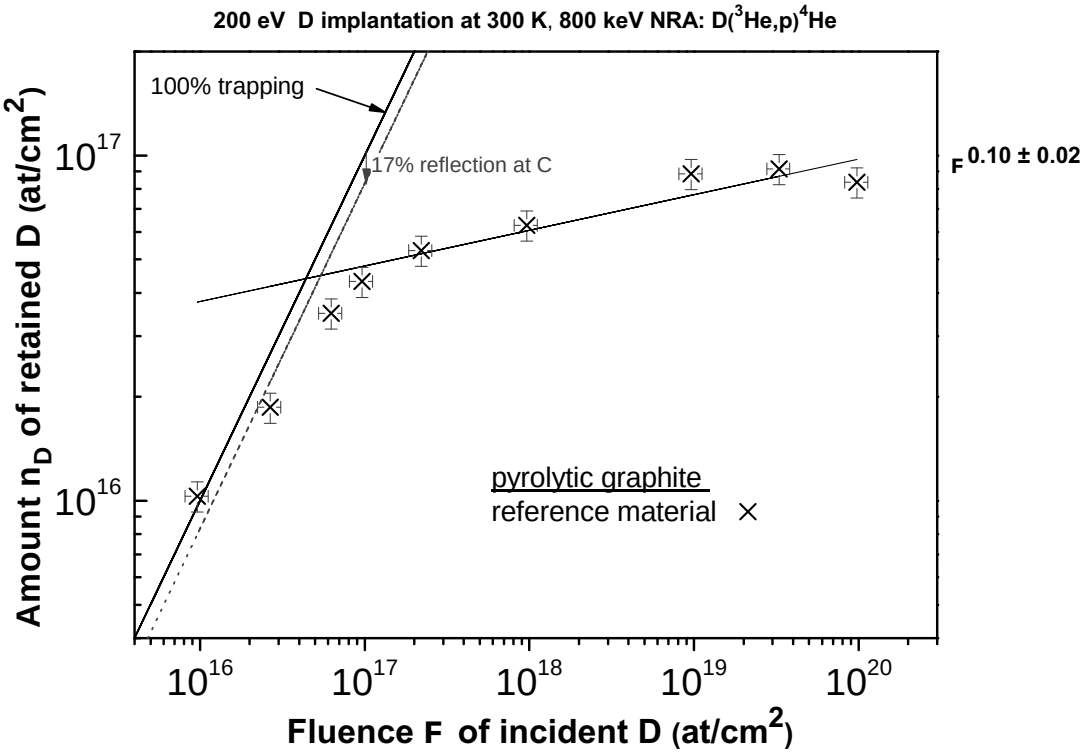

Figure 5.4: Amount of retained D in pyrolytic graphite implanted at 300 K versus the fluence of incident 200 eV D. Data points obtained for pyrolytic graphite in this study show a fluence dependence, which is determined by processes already observed in graphites and well known in literature [69, 74].

For the first step, the D retention behaviour of pyrolytic graphite is discussed for the case of the 200 eV D beam exposure. In the second step, the D retention behaviour of a-C and

a-C:W is compared to the behaviour of pyrolytic graphite. In the third step, the influence of the heat treatment before the D beam exposure is analysed for a-C, in a fluence range between 10^{19} D/cm^2 and 10^{20} D/cm^2, and for 7.5% a-C:W and 15% a-C:W, at a fluence of 10^{17} D/cm^2 and of 10^{20} D/cm^2, respectively.

Figure 5.4 shows the amount of retained D, n_D, (D inventory) in pyrolytic graphite a as function of the fluence Φ of incident D. Additionally, a solid line through the origin is shown, which has a slope of 100%. Along this line the D inventory equals the fluence of incident D, i.e. 100% of the incoming D are retained. Taking reflection of the incoming D beam into account the slope of the line through the origin is reduced by the value of the reflection coefficient, e.g. 17% for C and 55% for W [78]. This results in a new line through the origin (dotted line). Data points obtained for pyrolytic graphite in this study show a fluence dependence, which is determined by processes already observed in graphites and well known in literature [69, 74]. Below a fluence of $3{\cdot}10^{16}$ D/cm^2 data points of pyrolytic graphite are close to the dotted line (17% reflection), taking an accuracy of 10% and 16% for the D inventory and for the fluence, respectively, into account. For fluences between $3{\cdot}10^{16}$ D/cm^2 and $1{\cdot}10^{17}$ D/cm^2 data points follow a curve rather than a line. With increasing fluence the D inventory increases along this curve and the gradient of the curve decreases. This means, the implantation zone saturates at fluences between $3{\cdot}10^{16}$ D/cm^2 and $1{\cdot}10^{17}$ D/cm^2. Above a fluence of $1{\cdot}10^{17}$ D/cm^2, the curve shows a constant increase with fluence in a double logarithmic scale, i.e. data points follow a line (within the accuracies for the inventory and the fluence mentioned above) and it is possible to fit data points by the power law Φ^X. In this study (200 eV D beam exposure) the magnitude X obtains the value 0.10 ± 0.02. This confirms that in pyrolytic graphite the D inventory shows a constant increase with increasing fluence and does not reach a limit, as already shown in literature [69, 74]. For instance, $\sim$0.1% of the incoming D beam contributes to the D inventory at a fluence of 10^{20} D/cm^2. In literature, this kind of increase of the D inventory is attributed to a diffusion of D into depth [69, 74]. Thus, a reference curve is given and the D retention behaviour of a-C and a-C:W can be compared to the behaviour of pyrolytic graphite. This is carried out by dividing the whole fluence range between 10^{16} D/cm^2 and 10^{20} D/cm^2 into three parts. In the first part, below a fluence of $4{\cdot}10^{16}$ D/cm^2, reflection coefficients can be compared with each other, in the second part, at fluences between $4{\cdot}10^{16}$ D/cm^2 and $1{\cdot}10^{17}$ D/cm^2, saturation ratios can be compared with each other and in the third part, above a fluence of $1{\cdot}10^{17}$ D/cm^2, the increase of the D inventory with fluence of a-C, a-C:W and pyrolytic graphite can be compared with each other.

Reflection coefficient

Figure 5.5 shows the amount of retained D, n_D, a as function of the fluence Φ of incident D for pyrolytic graphite, a-C and a-C:W (2.5%, 7.5% and 18.5% W), at fluences below $4{\cdot}10^{16}$ D/cm^2. Additionally two lines through the origin are shown (solid and dotted). The solid line represents the 100% retention line of the incoming beam and the dotted line is shifted by 17% to lower values. For each a-C and a-C:W data points follow the dotted line tightly. Among the data points of a-C and of a-C:W, some data points overlap with the dotted line, and other data points obtain values slightly above or below. Among the data points, which obtain values slightly above or below, none have a larger difference to the dotted line than the data points of pyrolytic graphite. This means, the D inventory of

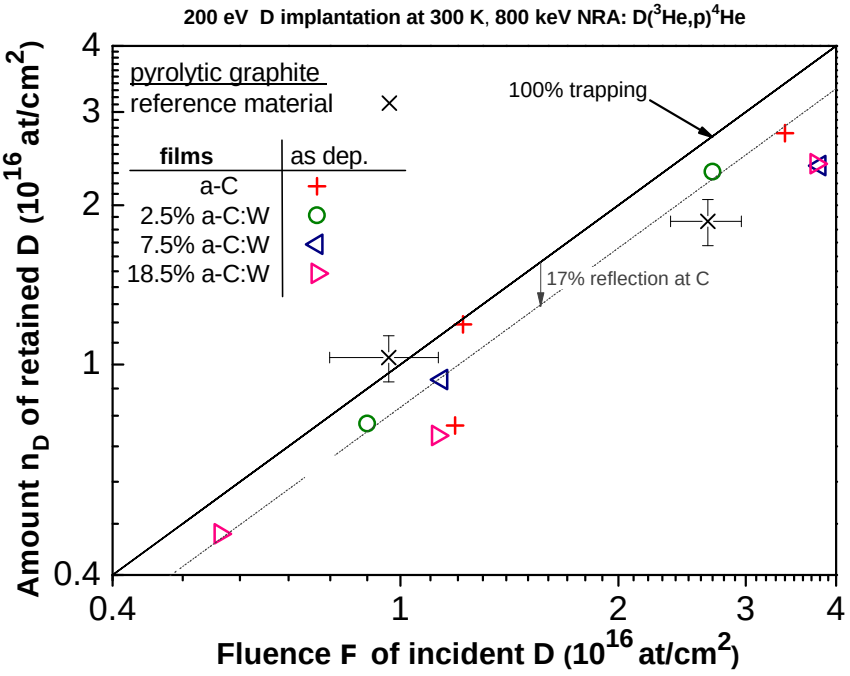

Figure 5.5: Amount of retained D implanted at 300 K versus the fluence of incident 200 eV D for pyrolytic graphite, a-C and a-C:W (2.5%, 7.5% and 18.5% W), at fluences below $4{\cdot}10^{16}$ D/cm^2; two lines through the origin are inserted (solid line: 100% trapping, dotted line: Shifted by 17% to lower values).

a-C and a-C:W can not be distinguished from the D inventory of pyrolytic graphite, within the accuracies mentioned. At fluences below $4{\cdot}10^{16}$ D/cm^2, a-C and a-C:W show the same retention behaviour as pyrolytic graphite. Therefore, a-C:W does not exhibit an intrinsically changed reflection coefficient compared to pyrolytic graphite (17%) for W concentrations of 18.5% and below. Note that at a fluence of $4{\cdot}10^{16}$ D/cm^2 already $\sim 10^{15}$ at/cm^2 of C are removed solely by physically sputtering, taking a sputtering yield of 0.02 for C into account. This is one atom layer of C and thus in the second remaining layer the W content is doubled, up to $\sim$40% for 18.5% a-C:W.

Saturation ratio of the implantation zone

Figure 5.6 (a) shows the amount of retained D, n_D, a as function of the fluence Φ of incident D for the same specimens mentioned in the latter paragraph, i.e. pyrolytic graphite, a-C and a-C:W (2.5%, 7.5% and 18.5% W), at fluences between $3{\cdot}10^{16}$ D/cm^2 and $1{\cdot}10^{17}$ D/cm^2. For each a-C and for each a-C:W data points follow a curve, which exhibits a decreasing gradient with increasing fluence, as previously observed for pyrolytic graphite. For a-C, which intrinsically exhibits an amorphous C structure, data points can not be distinguished from pyrolytic graphite. Consequently, a-C has the same saturation ratio of D/C in the implantation zone as pyrolytic graphite, which obtains a value of 0.4. In literature it is well known that each C structure is becoming amorphous by ion beam irradiation [77]. Therefore, the structure of the C matrix can not influence the saturation ratio inside the implantation zone. For a-C:W, however, the decrease of the gradient of the curve is more pronounced so that the D inventory results in lower values at a fluence of 10^{17} D/cm^2. For 7.5% a-C:W the D inventory is lowered to $3.5{\cdot}10^{16}$ D/cm^2, which is just different from the value of pyrolytic

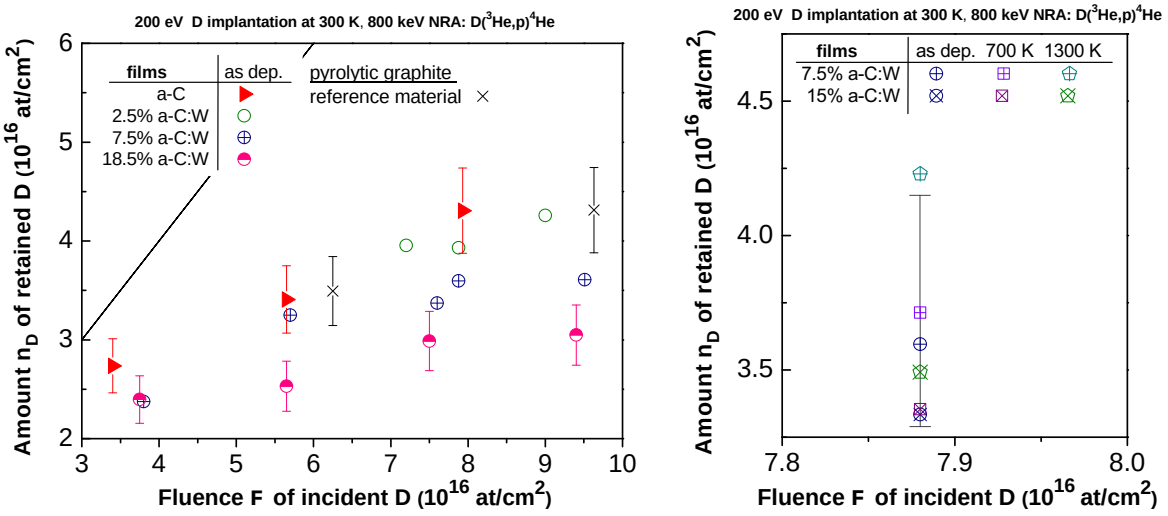

Figure 5.6: Amount of retained D implanted at 300 K versus the fluence of incident 200 eV D. In (a) for pyrolytic graphite, a-C and a-C:W (2.5%, 7.5% and 18.5% W), at fluences between $3{\cdot}10^{16}$ D/cm^2 and $1{\cdot}10^{17}$ D/cm^2; a line through the origin is inserted (100% trapping). In (b) for pyrolytic graphite and a-C:W, as-deposited, and pre-heated to 700 K and 1300 K, at fluences between $7{\cdot}10^{16}$ D/cm^2 and $1{\cdot}10^{17}$ D/cm^2.

graphite and a-C, within the accuracy of 10% for a data point. For 18.5% a-C:W the D inventory is even more lowered to $3{\cdot}10^{16}$ D/cm^2. Comparing these values to the D inventory of $4.3{\cdot}10^{16}$ D/cm^2 in a-C and pyrolytic graphite, the saturation ratio is lowered to 0.33 and to 0.28, respectively, for 7.5% a-C:W and for 18.5% a-C:W. In a further step, the influence of the heat treatment before the D beam exposure and thus the influence of the structure of the C matrix on the saturation ratio in a-C:W was investigated for W concentrations of 7.5% and 15%. Figure 5.6 (b) shows the amount of retained D, n_D, a as function of the fluence Φ of incident D for 7.5% a-C:W and for 15% a-C:W, pre-heated to 700 K and to 1300 K, respectively, at fluences close to 10^{17} D/cm^2. Data of specimens implanted without heat treatment are shown for comparison. Within the accuracy of 10%, data points of heat treated and non-heat treated samples can not be distinguished from one another, neither for 7.5% a-C:W nor for 15% a-C:W. For instance, the data points of the as-deposited 15% a-C:W and of 15% a-C:W, pre-heated at 700 K, are overlapping and can hardly be distinguished from one another in the graph. This confirms that the structure of the C matrix does not influence the saturation ratio inside the implantation zone, as it was already observed from the comparison of a-C and pyrolytic graphite and as it must be expected from literature [77].

Increase of D inventory with fluence after saturation of the implantation zone

Figure 5.7 shows the amount of retained D, n_D, a as function of the fluence Φ of incident D for pyrolytic graphite, a-C and a-C:W with W concentrations of 7.5% and below (1%, 2.5% and 7.5% W), at fluences between 10^{16} D/cm^2 and 10^{20} D/cm^2. The range above 10^{17} D/cm^2 will be discussed. At a fluence of 10^{17} D/cm^2 the D inventory in a-C is no different compared to the pyrolytic graphite, but the D inventory in a-C:W is lower than in pyrolytic graphite. For instance, in 7.5% a-C:W the D inventory is lowered by about $1{\cdot}10^{16}$ D/cm^2 compared to the D inventory in pyrolytic graphite. As previously mentioned, this is due to a lowered saturation ratio in a-C:W. At a fluence of 10^{19} D/cm^2, however, the

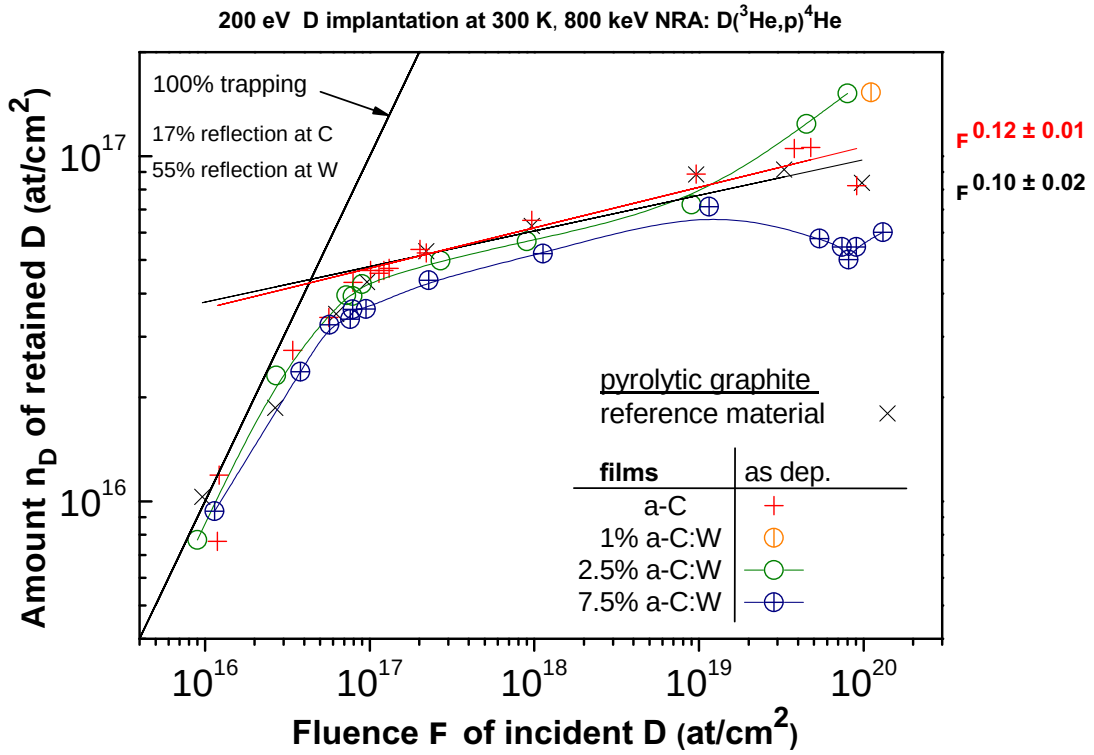

Figure 5.7: Amount of retained D implanted at 300 K versus the fluence of incident 200 eV D for pyrolytic graphite, a-C and a-C:W ($\leq$7.5% W), at fluences between 10^{16} D/cm^2 and 10^{20} D/cm^2. Curves are a guide to the eye.

D inventory in 7.5% a-C:W is lowered by about $2{\cdot}10^{16}$ D/cm^2 compared to the D inventory in pyrolytic graphite. So the difference in the D inventory between a-C:W and pyrolytic graphite is only mildly changed with increasing fluence above 10^{17} D/cm^2. In the fluence range between 10^{17} D/cm^2 and 10^{19} D/cm^2, the increase of the D inventory of a-C and a-C:W (2.5% and 7.5%) can only hardly be distinguished from the increase of the D inventory of pyrolytic graphite. a-C, 2.5% a-C:W and 7.5% a-C:W do not exhibit a significantly changed retention behaviour up to a fluence of 10^{19} D/cm^2 compared to the pyrolytic graphite. Above, the D inventory depends strongly on the W concentration. For a-C the D inventory increases monotonically above a fluence of 10^{19} D/cm^2. Therefore, it is possible to compare results with results obtained for pyrolytic graphite by the magnitude X in the power law Φ^X, in the fluence range between 10^{17} D/cm^2 and 10^{20} D/cm^2. The magnitude X results in a value of 0.12 ± 0.01 for a-C. This value can not be distinguished from the value obtained for pyrolytic graphite, which has an error bar of $\pm$ 0.02. Taking results previously mentioned into account, as-deposited a-C exhibits about the same increase of the D inventory with fluence as pyrolytic graphite, along the whole analysed fluence range between 10^{16} D/cm^2 and 10^{20} D/cm^2. For 2.5% a-C:W the D amount rises to higher values at a fluence of 10^{20} D/cm^2 compared to pyrolytic graphite and a-C. A similar D content, i.e. the 1.5-fold of the inventory in a-C, was observed for 1% a-C:W, implanted at a fluence of 10^{20} D/cm^2. In contrast, for 7.5% a-C:W the amount of retained D is reduced to the half value of a-C at a fluence of 10^{20} D/cm^2. Both effects, the increase of the D inventory for 2.5% a-C:W and the decrease of the D inventory for 7.5% a-C:W, above a fluence of 10^{19} D/cm^2, are reproducible. Note that data

points of 7.5% a-C:W follow a curve, which shows a minimum at a fluence of $8{\cdot}10^{19}$ D/cm^2 and increases again above this minimum with further increasing fluence. The minimum, however, must be presumed as a trend, since the difference of the D inventory of these five data points is not significant, within the accuracy of 10%.

In a further step, a-C, 7.5% a-C:W and 15% a-C:W, which were heat treated at different temperatures (700 K and 1300 K) were implanted at a fluence of 10^{20} D/cm^2. a-C, which was heat treated at 1300 K, was implanted at a fluence of 10^{19} D/cm^2, too. For a-C the influence of the heat treatment before the D beam exposure and thus the influence of the structure of the C matrix on the increase of the D inventory with fluence was investigated. For a-C:W the influence of heat treatment as well as the influence of a variation of the W concentration on the reduction of the D inventory above a fluence of 10^{19} D/cm^2 was investigated. Figure 5.8 shows a magnification including data points of pyrolytic graphite and data points of a-C and a-C:W (7.5% and 15% W), as-deposited and pre-heated to 700 K and to 1300 K. For a-C, pre-heated

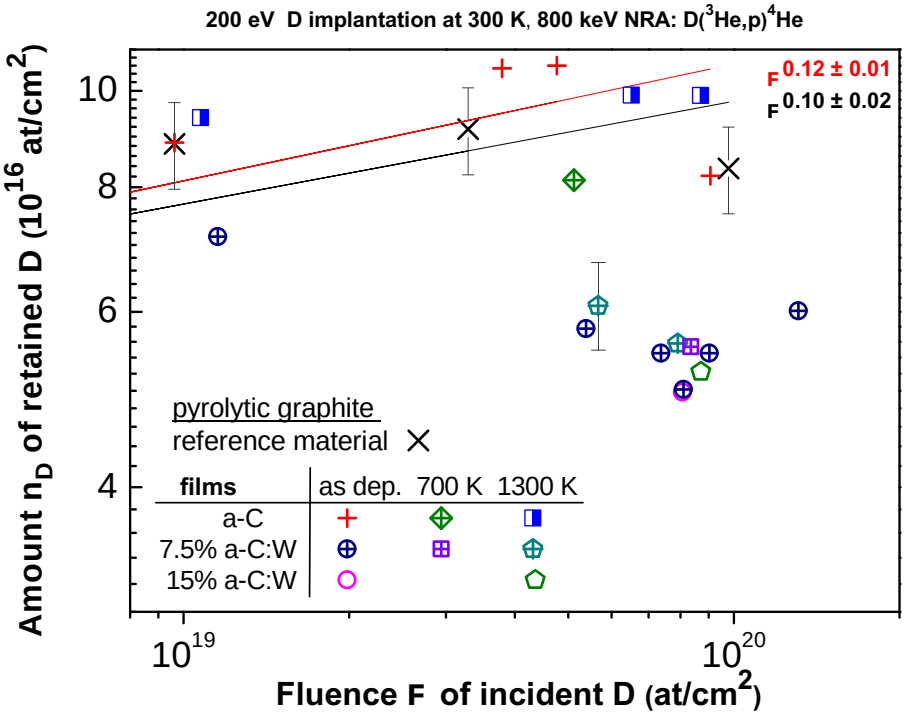

Figure 5.8: Amount of retained D implanted at 300 K versus the fluence of incident 200 eV D. A magnification above a fluence of 10^{19} D/cm^2 is shown (including data points of pyrolytic graphite, of a-C and of a-C:W (7.5% and 15% W), as-deposited and pre-heated to 700 K and to 1300 K).

at 1300 K and implanted at a fluence of 10^{19} D/cm^2, the D inventory can not be distinguished from the value of as-deposited a-C implanted at the same fluence, within the accuracy of 10%. For a-C, implanted at a fluence close to 10^{20} D/cm^2, some details need to be considered first. Two data points of as-deposited a-C are given at a fluence of $\sim 4{\cdot}10^{19}$ D/cm^2. They can be compared with a-C, pre-heated at 700 K. The difference of the D inventory between as-deposited a-C and a-C, pre-heated at 700 K, is just larger than the width of the error bar. Nevertheless, this difference is not believed to be significant, since a-C, pre-heated at 700 K, does not deviate more strongly from the fitting curve than the corresponding data points of as-deposited a-C. At a fluence of $\sim 9{\cdot}10^{19}$ one data point is given for an as-deposited a-C.

This data point can be compared with the two data points of a-C, pre-heated to 1300 K. The difference of the D inventory, of the as-deposited a-C and of a-C, pre-heated at 1300 K, is just within the width of the error bar. Comparing the D inventory of a-C, pre-heated to 700 K and to 1300 K, with the D inventory of as-deposited a-C shows that the heat treatment before the D beam exposure does not influence the increase of the D inventory with fluence. For a-C:W, on the other hand, parameter variation does not affect the D inventory at a fluence close to 10^{20} D/cm^2 as well. For as-deposited 7.5% a-C:W five data points are given, a data point at a fluence of $5{\cdot}10^{19}$ D/cm^2, three data points at a fluence of $8{\cdot}10^{19}$ D/cm^2 and one data point at a fluence slightly above 10^{20} D/cm^2. Values for the D inventory can not be distinguished from one another, within the accuracy of 10%, as previously mentioned. Nevertheless, it seems to be appropriate to compare the pre-heated specimens with the as-deposited specimens, implanted at the same fluence. At a fluence of $5{\cdot}10^{19}$ D/cm^2 the D inventory of 7.5% a-C:W, pre-heated at 1300 K, and of as-deposited 7.5% a-C:W can not be distinguished from one another, within the accuracy of 10%. At a fluence of $8{\cdot}10^{19}$ D/cm^2 the D inventory of 7.5% a-C:W, pre-heated at 700 K, and of 7.5% a-C:W, pre-heated at 1300 K, and of as-deposited 7.5% a-C:W can not be distinguished from one another, within the accuracy of 10%. For 7.5% a-C:W the heat treatment before the D beam exposure does not affect the extent of the reduction of the D inventory above a fluence of 10^{19} D/cm^2. For as-deposited 15% a-C:W one data point exists at a fluence of $8{\cdot}10^{19}$ D/cm^2. The D inventory of as-deposited 15% a-C:W and of as-deposited 7.5% a-C:W can not be distinguished from one another at a fluence of 10^{20} D/cm^2. Heat treatment of 15% a-C:W was performed once at 1300 K. The D inventory of 15% a-C:W, pre-heated at 1300 K, and of as-deposited 15% a-C:W can not be distinguished from one another. Therefore, the lowering of the D inventory with fluence is also insensitive to pre-heating in 15% a-C:W and the magnitude of this lowering equals the magnitude in 7.5% a-C:W.

Thermal desorption spectroscopy

TDS measurements were performed in order to compare the trapping behaviour of a-C and a-C:W. Chemical C bondings are changed in the vicinity of a W carbide bonding. These changes might result in an intrinsically altered trapping behaviour at fluences around 10^{17} D/cm^2 and below. Furthermore, with increasing fluence above 10^{17} D/cm^2 a surface enriched with W is formed, which exhibits an altered trapping behaviour. This might be reflected in the trends observed for fluence dependences of the D retention, especially above a fluence of 10^{19} D/cm^2. TDS spectra were measured for a-C and for 1%, 2.5% and 7.5% a-C:W, which were exposed to the D beam at different fluences (10^{17} D/cm^2, 10^{19} D/cm^2 and 10^{20} D/cm^2).

Influence of W and of enrichment on the D_2 signal

Interpreting a TDS spectrum, D released at high temperatures was released from high energetic bonding states and D released at low temperatures was released from low energetic bonding states. Thereby, the effect of diffusion on the position of peaks is neglected.

Figure 5.9 (a)/(b) shows the temperature dependence of the D_2 signal for a-C, implanted at different fluences (in (a): D_2 amount, in (b): normalised D_2 amount). Each peak shows a flat shape with a full width at half maximum (FWHM) of about 400 K. The peak maximum of

the specimens implanted at 10^{17} D/cm^2 is between 900 K and 1000 K. Between ~1100 K and ~1200 K a weak hump occurs, indicating a second maximum, which is lower than the first maximum. Bonding states belonging to lower temperatures have a slightly higher occupation rate compared to states belonging to higher temperatures. With increasing fluence the peak maximum shifts slightly to ~1000 K and the second peak increases more strongly than the first peak so that both peaks can not be distinguished from one another. This is observable as an increase of the amount of retained D with increasing fluence.

From HREELS analysis of the hybridization states of the bound hydrogen in ultra thin, ion-beam deposited CH films given in [139, 140] it is known that hydrogen is released from sp^3 bonds at around 920 K and from sp^2 bonds at around 1120 K. Both values are in good agreement with the two maximums observed in the TDS spectra of a-C implanted at a fluence of 10^{17} D/cm^2, respectively. At low fluences sp^2 bonds are present in the implantation zone of a-C, which is modified with increasing fluence leading to an increased presence of sp^3 bonds. This explains the presence of the two maximums at a fluence of 10^{17} D/cm^2, the higher intensity of the first maximum and the strong increase of the second maximum with increasing fluence.

In figure 5.9 (c) /(d) the temperature dependence of the D_2 signal for 2.5% a-C:W, implanted at 10^{19} D/cm^2 and at 10^{20} D/cm^2, is depicted (in (c): D_2 amount, in (d): normalised D_2 amount). The spectrum of 1% a-C:W implanted at 10^{20} D/cm^2 is inserted. At a fluence of 10^{19} D/cm^2 a maximum occurs at ~950 K and a hump at ~1100 K. The hump is due to D released from sp^2 bonds. Increasing the fluence from 10^{19} D/cm^2 to 10^{20} D/cm^2 the maximum slightly decreases to ~900 K. The FWHM increases from ~300 K to ~400 K and the overall peak intensity increases strongly and in equal portions, i.e. the whole energy range was occupied with D. This leads to the drastic increase of the D inventory, observed for fluences between 10^{19} D/cm^2 and 10^{20} D/cm^2. Note that the hump, due to D released from sp^2 bonds, is still present at a fluence of 10^{20} D/cm^2. This means that D was still bound to C at a fluence of 10^{20} D/cm^2. This is confirmed by the fact that the W enrichment zone is not in steady state in 2.5% a-C:W, implanted at a fluence of 10^{20} D/cm^2. 1% a-C:W, implanted at 10^{20} D/cm^2, shows a similar shape compared to 2.5% a-C:W, implanted at 10^{19} D/cm^2. It has a maximum at ~950 K. At ~1100 K the hump is even more pronounced and thus larger portions of D were bound to C. The spectrum shows a large FWHM and the peak is asymmetrically extended to higher temperatures. In 1% a-C:W D was predominantly bound to C, similar to a-C.

Figure 5.9 (e) /(f) shows the temperature dependence of the D_2 signal for 7.5% a-C:W, implanted at different fluences (in (e): D_2 amount, in (f): normalised D_2 amount). For all fluences the peak maximum is at ~850 K. 7.5% a-C:W seems to exhibit an intrinsically changed trapping behaviour, without respect to the extent of W enrichment. Nevertheless, a fluence dependence exists for the energy range of occupied bonding states. The specimen exposed to the D beam at a fluence of 10^{17} D/cm^2 shows a FWHM of about 300 K. The increase of the fluence to 10^{19} D/cm^2 leads to an increase of the peak intensity, which is pronounced at high temperatures. Specifically a sharp peak occurs at ~1100 K, which can be attributed to D released from sp^2 bonds. The FWHM increases by about 50 K to 350 K. Bonding states at higher temperatures were occupied, which belong to C. At a fluence of 10^{20} D/cm^2 the peak width decreases at its high temperature edge to a FWHM of about 300 K.

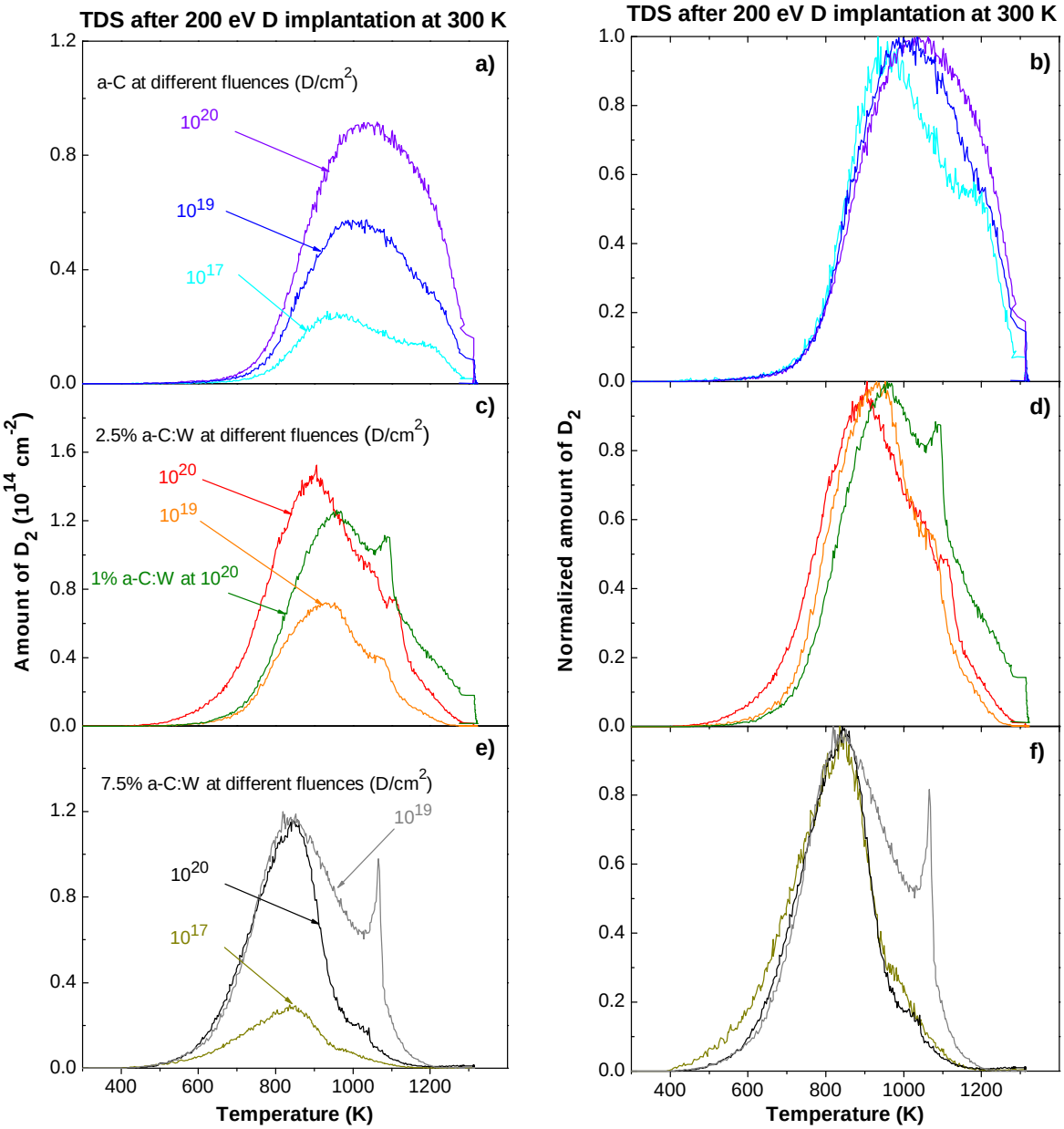

Figure 5.9: TDS spectra of the D_2 signal (a)/(b) of a-C, (c)/(d) of 2.5% (and 1%) and (e)/(f) of 7.5% a-C:W, which were exposed to a 200 eV D beam at 300 K and at different fluences (10^{17} D/cm^2, 10^{19} D/cm^2, 10^{20} D/cm^2). To the left hand column the amount of released D molecules is depicted. To the right hand column the spectra are normalized.

In figure 5.10 (a) /(b) a concentration series of the temperature dependence of the D_2 signal for a-C and a-C:W, implanted at 10^{20} D/cm^2, is depicted (in (a): D_2 amount, in (b): normalised D_2 amount). In general, the peak maximum shifts to lower temperatures for

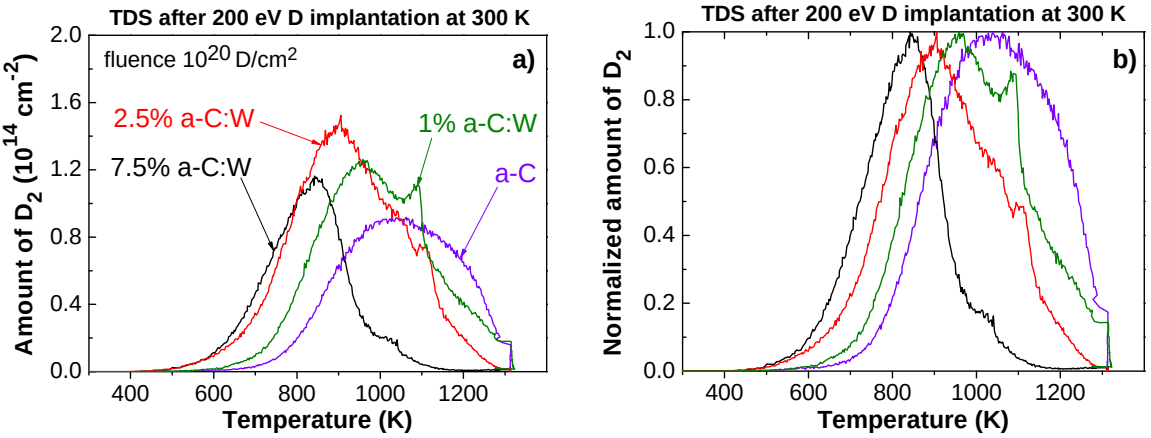

Figure 5.10: TDS spectra of the D_2 signal of a-C and of a concentration series of a-C:W, which were exposed to a 200 eV D beam at 300 K and at a fluence of 10^{20} D/cm^2. To the left the amount of released D molecules is depicted. To the right the spectra are normalized.

a-C:W (up to ∼200 K compared to a-C). The maximum decreases from ∼950 K to ∼850 K increasing the W concentration from 1% to 7.5%. D was bound at lower energies. Regarding the FWHMs of the concentration series, 7.5% a-C:W shows the lowest value. Only a small range of bonding energies was occupied. The FWHM of a-C is larger and thus a larger range of bonding energies was occupied. The largest values for the FWHM are obtained for 1% a-C:W and for 2.5% a-C:W, which extent over a large range, including both the range of a-C and 7.5 % a-C:W. For W concentrations of 2.5% and below both W like and C like ranges of bonding energies were occupied. This results in the largest amount of retained D, observed in 2.5% a-C:W (and in 1% a-C:W) and in the lowest amount observed in 7.5% a-C:W, at a fluence of 10^{20} D/cm^2.

Influence of W and of enrichment on the CD_4 signal

In addition to the D_2 signal, the CD_4 signal was recorded for all specimens mentioned above. The release of methane is one of the reaction steps described in Küppers cycle [141, 103, 140]. This step describes a transition from a hydrogenated sp^3 bond to a sp^2 bond between C atoms, which is thermally activated and occurs in absence of the D beam. Interpreting a TDS spectrum, methane released at high temperatures was released from high energetic bonding states and methane released at low temperatures was released from low energetic bonding states. Thereby, the effect of diffusion on the position of peaks is neglected.

Figure 5.11 (a) /(b) shows the temperature dependence of the CD_4 signal for a-C, implanted at different fluences (in (a): CD_4 amount, in (b): normalised CD_4 amount). Humps below 600 K are due to non-linearities in the temperature increase with time, which are difficult to eliminate. This temperature range is not considered in the data evaluation for any of the analysed specimens (a-C as well as a-C:W). For each a-C the peak maximum is between ∼800 K and ∼900 K and the FWHM is about 150 K. Increasing the fluence from 10^{17} D/cm^2

to 10^{19} D/cm^2 leads to an overall peak growth. Above 10^{19} D/cm^2 the peak intensity is unchanged.

In figure 5.11 (c)/(d) the temperature dependence of the CD_4 signal for 2.5% a-C:W, implanted at 10^{19} D/cm^2 and 10^{20} D/cm^2, is depicted (in (c): CD_4 amount, in (d): normalised CD_4 amount). The spectrum of 1% a-C:W, implanted at 10^{20} D/cm^2 is inserted. In this range the FWHM of 2.5% a-C:W shows a slight increase from ∼150 K to ∼200 K. The peak intensity increases asymmetrically towards lower temperatures. Peak maximums are around 800 K. The peak of 1% a-C:W has shifted slightly by about 50 K towards higher temperatures, but shows no difference in the FWHM and the intensity.

Figure 5.11 (e)/(f) shows the temperature dependence of the CD_4 signal for 7.5% a-C:W, implanted at different fluences (in (e): CD_4 amount, in (f): normalised CD_4 amount). The maximum shifts slightly with increasing fluence from ∼700 K to ∼750 K and the overall peak intensity increases. Note, the peak intensity does not decrease from 10^{19} D/cm^2 to 10^{20} D/cm^2, as it was observed for the D_2 signal. This must be due to methane released from depths beyond the enrichment zone, which contains nearly 100% W at a fluence of 10^{20} D/cm^2. If it is possible to release methane from depths beyond the enrichment zone, one must conclude that D diffused into depths beyond the enrichment zone, where it was bound to C.

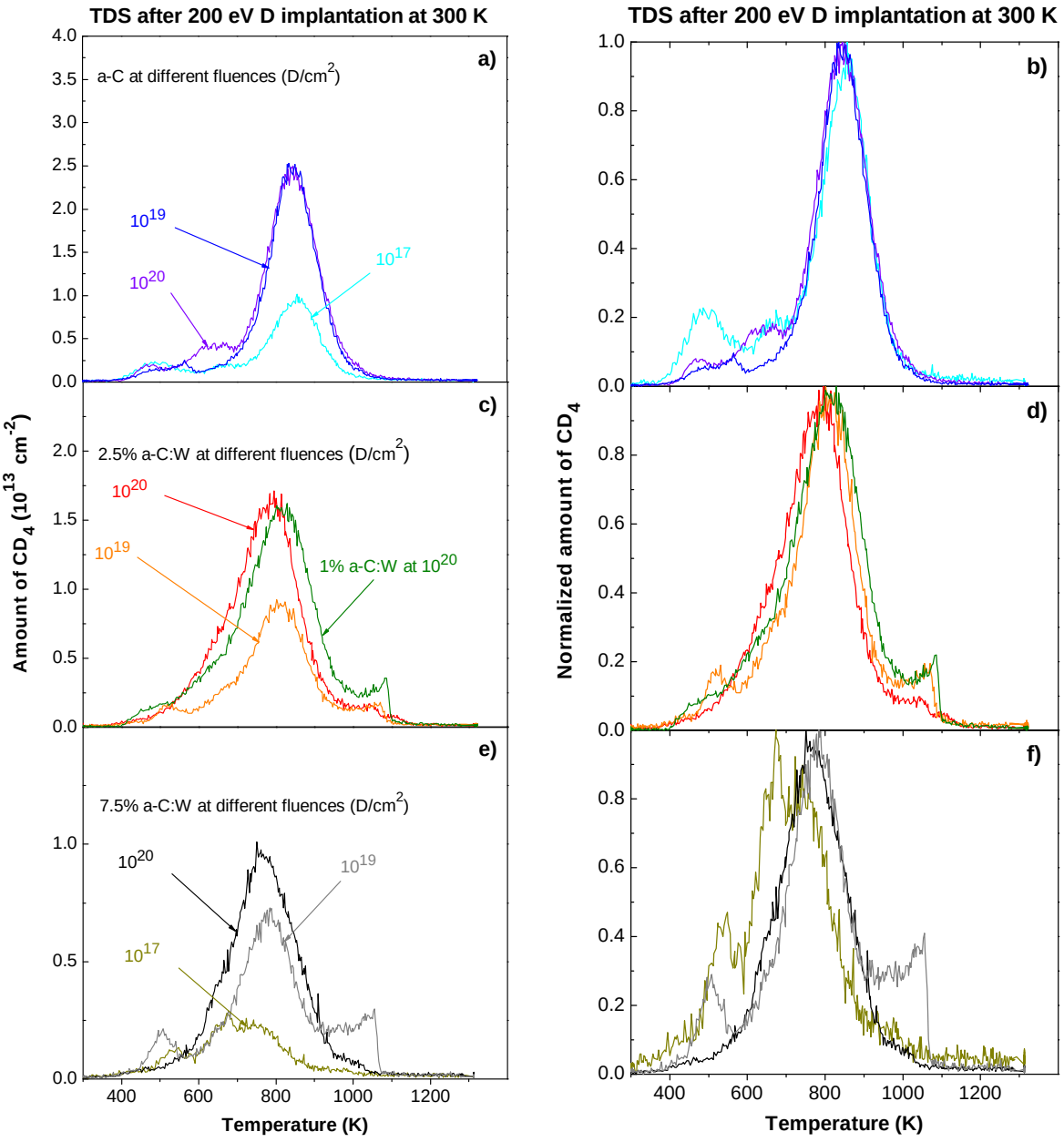

Figure 5.11: TDS spectra of the CD_4 signal (a)/(b) of a-C, (c)/(d) of 2.5% (and 1%) and (e)/(f) of 7.5% a-C:W, which were exposed to a 200 eV D beam at 300 K and at different fluences (10^{17} D/cm^2, 10^{19} D/cm^2, 10^{20} D/cm^2). To the left hand column the amount of released methane molecules is depicted. To the right hand column the spectra are normalized.

In figure 5.12 (a) /(b) a concentration series of the temperature dependence of the CD_4 signal for a-C and a-C:W, implanted at 10^{20} D/cm^2, is depicted (in (a): CD_4 amount, in (b): normalised CD_4 amount). With increasing concentration, maximums shift to lower

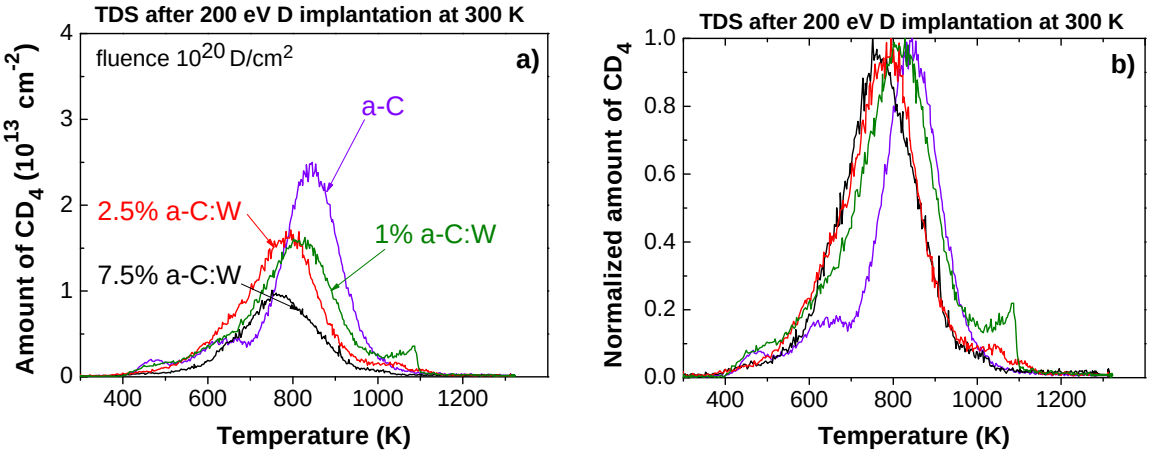

Figure 5.12: TDS spectra of the CD_4 signal of a-C and of a concentration series of a-C:W, which was exposed to a 200 eV D beam at 300 K and at a fluence of 10^{20} D/cm^2. To the left the amount of released methane molecules is depicted. To the right the spectra are normalized.

temperatures, by about 200 K. This trend was also observed for the concentration series of the D_2 signal, but it is less pronounced.

In general, peak maximums of the CD_4 signals obtain lower values compared to the D_2 signal (between 1/3 and 1/10). Peaks are symmetric and extended over a smaller temperature range. The temperature difference between peak maximums is smaller. Despite these minor differences, trends observed for the D_2 signal were observed for the CD_4 signal, too. Since shifts in the peak maximums are observed in a-C:W, in contrast to a-C, it can be assumed that the build-up of the enrichment zone with increasing fluence affects the activation energy for methane release. Furthermore, the peak maximum shifts to lower temperatures with increasing W concentration, indicating a lowering of the activation energy of the methane release. The total amount of released methane decreases with increasing W concentration as well.

Influence of W and of enrichment on the ratio of CD_4 to D_2

Another aspect lies in changes of the CD_4/D_2 ratio, induced by W. Figure 5.13 plots the ratio of the integrated CD_4 signal to the integrated D_2 signal over the W concentration for different fluences of incident D. In general, a-C:W exhibits a clearly reduced CD_4/D_2 ratio compared to a-C and to pyrolytic graphite. This reduction depends on the W concentration. With increasing W concentration the CD_4/D_2 ratio tends to decrease, except for 7.5% a-C:W, implanted at a fluence of 10^{20} D/cm^2. This data point is slightly enhanced over the value of 2.5% a-C:W, implanted at a fluence of 10^{20} D/cm^2. For 7.5% a-C:W the CD_4/D_2 ratio does not monotonically decrease with fluence, in contrast to 2.5% a-C:W and to a-C. In fact, it increases again increasing the fluence from 10^{19} D/cm^2 to 10^{20} D/cm^2. This is due to a decreased amount of released D_2, which was observed in the TDS spectra for the D_2 signal,

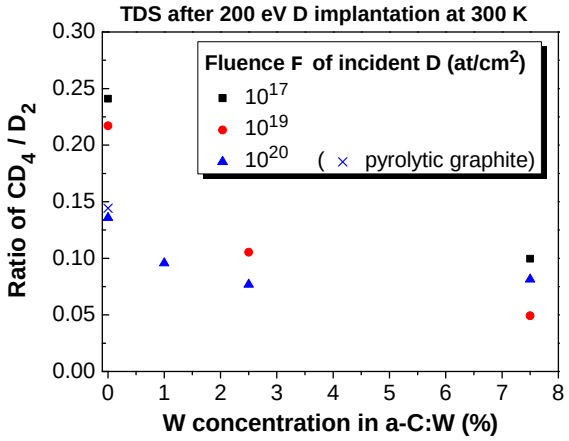

Figure 5.13: Ratio of CD_4 to D_2 obtained from the integrated TDS spectra of a-C and of the concentration series of a-C:W, which were exposed to a 200 eV D beam at 300 K and different fluences (10^{17} D/cm^2, 10^{19} D/cm^2, 10^{20} D/cm^2).

in convolution with an increased amount of released CD_4. In general, a larger portion of the D is released in molecular form from a-C:W. This is pronounced with increasing W concentration.

Reflection coefficient and D inventory of enriched a-C:W

Besides an altered trapping behaviour, the build-up of a W enrichment zone changes the reflection coefficient for the incoming D beam. In order to estimate the reflection coefficient after build-up of a W enrichment zone and to study the influence of a W enrichment zone in steady state on the fluence dependence of the D inventory, a special investigation was performed. Within the frame of this investigation 7.5% a-C:W were exposed to a 200 eV D beam at 300 K and at a fluence of 10^{20} D/cm^2, for the first step. Thus they were enriched with W at the surface. For the second step, these enriched 7.5% a-C:W were in-situ outgased at 1300 K. For the third step, the enriched 7.5% a-C:W were implanted in the second run of a D beam exposure at 300 K and at different fluences between 10^{15} D/cm^2 and 10^{20} D/cm^2. NRA measurements on the outgased specimens, before the second exposure to the D beam, showed that $\sim$0.1% of the D from the first run remained in the films. These amounts can be neglected compared to the inventory after the second exposure to the D beam.

Figure 5.14 shows the amount of retained D, n_D, a as function of the fluence Φ of incident D for different materials. Those 7.5% a-C:W, treated in the way mentioned above and thus enriched with W at the surface (in the following called enriched 7.5% a-C:W), are compared to characteristic reference materials, which were exposed to a 200 eV D beam at 300 K and at different fluences between 10^{16} D/cm^2 and 10^{20} D/cm^2: 7.5% a-C:W (see subsection 5.2 *Influence of W and pre-heating on accumulation of D*) and a W film of 200 nm thickness, which was deposited on pyrolytic graphite at 300 K (W-coated graphite) [142]. The solid line and the dashed line represent the 100% retention line of the unreflected part of the incoming beam (0% and 55% reflection, respectively). The dotted curve belongs to the data of the enriched 7.5% a-C:W and is a guide to the eye.

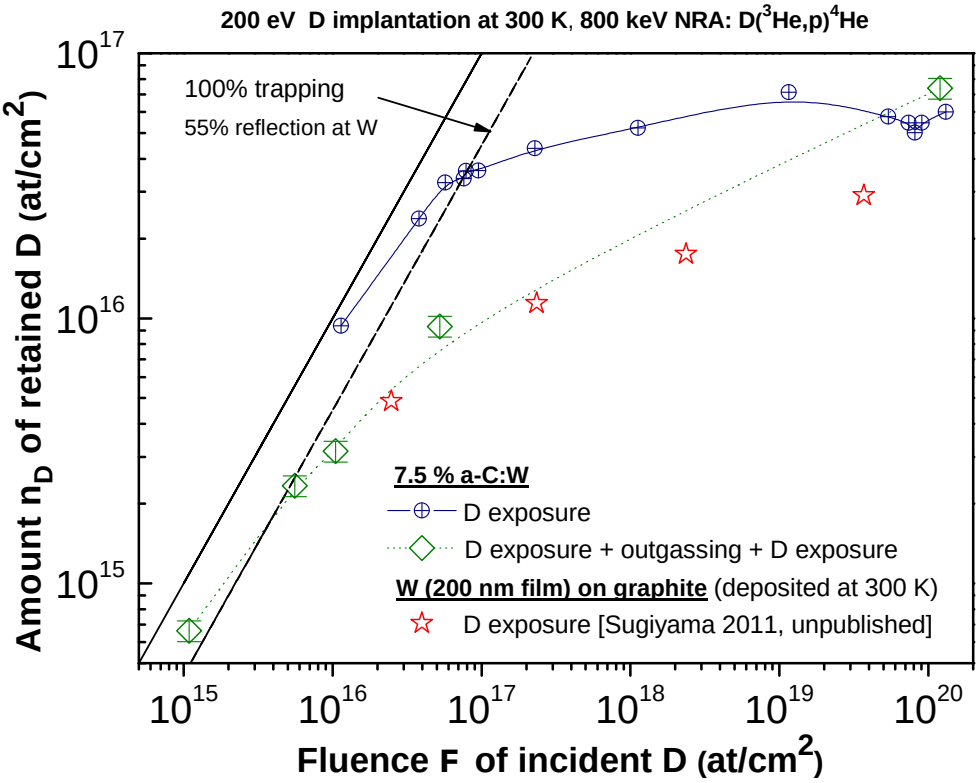

Figure 5.14: Amount of retained D implanted at 300 K versus the fluence of incident 200 eV D. W-enriched 7.5% a-C:W (prior treated by the D beam exposure and outgasing) are compared to two different, characteristic reference materials (see legend). The curves a guide to the eye.

Firstly, characteristics of the reference materials are named. 7.5% a-C:W shows the known curve as mentioned in the subsection 5.2 *Influence of W and pre-heating on accumulation of D*. In contrast, the W-coated graphite shows a lower D inventory, in a fluence range between 10^{16} D/cm^2 and 10^{20} D/cm^2, and a larger increase of the D inventory with fluence, which slows down slightly [142]. For each of the data points of the W-coated graphite a D depth profile was obtained from the energy spectrum of alpha particles obtained from the 800 keV D(^{3}He,^{4}He)p NRA (angle of incidence 0°, scattering angle 102°) [142]. Figure 5.15 plots the D concentration versus the depth for different fluences. The graph is filled with two areas of different colour. The white area, which extends up to a depth of 0.2 μm, marks the W coating and the grey area, which starts from a depth of 0.2 μm, marks the graphite substrate. With increasing fluence the diffusion depth increases. For fluences of $2.4{\cdot}10^{18}$ D/cm^2 and above D diffused into the graphite up to a depth of 0.3 μm. D diffused inside the graphite over a distance of 0.1 μm. This means, the increase of the D inventory with fluence in the W-coated graphite is predominantly caused by diffusion of D into depth; the D concentration in the shallow zones only mildly increases with increasing fluence.

Implanting the enriched 7.5% a-C:W to different fluences leads to the following behaviour: At fluences below 10^{16} D/cm^2, data points are closer to the dashed line compared to the solid line. Therefore, the reflection coefficient seems to be close to 55%, i.e. the value for W. This behaviour confirms that the enrichment zone has a high W concentration. It appears that 7.5% a-C:W, implanted at a fluence of 10^{20} D/cm^2, exhibits an enrichment zone already developed at steady state. At a fluence of 10^{16} D/cm^2 and above, data points

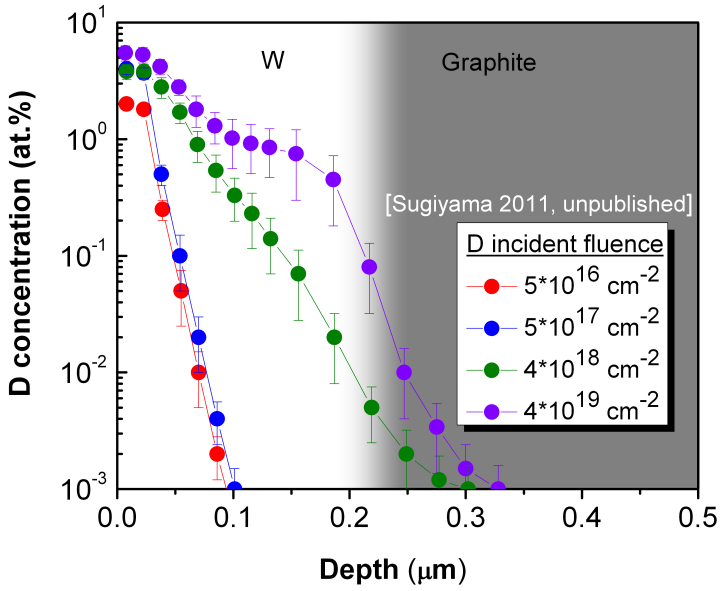

Figure 5.15: D concentration versus the depth in W-coated pyrolytic graphite, exposed to a 200 eV D beam at 300 K and at fluences between $2.5 \cdot 10^{16}$ D/cm^2 and $3.7 \cdot 10^{19}$ D/cm^2 [142]. Depth profiles were obtained from the energy spectrum of alpha particles from the 800 keV D(^{3}He,^{4}He)p NRA (angle of incidence 0°, scattering angle 102°) [142]. The white area marks the W coating and the grey area marks the graphite substrate.

tend to increasingly follow a curve rather than a line. Since the data point at a fluence of 10^{16} D/cm^2 is still close to the line through the origin, the implantation zone appears to be saturated with D at this fluence. The D content in the saturated implantation zone of the enriched 7.5% a-C:W is reduced to about one third of the D content in the saturated implantation zone of 7.5% a-C:W. This leads to a saturation ratio of D/W of 0.03 - 0.08, assuming an amount of W of $40 - 100 \cdot 10^{15}$ D/cm^2 in the enrichment zone. The enriched 7.5% a-C:W and the W-coated graphite exhibit about the same D inventory. This means, the saturation behaviour inside the implantation zone is dominated by W. At fluences above 10^{16} D/cm^2 the increase of the D inventory with fluence is slowed down, but does not reach a limit. The D inventory of the enriched 7.5% a-C:W increases over the inventory of the W-coated graphite.

Since the increase of the D inventory with fluence in the W-coated graphite is predominantly caused by diffusion of D into depth, the increase of the D inventory above the saturation level with increasing fluence in the enriched 7.5% a-C:W must be due to a diffusion of D into depths beyond the width of the enrichment zone as well. D is able to diffuse into depths beyond the enrichment zone. The enrichment zone does not hinder D from diffusing into depth. In consequence, a similar behaviour is also expected for 7.5% a-C:W, implanted at fluences around 10^{20} D/cm^2. For 7.5% a-C:W, implanted at fluences around 10^{20} D/cm^2, a trend is observable: Data points follow a curve, which shows a minimum at a fluence of $8 \cdot 10^{19}$ D/cm^2 and increases again above this minimum with further increasing fluence. Note that this trend is not quatifiable within the accuracy of 10%. Nevertheless, since at a fluence of $8 \cdot 10^{19}$ D/cm^2 D is implanted in a 7.5% a-C:W, which exhibits a W enrichment zone already in steady state, and since it was shown for the enriched 7.5% a-C:W that the increase of the D inventory with fluence does not reach a limit, it is expected that the D inventory in 7.5% a-C:W increases again for fluences above $8 \cdot 10^{19}$ D/cm^2, too, so that the D inven-

tory at fluences far above $8{\cdot}10^{19}$ D/cm^2 should be distinguishable from the D inventory at a fluence of $8{\cdot}10^{19}$ D/cm^2. Furthermore, it is expected that this increase of the D inventory with fluence is accompanied by a diffusion of D into depths beyond the width of the enrichment zone, because it was shown by the implantation of the enriched 7.5% a-C:W that the W enrichment zone does not hinder D from a diffusion into depth.

5.3 Influence of temperature on accumulation of D

Concerning the D retention behaviour, the influence of temperature on the increase of the D inventory with fluence was investigated for a-C and 7.5% a-C:W. These investigations were motivated by the following observed trends: With rising temperature, the number of available bonding states of D decreases in 7.5% a-C:W, leading to an enhanced diffusion of D into depth (see subsection *Diffusion and Trapping* of setion 5.1 *Diffusion of D: Depth profiles*). Furthermore, it was shown (see section 5.2 *Influence of W and pre-heating on accumulation of D*) that D is bound at lower energies in a-C:W compared to a-C. This may lead to an enhanced diffusion into depth in a-C:W compared to a-C. For the first step, it was investigated for 7.5% a-C:W, whether changes in the diffusion into depth with temperature are observable as changes of the increase of the D inventory with fluence. In the second step, 7.5% a-C:W and a-C were compared to pyrolytic graphite, with respect to the increase of the D inventory with fluence.

In order to draw conclusions from measurements of the fluence dependence of the D inventory at elevated temperatures, it was assumed that curves show similar characteristics as observed for measurements at 300 K: At the beginning of the D beam exposure data points follow a line through the origin and are shifted by the reflection coefficient to lower values. At a sufficiently high fluence the implantation zone saturates and the increase of the D inventory with fluence is slowed down but does not reach a limit. Investigations aimed to observe trends with regard to the influence of temperature on the amount of retained D inside the saturated implantation zone (in the following called saturation level) as well as on the increase of the D inventory with fluence. Additionally, it was investigated whether the influence of W inclusions and of the C structure dominates over the influence of temperature at 900 K.

For a-C as well as for a-C:W each D depth profile shows that more than 95% of the retained D is located within 0.5 μm below the surface (see chapter 5.1 *Diffusion of D: Depth profiles*). Therefore, it is ensured that the information depth of the IBA experiment is sufficient and the detected amount of retained D does not depend on film thickness.

Temperature series of the fluence dependence of the D inventory

Figure 5.16 shows a temperature series between 300 K and 1300 K of the amount of retained D, n_D, a as function of the fluence Φ of incident D for 7.5% a-C:W. Additionally, a solid line through the origin is shown, which has a slope of 100%. Along this line the D inventory equals the fluence of incident D, i.e. 100% of the incoming D are retained.

The curve at 300 K shows the progression, previously described in section 5.2 *Influence of W and pre-heating on accumulation of D*. Data points are connected by a spline function, which illustrates the curve shape. Below a fluence of $4{\cdot}10^{16}$ D/cm^2, data points follow a line through the origin. 100% of the unreflected part of the incoming D beam is retained. For fluences between $4{\cdot}10^{16}$ D/cm^2 and $1{\cdot}10^{17}$ D/cm^2 data points follow a curve. The implantation zone becomes saturated. For fluences between 10^{17} D/cm^2 and 10^{19} D/cm^2 data points follow a line in double logarithmic scale. The exponent X over the fluence Φ obtains the value 0.1. Above a fluence of 10^{19} D/cm^2, the D inventory decreases to $5{\cdot}10^{16}$ D/cm^2.

At 500 K two data points are given, at a fluence of 10^{17} D/cm^2 and of 10^{20} D/cm^2. At a fluence of 10^{17} D/cm^2 the D inventory equals the value at 300 K. From the comparison

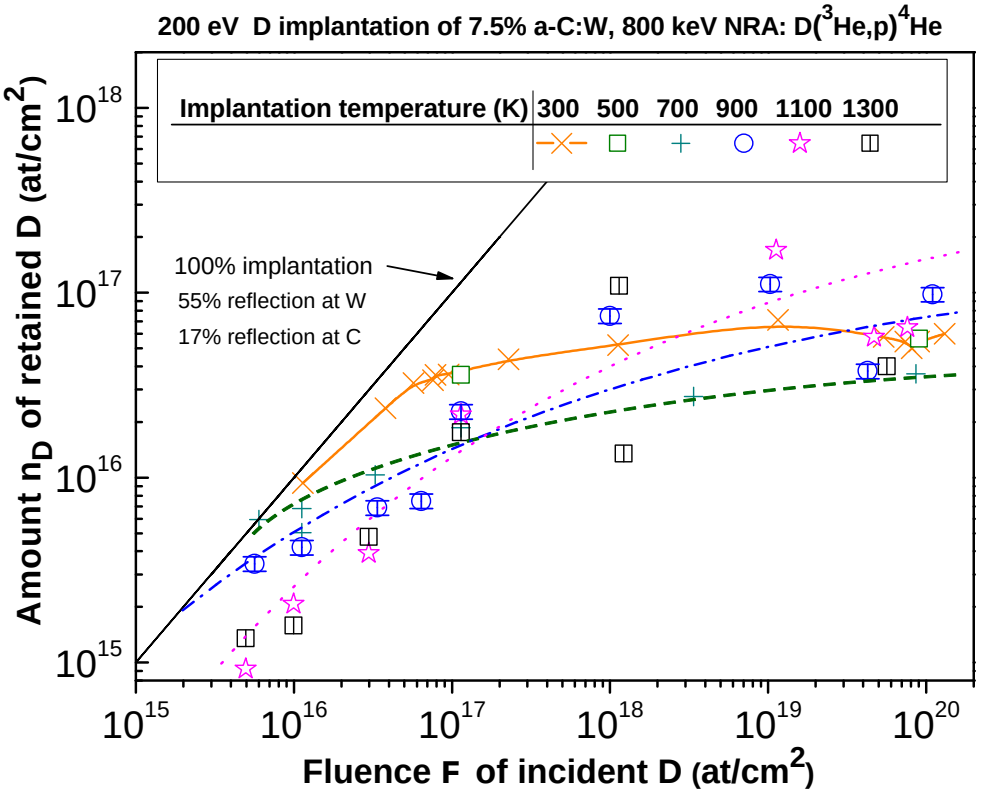

Figure 5.16: Amount of retained D in 7.5% a-C:W, implanted to different temperatures between 300 K and 1300 K versus the fluence of incident 200 eV D. Specccimens implanted above 300 K were pre-heated at 1300 K.

of a-C:W with pyrolytic graphite at 300 K it is evident that the difference of the D inventory between a-C:W and pyrolytic graphite after saturation of the implantation zone remains about constant with increasing fluence, up to a fluence of 10^{19} D/cm^2, i.e. the difference is determined by the saturation level of the implantation zone. Therefore, it can be concluded that the saturation level of the implantation zone for 7.5% a-C:W, implanted at 500 K, does not differ from the saturation level at 300 K. The D inventory of the data point given at a fluence of 10^{20} D/cm^2 obtains the same value compared to the D inventory at 300 K. For 7.5% a-C:W, implanted at 300 K, the D inventory was decreased at a fluence of 10^{20} D/cm^2. Since it is assumed that the D inventory obtains the same values at 500 K compared to 300 K up to a fluence of 10^{19} D/cm^2, it appears that the increase of the D inventory with fluence decreases again above a fluence of 10^{19} D/cm^2 for the specimens implanted at 500 K as well.

At 700 K the D inventory obtains lower values in the fluence range between $\sim 5 \cdot 10^{15}$ D/cm^2 and 10^{20} D/cm^2. Data points given at fluences between $\sim 5 \cdot 10^{15}$ D/cm^2 and $4 \cdot 10^{16}$ D/cm^2 do not follow the line through the origin, but rather a curve. The data point at a fluence of $6 \cdot 10^{15}$ D/cm^2 is very close to the line through the origin so that the implantation zone obviously becomes saturated at fluences around 10^{16} D/cm^2. The saturation level results in a value of $6 - 8 \cdot 10^{15}$ D/cm^2. Above the D inventory levels out over a wider range of fluences as observed at 300 K. For fluences above 10^{17} D/cm^2 the increase of the D inventory with fluence can be described by a power law Φ^X, in good agreement with the experimental data. The exponent X over the fluence Φ is slightly enhanced to 0.14 compared to the value

of 0.10 at 300 K. This means, the diffusion of D is enhanced at 700 K, which was already observed from the depth profiles of D. Due to the low number of data points given the decrease of the D inventory for fluences above 10^{19} D/cm^2, which is observable at 300 K, is not observable at 700 K. For instance, at a fluence of 10^{20} D/cm^2, the D inventory results in a value of $4{\cdot}10^{16}$ D/cm^2, which is enhanced by $1{\cdot}10^{16}$ D/cm^2 compared to the inventory at a fluence of $3{\cdot}10^{18}$ D/cm^2. In contrast, at 300 K, the decrease of the D inventory for fluences above 10^{19} D/cm^2 is also observable by comparing the value obtained at a fluence of 10^{20} D/cm^2 to the value given by the curve at a fluence of $3{\cdot}10^{18}$ D/cm^2. However, it can not be decided from this point of view whether this lowering is less pronounced or even does not exist at 700 K.

Above 700 K, it is not possible to describe the increase of the D inventory with fluence by a power law. Specifically at high fluences, data points can not be related to this kind of curve progression, since the D inventory shows a non-monotonic increase of the D inventory with fluence, which is becoming very pronounced with increasing temperature. Nevertheless, note that the accuracy of the data points (i.e. the accuracy of the D inventory and the accuracy of the fluence of incident D) is as high as the accuracy of those data points presented in section 5.2 *Influence of W and pre-heating on accumulation of D*. For the fluence of incident D a calibration factor was evaluated in each campaign, characterizing the beam profile of the Garching high current ion source. This is described in appendix A *Characterization of the D beam profile*. The calibration factor at the reference zone can be given with an accuracy of 8%. Through a defined positioning of the specimens on the specimen holder of the high current ion source and of the tandem accelerator, it is possible to hit the reference zone with a good precision by the analysing beam. The D inventory, on the other hand, is evaluated by integrating the sharp proton peak in the energy spectrum of protons from the D(^{3}He,p)^{4}He nuclear reaction under an exit angle of 135°, as described in section 3.3.1 *Total amount of retained D and removed C*. Thereby, data points obtained from a scan across the reference zone were averaged, resulting in an averaged D inventory. The averaged D inventory was understood as a mean value from a series of measurements of single values, each integral of the proton peak obtained in the reference zone. For the series of measurements of peak integrals a standard derivation is given. Relating the standard derivation to the mean value reveals a relative error of the measurement series. The relative error obtained this way was defined as accuracy of the D inventory. Data evaluation performed in the manner described, leads to an accuracy of 10% for the D inventory and to an accuracy of 16% for the fluence of incident D. In figure 5.16, both error bars are added to data points obtained at 900 K. Further to this, it was ensured that the influence of temperature on trapping and diffusion of D does not result in a discrepancy between the measured D inventory and the D inventory at the very moment of the switch off of the D beam. For each implantation at elevated temperatures heating of the specimen was stopped $\sim$0.5 s after the switch off of the D beam. It is known from a cross-checking experiment that D does not effuse from the specimen at implantation temperature, after the switch off of the D beam. This was shown in section 5.1 *Diffusion of D: Depth profiles*. In figure 5.1 (b) of section 5.1 D depth profiles are shown, which stem from a series of a-C:W, heat treated at 900 K for different time spans below 36 s, after implantation at 900 K and at a fluence of 10^{18} D/cm^2. Both the shape of the depth profile and the peak integral do not depend on the time span of further heat treatment at 900 K after the switch off of the D beam. From this result, an effusion of D from the specimen can be excluded for at least a further 36 s of heat treatment at constant temperature after the D

beam exposure. This conclusion, of course, must also be valid for the steep decrease of the temperature after the D beam exposure, as imposed by a switch off of the specimen heating, which was immediately following ($\sim$0.5 s) the switch off of the D beam.

Since no analytic description was found for the increase of the D inventory with fluence, for implantation temperatures above 700 K, only trends can be observed. Curves in the graph are a guide to the eye and try to illustrate overall trends for the saturation level and the increase of the D inventory with fluence. Increasing the temperature from 700 K to 1100 K shows that trends already observed at lower temperatures are continued. At 900 K the D inventory obtains lower values compared to the case at 300 K for fluences below 10^{17} D/cm^2. The implantation zone is saturated at fluences around $5{\cdot}10^{15}$ D/cm^2. At fluences above 10^{17} D/cm^2 the D inventory increases above the level at 300 K. The whole curve progression in gently inclined. For fluences between 10^{19} D/cm^2 and 10^{20} D/cm^2, however, the inventory shows a minimum. Increasing the fluence from 10^{19} D/cm^2 to $5{\cdot}10^{19}$ D/cm^2 the D inventory decreases more than a half order of magnitude from a level of 10^{17} D/cm^2 to $4{\cdot}10^{16}$ D/cm^2. Increasing the fluence further to 10^{20} D/cm^2 increases the D inventory again to a level close to 10^{17} D/cm^2. At 900 K, the decrease of the D inventory with fluence above a fluence of 10^{19} D/cm^2 is more pronounced than the decrease observed at 300 K. In contrast to 300 K, it can be observed at 900 K that this decrease is followed again by an increase of the D inventory with further increasing fluence. This behaviour was suggested for implantations at 300 K, too. At 1100 K trends are even more pronounced. The lowering of the D inventory at low fluences is pronounced strongly. The D inventory obtained at fluences of 10^{16} D/cm^2 and below is lowered to 1/5 of the line through the origin. This means, the implantation zone appears to become saturated already at very low fluences, outside the measurement range. At a fluence of 10^{19} D/cm^2, on the other hand, the D inventory obtains a value even larger than at 900 K. Note the two data points at fluences around $\sim 10^{20}$ D/cm^2. They exhibit a lowered D inventory compared to the data point at a fluence of 10^{19} D/cm^2. This decrease is in line with the decrease already observed at 300 K and at 900 K, and confirms that these values can not be interpreted as runaway values. The non-monotonic increase of the D inventory with fluence is even more pronounced at 1300 K. For instance, at a fluence of 10^{18} D/cm^2 two data points exist. The higher value among these two data points is about one order of magnitude above the lower value. Such a kind of decrease of the D inventory, however, is not due to effusion of D during the decrease of the temperature after the beam stop. This was shown in the subsection *Diffusion and Trapping*.

Influence of W inclusions and of the C structure on the accumulation of D at 900 K

In a further step, the influence of W inclusions and the influence of the C structure were investigated at 900 K. In figure 5.17, 7.5% a-C:W is compared to a-C and pyrolytic graphite after the D beam exposure at 900 K. Data obtained from implantations at 300 K are inserted for comparison. Since the specimens were heat treated at 1300 K, a-C and a-C:W have the same C structure. The mosaic spread of pyrolytic graphite, however, is insensitive to temperature. Therefore, the influence of W is studied by comparing a-C:W with a-C and the influence of the C material is studied by comparing a-C with pyrolytic graphite.

Comparing data points of a-C implanted at 900 K with data points of pyrolytic graphite implanted at 900 K and at the same fluence shows that the D inventory has shifted by about a half order of magnitude to higher values in a-C. Comparing the increase of the D inventory

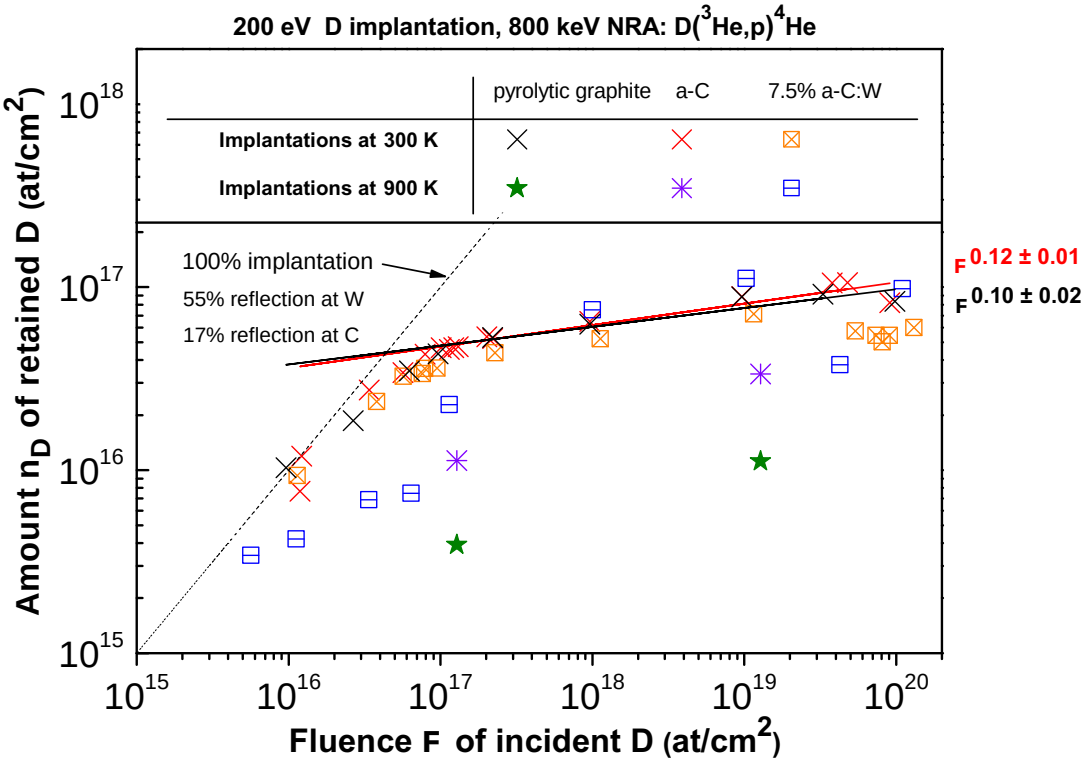

Figure 5.17: Amount of retained D implanted at 900 K versus the fluence of incident 200 eV D. a-C and 7.5% a-C:W are compared to pyrolytic graphite. Specccimens implanted at 900 K were pre-heated at 1300 K.

with fluence of a-C and of pyrolytic graphite with each other, no difference can be observed. This suggests that a-C shows a higher saturation level than pyrolytic graphite at 900 K. This means, the C material affects the saturation ratio in the implantation zone at 900 K, in contrast to the case at 300 K. Comparing a-C, implanted at 900 K and at a fluence of 10^{17} D/cm^2, and 7.5% a-C:W, implanted at 900 K and at the same fluence, with each other, both data points obtain values in a similar order of magnitude. At a fluence of 10^{19} D/cm^2, however, the D inventory of a-C obtains a value of about a third of the value of 7.5% a-C:W. Therefore, the D inventory of a-C seems to exhibit a slightly decreased increase with fluence compared to 7.5% a-C:W. This suggests that 7.5% a-C:W shows a saturation level at 900 K, which is slightly lowered compared to the saturation level of a-C at 900 K, but still above the saturation level of pyrolytic graphite at 900 K. Therefore, W inclusions lead to a slight intrinsic change of the D retention behaviour at an implantation temperature of 900 K, which is in contrast to the behaviour observed at 300 K.

The influence of the C material on the saturation level dominates over the influence of W at 900 K, and is of the same order of magnitude as the influence of temperature. Regarding the increase of the D inventory with fluence, W inclusions exhibit a slight influence at 900 K, in contrast to the C structure.

5.4 Summary: Retention behaviour

In order to characterize the retention behaviour of a-C and a-C:W, D has been implanted with a 200 eV D beam at 300 K - 1300 K substrate temperature. Implantations were performed at different fluences below 10^{20} D/cm^2. The total amount of retained D was obtained by D(^{3}He,p)^{4}He nuclear reaction analysis at 800 keV. The depth profiles of D were obtained from the energy spectrum of alpha particles, obtained from the same nuclear reaction (NRA spectrum).

In order to study the influence of W and the influence of the structure of the C matrix on the retention behaviour of a-C:W, measurements on D retention in a-C:W were performed at an implantation temperature of 300 K and compared to measurements on a-C and pyrolytic graphite. Thereby, the W concentrations were varied below 18.5% and pre-annealing temperatures were varied below 1300 K.

At 300 K, the D retention behaviour of a-C and a-C:W show the same characteristics as the D retention behaviour of pyrolytic graphite. For low fluences the D inventory increases with fluence along a line through the origin. This kind of increase with fluence is slowed down at fluences between $4{\cdot}10^{16}$ D/cm^2 and $2{\cdot}10^{17}$ D/cm^2. For higher fluences the D inventory only slightly increases with fluence.

The reflection coefficient of a-C and a-C:W was measured at fluences below $4{\cdot}10^{16}$ D/cm^2. No difference was observed to the reflection coefficient of pyrolytic graphite. The saturation ratio was determined by means of the D inventory at a fluence of $1{\cdot}10^{17}$ D/cm^2. In a-C the saturation ratio equals the saturation ratio in pyrolytic graphite of 0.4. In a-C:W the saturation ratio decreases with increasing W concentration up to 0.28 for 18.5% W. At fluences between 10^{17} D/cm^2 and 10^{19} D/cm^2, the increase of the D inventory with fluence in a-C, a-C:W and pyrolytic graphite can not be distinguished from one another. Above a fluence of 10^{19} D/cm^2 a-C shows a monotonic increase of the D inventory with fluence. This increase can be expressed by the power law Φ^X for fluences between 10^{17} D/cm^2 and 10^{20} D/cm^2. The exponent X obtains the value 0.1 and can not be distinguished from the value for pyrolytic graphite. For a-C:W the increase of the D inventory with fluence depends strongly on the W concentration. At a fluence of 10^{20} D/cm^2 the D inventory is increased to the 1.5-fold of the D inventory of pyrolytic graphite for 1% and 2.5% a-C:W and it is decreased to the half value of the D inventory of pyrolytic graphite for 7.5% a-C:W. The decrease observed for 7.5% a-C:W was observed to the same extent for 15% a-C:W as well. Pre-heating of a-C and a-C:W does not affect these results.

For enriched a-C:W the reflection coefficient is close to the value of W (55%) and the saturation ratio of D/W in the implantation zone is lowered to 0.03 - 0.08. For fluencees above saturation of the implantation zone no saturation of the total D inventory was observed.

The trapping behaviour of a-C and 1%, 2.5% and 7.5% a-C:W was compared with each other performing TDS measurements on the specimens implanted at 300 K and at different fluences (10^{17} D/cm^2, 10^{19} D/cm^2, 10^{20} D/cm^2). Both for the D_2 signal and for the CD_4 signal, similar trends are observed. The peak maximum is shifted to lower temperatures in a-C:W compared to a-C, indicating a lowering of the trapping energy through the presence of W. The peak width is decreased in a-C:W compared to a-C, indicating a lowering of the magnitude of the energy range of occupied bonding states through the presence of W. Both trends are pronounced with increasing W concentration. A rather weak change of the peak

width with increasing fluence is observed for a-C. For a-C an increase of the D inventory with fluence is observable as an increase of the overall peak intensity. For a-C:W, on the other hand, the peak width changes with increasing fluence, besides an overall increase of the peak intensity with fluence. Increasing the fluence from 10^{19} D/cm^2 to 10^{20} D/cm^2, the peak width increases for 2.5% a-C:W and it decreases for 7.5% a-C:W. This is observable as an increase of the D inventory for 2.5% a-C:W and in a decreases of the D inventory for 7.5% a-C:W.

In investigating the influence of implantation temperature on the retention behaviour of a-C:W, on the other hand, measurements on the D retention in a-C:W were performed at implantation temperatures between 300 K and 1300 K. Thereby, the W concentration was fixed at 7.5% and the pre-heating temperature was fixed at 1300 K. Additionally, the retention behaviour of 7.5% a-C:W, of a-C and of pyrolytic graphite were compared with each other at 900 K.

In the temperature range between 300 K and 1300 K overall trends are observable, with regard to the saturation level of the implantation zone and the increase of the D inventory with fluence. The quantification of these trends, however, is becoming complicated with increasing temperature. The effect of temperature starts to become dominant between 500 K and 700 K: The saturation level decreases from $3.5{\cdot}10^{16}$ D/cm^2 to $6\text{-}8{\cdot}10^{15}$ D/cm^2. The exponent X in the power law Φ^X increases from 0.10 to 0.14. In the temperature range between 300 K and 900 K, the saturation level decreases to about 1/10. For the temperature range between 300 K and 1300 K only qualitative statements can be given, due to a very pronounced non-monotonic increase of the D inventory with fluence: A decreasing saturation level of the implantation zone is in convolution with a rising increase of the D inventory with fluence. At 900 K, the saturation level of a-C:W is about a half order of magnitude above the saturation level of pyrolytic graphite and gently enhanced compared to a-C. The increase of the D inventory with fluence in a-C:W is gently increased compared to a-C and to pyrolytic graphite; no difference is observable between a-C and pyrolytic graphite.

The depth profiles of D obtained from a-C:W implanted at temperatures between 300 K and 900 K qualitatively reveal the influence of temperature on diffusion depth and D concentration. For temperatures below 700 K D does not diffuse into depths, which are larger than the resolvable depth ($\sim$50 nm). The average D concentration at this depth range is $\sim$5%. For the temperature range between 700 K and 900 K a decrease of the saturation ratio in the implantation zone with increasing temperature is qualitatively observable. Further to this, it can be shown that D is trapped at depths not larger than $\sim$0.5 μm. At 700 K, 50% of the D is trapped below the resolvable depth of 60 nm and 50% are trapped at depths larger than the resolvable depth. The concentration of D is 2% in the surface near peak and 0.3% in the tail into depth. The enhanced diffusion depth at 700 K is in convolution with an enhanced exponent X in the power law Φ^X compared to 300 K. At 900 K, D is homogeneously dissipated over a depth of $\sim$0.5 μm and the concentration of D obtains an averaged value of 2%. For each specimen from the temperature series the diffusion depth is larger than the width of the W enrichment zone. In general, the D depth profiles showed that in a-C:W, D can diffuse into depths beyond the implantation zone.

Chapter 6

Discussion

The erosion behaviour, which is affected by W enrichment, affects the deuterium (D) retention behaviour. Therefore, the retention behaviour is discussed taking results from the investigations of the erosion behaviour into account.

6.1 Erosion behaviour of a-C:W under D beam exposure

Enrichment of W: Depth profiles

For specimens exposed to a 200 eV deuterium (D) beam at a fluence of 10^{20} D/cm^2 and at temperatures between 300 K and 1100 K it was possible to convert RBS spectra into depth profiles of tungsten. While at 700 K and below, the width of the enrichment zone is between the width of the ion range in tungsten at 1 keV (16 nm) and at 200 eV (6.3 nm), the width of the enrichment zone increases above the width of the ion range at 900 K (50 nm) and at 1100 K (80 nm). This increase of the width of the enrichment zone is in convolution with a decrease of the W concentration, from nearly 100% of W at 500 K and below to 75% at 700 K, 60% at 900 K and finally to 35% at 1100 K.

From the increase of the width of the enrichment zone at elevated temperatures above the width of the ion range, the question is raised whether it is possible to remove carbon (C) in the form of volatile hydrocarbons from the whole depth, which matches the width of the enrichment zone. C is removed from depths, which are not reached by energetic D. Therefore, one or several processes must be thermally activated, which enable D and C to get in contact and thus to react with each other.

If D and C get into contact and react with each other beyond the width of the ion range, one must assume that thermalised D diffuses into depth and reacts with the undamaged C matrix, i.e. that the thermal chemical erosion occurs at the undamaged C beyond the width of the ion range. The reactivity of the undamaged C depends on structure, i.e. on the amount of open sp^2 sites. While undamaged pyrolytic graphite exhibits a yield for the thermal chemical erosion of an order of magnitude lower than pre-irradiated pyrolytic graphite, co-deposited C exhibits a yield for the thermal chemical erosion in the same order of magnitude as pre-irradiated pyrolytic graphite [143]. If a-C:W has a similar structure to co-deposited C, i.e. a similar amount of open sp^2 sites, the thermal chemical erosion is pronounced to a similar extent in the undamaged C matrix as within the width of the ion range.

In this case, one would expect that C reacts with D over the entire diffusion depth of D, which extends up to 0.5 μm at 900 K, and thus that C is lost from depths up to 0.5 μm. From this point of view, however, it is unclear why the width of the W enrichment zone, which is 50 nm at 900 K, is considerably smaller than 0.5 μm at 900 K. If the thermal chemical erosion occurred beyond the width of the ion range, over the entire diffusion depth, this would mean that hydrocarbons are released from depths matching the width of the enrichment zone but retained at depths beyond the width of the enrichment zone. This problem, however, can not be clarified within the framework of the study presented in this thesis.

Further to this, the question is raised whether a process may be thermally activated, which enables energetic D to get in contact with C from the depth, inside the width of the ion range. At this point only speculation is possible; no measurements exist explaining the observed increase of the width of the enrichment zone with temperature. If energetic D can not reach C in the depth, C from the depth must reach energetic D, i.e. C must diffuse towards the width of the ion range. In literature studies exist, which examine thermal activated diffusion of C into W [144]. Note that these studies were not performed on tungsten-containing carbon films (a-C:W). In fact, amorphous C was deposited on W, i.e. on polycrystalline W and on a W (111)-crystal. Reactive diffusion of C atoms into W and successive formation of W carbide phases by annealing steps was investigated applying XPS [144]. With increasing temperature, an increasing amount of C atoms diffused through interstitials of W into depth. A measure for the extent of diffusion was the formation of carbide phases, which was measured by changes in XPS peaks with temperature, i.e. for the successive formation of W carbide phases, the limiting factor was the diffusion of C in W, which is temperature dependent. The temperature range, which led to a diffusion of C into W, was different among polycrystalline W and the W (111)-crystal. For polycrystalline W, the diffusion of C increased clearly in a range between 900 K and 1100 K and for the W (111)-crystal, the range was between 1000 K and 1100 K. This result may be transferable to the case of the formation of a W enrichment zone in a-C:W during the D beam exposure at elevated temperatures. As soon as W is temporarily enriched over the width of the ion range, a concentration gradient may drive a diffusion of C, which is thermally activated. In this case the temperature range, which exhibits a growing width of the enrichment zone (above 700 K), would correspond to a temperature range, which exhibits an enhanced diffusion of C in W. This temperature range, however, is decreased compared to the ranges observed in [144]. Nevertheless, this example from literature shows that such a kind of thermally activated processes were observed once, in a system similar to a-C:W covered by a W enrichment zone. Of course, it should also be mentioned here that processes in a-C:W occur under D beam impact, which serves as an additional entry of energy. This additional entry of energy may decrease the temperature range, which leads to a diffusion of C into W. In literature such a process is denoted as radiation enhanced segregation [104]. In [104] radiation enhanced segregation was suggested to occur in titanium carbide exposed to a D beam at 300 K and at energies below 200 eV. This led to a composition of C and titanium at the surface similar to titanium carbide and thus to a formation of carbide phases, i.e. titanium carbide. Further enrichment of titanium at the surface was hindered. Note that this process was not observed in [104] for WC exposed to a D beam at 300 K and at low energies. Nevertheless, since a-C:W was exposed to the D beam at elevated temperatures in the study presented in this thesis, radiation enhanced segregation appears to be possible.

If radiation enhanced segregation is the process, which leads to an increase of the width of the enrichment zone and to a dilution of W in the enrichment zone with increasing temperature, the temperature dependence of the W enrichment should be interpreted as a trend, which may be influenced by roughening and thus shows variations in its values. For instance, at 1100 K two specimens were investigated. It was shown that roughening was different among these two specimens. The FWHM of the distribution of local tilt angles was about 30° for one specimen so that it was not possible to convert the RBS spectrum into a depth profile of W. This means, roughening shows variations, even among specimens investigated with the same set of parameters (W concentration, pre-heating temperature, implantation temperature and fluence). In literature [78] it is known that the energy reflection coefficient depends on the angle of incidence. For 200 eV D on C the energy reflection coefficient increases to the ∼1.5-fold, by increasing the angle of incidence from 0° to 30°. So, the amount of energy deposited by the D beam is thought to change with roughness, too. This would certainly influences the temperature dependence of the W enrichment. Radiation enhanced segregation is not yet quantifiable. The impact of roughness on radiation enhanced segregation is also not yet quantifiable. From this point of view it is unclear whether the depth resolution of the analysing method still has the dominating effect on the uncertainty of the width and the composition of the W enrichment zone.

Influence of W and of pre-heating on total yields of C

For a-C:W exposed to a 200 eV D beam at 300 K and at a fluence of 10^{20} D/cm^2 it was shown that the total yield of removed C is significantly reduced compared to pure carbon films (a-C). This reduction is less sensitive on the W concentration and insensitive to the heat treatment before the D beam exposure.

In literature two explanations can be found for a reduction of the total yield of C in metal-containing carbon, a changed chemistry between C and D [109, 110, 111], on one hand, and the shielding effect [104], on the other hand. Concerning a changed chemistry between C and D it was shown that for boron-containing carbon the activation energy of the D release is lowered compared to pure carbon. Nevertheless, the concentration of boron was not varied and it is not known whether this effect is present for other metal inclusions as well. The shielding effect, however, is the most widely used explanation for a reduction of the total yield of removed C in metal-containing carbon [116, 104]. With increasing fluence a surface near zone enriched with W builds up (W enrichment zone), due to preferential sputtering of C. The W enrichment zone exhibits a larger reflection coefficient, and thus lower amounts of D can penetrate into the material. Furthermore, the maximum width of the enrichment zone, which is reached in steady state, is supposed to match the width of the ion range in W. Therefore, incoming D can not reach C. The erosion process is mitigated.

In this context the question raises, for which specimen from the concentration series the enrichment zone is already developed in steady state, at a fluence of 10^{20} D/cm^2. This would give a hint to whether it can be expected that - already at a fluence of 10^{20} D/cm^2 - erosion and retention behaviour of a specimen are considerably affected by the presence of a W enrichment zone. The following features may be relevant for a-C:W: The W content near the surface is close to 100% in steady state. The reflection coefficient for D increases from 17% (C) to 55% (W), with increasing fluence of incident D. The fluence, which must be reached

so that steady state is reached for a specimen from the concentration series, however, is not known. But it is possible to calculate a minimum amount of C, which needs to be removed to reach steady state. If this minimum amount of removed C is larger than the measured amount of removed C at a fluence of 10^{20} D/cm^2, it can be concluded that steady state has not been reached at a fluence of 10^{20} D/cm^2. In steady state, the width of the enrichment zone and the W concentration do not change with fluence of incident D, i.e. the enrichment zone contains a certain amount of W atoms. By taking the amount of W atoms in the enrichment zone and the initial W concentration into account, it is possible to calculate a minimum amount of removed C at steady state. The amount of W atoms, N_W, in an enrichment zone, containing 100% W, is the ratio between the width, w_{ion}, of the ion range and the areal density, ρ_{areal}, of W atoms:

$$N_W = \frac{w_{ion}}{\rho_{areal}}, \text{ with } \rho_{areal} = 0.1583\,\text{nm}/\,10^{15}\text{at}\cdot\text{cm}^{-2}. \tag{6.1}$$

The amount, ΔN_C, of removed C at steady state is the ratio out of the amount of W atoms, N_W, in the enrichment zone and the initial W concentration c_0:

$$\Delta N_C = \frac{N_W}{c_0}. \tag{6.2}$$

For a 200 eV D beam free of neutral particles the width of the ion range in W is 6.3 nm ($40\cdot10^{15}$ at/cm^2) [99]. Taking the presence of 1.2 keV neutral particles into account (see chapter 3.2 *Specimen exposure and beam profile characterization*; content ~5% at the reference zone), the width of the ion range in W is 16 nm ($100\cdot10^{15}$ at/cm^2) [99]. This leads to different values for the minimum amount of removed C at steady state. In table 6.1 values obtained for the minimum amount of removed C at steady state are compared to measured amounts of removed C, for the different W concentrations.

Initial W content (%)	1	2.5	4	6	7.5	15
Amount of removed C (10^{15} at/cm^2)						
- measured at 10^{20} D/cm^2	1900	1900	3100	3100	2300	1800
- minimum at steady state (200 eV D)	4000	1600	1000	700	500	300
- minimum at steady state (1.2 keV D)	10000	4000	2500	1700	1300	700

Table 6.1: Comparison of the minimum amount of removed C at steady state to the measured amount of removed C at a fluence of 10^{20} D/cm^2. Multiple data points at a concentration were averaged.

For a 200 eV D beam conclusions can be easily drawn. At a concentration of 1% the minimum amount of removed C is larger than the measured amount of removed C. Therefore, steady state has not been reached for 1%a-C:W at a fluence of 10^{20} D/cm^2. Since at 200 eV the yield of physical sputtering of W can be neglected, no additional amounts of C need to be removed to reach steady state. So the minimum amount of removed C can be compared with the measured amount of removed C, in order to figure out whether steady state has been reached for the W concentrations above 1%. For higher concentrations the minimum amount of removed C is lower than the measured amount of removed C. Therefore, steady state has been reached at a fluence of 10^{20} D/cm^2 for a-C:W, containing more than 1% W.

The situation is complicated for a D beam, containing 1.2 keV neutrals. Steady state has not been reached for the W concentrations of 2.5% and below. Above 2.5%, however, it can

not be concluded whether steady state has been reached, since the sputtering yield of W is considerable at 1 keV [61]. Therefore, additional amounts of C need to be removed to reach steady state. The additional amount of removed C, ΔN_C^{add}, is given by the erosion yield of W, Y_W^{1keV}, at 1 keV, the content of neutral particles in the 200 eV D beam, $c_{1.2keV}$, the initial W concentration, c_0, and a fluence, Φ, which needs to be reached to reach steady state:

$$\Delta N_C^{add} = Y_W^{1keV} \cdot c_{1.2keV} \cdot \Phi / c_0. \tag{6.3}$$

The fluence, which depends on the initial W concentration, however, is not known. Therefore, it is not possible - taking the presence of 1.2 keV neutrals in the 200 eV beam into account - to estimate whether steady state has been reached at a fluence of 10^{20} D/cm^2 for the W concentrations above 2.5%.

This result needs to be compared to results obtained from the analysis of the width and the composition of the W enrichment zone. Those results are presented in section 4.1 *Enrichment of W: Depth profiles* for 7.5% a-C:W. If an enrichment zone contains 100% W, it can be concluded that steady state has been reached. For 7.5% a-C:W exposed to a 200 eV D beam (containing 5% 1.2 keV neutral particles) at 300 K and at a fluence of 10^{20} D/cm^2 it was shown that the W concentration is close to 100% and thus that steady state has been reached. Since equations (6.2) and (6.3) show that the amount of C, which needs to be removed to reach steady state, is directly proportional to the inverse of the initial W concentration, it can be concluded that the W enrichment zone is in steady state for the W concentrations above 7.5%, too. Altogether, from the analysis of the W enrichment zone and from the estimations mentioned above it is known that for the W concentrations of 2.5% and below, the enrichment zone is not in steady state, and that for the W concentrations of 7.5% and above, the W enrichment zone is in steady state. For concentrations above 2.5% and below 7.5%, e.g. for 4% a-C:W and for 6% a-C:W, however, it can not be decided whether the W enrichment zone is in steady state or not.

Note that the measured amount of removed C does not equal the minimum amount of removed C for 7.5% a-C:W and for 15% a-C:W. For both specimen the enrichment zone is in steady state. This means, C is removed even after steady state has been reached. Enrichment does not bring the erosion to a stop. This must be attributed to the presence of 1.2 keV neutrals in the D beam. At 1 keV/D the sputtering yield of W is considerable so that the enrichment zone does not protect additional amounts of C to be removed. Therefore, it can not be decided from these investigations whether enrichment brings the erosion process to a stop for D energies beyond the sputtering threshold of W.

Concerning the mechanisms, which lead to a reduction of the total yield of removed C in a-C:W, the low values of the total yield of C in 7.5% a-C:W and in 15% a-C:W can be explained by the shielding effect. In contrast, for 1% a-C:W and 2.5% a-C:W, which do not exhibit an enrichment zone developed in steady state, the shielding effect is expected to be less pronounced, and thus it is expected that the total yield of C obtains a value between the values for a-C and for 4% a-C:W. Note that energetic D is still able to reach C. Nevertheless, the total yields of C of 1% a-C:W and of 2.5% a-C:W obtain values clearly below the values for a-C and similar to 7.5% a-C:W and to 15% a-C:W. Therefore, it can not be excluded that even small amounts of W change the chemistry between D and C. From this point of view it may be speculated that a changed chemistry between D and C serves as explanation for the

strong lowering of the total yield of C in 1% a-C:W and 2.5% a-C:W.

Influence of implantation temperature on shielding and total yields of C

In literature it was shown that a-C:Me exhibits a significantly reduced total erosion yield [115, 75], at fluences up to 10^{20} D/cm^2 and at implantation temperatures of 300 K and of 650 - 750 K. This agrees with the results presented within the framework of the study presented in this thesis. Nevertheless, in this study the total erosion yield was increasing between 700 K and 900 K, from a nearly constant level of 0.023 at 700 K and below to a nearly constant level of 0.037 at 900 K and above. This temperature dependence seems to be in contradiction with the temperature dependence of the methane production yield given in literature [115, 143]. For a-C:W exposed to a 200 eV D beam the temperature dependence of the methane production yield shows a maximum at $\sim$700 K [115]. Above 700 K the methane production yield decreases clearly, e.g. at 900 K the methane production yield is already decreased to 1/10 of the maximum [115]. The formation of volatile hydrocarbons is hindered; only physical sputtering of C can occur [143].

Comparing the temperature dependence of the methane production yield of a-C:W known in literature [115] with the temperature dependence of the total erosion yield evaluated in this study, one has to keep in mind some important differences. Firstly, in this study a temperature dependence of the total erosion yield was evaluated. This yield corresponds to a sum of all yields of all species of volatile hydrocarbons. The composition of the spectrum of volatile hydrocarbons changes with temperature, as already mentioned in literature [75]. Therefore, the temperature dependence of the production yield is not necessarily the same among all hydrocarbon species. For the maximum of the total erosion yield this may lead to a different intensity and to a shift in temperature. Furthermore, the temperature dependence of the methane production yield was measured at sufficiently low fluences, so that enrichment of W at the surface can be neglected [115].

In this study, however, the total erosion yield was evaluated for the specimens exposed to the D beam at a fluence of $\sim 10^{20}$ D/cm^2. The depth profiles of W show that an enrichment zone has already built-up among all specimens from the temperature series of this study. Therefore, enrichment of W at the surface can not be neglected. For the specimens investigated in this study two trends influence the temperature dependence of the total erosion yield. The first trend is a temperature dependence of the chemistry between D and C, which shows a maximum over the implantation temperature. The second trend is the shielding effect. The shielding effect leads to a decrease of the total erosion yield with increasing W concentration in the enrichment zone [116, 104, 145]. Since it was shown in this study that the W concentration in the enrichment zone decreases with increasing implantation temperature, the impact of the shielding effect on the total erosion yield must increase with decreasing temperature. Both trends, the temperature dependence of the shielding effect and the temperature dependence of the chemistry between D and C, act together and result in a temperature dependence of the total erosion yield. Consequently, the temperature dependence of the total erosion yield measured in this study does not contradict the temperature dependence of the methane production yield known in literature. For instance, if the chemistry between D and C can be neglected at 900 K and above, only physical sputtering occurs. In the case of physical sputtering, the component sputtering yield equals the ratio between the partial sputtering yield and the surface concentration in steady state [104]. At 900 K and above,

component sputtering yields can be calculated for C and can be compared with measured sputtering yields. For a C partial sputtering yield of 0.02 [61] and a C surface concentration of 0.4 (at 900 K) and of 0.65 (at 1100 K) the component sputtering yields for C are 0.05 and 0.03, respectively. As previously mentioned, the total erosion yield at 900 K and above is $\sim$0.04 and thus close to the component sputtering yields at 900 K and 1100 K. Note that from this point of view it appears that physical sputtering dominates at temperatures of 900 K and above. Therefore, it is unlikely that C is lost from depths beyond the width of the ion range through the thermal chemical erosion. (This process was suggested above (see *Enrichment of W: Depth profiles*) to result in an increase of the width of the W enrichment zone above the width of the ion range at 900 K and above.)

The increase of the width of the enrichment zone with temperature together with a decrease of the W concentration with temperature may give an explanation for the observed temperature dependence of the amount of removed C of 7.5% a-C:W implanted at a fluence of $\sim 10^{20}$ D/cm^2.

6.2 Retention behaviour of a-C:W under D beam exposure

Influence of W and pre-heating on accumulation of D

From a comparison of the fluence dependence of the D inventory (under the 200 eV D beam exposure at 300 K) of a-C and a-C:W with the fluence dependence of the D inventory of pyrolytic graphite it could be shown that the D retention behaviour of a-C and a-C:W is, in principal, determined by the same processes, which are well known in literature to occur in graphites. For low fluences the D inventory increases with fluence along a line through the origin; 100% of the unreflected portion of the incoming D beam is retained. This kind of increase with fluence is slowed down at fluences between $3\cdot10^{16}$ D/cm^2 and $2\cdot10^{17}$ D/cm^2; the implantation zone becomes saturated with D in a certain saturation ratio (e.g. D/C = 0.4 for pyrolytic graphite). For higher fluences the D inventory only slightly increases with fluence; D diffuses into depths beyond the implantation zone and accumulates in the depth. Therefore, it is possible to compare the D retention behaviour by means of the reflection coefficient, of the saturation ratio in the implantation zone and of the increase of the D inventory with fluence.

Reflection coefficient

For fluences below $3\cdot10^{16}$ D/cm^2 reflection coefficients can be compared by means of the 100% retention line. This shows that the W concentrations of 18% and below are not sufficiently high to affect the reflection coefficient of a-C:W, which is not yet enriched with W at the surface, i.e. the reflection coefficient is not changed intrinsically by the W inclusions.

Saturation ratio in the implantation zone

At fluences between $3\cdot10^{16}$ D/cm^2 and $2\cdot10^{17}$ D/cm^2 saturation ratios can be compared by means of a decreasing slope of the curve, which is caused by the saturation of the implantation zone and thus results in different values of the D inventory for the different W concentrations at a fluence of $1\cdot10^{17}$ D/cm^2. In a-C the saturation ratio equals the saturation ratio

in pyrolytic graphite of 0.4. The saturation ratio is lowered intrinsically in a-C:W compared to a-C and pyrolytic graphite. This is due to an intrinsically lowered amount of available bonding states in a-C:W, which was shown by TDS experiments, for 7.5% a-C:W implanted at a fluence of 10^{17} D/cm^2. This effect becomes more pronounced with increasing W concentration, i.e. the saturation ratio decreases with increasing W concentration up to 0.28 for 18.5% W; for 7.5% a-C:W, only a slight decrease was observed, within the accuracy of 10%.

Increase of the D inventory with fluence - Diffusion of D into depth

Above a fluence of $1{\cdot}10^{17}$ D/cm^2, the increase of the D inventory with fluence in a-C is caused by a diffusion of D into depth and it can be excluded from AFM analysis (see subsection *Roughening at 300 K* of appendix E *Surface morphology: Roughening*) that roughening causes this increase of the D inventory with fluence. By applying AFM it was shown that the difference of surface roughness for the different W concentrations (the specimen implanted at a fluence of 10^{19} D/cm^2) is even slightly above the extent of roughening with increasing fluence in a-C (increasing the fluence from 10^{19} D/cm^2 to 10^{20} D/cm^2). At a fluence of 10^{19} D/cm^2, however, the D inventory can not be distinguished for the different W concentrations. This means, differences of surface roughness in the magnitudes mentioned do not influence the D inventory. This observation must also be valid for increasing the fluence on a-C from 10^{19} D/cm^2 to 10^{20} D/cm^2. Above a fluence of $1{\cdot}10^{17}$ D/cm^2 the diffusion of D into depth can be observed by means of the increase of the D inventory with fluence.

As-deposited a-C exhibits about the same increase of the D inventory with fluence as pyrolytic graphite for fluences below 10^{19} D/cm^2. The difference of the D inventory between a-C and a-C:W at a fluence of $1{\cdot}10^{17}$ D/cm^2, which is caused by an altered saturation ratio, remains about constant with increasing fluence up to a fluence of 10^{19} D/cm^2. In order to study the influence of W inclusions on the trapping behaviour and thus the influence of the trapping behaviour on the increase of the D inventory with fluence, the trapping behaviour of a-C and a-C:W was compared by TDS measurements. W seems to promote the release of D at lower temperatures, in molecular form as well as bound in deuterated methane. For both molecules a concentration dependence was observed. a-C:W exhibits an intrinsically changed trapping behaviour. Nevertheless, an intrinsically changed trapping behaviour does not result in a changed increase of the D inventory with fluence, at fluences below 10^{19} D/cm^2.

Altogether, at 300 K the diffusion of D into depth is no different between a C material, which exhibits a graphite structure (pyrolytic graphite), and a C material, which exhibits an amorphous structure (a-C) and furthermore the diffusion of D into depth is not affected by the W inclusions and thus by a changed trapping behaviour observed in a-C:W.

Increase of the D inventory with fluence - Enrichment

Above a fluence of 10^{19} D/cm^2 the increase of the D inventory with fluence is still dominated by the diffusion of D into depth for pyrolytic graphite and for a-C, which is observable as a monotonic increase of the D inventory with fluence. In general, the fluence dependence of the D inventory of as-deposited a-C and of pyrolytic graphite are no different from each other, within the entire analysed fluence range between 10^{16} D/cm^2 and 10^{20} D/cm^2. This means,

for as-deposited a-C and for pyrolytic graphite the reflection coefficient, the saturation ratio in the implantation zone and the diffusion of D into depth can not be distinguished from one another; as-deposited a-C and pyrolytic graphite show the same D retention behaviour.

In a-C:W the increase of the D inventory with fluence is not dominated by a diffusion of D for fluences between 10^{19} D/cm^2 and 10^{20} D/cm^2. In this fluence range the increase of the D inventory depends strongly on the W concentration. For 1% a-C:W and for 2.5% a-C:W the D inventory increases to the 1.5-fold of the D inventory of pyrolytic graphite at a fluence of 10^{20} D/cm^2 and for 7.5% a-C:W the D inventory decreases to the half value of the D inventory of pyrolytic graphite at a fluence of 10^{20} D/cm^2. For the concentration dependence of the D inventory an explanation can be given by TDS experiments, by analysis of surface roughness as well as by analysis of the W enrichment zone (see subsection *Thermal desorption spectroscopy* in section 5.2 *Influence of W and pre-heating on accumulation of D*, subsection *Surface roughness at 300 K* in appendix E *Surface morphology: Roughening* and section 4.1 *Enrichment of W: Depth profiles*).

By TDS experiments it was possible to compare the energy range of bonding states, which are occupied with D, in a-C and a-C:W, with each other. It was shown that the energy range of occupied bonding states in the implantation zone changes its magnitude in a-C:W increasing the fluence from 10^{19} D/cm^2 to 10^{20} D/cm^2, in contrast to a-C. The energy range of occupied bonding states increases its magnitude in 2.5% a-C:W above the magnitude in a-C and it decreases its magnitude in 7.5% a-C:W below the magnitude in a-C. Therefore, 2.5% a-C:W has a larger D inventory than a-C at a fluence of 10^{20} D/cm^2 and 7.5% a-C:W has a lower D inventory than a-C at a fluence of 10^{20} D/cm^2.

For 2.5% a-C:W surface roughness increases clearly increasing the fluence from 10^{19} D/cm^2 to 10^{20} D/cm^2, which is observable as an increase of the RMS value and the surface area to the 10-fold and to the 1.17-fold, respectively. An increase of the surface area to the 1.17-fold leads to an increase of the implantation volume to the 1.17-fold. This increase, however, is not sufficient to explain the doubling of the D inventory with fluence. Another explanation may be given by the erosion behaviour. It was shown that the total yield of C is clearly reduced in 1% a-C:W and 2.5% a-C:W compared to a-C. Additionally, it was shown that the enrichment zone is not in steady state at a fluence of 10^{20} D/cm^2 for 1% a-C:W and 2.5% a-C:W, which is also observable in an enlarged magnitude of the energy range of occupied bonding states (i.e. it covers the range observed in TDS spectra for a-C as well as the range observed for 7.5% a-C:W). This means that low portions of an enlarged amount of bound D are released through the formation of volatile hydrocarbons. Major portions are trapped, which leads to a strong increase of the D inventory.

For 7.5% a-C:W the RMS value and the surface area decrease with increasing fluence by 0.35 and 0.02, respectively, increasing the fluence from 10^{19} D/cm^2 to 10^{20} D/cm^2. But this does not explain the reduction of the D inventory. Similarly to the situation mentioned for a-C small changes in surface roughness with fluence do not lead to a change of the D inventory. In fact, for 7.5% a-C:W a surface enriched with 100% W is formed over the width of the ion range, increasing the fluence from 10^{19} D/cm^2 to 10^{20} D/cm^2 (see section 4.1 *Enrichment of W: Depth profiles*). Thereby, C is lost at the surface and thus D, which was bound to C. This is observable by comparing TDS spectra of 7.5% a-C:W, implanted to a fluence of 10^{19} D/cm^2 and of 10^{20} D/cm^2, with each other. The peak width of the TDS spectrum decreases at its high temperature edge, increasing the fluence from 10^{19} D/cm^2 to

10^{20} D/cm^2. The build-up of an enrichment zone, increasing the fluence from 10^{19} D/cm^2 to 10^{20} D/cm^2, and the successive removal of C atoms leads to a release of D from occupied bonding states through the formation of volatile hydrocarbons, i.e. preferentially from high energetic bonding states. This may be confirmed by the following assessment: Under the assumption that an averaged C erosion yield of ∼2% (see section 4.2 *Influence of W and of pre-heating on total yields of C*; 7.5% a-C:W) is close to the erosion yield at a fluence of 10^{19} D/cm^2, a C layer of about 20 nm would have been removed at a fluence of 10^{19} D/cm^2, leaving behind a W enrichment zone with a width of about 2 nm. Since the width of the ion range is 5.5 nm in pure C and 6.3 nm in pure W, for a 200 eV/D beam, D atoms are able to reach the unaffected C matrix, where they are trapped. At a fluence of 10^{20} D/cm^2 the W enrichment zone is close to steady state for 7.5% a-C:W. The width of the enrichment zone matches the width of the ion range. The W content is close to 100% (this was shown in section 4.1 *Enrichment of W: Depth profiles*). In this case the impacting D beam is stopped and thermalised inside the enrichment zone and - neglecting diffusion into depth - bound to W atoms. Note that the amount of D released, of course, depends on the width of the W enrichment zone. This value is strongly determined by the presence of neutrals at a fluence of 10^{20} D/cm^2 (see section 4.2 *Influence of W and of pre-heating on total yields of C*). The amount of D released can be estimated to be the 2.5-fold of the amount released, assuming a 200 eV D beam without neutrals (note, width of the ion range in W at 1 keV is about 2.5 times the width at 200 eV).

The D inventory of as-deposited 15% a-C:W and of as-deposited 7.5% a-C:W can not be distinguished from one another at a fluence of 10^{20} D/cm^2. For 15% a-C:W two data points are given at a fluence of 10^{17} D/cm^2 and of 10^{20} D/cm^2. At a fluence of 10^{17} D/cm^2 the D inventory equals the value of 7.5% a-C:W. From the comparison of 7.5% a-C:W with pyrolytic graphite at 300 K it is known that the difference of the D inventory in 7.5% a-C:W and in pyrolytic graphite, after saturation of the implantation zone, remains about constant with increasing fluence, up to a fluence of 10^{19} D/cm^2, i.e. the difference is determined by the saturation level of the implantation zone. The data point given at a fluence of 10^{20} D/cm^2, on the other hand, obtains the same value for the D inventory as 7.5% a-C:W. For 7.5% a-C:W implanted at 300 K the D inventory was decreased at a fluence of 10^{20} D/cm^2. Since it is assumed that the D inventory obtains the same values, for 15% a-C:W compared to 7.5% a-C:W, up to a fluence of 10^{19} D/cm^2, it appears that the increase of the D inventory with fluence decreases again above a fluence of 10^{19} D/cm^2, for 15% a-C:W as well. Consequently, it can be assumed that the D inventory is lowered in 15% a-C:W by the same mechanisms as observed for 7.5% a-C:W, increasing the fluence from 10^{19} D/cm^2 to 10^{20} D/cm^2.

Variations of the structure of the C matrix in a-C and a-C:W do not affect the results previously mentioned. For a-C it was shown that the increase of the D inventory with fluence is insensitive to the pre-heating temperature (700 K, 1300 K) and thus to the structure of the C matrix. This result also explains the observation that pyrolytic graphite, which consists of mosaic spread graphite planes, and a-C, which has an amorphous structure, show the same increase of the D inventory with fluence. The diffusion of D into depth in a-C is not affected by the structure of the C matrix and can not be distinguished from the diffusion in pyrolytic graphite. For a-C:W it was shown that those changes in the D retention behaviour, which are caused by the W inclusions, e.g. the lowering of the saturation ratio and the

lowering of the D inventory above a fluence of 10^{19} D/cm^2, are insensitive to changes in the W concentration ($\geq$7.5% of W) and to the pre-heating temperature (700 K, 1300 K), and thus to the structure of the C matrix. Since the decrease of the D inventory with increasing fluence above 10^{19} D/cm^2 was shown to be caused by a removal of D through the formation of volatile hydrocarbons and since it was shown that the total yield of removed C is insensitive to changes in the structure of the C matrix, it is quite clear that the structure of the C matrix does not affect this kind of lowering of the D inventory with increasing fluence. Thus, the interpretation made for the decrease of the D inventory for fluences above 10^{19} D/cm^2 (a loss of D through the formation of volatile hydrocarbons) is confirmed in this case, too.

Increase of the D inventory with fluence - Extrapolation

The most obvious effect of W inclusions on the accumulation of D in a-C:W lies in the enrichment of W at fluences above 10^{19} D/cm^2. At fluences between 10^{19} D/cm^2 and 10^{20} D/cm^2, the evolution of an enrichment zone changes the D inventory in a-C:W compared to a-C. In ITER a fluence of 10^{20} D/cm^2 will be reached at baffle and dome after about 25 of 400 s ITER-discharges and at the vertical target after about a second. Concerning the effect of enrichment on the increase of the D inventory with fluence and its relevance for ITER, however, a fluence range far above 10^{20} D/cm^2 is of major interest. For instance, for an all W machine the safety limit would be reached for fluences above 10^{22} D/cm^2. Therefore, a fluence range above 10^{22} D/cm^2 is of interest, in comparing the retention behaviour of W with the retention behaviour of a-C:W. For such high fluences it can be assumed that the enrichment zone is already in steady state, in a-C:W, without respect to the W concentration. In this case, D is implanted into enriched a-C:W.

In this study the retention behaviour of enriched a-C:W was investigated at 300 K and for fluences between 10^{15} D/cm^2 and 10^{20} D/cm^2. For the enriched a-C:W reflection coefficient and saturation ratio of D/W inside the implantation zone are changed significantly compared to the saturation ratio of D/C in a-C:W. The reflection coefficient is close to the value of W (55%) and the saturation ratio is lowered to 0.03 - 0.08. As already observed in the TDS spectra of 7.5% a-C:W, the energy range of occupied bonding states is reduced inside the enrichment zone. This gives an explanation for a lowering of the saturation ratio. Nevertheless, for the enriched 7.5% a-C:W no saturation of the D inventory was observed for fluences above saturation of the implantation zone (above 10^{16} D/cm^2). It appears that D is able to reach unoccupied bonding states in the unaffected C matrix, after local saturation in the enrichment zone is reached. This observation is in line with the diffusion of D into depth in the W-coated graphites. D reaches depths beyond the W coating. This means, W at the surface (e.g. the W enrichment zone and the W coating) can not hinder D to diffuse into depth. Therefore, it can be assumed that D diffuses into depths beyond the enrichment zone in a-C:W, at fluences above 10^{20} D/cm^2 as well. In other words, for an evolution of the enrichment zone close to steady state, the influence of diffusion into depth on the increase of the D inventory with fluence becomes dominant over the influence of enrichment and of the trapping behaviour inside the enrichment zone. Therefore, the increase of the D inventory with fluence appears to become dominated again by the retention behaviour of the unaffected C matrix in the depth for 7.5% a-C:W at fluences above 10^{20} D/cm^2.

It was already shown that the increase of the D inventory with fluence and the diffusion

of D into depth is no different in a-C:W compared to a-C and pyrolytic graphite for fluences below 10^{19} D/cm^2. In this fluence range, the increase of the D inventory with fluence is governed by diffusion through the unaffected C matrix. If the increase of the D inventory with fluence in a-C:W, above a fluence of 10^{20} D/cm^2, is dominated by diffusion through the unaffected C matrix, it is suggested that diffusion into depth and the increase of the D inventory with fluence are no different in a-C:W and in a-C for fluences above 10^{20} D/cm^2, too. Therefore, the difference of the D inventory between a-C and a-C:W is supposed to be limited to a small fluence range around 10^{20} D/cm^2, and thus the increase of the D inventory with fluence in a-C:W can be described by the power law Φ^X for very large fluences. The exponent X must be the same in a-C and a-C:W. For a-C the exponent X was verified to be 0.1.

Influence of implantation temperature on accumulation of D

Influence of temperature on mechanisms of trapping and diffusion in a-C:W

The influence of implantation temperature on the diffusion of D into depth was studied in a cross-checking experiment. Thereby, a set of a-C:W was treated in the following manner (see section 5.1 *Diffusion of D: Depth profiles*): Each a-C:W of the set was implanted with a 200 eV D beam at 900 K and at a fluence of 10^{18} D/cm^2. At this fluence the heat treatment was stopped and the D beam exposure was continued for different time spans. During the decrease of the temperature D was implanted at additional fluences up to 10^{17} D/cm^2; the D beam exposure was stopped at different temperatures during the decrease of the temperature. From the analysis of the NRA spectra obtained from these specimens, it was shown that the extent of diffusion into depth is affected by the number of available bonding states and thus by the implantation temperature. (D is not bound to C, if its thermal energy is larger than the bonding energy between D and C, i.e. if the bonding is not available.) An increased implantation temperature leads to a deceased number of available bonding states and thus to an increased diffusion into depth, and vice versa.

This behaviour, i.e. the temperature dependence of the diffusion depth, is quantifiable for 7.5% a-C:W implanted at temperatures between 300 K and 900 K and at a fluence of $\sim 10^{20}$ D/cm^2 and, further to this, an increased diffusion into depth is observable as a decreased saturation level of the implantation zone at high implantation temperatures and in an enhanced increase of the D inventory with fluence at high implantation temperatures. This is the most obvious effect of the implantation temperature on the retention behaviour of a-C:W. This means, for the overall trends observed concerning the D retention behaviour in a-C:W at elevated temperatures, an explanation can be found by relating the diffusion into depth and thus the increase of the D inventory with fluence to the number of available bonding states, which depends on temperature. Nevertheless, the retention behaviour at fluences above 10^{19} D/cm^2, which exhibits a non-monotonic increase of the D inventory with fluence, can not be explained by these mechanisms of trapping and diffusion.

Another aspect lies in the influence of W on the retention behaviour of a-C:W at elevated temperatures. The intrinsic effect of W was investigated by comparing the retention behaviour of 7.5% a-C:W and a-C at 900 K. For 7.5% a-C:W the saturation level is slightly decreased and the increase of the D inventory with fluence is slightly enhanced compared to a-C. These differences are confirmed by TDS measurements. In the spectrum of the D_2 sig-

nal, the maximum is shifted by about 200 K, from 1050 K for a-C to 850 K for 7.5% a-C:W. Therefore, in 7.5% a-C:W the number of available bonding states is lower at 900 K than in a-C. From the conclusions made above, this must lead to a decreased saturation level of the implantation zone and to an enhanced diffusion depth in 7.5% a-C:W, which is observable as an enhanced increase of the D inventory with fluence. Consequently, the intrinsic effect of W on retention can be explained by the changed number of available bonding states and thus by the changed trapping behaviour of 7.5% a-C:W. Nevertheless, the changed trapping behaviour of 7.5% a-C:W does also not explain the non-monotonic increase of the D inventory above a fluence of 10^{19} D/cm^2.

Influence of enrichment and carbide formation on the retention behaviour at elevated temperatures

For the retention behaviour of 7.5% a-C:W, implanted at temperatures above 700 K and at fluences above 10^{19} D/cm^2, no explanation has yet been found. In fact, it seems to be necessary to discuss the appearance of temperature induced effects (e.g. carbide formation in the enrichment zone), which might impose an additional influence on the retention behaviour.

Enrichment of W is one issue, which must be addressed in trying to find a possible influence on the retention behaviour of 7.5% a-C:W, implanted at high temperatures and fluences above 10^{19} D/cm^2. As already discussed, at 300 K the enrichment of W in 7.5% a-C:W leads to a decrease of the D inventory with fluence, for fluences above 10^{19} D/cm^2. D bound to C inside the implantation zone is lost in the form of volatile hydrocarbons during enrichment and an enrichment zone, containing 100% W, is left in steady state. A decrease of the D inventory for fluences above 10^{19} D/cm^2 is observable for 7.5% a-C:W, exposed to the D beam at 500 K, at 900 K and at 1100 K, too. (Note that this behaviour is not observable for the data given at 700 K.) From the analysis of W enrichment at 500 K it is known that the enrichment zone is in steady state at a fluence of 10^{20} D/cm^2, containing 100% W over depths, matching the width of the ion range. This suggests that D is lost by the formation of volatile hydrocarbons during W enrichment. At 500 K W enrichment dominates the retention behaviour of 7.5% a-C:W, in a fluence range between 10^{19} D/cm^2 and 10^{20} D/cm^2. For implantations at 900 K and above, however, it is not clear whether this kind of decrease of the D inventory is due to the enrichment of W. From the analysis of the W enrichment zone of the specimen implanted at a fluence of $\sim 10^{20}$ D/cm^2 it is not known whether steady state has been reached. This information is necessary, in order to decide, for which data point between 10^{19} D/cm^2 and 10^{20} D/cm^2 steady-state is still to be reached and thus the loss of D is still under progress. Therefore, it is not possible to relate the proceeding of the curve at 900 K and above to the proceeding of W enrichment, as it is possible at 300 K, and it remains unclear whether W enrichment influences the retention behaviour at fluences above 10^{19} D/cm^2 in the same way as it was observed at 300 K, i.e. through the loss of D bound to volatile hydrocarbons.

Another influence on the retention behaviour of 7.5% a-C:W at fluences above 10^{19} D/cm^2 might be given by carbide formation during enrichment. In [146] the D retention in chemically vapour deposited (CVD) coatings of W carbides W_2C and WC was investigated in a temperature range between $\sim$400 K and $\sim$800 K, and compared to the D retention in e.g. C films. The D concentration depends strongly on the material and on the temperature.

At 400 K, the D concentration in the CVD coatings of W carbides (W_2C, WC) is decreased to 1/10 of the D concentration in the C films, which is 0.4. For each material the D concentration decreases with increasing temperature. This decrease is more pronounced for the CVD coatings of W carbides. At 800 K, for instance, the D concentration is lowered to $\sim 5 \cdot 10^{-4}$ in the CVD coatings compared to a D concentration of $\sim 5 \cdot 10^{-2}$ in the C films. The influence of carbide formation on the D concentration is pronounced with increasing temperature, i.e. the D concentration in the CVD coatings can be neglected compared to the D concentration in the C films at 800 K. Altogether, the study given in [146] shows that the presence of carbides strongly influences the D retention.

Concerning 7.5% a-C:W, which builds up an W enrichment zone, containing C and W ($\geq$22% of W) it is unclear whether carbide formation is present during enrichment at temperatures below 1300 K. The formation of carbide phases in a-C:W by annealing is presented in the appendix F. It was shown that the temperature range, in which carbide formation and crystallite growth is observable, decreases to lower temperatures with increasing W concentration. While no significant formation of carbide phases was observed at temperatures below 1300 K and for the W concentrations of 22% and below, the formation of carbide phases already appears to be possible at temperatures below 1300 K for a W enrichment zone, containing W concentrations above 22%. Further to this, the formation of carbide phases may also be affected by the deposited energy from the D beam. This is denoted as radiation enhanced solid state reaction. Such a process was already observed in [104].

Firstly, it needs to be figured out whether carbide formation is enhanced by the presence of an impacting D beam. Since radiation enhanced solid state reaction is most likely to occur at a high temperature, 7.5% a-C:W implanted at the highest accessible temperature (1300 K) is compared to as-deposited 7.5% a-C:W (the initial specimens) of the same batch. Note that carbide formation was not observed in as-deposited a-C:W, containing less than 10% of W, which was heat treated at 1300 K. Attention was paid to the effect of the D beam on the modification of the surface. In figure 6.1 four SEM images are given, which illustrate the surface topography in the secondary electron mode. Features visible are in nanometre-scale. To the left column and to the right column two images of specimens of the WS83J batch and of the WS69 batch are given, respectively. The images on the top and on the bottom were taken from the initial specimen and from the specimen implanted at 1300 K, respectively. For the initial specimen circular zones of different shades of grey are visible, which are composed of sub-features and sub-sub-features with decreasing size and different shades of grey. Between the features very dark zones are visible. In the secondary electron mode the contrast is given by the topography of the surface in many cases, i.e. bright zones are generated by the tilted surface segments and dark zones by the flat surface segments. (Among the tilted surface segments, segments directed towards the detector are brighter than segments tilted away from the detector.) Such a kind of pattern could simply be interpreted as an uneven surface, which consists of valleys (very dark zones) and humps (sub-features and sub-sub-features). In contrast, the images of the specimen implanted at 1300 K exhibit rather bimodal patterns. A background in dark grey is superposed by very small dots in light grey with a diameter between 5 nm and 10 nm. Under the assumption that this contrast is built by topography one would find a rough surface, consisting of very narrow tips. Inside such tips secondary electrons need to overcome only a short pathway towards the surface, leading to a large fraction of emitted electrons and thus to a high signal. Another possibility is given by material contrast, which is usually probed in the backscattering mode.

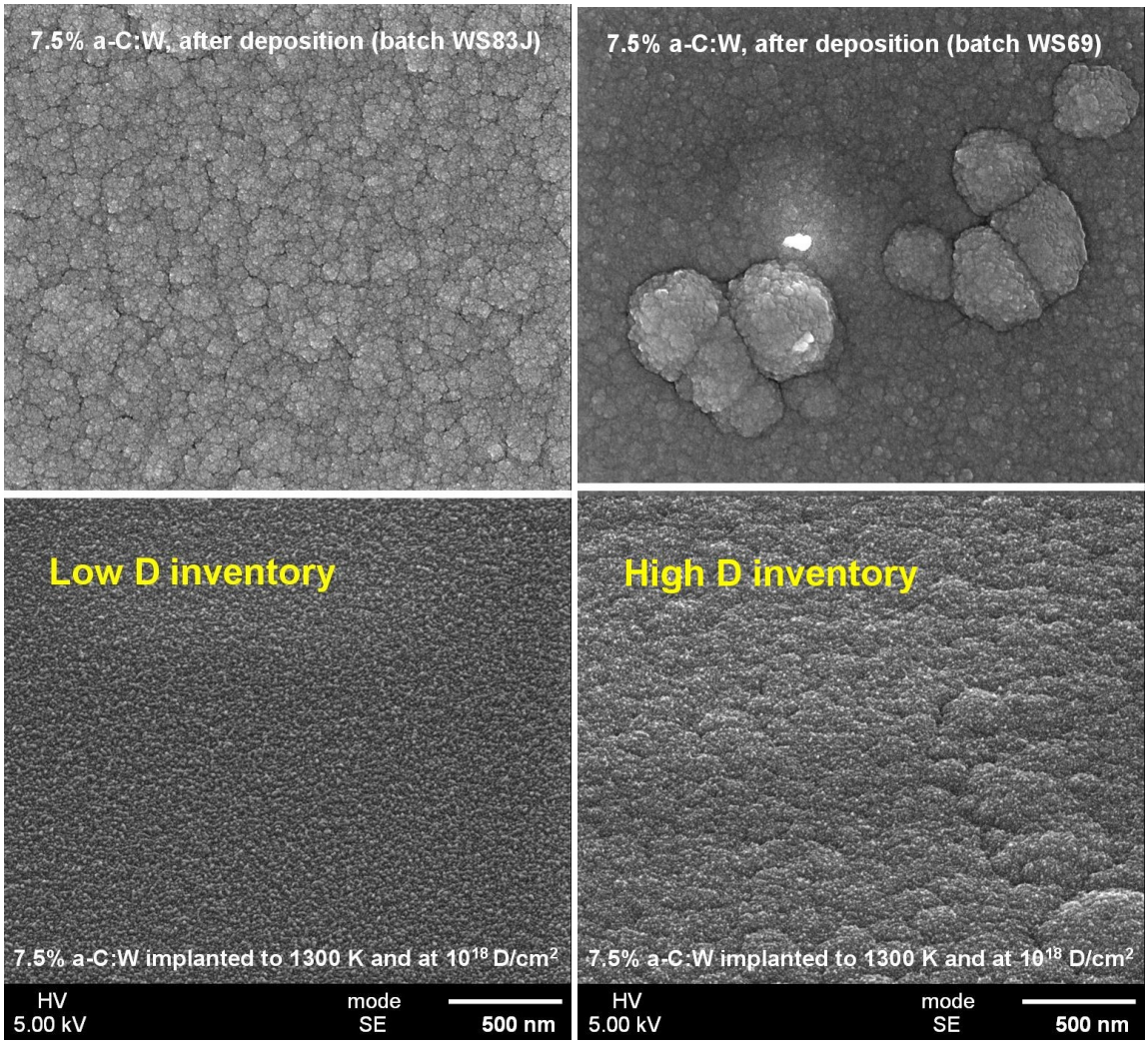

Figure 6.1: SEM images of 7.5% a-C:W taken from different batches (left column: WS83J, right column: WS69; top: as-deposited specimens, bottom: implanted at 1300 K and at a fluence of 10^{18} D/cm^2, respectively), illustrating the surface modification by the D beam exposure.

Nevertheless, in principal it is possible that backscattered electrons from some depth generate additional amounts of secondary electrons during their travel towards the surface leading to an enhanced signal of secondary electrons as well. Therefore, zones generating huge amounts of backscattered electrons would appear in light grey. A heavy element such as W has a large backscattering coefficient. This would suggest a kind of agglomeration of W at surface near zones. Since dots are of a size of up to 10 nm, it could be speculated that clustering of W occurred, and thus - under the presence of temperature and of the D beam - carbides were formed. Note, however, that the latter interpretation can not be distinguished from the first one (very narrow tips) by means of SEM analysis in the secondary electron mode. The comparison of the surface of the initial specimen with the surface of the specimen exposed to the D beam shows that a significant modification of the surface is imposed by the D beam. Roughening as well as carbide formation appears to be possible.

Besides this conclusion, which is of major interest for the following discussion, it needs to be mentioned here that the D inventory among these two specimens, which were exposed

to the D beam at the same condition (at a fluence of 10^{18} D/cm^2 and to 1300 K), differs by an order of magnitude. No explanation has yet been found. From the two images of these specimens the individual degree of carbide formation or roughening can not be established. Therefore, it is difficult to explain this huge difference of the D inventory by differences of the extent of carbide formation and of roughening. This suggests that further processes exist, which might influence the D retention behaviour of 7.5% a-C:W at elevated temperatures. This aspect, however, will be discussed later on.

The presence of carbide phases leads to a different D retention, as shown in [146]. Therefore, a change of the D inventory in 7.5% a-C:W, caused by carbide formation during enrichment of W, is to be expected. The degree of this change must be affected by the individual degree of carbide formation in a specimen. In figure 6.2 a specimen implanted at 900 K and at a fluence of $1{\cdot}10^{19}$ D/cm^2 (left hand) is compared to a specimen implanted at the same temperature and at a fluence of $5{\cdot}10^{19}$ D/cm^2 (right hand). For both specimens a SEM im-

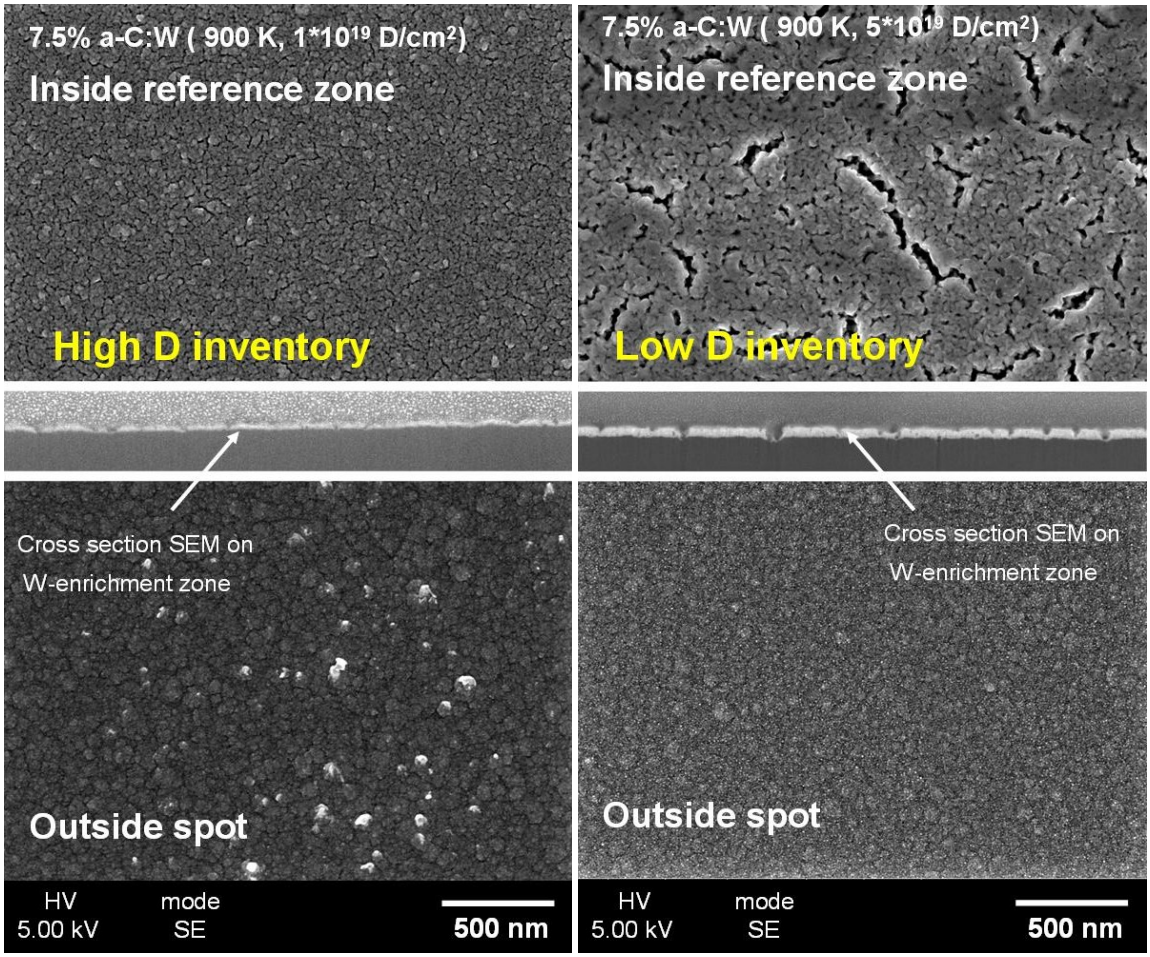

Figure 6.2: SEM (top: inside reference zone, bottom: outside 200 eV D spot) and cross section SEM (middle: inside reference zone) images of 7.5% a-C:W implanted at 900 K and at a different fluences (left column: $1{\cdot}10^{19}$ D/cm^2, right column: $5{\cdot}10^{19}$ D/cm^2), illustrating differences of the surface modification by the D beam exposure. Cross sections illustrate changes of the W enrichment zone with fluence.

age (secondary electron mode) of the surface inside the reference zone (top) and outside the 200 eV spot (bottom) is given; additionally a cross section SEM is given, which illustrates the enrichment (middle). Among these two specimens the D inventory deceases to a lower

value with increasing fluences, i.e. the specimen implanted at the higher fluence contains a lower amount of D than the specimen implanted at the lower fluence. SEM analysis were performed in order to observe differences in the degree of the surface modification, e.g. carbide formation and W enrichment. For the specimen implanted at a fluence of $1{\cdot}10^{19}$ D/cm^2 dark zones are visible, between grey zones of 50 nm diameter. Since features are due to a topographic contrast, dark zones are valleys and bright zones are humps. Note that no features are visible, which could hint at carbide formation. In the middle image a narrow zone in bright grey indicates the onset of W enrichment already at a fluence of $1{\cdot}10^{19}$ D/cm^2. Beyond the enrichment zone the unaffected film is visible as a zone in dark grey and above the C-Pt-(Ga) protection layer is visible as a grey zone including light grey spots. This protection layer penetrates into grooves of the enrichment zone. This indicates the presence of grooves, which are visible as trajectories in the upper image, i.e. the enrichment zone is riddled with cracks ($\sim$12%). Outside the 200 eV spot a topography is visible, which also indicates a morphology consisting of hills and valleys. Nevertheless, no hints are given for cracks. It appears that cracks are present only at zones where enrichment occurs, i.e. inside the 200 eV spot. (Note the zones in bright grey in the image at the bottom. They may originate from impurities and are not believed to be due to carbide formation.) For the specimen implanted at a fluence of $5{\cdot}10^{19}$ D/cm^2, on the other hand, cracks are larger and inhomogeneous in size ($\sim$17% of the total surface area). (Note that a coverage of 17% for the cracks does not explain the lowering of the W concentration to 60% in the enrichment zone at 900 K. This means, at 900 K the enrichment zone is a mixture of C and W. This confirms the interpretations made by ion beam analysis.) The cross section SEM given in the middle shows that some of these cracks extent to the unaffected film. This means, the enrichment zone is riddled with narrow zones, which are not enriched with W. The coverage of this kind of cracks is ($\sim$7%). On the bottom, the area outside the 200 eV spot is shown. No cracks are visible, but a topography consisting of hills and valleys. Despite this topography tiny spots in nanometre scale are visible, which appear as light grey. This punctual increase of the signal intensity for the secondary electrons may be interpreted as a material contrast, indicating an agglomeration of W and thus the onset of a formation of carbide phases. This slight agglomeration of W may be due to an additional entry of energy from 1 keV neutrals, which are also present at zones outside the 200 eV spot. This, on the other hand, suggests a formation of carbide phases inside the 200 eV spot as well. From the increase of the width of the enrichment zone at fluences between $1{\cdot}10^{19}$ D/cm^2 and $5{\cdot}10^{19}$ D/cm^2 together with the appearance of clustering, it could be speculated that the enrichment is in convolution with a formation of carbide phases. (In many cases phase formation leads to tension. Thus, the process of enrichment and carbide formation may be accompanied with an increase in the size of the cracks.)

If carbides are formed during enrichment, the D inventory should decrease in the W enrichment zone, increasing the fluence from $1{\cdot}10^{19}$ D/cm^2 to $5{\cdot}10^{19}$ D/cm^2, in line with the results given in [146]. In CVD coatings of W carbides the D concentration is reduced to about 1/100 of the value of pure C films at temperatures close to 900 K. The opposite trend is imposed by roughening during enrichment. If the tiny spots in light grey, which are visible in the SEM image of 7.5% a-C:W implanted at $5{\cdot}10^{19}$ D/cm^2, are not due to clustering but due to roughening, roughness would influence the retention, instead of carbide formation. A rough surface exhibits an increased implantation volume, and thus an increased D inventory would be expected for a rough surface. This expectation is based on the observation made for 2.5% a-C:W, implanted at 10^{20} D/cm^2 and to 300 K. In this case, the D inventory is

significantly increased due to roughening compared to a-C. Nevertheless, since neither carbide formation nor roughening can be excluded, it is not possible, from this point of view, to quantify the decrease of the D inventory for fluences between $1{\cdot}10^{19}$ D/cm^2 to $5{\cdot}10^{19}$ D/cm^2, by means of the results given in [146]. This means, it is not possible to weigh up trend and anti-trend against each other. Further to this, roughening and carbide formation do no necessarily have to exclude each other, but may be in convolution with each other. In this case, the extent of carbide formation would be influenced by the extent of roughening. Changes of roughness already observed for a-C:W (see appendix E *Surface morphology: Roughening*) can change the entry of energy imposed by the D beam by 50%, which is suggested from the angular dependence of the energy reflection coefficient given in [78]. In appendix E *Surface morphology: Roughening* it was shown that roughening shows variations, even among the specimens treated with the same set of parameter, e.g. W concentration, pre-heating temperature, implantation temperature, fluence. Since carbide formation at temperatures well below 1300 K was suggested to be driven by the additional entry of energy from the D beam, variations of the entry of energy imposed by fluctuations of roughening should go in convolution with variations of the extent of carbide formation and thus with variations of the D inventory. Radiation enhanced solid state reaction during enrichment is not yet quantifiable. Therefore, the impact of variations of the entry of energy by 50% on the extent of carbide formation and on the D inventory is also not yet quantifiable.

In general, many effects may influence the retention behaviour, e.g. W enrichment, carbide formation, roughening. These effects are in convolution with each other and may show strong, non linear interdependences. Therefore, it is difficult to figure out, which of these effects is dominating and it is difficult to find a final explanation for the retention behaviour of 7.5% a-C:W, implanted at temperatures above 700 K and fluences above 10^{19} D/cm^2.

Influence of pores on the retention behaviour at elevated temperatures

Finally, an example is presented, which clearly illustrates the multitude of possible influences on the retention behaviour. As previously mentioned, two specimens exist, which were exposed to the D beam at the same conditions (1300 K, 10^{18} D/cm^2). Among these two specimens the D inventory differs by an order of magnitude. No explanation has yet been found. These two specimens were taken from different batches, which might exhibit a different porosity. In the following the influence of porosity is discussed, which might impose an influence on the D retention at high temperatures, additionally to the effects previously mentioned. In literature it is known that D diffuses along pores into depth [69, 74]. The presence of pores in a-C:W was investigated by applying cross section SEM. In figure 6.3 a cross section SEM image of 7.5% a-C:W after deposition is given, which illustrates the film growth. The silicon substrate (black area at the bottom) is covered by the film (dark grey area). The grey area and the light grey area above are mixed C-Pt-(Ga) protection layers necessary in producing cross sections. Shades of grey inside the film are due to local differences of the material density. Two V-shaped zones are visible, which are riddled with lines (dark grey) producing a V-shaped pattern. These lines are due to zones of lower density, which indicates - together with the V-shaping - a certain direction of film growth. This feature - a kind of V-shaped column - extends from the depth to the surface and emerges out

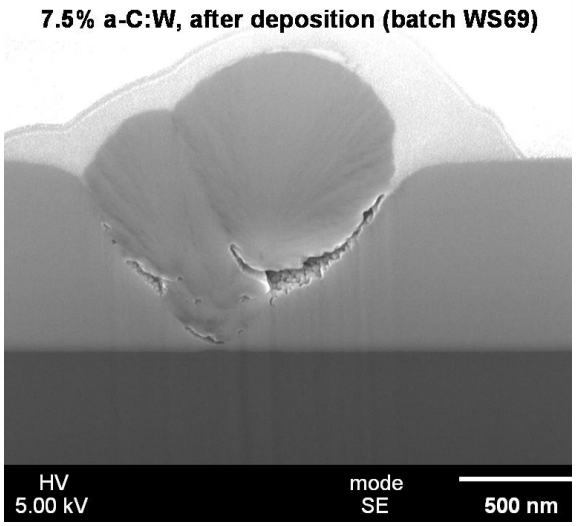

Figure 6.3: Cross section SEM image of as-deposited 7.5% a-C:W (batch WS69) illustrating the film growth. The image is composed of three zones. Black area at the bottom: Si-substrate; dark grey area above: 7.5% a-C:W; grey area and light grey area at top: mixed C-Pt-(Ga) protection layers.

of the surface. Close to the substrate a cavity is visible. This cavity may be due to film growth onto an impurity. Parts of the underling film may be shadowed by the impurity, leading to local differences in the material density during film growth. Since the cathodes of the sputtering device are tilted and since the specimen holder is rotating during the deposition process, a V-shaped film growth is probable. These irregularities of film growth also exhibit larger pores, which extent from the film surface into depth, in some cases to the substrate. The Diffusion of D into depth is facilitated through such a kind of pores and the extent of accumulation of D may depend on their frequency.

In perpendicular position to the film surface V-shaped columns are visible as spheric features emerging from the film surface. The coverage of these V-shaped columns of both specimens implanted at 1300 K and at a fluence of 10^{18} D/cm^2 was compared with each other. In figure 6.4 SEM images of both specimens implanted at 1300 K and at a fluence of 10^{18} D/cm^2 are given, which illustrate the surface topography. The surface of both specimens is riddled with spheric features emerging from the film surface. It appears that these features are confined within the surrounding film by narrow cavities, i.e. pores into depth as illustrated in figure 6.3. It can be assumed that these features represent V-shaped columns. For the specimen containing the higher D inventory (taken from batch WS69) the coverage of such V-shaped columns is between 5% and 10% and for the specimen containing the lower D inventory (taken from batch WS83J) the coverage is less than 1%. A rather smooth surface is visible for the latter specimen. The difference of the coverage of V-shaped columns between these two specimens implanted at the same conditions may give a hint on the huge difference of the D inventory.

This example shows that in case of a significantly different porosity among two specimens exposed to the D beam at the same conditions, the D inventory among these specimens is significantly different as well.

In this context, it should be mentioned that the influence of porosity is rather a matter

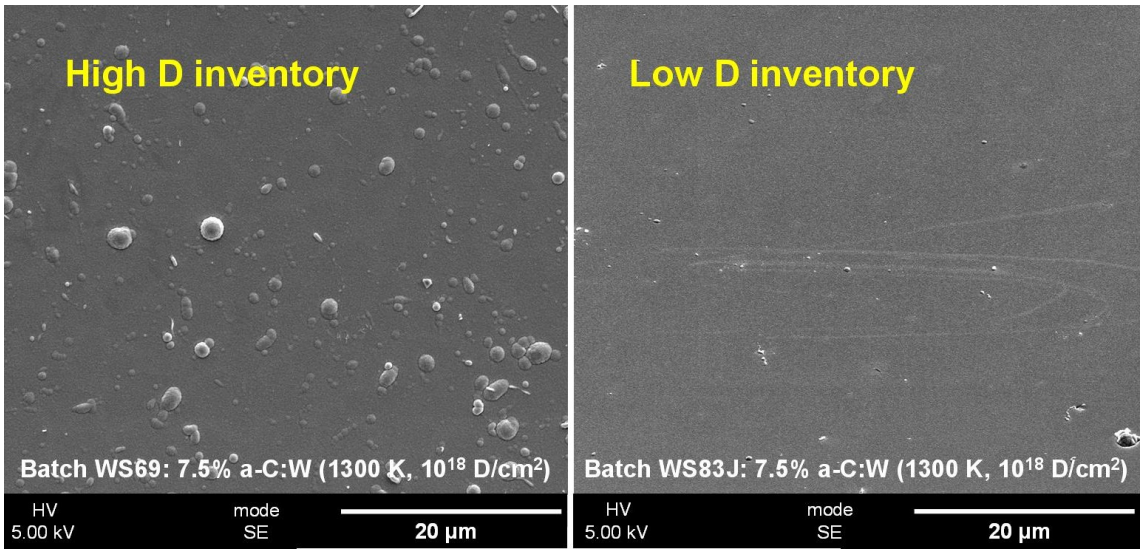

Figure 6.4: SEM images of two specimens of 7.5% a-C:W, taken from different batches (left: WS69, right: WS83J) implanted at 1300 K and at a fluence of 10^{18} D/cm^2, illustrating the coverage of V-shaped columns.

of the used batch than a matter of the implantation temperature. The specimens implanted at temperatures below 1300 K were taken from batches, which were deposited in the Denton Vacuum Discovery 18 device. It is assumed that these specimens exhibit nearly the same porosity; however, no statistics exist. From the two specimens implanted at 1300 K, the specimen with the lower D content was taken from a batch (WS83J), which was deposited in the Leybold Unnex 450 C device. Less impurities were present in the Leybod device, since this machine was utilised with a lower frequency for the deposition of layers, other than a-C:W or a-C. This may give a hint on the lower porosity of the WS83J batch, since the presence of impurities is suggested to result in a film growth, which exhibits pores.

6.3 Conclusion

With regard to the results of investigations on the erosion behaviour of a-C:W, it was shown that enrichment of W reduces the influence of temperature on the total yield of removed C. This is a further influence of enrichment on the erosion behaviour of a-C:W, besides the reduction of the total yield of removed C. This means, enrichment dominates the erosion behaviour of a-C:W for the W concentrations of 7.5% and above.

Concerning the retention behaviour of a-C:W, it was figured out, whether temperature or enrichment dominates. A further aspect was the intrinsic effect of W on the retention behaviour of a-C:W. For the first step, the intrinsic influence of W and the influence of enrichment on the retention behaviour was investigated at 300 K. At elevated temperatures, additionally the influence of implantation temperature on the retention behaviour of a-C:W was investigated.

In a-C, in a-C:W and in pyrolytic graphite, the increase of the D inventory with fluence is based on mechanisms of trapping and diffusion. At 300 K, these mechanisms are not affected intrinsically by W inclusions, but by enrichment of W. By applying TDS measurements, a fluence dependence of the trapping behaviour of a-C:W was observed and it is possible to identify changes in the trapping behaviour with fluence as cause for the fluence dependence of the D retention. For fluences of 10^{19} D/cm^2 and below all materials show a common property. Unoccupied bonding states are occupied with increasing fluence, which is observable as an increase of the overall intensity of the D_2 signal in all TDS spectra. The occupation of unoccupied bonding states certainly enables the total amount of retained D to increase with fluence. At fluences between 10^{17} D/cm^2 and 10^{19} D/cm^2, when all bonding states in the implantation zone are occupied, further occupation of bonding states occurs at larger depths. This requires a diffusion of D into depth. This behaviour is not affected intrinsically by W inclusions. Therefore, the extent of diffusion of D into depth and thus the increase of the D inventory with fluence is no different in a-C:W compared to a-C and pyrolytic graphite. Above a fluence of 10^{19} D/cm^2 the trapping behaviour, i.e. the energy range of occupied bonding states, depends strongly on the W concentration. This is observable as an increase of the D inventory with fluence, which depends on the W concentration. It appears that the D retention in the fluence range between 10^{19} D/cm^2 and 10^{20} D/cm^2 is dominated by the evolution of a W enrichment zone, which determines the saturation ratio in the implantation zone. After the build-up of the W enrichment zone is completed, further incoming D diffuses beyond the W enrichment zone. In the depth, the retention behaviour is dominated by the unaffected C matrix, which shows no different retention behaviour to a-C and pyrolytic graphite.

By comparing the D retention behaviour of a-C and a-C:W with pyrolytic graphite at 300 K, the main conclusion is that no significant difference was found concerning the increase of D inventory with fluence over a wide range of fluences. Changed bondings in the C matrix and in the near vicinity of W inclusions do not affect the D inventory at any fluence. Implantations of enriched 7.5% a-C:W suggest that the build-up of a W enrichment zone, which exhibits a changed trapping and diffusion behaviour, affects the D inventory in a closed range of fluence around 10^{20} D/cm^2. Outside this range, a-C and a-C:W exhibit the same D retention behaviour as pyrolytic graphite at 300 K.

Mechanisms of trapping and diffusion are affected by the implantation temperature.

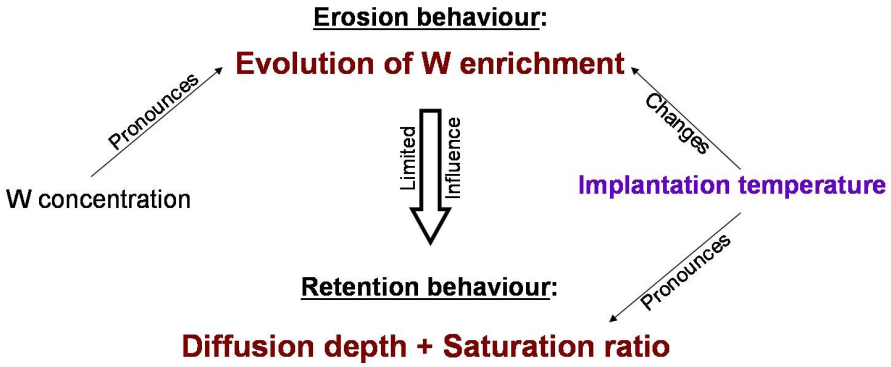

Figure 6.5: Sketch illustrating the influences on the retention behaviour of a-C:W: The W concentration, the implantation temperature and the W enrichment, in which the enrichment is affected by the W concentration and by the implantation temperature.

In the subsection *Diffusion and Trapping* (see 5.1 *Diffusion of D: Depth profiles*) it was shown that the diffusion of D and the number of available bonding states are in convolution with each other. With increasing temperature the number of available bonding states decreases resulting in a lowered saturation ratio in the implantation zone and in an enhanced diffusion into depth. This behaviour is observable as a rising increase of the D inventory with fluence and in a decreasing saturation level with increasing temperature. This is the main message, which can be drawn from investigations concerning the influence of temperature on the accumulation of D. Furthermore, W inclusions seem to intrinsically affect the D retention behaviour at elevated temperatures, in contrast to the retention behaviour at 300 K. This conclusion can be drawn from the comparison of a-C with 7.5% a-C:W at 900 K. At 900 K, 7.5% a-C:W showed a slightly decreased saturation level and a slightly enhanced increase of the D inventory with fluence compared to a-C. This points to a slightly enhanced diffusion of D and to a lowered saturation ratio in the implantation zone. In the subsection *Thermal desorption spectroscopy* (see 5.2 *Influence of W and pre-heating on accumulation of D*) it was shown that D is bound at lower energies in a-C:W. The maximum of the D_2 signal in the TDS spectrum is shifted to temperatures slightly below 900 K. In contrast, the maximum is slightly above 900 K for a-C. Therefore, the amount of available bonding states for implantations at 900 K is lower in 7.5% a-C:W compared to a-C. This must lead to an enhanced diffusion of D and to a decreased saturation ratio in 7.5% a-C:W implanted at 900 K, leading to an enhanced increase of the D inventory with fluence and to a lowered saturation level. This is exactly the observed behaviour. However, concerning the influence of enrichment on the accumulation of D in a fluence range between 10^{19} D/cm^2 and 10^{20} D/cm^2 only speculation is possible. The composition of the enrichment zone at a temperature was suggested to be affected by radiation enhanced segregation, i.e. by the amount of an additional entry of energy from the D beam and thus by roughening.

Carbide formation in the enrichment zone was suggested with increasing temperature as well, affecting the retention behaviour through changed trapping energies. The extent of the formation of carbides in the enrichment zone was suggested to depend on the entry of energy from the D beam and thus on the evolution of roughness. For these effects interdependences appear to be possible and it is not possible to figure out the dominating effect. Therefore, the non-monotonic increase of the D inventory with fluence at temperatures above 700 K can not be explained finally.

Implantation temperature affects mechanisms of trapping and diffusion. Overall trends observed at elevated temperatures can be explained by these mechanisms. On the other hand, the influence of enrichment and of carbide formation in the enrichment zone on the retention behaviour at fluences between 10^{19} D/cm^2 and 10^{20} D/cm^2 is unclear. Nevertheless, if enrichment and carbide formation influenced the retention behaviour at elevated temperatures, it could be speculated - similarly to the situation at 300 K - that both influences are limited to a range of fluences around 10^{20} D/cm^2. Enrichment would decrease the D inventory through a loss of volatile hydrocarbons, until steady state is reached. Afterwards, this decrease would be stopped. Carbide formation would lead to a lowered saturation ratio in the enrichment zone. Since it was shown that D diffuses into depths far beyond the enrichment zone at elevated temperatures, up to 0.5 μm, the trapping behaviour in the unaffected C matrix must become dominant for large fluences again. The trapping behaviour of the unaffected C matrix, however, is dominated by the implantation temperature.

Chapter 7

Assessment of the ITER T inventory build-up

ITER will be operated in order to show the feasibility to extract fusion power from the T(D,n)^{4}He nuclear reaction [15]. This is going to be reached by magnetically confined D-T-plasma discharges, with 50%:50% of D:T [15]. A release of T to the atmosphere during an accident will result in a considerable threat to the neighbouring population and biosphere. Therefore, a safety limit for the in-vessel mobilizable T inventory of 330 g was imposed [147].

The in-vessel T inventory build-up, discovered in present day D-T-plasma operating fusion devices, e.g. JET [28], TFTR [148, 149], is governed by two processes: Implantation, trapping and diffusion in PFMs, on one hand, and co-deposition of T with eroded wall material, on the other hand. For each PFM, envisaged to be used in ITER, Be, C and W, one of the two processes mentioned is expected to dominate the accumulation of T [23]. T implanted into W diffuses into large depths, and thus W exhibits a strong increase of the T inventory with fluence. The increase of the T inventory is pronounced by the presence of radiation damage under neutron irradiation and it is lowered for W, covered with deposited layers. Accumulation of T in deposited layers is dominated by co-deposition of eroded Be with T and by co-deposition of re-eroded C with T. Thereby, the outer divertor and the main wall are expected to be net-erosion areas, acting as source for co-deposited layers. The inner divertor and surrounding zones, e.g. parts of the main wall, dome, gaps and remote areas, are expected to be net-deposition areas.

Sophisticated assessments of T inventory build-up in ITER already exist [23]. These assessments are based on a combination of experience made with present fusion devices and modelling approaches of erosion/deposition processes with edge transport codes. In [23], "estimates for the T inventory build-up are given for the initial choice of ITER materials, as well as for alternative options". Herein, co-deposition with C is the dominating T accumulation process and the safety limit is reached after a few hundred 400 s full performance discharges for the initial material choice of ITER. This limit can be extended to a few thousand discharges for the use of W at the vertical target, instead of CFC. For the all-W materials option the safety limit is reached after several thousand discharges. Note that, in general, the prediction of T inventory build-up is a very challenging task, which is afflicted with large uncertainties [23]. The T inventory build-up certainly depends on local erosion and deposition conditions, which are themselves affected by fuel and impurity

particle transport and by the power exhaust. Further to this the complex 3D geometry of PFMCs needs to be taken into account.

For the study presented in this thesis the assessment of the T inventory build-up during the T burning phase of ITER is performed, by focusing on the following two aspects: First, the deposition of eroded C and sputtered W during the initial phase, which results in the formation of C-W-mixed layers. During the T burning phase, these C-W-mixed layers serve as reservoir for the accumulation of T through implantation, trapping and diffusion into depth. Second, the co-deposition of re-eroded C together with T during the T burning phase, whereby the C originates from the C-W-mixed layers. Both aspects originate from the use of CFC at the vertical target of the divertor during the initial phase of ITER. CFC is used due to its high thermal shock resistance under transient loads and off-normal events [20]. At the vertical target, a surface temperature of $\sim$1300 K is expected around the strike point of the outer divertor and a surface temperature of $\sim$800 K, on the inner divertor [19]. Further more, CFC has the lowest ablation loss during a disruption ($\sim 10\,\mu$m) [20]. The ablation loss of W is considerably larger ($\sim$0.1 mm) so that under plasma conditions expected for the initial phase of ITER, a tolerable W impurity concentration of $\leq 10^{-5}$ can not be ensured and thus a considerable radiation loss is to be expected [20]. However, the most important draw-back for the use of CFC during the initial phase is due to the huge amounts of volatile hydrocarbons, formed through chemical sputtering, which leads to an unlimited growth of deposited layers [44]. Since W is used at locations of the divertor surrounding the vertical target (baffle and dome), C-W-mixed layers (e.g. $\leq$20% of W) are likely to be formed. Major portions of C-W-mixed layers, formed during the initial phase, will be on the vertical target of the inner divertor, which is removed against W. Minor portions will be left in remote areas and gaps, as well as on those parts of the main wall, of the baffle and of the dome, which surround the inner vertical target [23]. This circumstance raises the demand of an assessment of the extent of T inventory build-up in deposited, C-W-mixed layers.

In contrast to common approaches in assessing the T inventory build-up, assessments made in the study presented in this thesis are based on investigations under defined conditions, resulting, of course, in rough estimates. Fundamental research was performed on the retention and erosion behaviour of a model system for C-W-mixed layers, a-C:W. a-C:W was investigated under the 200 eV D beam exposure. This offered to perform parameter studies (W concentration, pre-heating temperature, implantation temperature). The erosion behaviour was characterised at a fixed fluence (10^{20} D/cm^2) and the retention behaviour was characterised for different fluences between 10^{15} D/cm^2 and 10^{20} D/cm^2. The extrapolation to ITER relevant ranges of flux, temperature and fluence is performed, by taking the following results, obtained from the study presented in this thesis, into account: The retention behaviour of a-C:W at 300 K is not significantly different compared to pyrolytic graphite for a wide range of fluences. Differences, which emerge from enrichment, are supposed to be limited to a small range of fluences around 10^{20} D/cm^2 so that extrapolation to large fluences appears to be uncritical. A similar procedure was followed for results at elevated temperatures. For temperatures of 700 K and below extrapolation to larger fluences is possible with the same rationale used for the data obtained at 300 K. At temperatures above 700 K, however, the non-monotonic increase of the D inventory with fluence could not be clarified finally. Note that temperatures far above 700 K are unlikely to occur during the T burning phase, since the surface temperature of the W tiles at the vertical target must be kept below

800 K. Nevertheless, data obtained at 900 K will be upscaled to large fluences as well, in order to asses a maximum for the accumulation of inventory through implantation and diffusion into depth. Thereby, the non-monotonic increase of the D inventory with fluence is just neglected.

The erosion behaviour of a-C:W, on the other hand, is nearly independent on the parameters investigated. From the results of the study presented in this thesis it is evident that neither W concentration, nor pre-heating temperature, nor implantation temperature significantly influence the total yield of removed C in a-C:W. The total yield of removed C of a-C:W is reduced to 1/2-1/3 of the value of a-C at 300 K and to 1/20 of the value of a-C at 700 K.

7.1 Situation after hydrogen phase: C amounts

The assessment of T inventory build-up, through the accumulation of T in deposited C-W-mixed layers and through the accumulation of T-containing co-deposited layers during the T burning phase, bases on the following constellation: After the initial phase, CFC tiles at the vertical target of the divertor will be replaced by tungsten tiles. The other components of the inner vessel wall (first wall, baffle and dome) will be covered by deposited layers, formed during the initial phase. This constellation is illustrated in figure 7.1. In [150] a

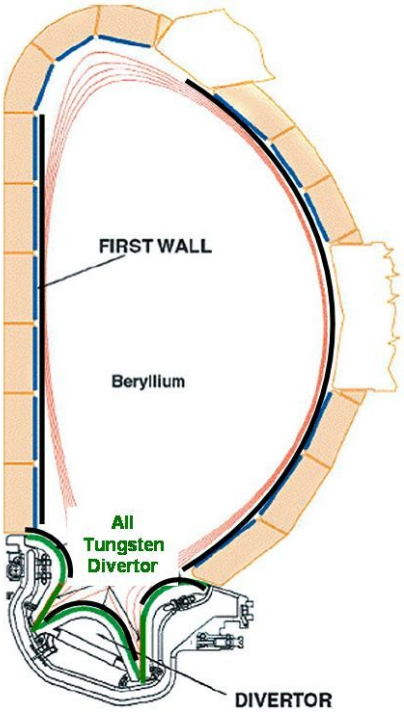

Figure 7.1: Schematic of ITER cross section illustrating the divertor configuration as well as showing the locations and choice of plasma facing materials Be, W, envisaged for the T burning phase. Initial constellation: First wall, baffle and dome are covered with deposited layers, marked in black.

model is given, which describes local erosion and co-deposition processes on each surface element of the first wall and thus calculates the re-distribution of Be, C and W inside the ITER vessel with time for ITER standard reference discharges (normal operation

conditions). The result of this calculation is depicted in figure 7.2. The upper diagram and

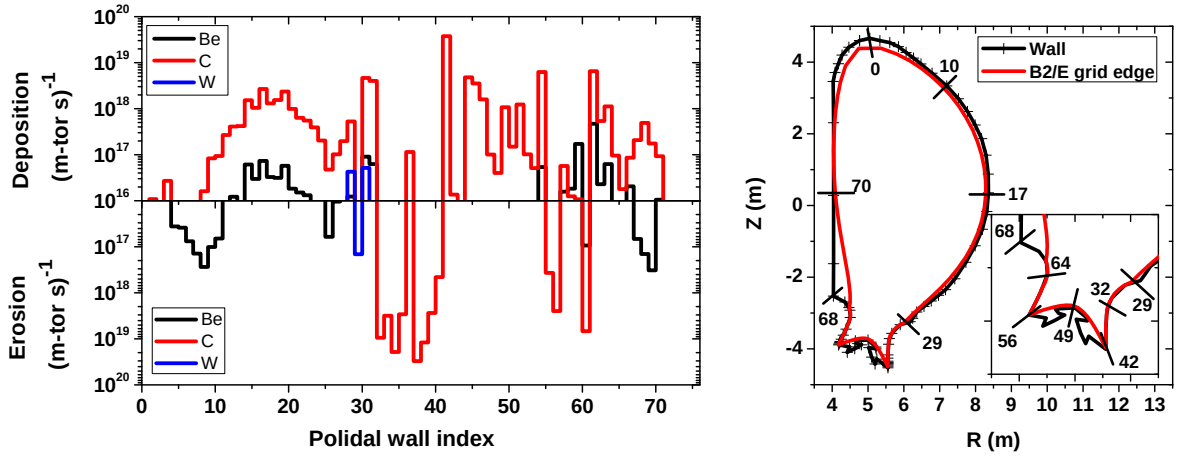

Figure 7.2: Left hand side: Upper diagram and lower diagram plot the amount of deposited and the amount of eroded Be, C, and W atoms, over the polidal wall index, respectively; based on a model [150], which calculates the re-distribution of Be, C and W inside the ITER vessel with time for ITER standard reference discharges (normal operation conditions). Right hand side: Assignment of the polidal wall indexes. Diagrams obtained from [151].

the lower diagram to the left plot the amount of deposited and the amount of eroded Be, C, and W atoms, over the polidal wall index, given per metre torus length and per second, respectively. The assignment of the polidal wall indexes is given in the diagram to the right hand side. According to these results, major portions of eroded C originate from the outer vertical target and are deposited on the outer first wall, on areas of the outer baffle, which are next to the outer vertical target, on the dome, on major parts of the inner divertor and on areas of the inner first wall, close to the inner divertor. Major portions of Be, eroded at the first wall, are deposited on the first wall and on the inner vertical target, minor portions are deposited on the outer baffle. Portions deposited on the dome can be neglected. W, eroded at the outer baffle is deposited on neighbouring areas of the outer baffle and on areas of the outer first wall, close to the outer baffle. Note that calculations given in [150] only apply for normal operation conditions. Therefore, under the presence of off-normal events, especially at the divertor, larger amounts of sputtered and deposited W must be expected. This fact gives reason to consider the presence of deposited C-W-mixed layers ($\leq$20% of W), e.g. at baffle and dome.

Firstly, the total amount of T shall be estimated, which can be retained in co-deposited layers after the removal of CFC against W. For that, the total amount of C, which is left in the machine after the removal of CFC against W, needs to be estimated, first. Second, the total amount of retained T can be estimated from the saturation ratio of (T+D)/C, which approximately covers a range between 0.4 and 1.0 [20]. The total amount of C, left in the machine, is obtained from integration of the amounts of deposited C, given in figure 7.2, over the polidal wall indexes 0-32, 42-56 and 64-75, over the torus length at polidal index and over the number of 400 s discharges during the initial phase. Thereby, the torus length at polidal index is approximated to be 6 m for each polidal index. Under the operation mode "good housekeeping approach", which is listed in [23], two years of ITER operation for the initial phase would yield a total number of 5 000 shots of 400 s duration. This is $2{\cdot}10^6$ s.

Integration over the polidal indexes yields a C amount of $4{\cdot}10^{19}$ /ms. Integration along the whole torus length of $2\pi{\cdot}6$ m yields a C amount $1.5{\cdot}10^{21}$ /s. Integration over the number of shots yields a total amount of deposited C of $3{\cdot}10^{27}$. This results in a total amount of retained T between $0.6{\cdot}10^{27}$ and $1.5{\cdot}10^{27}$. This is between 1 kg and 2.5 kg of T.

This result clearly shows that after 5 000 shots for the initial phase amounts of deposited layers are present, sufficiently large to take up such amounts of T during the T burning phase, which clearly exceed the safety limit of 330 g. A portion of these C amounts will be removed by a couple of recovery techniques, e.g. glow discharge cleaning at elevated surface temperatures and under the presence of oxygen, applied during the maintenance phase. Nevertheless, the efficiency of these recovery techniques is still unclear, since no profound experience exists for their application in Tokamks [16]. Especially the efficiency of the removal from remote areas, e.g. tile gaps, was proven to be limited already in laboratory experiments [42]. Even the removal of deposited layers from areas faced to the plasma appears to be inefficient from experience made in laboratory experiments. In the case of the presence of W inclusion, the C removal rate is lowered, depending on the W concentration ($\leq$10% of W), to 1/10-1/100 of the C removal rate of a-C [152]; W does not promote the oxidation. From this point of view, estimations for the efficiency of removal techniques, especially concerning local efficiencies, remain challenging and it must be kept in mind that the appliance of recovery techniques during the maintenance phase does not guarantee a sufficient reduction of deposited layers.

Before estimations with regard to the T inventory build-up can be given, input parameters have to be defined, first. Input parameters, necessary for estimations described in the following sections, are flux and energy of the fuel particles, e.g. T, and surface temperature of individual components of the inner vessel wall. These parameters, of course, are expected to show strong variations with time and location [18]. Temporal and local variations of input parameters are simplified for all estimations preformed in the following. A stationary plasma operation is assumed, without off-normal events. Fluxes and energies of T, and surface temperatures are averaged over the whole first wall, over baffle plus dome and over the vertical target, except the strike point. Values taken from [23] are listed in table 7.1.

	Area (m^2)	Surface temperature (K)	Flux (10^{16} T/cm^2s)	Energy (eV/T)
First wall: a-C:W on Be	700	400	$7{\cdot}10^{-1}$	200
Baffle + Dome: a-C:W on W	100	400	10^0	15
Vertical target: pure W				
- Strike point	3	775	10^4	15
- Elsewhere	47	500	10^3	15

Table 7.1: Input parameters used for the assessment of T inventory build-up, taken from [23].

7.2 Accumulation of T through implantation

The result obtained in the previous section clearly shows that after 5 000 shots in the initial phase a reservoir of deposited layers exists, sufficiently large to take up such amounts of T during the T burning phase, which clearly exceed the safety limit of 330 g. From this point of view, one aspect certainly lies in the accumulation of T in such a reservoir, through implantation and diffusion. How many shots are possible during the T burning phase, until the safety limit is reached, focusing on the accumulation of T through implantation and diffusion in C-W-mixed layers, which cover the first wall, baffle and dome? In other words, is the increase of the T inventory with fluence in C-W-mixed layers, i.e. in a-C:W, sufficiently large so that the safety limit will be reached after 20 years, i.e. after 50 000 shots, of ITER operation? An answer to this question can be found from a look at the results from the study presented in this thesis. Figure 7.3 depicts the increase of inventory with fluence for 7.5% a-C:W exposed to a 200 eV D beam at different temperatures between 300 K and 1300 K. In order to extrapolate these results to ITER relevant fluences, least square fits were

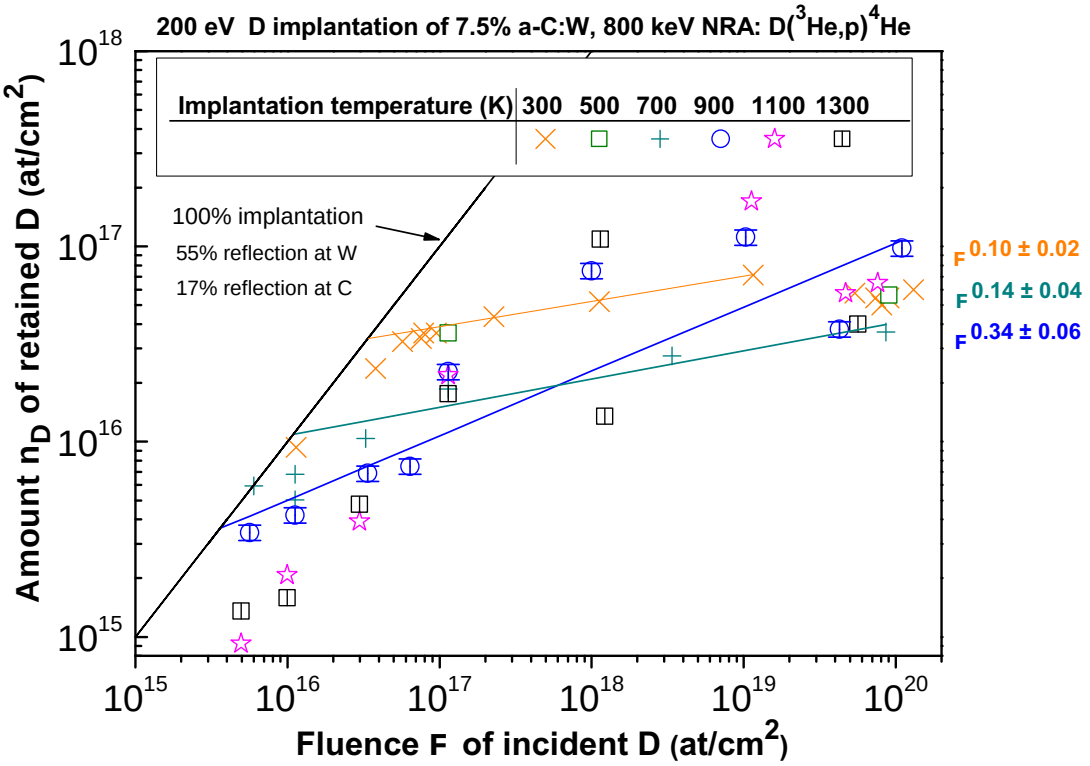

Figure 7.3: Amount of retained D in 7.5% a-C:W, implanted to different temperatures between 300 K and 1300 K versus the fluence of incident 200 eV D. Comparisons are drawn by a power law Φ^X for implantations at 300 K, 700 K and 900 K. Above 900 K, trends are not quantifiable.

performed on data points, obtained at temperatures between 300 K and 900 K and at fluences above saturation of the implantation zone. The expression $n = n_i \cdot \Phi^{Xi}$ was used as fitting function, where n is the T inventory (given in the unit at/cm^2) at fluence Φ, Xi is the exponent over Φ and n_i is the offset; Xi and n_i are fit parameters. In order to upscale the T inventory given in the unit at/cm^2, the total area of the inner vessel wall must be taken into account. Since different components of the inner vessel wall, i.e. baffle plus dome and first wall, are

exposed to different fluxes, the up scaling to the corresponding area and fluence must be performed on each component itself, first. These results must be summed up, in order to obtain the increase of the total amount of T, $\widehat{n}$, with the number of shots. The increase of the total amount of T with the number of shots is given by the following equation:

$$\widehat{n} = \underbrace{700\,m^2\; n_1 \cdot (\phi_{wall}\,\Delta t)^{X1}}_{\text{1st wall: a-C:W}} + \underbrace{100\,m^2\; n_1 \cdot (\phi_{dome+baffle}\,\Delta t)^{X1}}_{\text{dome+baffle: a-C:W}}. \tag{7.1}$$

ϕ_{wall} and $\phi_{dome+baffle}$ are the fluxes at the first wall and at dome plus baffle, respectively (see table 7.1). The first term of the sum describes the accumulation in C-W-mixed layers, covering the first wall, and the second term describes the accumulation in C-W-mixed layers, covering baffle and dome. The exponent X1 and the offset n_1 can be obtained from the fits given in figure 7.3.

Besides the accumulation of T in C-W-mixed layers, covering the first wall, baffle and dome, T will accumulate in W at the vertical target, too. Implantation and diffusion of T in W will considerably contribute to the total T inventory build-up. In view of this additional contribution, equation (7.1) must be completed by an additional term, which takes the accumulation of T in the vertical target into account:

$$\begin{aligned}\widehat{n} &= \underbrace{700\,m^2\; n_1 \cdot (\phi_{wall}\,\Delta t)^{X1}}_{\text{1st wall: a-C:W}} + \underbrace{100\,m^2\; n_1 \cdot (\phi_{dome+baffle}\,\Delta t)^{X1}}_{\text{dome+baffle: a-C:W}} \\ &+ \underbrace{47\,m^2\; n_2 \cdot (\phi_{vertical\,target}\,\Delta t)^{X2} + 3\,m^2\; n_2 \cdot (\phi_{strike\,point}\,\Delta t)^{X2}}_{\text{divertor: pure W}}.\end{aligned} \tag{7.2}$$

$\phi_{vertical\,target}$ and $\phi_{strike\,point}$ are the fluxes at the vertical target and at the strike point, respectively (see table 7.1). The first term of the additional term describes the accumulation at the vertical target and the second term of the additional term describes the accumulation at the strike point. The exponent X2 and the offset n_2 can be obtained from data given in [153]. In [154] it was shown that the retention behaviour of W covered with C does not significantly differ from the retention behaviour of pure W. Therefore, the accumulation of T at the vertical target can be described by the retention behaviour of pure W, even under the presence of co-deposited layers at the vertical target, growing during the T burning phase.

Results from equations (7.1) and (7.2) are depicted in figure 7.4 for different implantation temperatures between 300 K and 900 K. Two horizontal dashed lines are inserted, which mark the upper (700 g) and the lower (330 g) safety limit. The solid curves show the accumulation of T in a-C:W, covering 1st wall, baffle and dome, obtained from equation (7.1). The accumulation of T at the first wall plus full divertor, obtained from equation (7.2), which includes the accumulation at the vertical target, is shown by the dashed curves. Besides the strike point of the divertor, temperatures are not above 500 K. Since it was shown that temperature does not dominate the retention behaviour of a-C:W, for temperatures of 500 K and below, most attention must be paid to the curve obtained for 300 K. Note that the increase of inventory in pure W at 700 K is not significantly different to the case at 300 K [153]. Therefore, it was assumed that for 775 K, which is the temperature desired for the strike point of the divertor during the T burning phase, the retention behaviour of pure W does not significantly differ from the retention behaviour at 300 K as well. Nevertheless, for a-C:W, the increase of the total amount of T with the number of shots, given by equation (7.1), was calculated for 700 K and for 900 K, too, in order to asses a maximum increase

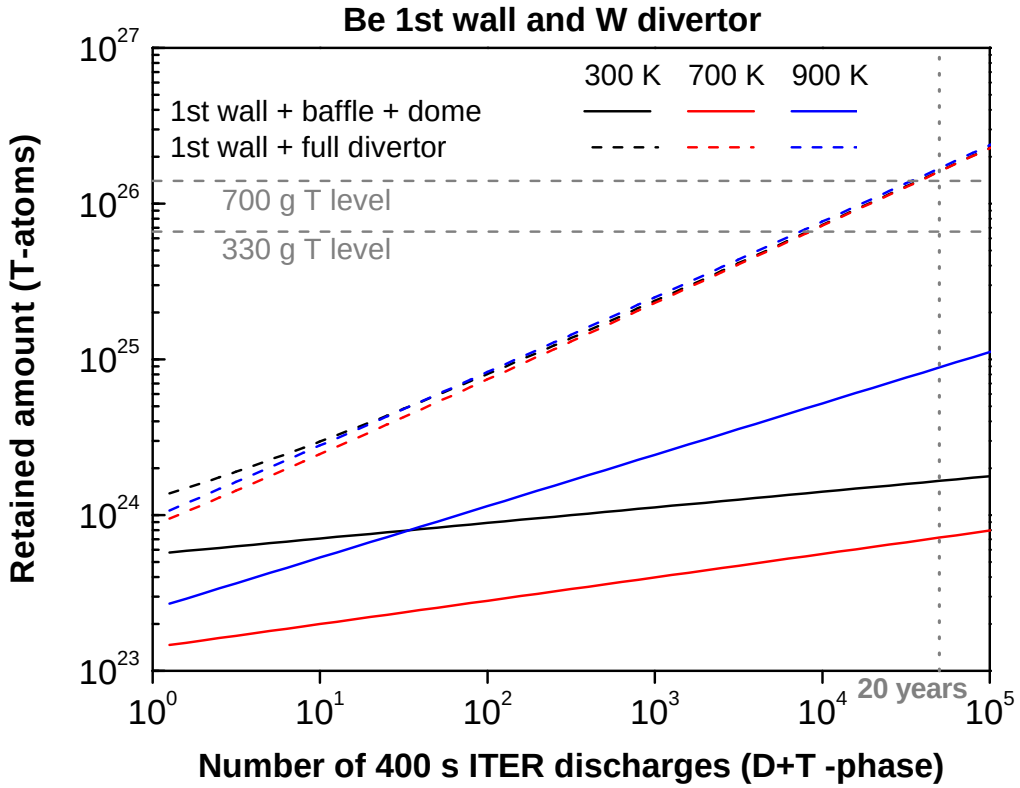

Figure 7.4: Amount of retained T atoms for different temperatures between 300 K and 900 K, versus the number of 400 s ITER discharges. Solid curves show the accumulation of T in a-C:W, covering 1st wall, baffle and dome. Dashed curves show the accumulation of T at the first wall plus full divertor. The two horizontal dashed lines mark the upper and lower safety limit.

for the T inventory in a-C:W. Even after 10^5 shots, which is 40 years of ITER operation, the total amount of T in C-W-mixed layers, covering the first wall, baffle and dome, is far below the lower safety limit of 330 g for temperatures at 900 K and below. This means, the T inventory build-up is clearly dominated by the accumulation of T in W at the vertical target. In the vertical target, the T safety limit would be reached after 4 years of operation.

Another aspect for C-W-mixed layers, deposited during the initial phase, lies in their potential to serve as protection coating. A strong accumulation of T must be expected, if it diffuses into large depths, i.e. through the entire thickness of the C-W-mixed layers and thus into the underlying wall material, e.g. into the W tiles. In this context, the ratio T/C between T and C at large depths beyond the implantation zone and the enrichment zone, i.e. in the unaffected C-W-mixed layer, is of major interest, besides the increase of the T inventory with fluence. In the depth of C-W-mixed layers a certain amount of T is trapped, corresponding to the ratio T/C between T and C, i.e. corresponding to the concentration c_T of T in the depth. Further T must diffuse into larger depths. This means, a C-W-mixed layer of a certain thickness has a certain capacity for T, which is - for large thicknesses - determined by the concentration c_T of T in the depth. Additional T must penetrate the entire layer. The numbers of shots during the T burning phase N_{TD}, which are necessary to result in a saturation of the entire thickness of the C-W-mixed layer with T, is given by the following equation:

$$N_{TD} = \Phi/(\phi_{dome+baffle} \cdot 400\,s) \cdot (\underbrace{c_T}_{\text{Depth profiles}} \cdot \overbrace{\Delta C}^{\text{Figure 7.2}} \cdot N_{DD}/n)^{1/X1}. \quad (7.3)$$

N_{TD}, of course, depends on the thickness of the C-W-mixed layer and thus on the number of shots N_{DD} during the initial phase, for a certain growth rate ΔC (obtained from [150]; unit: at·m^{-2}·shot^{-1}). The concentration c_T of T in the depth can be obtained from those D depth profiles, which were evaluated within the framework of the study presented in this thesis, for implantation temperatures between 300 K and 900 K (see figure 7.5 and section 5.1 *Diffusion of D: Depth profiles*). The other abbreviations are according to equations (7.1) and (7.2), e.g.

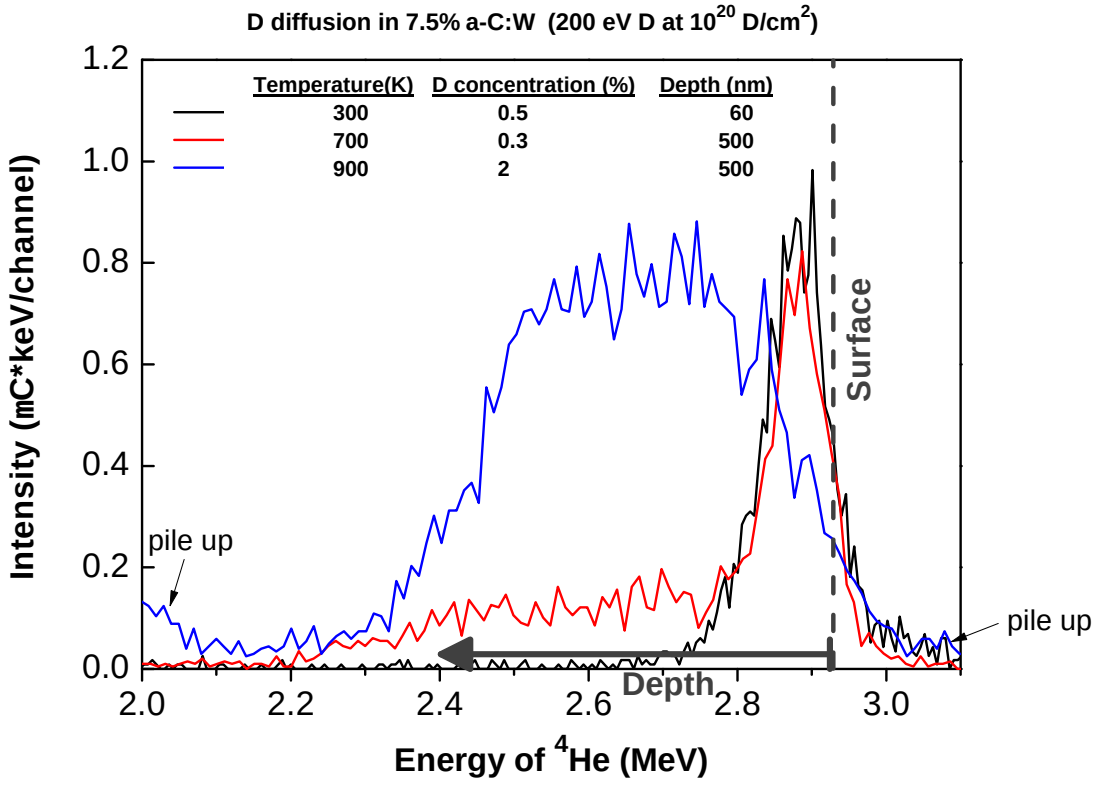

Figure 7.5: NRA spectra of 7.5% a-C:W, exposed to the 200 eV D beam between 300 K and 900 K and at a fluence of 10^{20}D/cm^2, describing D depth profiles. The ratio T/C in the depth of deposited C-W-mixed layers is assumed to match the D concentration in the depth of 7.5% a-C:W, given in the legend.

the T inventory n at fluence Φ. Main attention should be paid to dome and baffle. Diffusion into depth of Be tiles at the first wall can be neglected [155]. At the vertical target, the ratio between the C flux and the T flux determines, whether W sputtering or C deposition dominates. In [154] it was shown that the retention behaviour for the case of C deposition on W is not significantly different to the case of W sputtering and thus to the retention behaviour of pure W. Position dependent growth rates for dome and baffle were averaged over the entire area of 100 m^2, resulting in an averaged growth rate of ∼4·10^{21}C/m^{2}shot (∼40 nm/shot), abandoning on removal techniques, and in an effective growth rate of ∼2.3·10^{19}C/m^{2}shot

(∼0.23 nm/shot), applying removal techniques during maintenance. Thereby, a cleaning efficiency was assumed for the plasma facing surfaces, which matches the cleaning efficiency for plasma facing surfaces, observed for the maintenance after the JET DTE1 campaign [28, 23], i.e. ∼99.4%. Within the framework of the following assessments, it is assumed that the local distribution of growth rates of C matches the local distribution of growth rates of deposited C-W-mixed layers. Results from equation (7.3) are depicted in figure 7.6 for different implantation temperatures between 300 K and 900 K. The horizontal dotted line marks

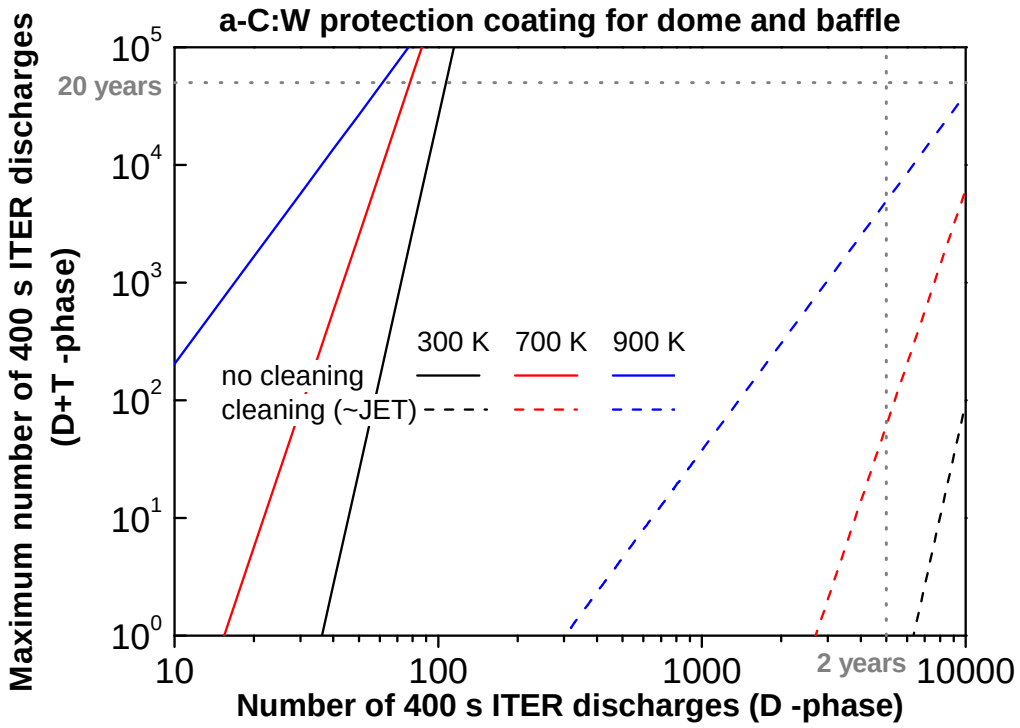

Figure 7.6: Maximum number of 400 s ITER discharges for the T burning phase (number of shots, necessary to penetrate the entire deposited layer) for different temperatures between 300 K and 900 K, versus the number of 400 s ITER discharges during the initial phase. Solid curves: Without removal techniques during maintenance. Dashed curves: Application of removal techniques during maintenance (removal efficiency according to JET DTE1 campaign; ∼99.4%). The horizontal and the vertical dotted line marks the number of shots after 20 years and after 2 years of ITER operation in the T phase and in the initial phase, respectively.

the number of shots after 20 years of ITER operation in the T phase. Since an operation of at least of 20 years is envisaged for the T phase, the number of shots during the initial phase must be sufficiently large so that thicknesses of deposited layers are sufficient to hinder T to diffuse through the entire thickness and thus to act as protection coating. For the solid curves (no cleaning techniques applied) less than 100 shots are necessary during the initial phase. For the dashed curves (cleaning techniques applied) the situation is quite different. For each of the curves of the temperature series the number of shots, which is necessary to grow layers of sufficient thickness, is significantly larger than 5 000, which is envisaged for the initial phase (marked by the vertical dotted line). From this point of view it must be recommended not to remove the deposited layers, which have been formed during the initial phase.

7.3 Re-erosion and accumulation of T in remote areas

If chemical erosion of C is brought to stop in the range of large fluences through the enrichment of W, the amount of re-eroded C and thus the amount of co-deposited C will be limited. Under these conditions, a maximum T inventory can be estimated.

For an erosion yield Y(Φ), which converges against zero in the range of large fluences Φ, the maximum amount of re-eroded C, ΔC_∞, is given by the following equation:

$$\Delta C_\infty = \int_0^\infty d\Phi\, Y(\Phi). \tag{7.4}$$

In this context, the maximum amount of re-eroded C and the erosion yield Y(Φ) of deposited C-W-mixed layers is to be identified with the maximum amount of removed C and the total yield of removed C of a-C:W, given in section 4.2 *Influence of W and of pre-heating on total yields of C*, respectively. For the decrease of the total yield of removed C, Y(Φ), of a-C:W with increasing fluence Φ, which is caused by enrichment, this expression is approximated by:

$$\Delta C_\infty \approx \int_0^\infty d\Phi\, Y_0\, e^{-\alpha\,\Phi}, \text{ which equals } \frac{Y_0}{\alpha}. \tag{7.5}$$

The offset Y_0 can be described by the total yield of removed C of a-C, under the assumption that the erosion behaviour of a-C:W is not affected intrinsically by the W inclusions, i.e. by a changed chemistry between C and hydrogen. This means, in the range of low fluences, in which a-C:W is not enriched with W, the total yield of removed C of a-C:W must equal the total yield of removed C of a-C, which obtains a value of 0.06, at 300 K (see section 4.2 *Influence of W and of pre-heating on total yields of C*). For a-C:W the total amount of removed C was measured at a fluence of 10^{20} D/cm^2 and is not larger than $3{\cdot}10^{18}$ C/cm^2, at 300 K (see section 4.2 *Influence of W and of pre-heating on total yields of C*). Thus, the parameter α is obtained from the following expression:

$$\Delta C_{10^{20}\,D/cm^2} = \int_0^{10^{20}\,D/cm^2} d\Phi\; 0.06\, e^{-\alpha\,\Phi} \stackrel{!}{=} 3\cdot 10^{18}\, C/cm^2, \tag{7.6}$$

where $\Delta C_{10^{20}\,D/cm^2}$ is the amount of removed C of a-C:W, measured at a fluence of 10^{20} D/cm^2. This yields $\sim 1.13{\cdot}10^{-22}$ cm^2/D, for the parameter α, and thus $\sim 4.42{\cdot}10^{18}$ C/cm^2, for ΔC_∞ in equation (7.5). Integration over the total area of the inner vessel wall of 800 m^2 yields a maximum amount of re-eroded C of $\sim 4{\cdot}10^{25}$. This results in a maximum amount of retained T in the remote areas of 200 g, if each re-eroded C atom is co-deposited at a remote area, together with T, in which the ratio of T/C does not exceed 1.

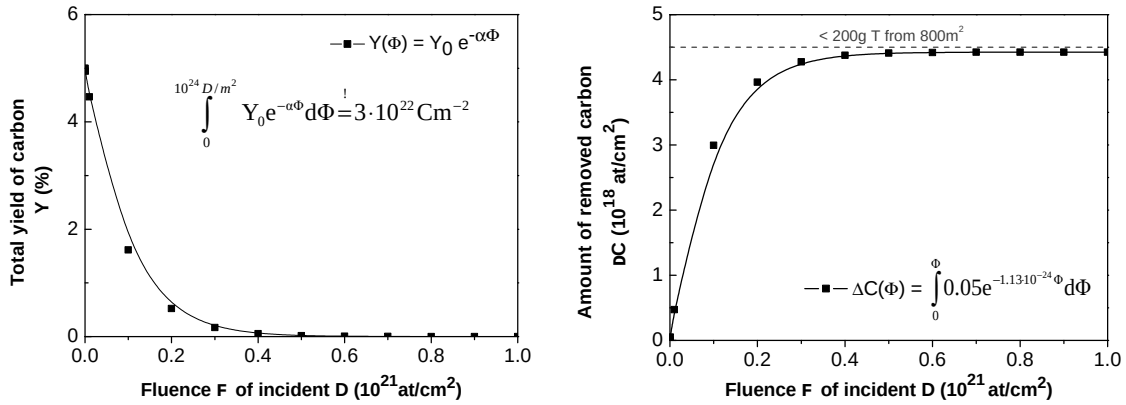

Figure 7.7: Illustration of the assessment of T inventory build-up by re-erosion of C and subsequent co-deposition in remote areas. Left hand: Decrease of the total yield of removed C in a-C:W, assuming an exponential decay over the fluence Φ of incident D. Right hand: Amount of removed C per unit area over the fluence Φ of incident D, obtained by integration between 0 and Φ, in equation (7.5). The horizontal-dotted line marks an amount of T, which corresponds to a level of 200 g, scaled to an area of 800 m^2.

7.4 Conclusion

The assessment of the T inventory build-up during the T burning phase of ITER was focused on the accumulation of T in deposited C-W-mixed layers through implantation, trapping and diffusion into depth, on one hand, and, on the other hand, on co-deposition of re-eroded C, originating from C-W-mixed layers, together with T during the T burning phase. Assessments made were based on investigations under defined conditions, i.e. on investigations of a model system for C-W-mixed layers, a-C:W, performed - within the framework of the study presented on this thesis - under the 200 eV D beam exposure. The extrapolation to ITER relevant ranges of flux, temperature and fluence was performed, by taking results obtained from these investigations into account. Up scaling was finally performed, by combining these results with energy and flux dependences of the retention and erosion behaviour of C, known in literature. The local distribution of deposited C-W-mixed layers after the initial phase, which is necessary in order to assess the accumulation of T through implantation and diffusion, was obtained from a model, which calculates the re-distribution of, e.g. C, inside the ITER vessel wall with time [150].

Based on the results of the model calculations given in [150], it is evident that deposited C-W-mixed layers will exhibit a significant reservoir for the build-up of T inventory, if no removal techniques will be applied: The C amounts, which will be left in the machine after the initial phase, will be able to take up between 1 kg and 2.5 kg of T. Nevertheless, after the JET DTE1 campaign, for instance, plasma facing surfaces were cleaned with an efficiency of $\sim$99.4%. Assuming that a similar efficiency will be reached for the plasma facing surfaces of ITER as well, this would lead to the conclusion that the build-up of T in such minor portions of remaining deposited C-W-mixed layers does not have to be expected to become a considerable threat, at the end.

Nevertheless, it is known from literature, on the other hand, that the safety limit will be reached after $\sim 10^3$ shots for the option of a full W divertor and Be first wall [23]. Note that this option can be compared to the initial situation of having removed nearly completely all

deposited layers after the maintenance phase, and note that for the T burning phase a number of shots between 10^4 and 10^5 is envisaged. In this case, a shut down of the ITER operation would be required several times. This raises the question whether deposited C-W-mixed layers have the ability to serve as protection coating for the underlying Be and W tiles. In order to solve this question, two aspects were considered: 1. How many shots are possible during the T burning phase, until the safety limit is reached, focusing on the accumulation of T through implantation and diffusion in C-W-mixed layers, which cover the first wall, baffle and dome? 2. How many shots are possible during the T burning phase, until T diffused through the entire thickness of C-W-mixed layers, which cover the first wall, baffle and dome? It was shown that the T inventory after 10^5 shots would be one or even two orders of magnitude below the safety limit. This leads to the conclusion that the thickness of the deposited C-W-mixed layers just needs to be sufficient, to serve as protection coating. The answer to question number two shows that already after 100 shots in the initial phase deposited C-W-mixed layers of sufficient thickness have been build-up, without applying removal techniques in the maintenance phase. For the case of the appliance of removal techniques with a local efficiency of $\sim$99.4% for the plasma facing surfaces during the maintenance phase, it could be shown that even 10^5 shots in the initial phase are not enough to grow deposited C-W-mixed layers, sufficiently thick to be able to perform 20 years of ITER operation for the T burning phase, without penetrating their entire thickness.

From this result, only one question remains: How large will those amounts of T become, which will deposit together with re-eroded C in remote areas, if no removal techniques will be applied? This assessment was performed for normal operation conditions, which allow the formation of a W enrichment zone and thus to bring chemical sputtering to stop. Assuming an exponential decay for the re-eroded C with increasing fluence, this results in a maximum amount of 200 g of T.

At the end of the initial phase, large amounts of deposited layers exist, which originate from the use of pure CFC at the vertical target during the initial phase. Besides the use of pure CFC, several attempts exist to optimize doping of pure CFC with metal carbides, in order to mitigate the erosion yield and thus to reduce the build-up of deposited layers during the initial phase [156, 157]. For the mitigation of erosion the formation of a macroscopically homogeneous enrichment zone at the surface needs to be ensured [68, 158]. Through an optimization of the fabrication process a homogeneous distribution of the dopants is desired [159], i.e. doping of the C matrix as well of the fibre bundles. Thereby, a drop of local concentrations needs to be avoided for the metal carbide dopants, which have a size of 0.1 - 1 μm. Besides the mitigation of erosion, good prospects are offered to improve the thermal conductivity and thus the thermal shock resistance of CFC through the presence of dopants [156]. An improved thermal shock resistance is also expected to prevent the loss of macroscopic particles, which are ejected from the C matrix, especially during transient loads [156]. Investigations of the erosion behaviour of a-C:W, performed within the framework of the studies presented in this thesis, showed that for the case of atomically dispersed nanometer-sized dopants the erosion yield is significantly reduced, even for low dopant concentrations of 1%. Thereby, the reduction of the erosion yield is nearly insensitive to the dopant concentration for concentrations of 15% and below, without respect to the mechanism, which leads to the mitigation of erosion (either enrichment or a changed chemistry between C and hydrogen). Therefore, small variations of local concentrations of the dopant,

leading to slight inhomogeneities of the extent of enrichment could be tolerated, if local concentrations do not exceed the range between 1% and 15%. This would result in a decreased build-up of deposited layers during the initial phase and thus to a reduced reservoir for the build-up of T inventory. For the case of the use of doped CFC, which exhibits a similar erosion behaviour as a-C:W, i.e. an exponentially decreasing erosion yield, which converges against zero in the range of large fluences, the total amount of deposited C per unit area after 5 000 shots in the initial phase will not be larger than the maximum amount of re-eroded C per unit area of $\sim 4.42 \cdot 10^{22}$ C/m^2, given by equation 7.5. Integration over the total area of the vertical target of 50 m^2 yields a maximum amount of deposited C of $\sim 2.2 \cdot 10^{24}$, after the initial phase. These C amounts can take up $\sim$11 g of T, assuming a maximum ratio between T and C of 1.

Chapter 8

Conclusion

The main scientific interest of the study presented in this thesis lies on the Tritium retention behaviour of tungsten-containing carbon films (a-C:W), which serve as model system for deposited layers. Deposited layers are mixed materials, i.e. amorphous and C rich layers, containing metal inclusions. At the divertor region, where C and W are close to each other, W is the main impurity in deposited layers, especially under the presence of off-normal events.

For pure carbon, e.g. graphite, the retention behaviour is well known in literature. Through the presence of W in deposited layers there is a need to study the influence of W inclusions on the retention behaviour. Concerning the influence of metal inclusions, the retention behaviour of boron-, silicon- and titanium-containing graphites was investigated in literature. From these investigations, however, it is unclear whether the retention behaviour is changed by a changed porosity in metal-containing graphites or by the presence of metal inclusions. a-C:W, on the other hand, is an amorphous and dense material, in which the porosity does not depend on the W concentration; the porosity is no different to the porosity of the pure carbon film (a-C). This allows to study the influence of W inclusions on the retention behaviour, without the need to take porosity into account, in contrast to graphite materials.

Furthermore, it is known from literature that in metal-containing carbon the surface enriches with metal with increasing fluence, which leads to a changed erosion behaviour. The investigation of the erosion behaviour of a-C:W gives the possibility to study the influence of enrichment on the retention behaviour.

Through the use of a defined experiment, the deuterium (D) beam exposure at the Garching high current ion source, and through the use of a defined material, a-C:W, which is produced by dual magnetron sputter deposition, it was possible to introduce a set of parameters (the W concentration, the pre-heating temperature and the implantation temperature). Through the analysis of the D beam profile of the Garching high current ion source it was possible to apply ion beam analysis inside a reference zone, which exhibits a calibrated value for the fluence of incident D, and thus it was possible to characterize the retention and the erosion behaviour by means of the total amounts of retained D and removed C and by means of the depth profiles of W and D at a given fluence.

8.1 Erosion behaviour: comparison a-C and a-C:W

- For 7.5% a-C:W the width and the composition of the W enrichment zone are significantly affected by the implantation temperature. At 700 K and below, the width of the enrichment zone is just resolvable. A range can be given, which is between the width of the ion range of 200 eV D in pure W (6.3 nm), as the lower limit, and the width of the ion range of 1200 eV D in pure W (16 nm), as the upper limit. While at 300 K and at 500 K the W concentration in the enrichment zone is close to 100%, the W concentration is already decreased to 75% at 700 K. Above 700 K, the width of the enrichment zone increases clearly above the width of the implanation zone and the W concentration in the enrichment zone decreases. At 900 K, the enrichment zone has a width of 50 nm and contains 60% W. At 1100 K, the W concentration is decreased to 33% and the width of the enrichment zone is increased to 80 nm. Radiation-enhanced segregation is suggested for the observed dilution of the W concentration in the enrichment zone and for the increase of the width of the enrichment zone with increasing temperature. Further to this, radiation-enhanced solid state reactions appear to be possible, resulting in carbide formation inside the enrichment zone, already at temperatures well below 1300 K. Changes of the width and the composition of the W enrichment zone are accompanied by a roughening of the surface morphology with increasing temperature. At 1300 K, the surface roughness significantly results in multiple surface crossings for the analysing beam of the applied the RBS so that it is not possible to convert the RBS spectrum into a depth profile of W.

- The erosion behaviour of 7.5% a-C:W was compared to the erosion behaviour of a-C, at temperatures between 300 K and 1300 K. At elevated temperatures, a-C:W exhibits a very pronounced reduction of the total yield of removed C compared to a-C. At 700 K, for instance, the total yield of removed C is reduced to 1/20. While a-C exhibits a strong temperature dependence, 7.5% a-C:W shows a rather weak temperature dependence.

- At an implantation temperature of 300 K, the total yield of removed C is significantly reduced for a-C:W compared to a-C (factor of 2-3). Varying the W concentration between 1% and 15% exhibits a weak increase of the total yield of removed C between 4% and 6% of W. Heat treatment up to 1300 K before the D beam exposure does not change the total yield of removed C, neither in a-C nor in a-C:W. This means, the structure of the C matrix does not affect the erosion behaviour. In fact, the erosion behaviour is affected by W inclusions. For the W concentrations of 7.5% and above it was shown by the analysis of the W enrichment zone that steady state has been reached in the enrichment zone, already at a fluence of 10^{20} D/cm^2. In this case the erosion behaviour is predominantly affected by enrichment and shielding. For the W concentrations of 2.5% and below, on the other hand, it was shown from the total yields of removed C that the enrichment zone is not yet in steady state at a fluence of 10^{20} D/cm^2. This means, the erosion behaviour is not predominantly affected by enrichment for the W concentrations of 2.5% and below.

8.2 Retention behaviour of a-C:W

- At 300 K, the accumulation of D with fluence in a-C and in a-C:W was compared to the accumulation in pyrolytic graphite. Within a wide range of fluences, i.e. for fluences at 10^{19} D/cm^2 and below, the retention behaviour in a-C and a-C:W is governed by the same processes as the retention behaviour of pyrolytic graphite. The retention behaviour was characterized by means of the reflection coefficient, the saturation ratio of D/C in the implantation zone and the increase of D inventory with fluence.

  For a-C the reflection coefficient is 17%, the saturation ratio is 0.4 and the exponent over the fluence, which describes the increase of the D inventory with fluence, is 0.1. These values match the values for pyrolytic graphite. Therefore, the amorphous C structure of a-C does not exhibit a different retention behaviour compared to the structure of pyrolytic graphite. Pre-heating also does not influence the increase of the D inventory with fluence in a-C. The retention behaviour of a-C is not affected by the structure of the C matrix.

  In a-C:W the W concentration was varied below 20%. The reflection coefficient of a-C:W is not different to the reflection coefficient of a-C and pyrolytic graphite, without respect to the W concentration. The saturation ratio in the implantation zone is slightly decreased to 0.3 for 18.5% a-C:W. For the lower W concentrations, however, no significant difference was observed compared to a-C and pyrolytic graphite. Pre-heating does not influence the saturation ratio of a-C:W. For fluences of 10^{19} D/cm^2 and below the increase of the D inventory with fluence is no different in a-C:W compared to a-C and pyrolytic graphite. In general, a-C:W does not show a changed accumulation of D for fluences of 10^{19} D/cm^2 and below. While the TDS spectra show that D is bound at lower energies in a-C:W, i.e. the maximum of the D_2 desorption peak is shifted by 200 K to lower temperatures, the accumulation of D with fluence at 300 K is not changed intrinsically in a-C:W. In fact, changes in the accumulation of D develop with increasing fluence above 10^{19} D/cm^2. These changes strongly depend on the W concentration. While for the W concentrations of 2.5% and below the D inventory increases to the 1.5-fold of the value of a-C, increasing the fluence to 10^{20} D/cm^2, the D inventory for the W concentrations of 7.5% and above decreases in the same fluence range to the half value of a-C. The increase of the D inventory for the low W concentrations can be attributed to roughening and the decrease of the inventory for the high W concentrations can be attributed to the build-up of a W enrichment zone over the width of the ion range. Both effects develop in a fluence range between 10^{19} D/cm^2 and 10^{20} D/cm^2. This is confirmed by the TDS measurements: It was shown that the energy range of occupied bonding states is changed for fluences between 10^{19} D/cm^2 and 10^{20} D/cm^2, both for the low and for the high W concentrations. While for 2.5% of W and below the energy range of occupied bonding states increases, it decreases for 7.5% of W and above.

  Nevertheless, the differences between a-C and a-C:W, concerning the accumulation of D with fluence, are supposed to occur in a closed range of fluences around 10^{20} D/cm^2. This is confirmed by the additional experiments with 7.5% a-C:W, already enriched with W at the surface. Enriched 7.5% a-C:W was prepared by the D beam exposure of 7.5% a-C:W at a fluence of 10^{20} D/cm^2 and the subsequent outgasing of retained

D. The accumulation of the D inventory with fluence does not saturate at high fluences. This means, D is able to diffuse through the enrichment zone into depth. At a fluence of 10^{20} D/cm^2, the D inventory has again the same value as the inventory of non-enriched 7.5% a-C:W, exposed to the D beam at a fluence of 10^{19} D/cm^2. This means, the accumulation of D with fluence in the enriched 7.5% a-C:W is not dominated by the influence of the enrichment zone, but by the diffusion of D into depth, through the unaffected C matrix. From the comparison of non-enriched a-C:W with a-C and pyrolytic graphite it is known that W inclusions in the unaffected C matrix do not affect the increase of the D inventory with fluence. This suggests that for fluences far beyond 10^{20} D/cm^2 the increase of the D inventory with fluence in a-C:W is not different to the increase of the D inventory with fluence of a-C and of pyrolytic graphite.

- At elevated temperatures a diffusion of D into depths larger than the width of the implantation zone is observable, in the NRA spectra obtained from 7.5% a-C:W exposed to the D beam. It was shown that the amount of available bonding states in the implantation zone decreases with increasing temperature. This leads to a lowered D/(C+W) saturation ratio in the implantation zone. Under the presence of the D beam, D is forced to diffuse into larger depths. For 7.5% a-C:W exposed to the D beam at a fluence of 10^{20} D/cm^2 and at temperatures between 300 K and 900 K it was possible to quantify the influence of temperature on the diffusion depth and on the D concentration, averaged over the diffusion depth. At 300 K, D does not diffuse beyond the resolvable depth (50 nm). For this range, however, only an averaged D concentration can be given (5%). At 700 K, 50% of the retained D diffuses to depths up to 0.5 μm, which is considerably beyond the resolvable depth. While the D concentration is 2% below the resolvable depth, the D concentration beyond the resolvable depth is 0.3%. At 900 K, major portions of the retained D are located at depths up to 0.5 μm, i.e. the D concentration below the resolvable depth can not be distinguished from the D concentration beyond the resolvable depth (2%). In general, for a-C:W exposed to the D beam at a fluence of 10^{20} D/cm^2 and at temperatures up to 900 K the diffusion depths are not larger than 0.5 μm.

- For the accumulation of D with fluence in a-C and in 7.5% a-C:W at elevated implantation temperatures following characteristics were observed: At low fluences, 100% of the unreflected D is trapped in the implantation zone until a temperature dependent saturation level is reached. At fluences above $\sim 10^{16}$ D/cm^2 the accumulation of D with fluence is slowed down. The further increase of the D inventory with fluence depends on the temperature. These characteristics show that trends observed by analysing the depth profiles of D, i.e. a decreased number of available bonding states in the implantation zone with increasing implantation temperature, which is in convolution with an enhanced diffusion into depth, are observable in changes in the accumulation of D with temperature. A decreased number of available bonding states at elevated temperatures is observable as a decreased saturation level and an increased diffusion into depth at elevated temperatures is observable as an increased accumulation of D with fluence. These trends are quantifiable for temperatures between 300 K and 500 K. At 300 K, the saturation level is $3.5 \cdot 10^{16}$ D/cm^2 and the exponent over the fluence, which describes the increase of the inventory with fluence, is 0.1. At 500 K, neither the saturation level,

nor the exponent over the fluence are different to 300 K. This means, for 500 K and below the accumulation of D is not sensitive on implantation temperature. At 700 K, the saturation level is lowered to $6 - 8 \cdot 10^{15}$ D/cm^2 and the exponent over the fluence is increased to 0.14. The effect of temperature on the retention behaviour and thus on the accumulation of the D inventory with fluence becomes dominant between 500 K and 700 K. Above 700 K, trends are still present, but difficult to quantify, since curves show a non-monotonic increase with fluence, especially at high fluences. At 900 K and at 1100 K, a decrease of the D inventory above a fluence of 10^{19} D/cm^2 was observed, similar to the case at 300 K and at 500 K. However, it remains unclear whether this decease is caused by enrichment and carbide formation.

While the strongest effect on number of available bonding states and on diffusion into depth, and thus on the saturation level and on the accumulation of D with fluence is given by temperature, W inclusions also show a small effect. This is due to a slight lowering of the bonding energies in 7.5% a-C:W to temperatures below 900 K compared to a-C, in which bonding energies are slightly above 900 K. Therefore, the number of available bonding states at 900 K is slightly decreased in 7.5% a-C:W compared to a-C. This is observable, by comparing the increase of the D inventory with fluence and the saturation level of a-C and of 7.5% a-C:W at 900 K; the saturation level is slightly decreased and the increase of the D inventory with fluence is slightly increased in 7.5% a-C:W. The intrinsic influence of W inclusions on the retention behaviour at elevated temperatures, however, is weak compared to the influence of temperature. Further to this, if enrichment and carbide formation influenced the retention behaviour at elevated temperatures, it could be speculated that both influences are limited to a range of fluences around 10^{20} D/cm^2, similarly to the situation at 300 K. Since it was shown that D diffuses into depths far beyond the enrichment zone at elevated temperatures, i.e. up to 0.5 μm, the trapping behaviour in the unaffected C matrix must become dominant for large fluences again. The trapping behaviour of the unaffected C matrix, however, is dominated by the implantation temperature.

8.3 ITER relevance

Concerning the Tritium retention behaviour of a-C:W, W inclusions do not intrinsically affect the accumulation of D for implantations at 300 K, although a-C:W exhibits slightly decreased bonding energies compared to a-C. At elevated temperatures, this slight decrease of the bonding energies is observable as a slightly enhanced accumulation of D compared to a-C. This means, the intrinsic effect of W inclusions on the accumulation of D can be neglected; for a wide range of fluences a-C:W shows a retention behaviour, which is similar to the retention behaviour of a-C. The accumulation of D increases with increasing temperature, through a decreasing saturation ratio in the implantation zone and an increasing extend of diffusion of D into depth.

Concerning the erosion, on the other hand, a-C:W shows a behaviour, which is well known for metal-containing carbon. The total yield of removed C is reduced significantly compared to a-C. From the investigations presented in this thesis it can be concluded that this behaviour is observable for the implantation temperatures between 300 K and 1300 K, the W concentrations between 1% and 15% and the pre-heating temperatures up to 1300 K. The reduction of the total yield of removed C in a-C:W is only gently changed by varying the afore mentioned parameters.

Transferring these results to the retention and erosion behaviour of deposited C-W-mixed layers, this leads to the following estimations:

Since the influence of W enrichment on the retention behaviour of a-C:W appears to be limited to a small range of fluences around 10^{20} D/cm^2, it appears that the increase of the D inventory with fluence can be extrapolated to ITER-relevant fluence ranges, neglecting the influence of enrichment. In this case, a-C:W exhibits the same increase of the D inventory with fluence as pure C. Furthermore, the increase of the hydrogen inventory with fluence does neither depend on particle energy and flux, nor on the isotope species. Therefore, it is possible to describe the accumulation of T in deposited C-W-mixed layers through implantation and diffusion into depth. This can be performed by the extrapolation of that increase of the D inventory with fluence, which was observed for a-C:W within the framework of the study presented in this thesis. Since the surface temperature of the inner vessel walls must be kept below 800 K, the increase of the D inventory with fluence is only of interest for temperatures of 900 K and below. In this temperature range, the increase of the D inventory with fluence results in such low values that an accumulation of T in deposited C-W-mixed layers through implantation and diffusion into depth is uncritical. This means, even after 10^5 400 s ITER-discharges in the T burning phase, which is longer than the scheduled operation time of the T burning phase of ITER, the T inventory in a-C:W is between one and two orders of magnitude below the safety limit of 330 g. Furthermore, already a hundred 400 s ITER-discharges in the initial phase are sufficient to grow deposited C-W-mixed layers on baffle and dome of such a thickness, which is sufficient to hinder T to diffuse into the underlying W tiles.

For the case of normal operation conditions and for impact energies of 200 eV/T and below deposited C-W-mixed layers may face a lowered re-erosion through the enrichment of W. This lowering is insensitive to the W concentration and to the operation temperature, at least in the medium range up to 1300 K. Therefore, the growth of T-containing co-deposited layers in remote areas can be expected to be lowered or even brought to stop so that the T

safety limit will not be reached.

Bibliography

[1] J. Fricke. *Energie*. R. Oldenburg Verlag, München, 1984.

[2] R. Kümmel. *Energie und Kreativität*. B.G. Teubner Verlagsgesellschaft, Leipzig, 1998.

[3] L.A. Artsimovic. *Controlled Thermonuclear Reactions*. Oliver and Boyd, Edinburgh and London, 1964.

[4] D.M. Meade. Effect of high-Z impurities on ignition and Lawson conditions for a thermonuclear reactor. *Nucl. Fusion*, 14(2):289–291, 1974.

[5] R. Aymar and Int Team. ITER status, design and material objectives. *J. Nucl. Mater.*, 307(Part A):1–9, 2002.

[6] J.A. Wesson. *Tokamaks*. Oxford Engineering Science Series 48. Calderon Press, Oxford, 1997.

[7] U. Schuhmacher. *Fusions Forschung. Eine Einführung.* Wissenschaftliche Buchgesellschaft, Darmstadt, 1993.

[8] http://www. bmbf.de/de/2270.php.

[9] R. Behrisch and V. Prozesky. Particle and power exhaust for a fusion plasma. *Nucl. Fusion*, 30(10):2166–2170, 1990.

[10] M.H. Redi and S.A. Cohen. Influence of MHD effects and edge conditions on ITER helium ash accumulation and sustained ignition. *J. Nucl. Mater.*, 176:262–267, 1990.

[11] D. Reiter, G.H. Wolf, and H. Kever. Burn condition, helium particle confinement and exhaust efficiency. *Nucl. Fusion*, 30(10):2141–2155, 1990.

[12] R. Behrisch. Particle bombardment and energy fluxes to the vessel walls in controlled thermonuclear fusion devices. *Nucl. Fusion*, 1(Suppl. S):7–16, 1991.

[13] D. Reiter, H. Kever, G.H. Wolf, M. Baelmans, R. Behrisch, and R. Schneider. Helium removal from Tokamaks. *Plasma Physics and Controlled Fusion*, 33(13):1579–1600, 1991.

[14] J.C. Rauch, K.J. Greve, and R.K. Maix. D-shaped main field-coil for ASDEX fusion experiment of Max-Planck-Institute-for-Plasma-Physics at Garching near Munich. *Brown Boveri Review*, 64(2):92–98, 1977.

[15] R. Aymar, Y. Shimomura, M. Huguet, V. Chuyanov, and Int Team. ITER: Fusion research at the dawn of a new era. International Atomic Energy Agency (IAEA), 2002.

[16] R. A. Pitts, A. Kukushkin, A. Loarte, A. Martin, M. Merola, C. E. Kessel, V. Komarov, and M. Shimada. Status and physics basis of the ITER divertor. *Phys. Scr.*, T138:014001 (10pp), 2009.

[17] R. Behrisch. Plasma-facing materials for fusion devices. *Journal of Surface Investigation-X-Ray Synchrotron and Neutron Techniques*, 4(4):549–562, 2010.

[18] R. Behrisch, G. Federici, A. Kukushkin, and D. Reiter. Material erosion at the vessel walls of future fusion devices. *J. Nucl. Mater.*, 313:388–392, 2003.

[19] G. Federici, J.N. Brooks, D.P. Coster, G. Janeschitz, A. Kukuskhin, A. Loarte, H.D. Pacher, J. Stober, and C.H. Wu. Assessment of erosion and tritium codeposition in ITER-FEAT. *J. Nucl. Mater.*, 290:260–265, 2001.

[20] H. Bolt, V. Barabash, G. Federici, J. Linke, A. Loarte, J. Roth, and K. Sato. Plasma facing and high heat flux materials - needs for ITER and beyond. *J. Nucl. Mater.*, 307(Part A):43–52, 2002.

[21] J.M. Linke, T. Hirai, M. Rodig, and L.A. Singheiser. Performance of plasma-facing materials under intense thermal loads in Tokamaks and Stellarators. *Fusion Sci. Technol.*, 46(1):142–151, 2004.

[22] V. Riccardo, M. Firdaouss, E. Joffrin, G. Matthews, Ph. Mertens, V. Thompson, and E. Villedieu. Operational limits for the ITER-like wall in JET. *Phys. Scr.*, T138:014033 (5pp), 2009.

[23] J. Roth, E. Tsitrone, Th. Loarer, V. Philipps, S. Brezinsek, Al. Loarte, G.F. Counsell, R.P. Doerner, K. Schmid, O.V. Ogorodnikova, and R.A. Causey. Tritium inventory in ITER plasma-facing materials and tritium removal procedures. *Plasma Phys. Control Fus.*, 50(10), 2008.

[24] J. Roth, E. Tsitrone, A. Loarte, Th. Loarer, G. Counsell, R. Neu, V. Philipps, S. Brezinsek, M. Lehnen, P. Coad, Ch. Grisolia, K. Schmid, K. Krieger, A. Kallenbach, B. Lipschultz, R. Doerner, R. Causey, V. Alimov, W. Shu, O. Ogorodnikova, A. Kirschner, G. Federici, A. Kukushkin, EFDA PWI Task Force, ITER PWI Team, Fusion Energy, and ITPA SOL DIV. Recent analysis of key plasma wall interactions issues for ITER. *J. Nucl. Mater.*, 390-91:1–9, 2009.

[25] V. Kotov, D. Reiter, A. S. Kukushkin, and H. D. Pacher. Numerical estimates of the ITER first wall erosion due to fast neutral particles. *Phys. Scr.*, T138:014020 (4pp), 2009.

[26] N. Baluc. Material degradation under DEMO relevant neutron fluences. *Phys. Scr.*, T138:014004 (6 pp.), 2009.

[27] R. Behrisch, V. Khripunov, R.T. Santoro, and J.M. Yesil. Transmutation of plasma facing materials by the neutron flux in a DT fusion reactor. *J. Nucl. Mater.*, 258(Part A):686–693, 1998.

[28] P. Andrew, P.D. Brennan, J.P. Coad, J. Ehrenberg, M. Gadeberg, A. Gibson, D.L. Hillis, J. How, O.N. Jarvis, H. Jensen, R. Lasser, F. Marcus, R. Monk, P. Morgan, J. Orchard, A. Peacock, R. Pearce, M. Pick, A. Rossi, P. Schild, B. Schunke, and D. Stork. Tritium retention and clean-up in JET. *Fusion Eng. Des.*, 47:233–245, 1999.

[29] R. Behrisch, M. Mayer, and C. GarciaRosales. Composition of the plasma facing material Tokamakium. *J. Nucl. Mater.*, 233(Part A):673–680, 1996.

[30] R. Kawakami, T. Shimada, Y. Ueda, and M. Nishikawa. Simulation study of dynamical material mixing on tungsten surfaces at elevated temperatures due to hydrogen and carbon mixed ion beam irradiation. *J. Nucl. Mater.*, 329(Part A):737–741, 2004.

[31] M. Mayer, M. Andrzejczuk, R. Dux, E. Fortuna-Zalesna, A. Hakola, S. Koivuranta, K. Krieger, K. J. Kurzydlowski, J. Likonen, G. Matern, R. Neu, G. Ramos, M. Rasinski, V. Rohde, K. Sugiyama, A. Wiltner, W. Zielinski, and ASDEX-Upgrade Team. Tungsten erosion and redeposition in the all-tungsten divertor of ASDEX Upgrade. *Phys. Scr.*, T138:014039 (7pp), 2009.

[32] M. Mayer, R. Behrisch, H. Plank, J. Roth, G. Dollinger, and C.M. Frey. Codeposition of hydrogen with beryllium, carbon and tungsten. *J. Nucl. Mater.*, 230(1):67–73, 1996.

[33] P. Staib and G. Staudenmaier. Surface effects and impurity production in Tokamak machines. *J. Nucl. Mater.*, 76-7(1-2):78–91, 1978.

[34] Y. Ueda, M. Fukumoto, I. Sawamura, D. Sakizono, T. Shimada, and M. Nishikawa. Carbon impurity behavior on plasma facing surface of tungsten. *Fusion Eng. Des.*, 81(1-7):233–239, 2006.

[35] G. F. Matthews, P. Edwards, H. Greuner, A. Loving, H. Maier, Ph. Mertens, V. Philipps, V. Riccardo, M. Rubel, C. Ruset, A. Scmidt, E. Villedieu, and JET-EFDA Contributors ITER Wall Pr. Current status of the JET ITER-like Wall Project. *Phys. Scr.*, T138:014030 (4pp), 2009.

[36] J. Roth. Status of knowledge of chemical erosion of carbon and critical issues for extrapolation to ITER. *Phys. Scr.*, T124:37–43, 2006.

[37] C.H. Skinner. Tritium retention and removal in Tokamaks. *AIP Conf. Proc.*, 1095:127–145, 2009.

[38] M. Balden and M. Mayer. Removal of deuterium from co-deposited carbon-silicon layers. *J. Nucl. Mater.*, 283(Part B):1057–1061, 2000.

[39] M. Balden and M. Mayer. Deuterium in re-deposited silicon-doped carbon layers and its removal by heating in air. *J. Nucl. Mater.*, 298(3):225–230, 2001.

[40] J. Roth and C. Hopf. Sticking coefficient and surface loss probability of eroded species during bombardment of carbon with deuterium. *J. Nucl. Mater.*, 334(2-3):97–103, 2004.

[41] W.M. Shu, C.A. Gentile, C.H. Skinner, S. Langish, and M.F. Nishi. The effect of oxygen on the release of tritium during baking of TFTR D-T tiles. *Fusion Eng. Des.*, 61-2:599–604, 2002.

[42] T. Schwarz-Selinger, U. von Toussaint, C. Hopf, and W. Jacob. Fuel removal from tile gaps with oxygen discharges: Reactivity of neutrals. *Phys. Scr.*, T138:014009 (8pp), 2009.

[43] H. Roche, C. Grisolia, C. Hernandez, C. Pocheau, A. Semerok, D. Farcage, X. Courtois, and N. Vignal. Deposited layer removal by laser ablation: From laboratory to Tore Supra integration. *Phys. Scr.*, T138:014028 (4pp), 2009.

[44] C.H. Skinner and G. Federici. Is carbon a realistic choice for ITER's divertor? *Phys. Scr.*, T124:18–22, 2006.

[45] D. P. Stotler, T. D. Rognlien, and S. I. Krasheninnikov. Mini-conference on the first microns of the first wall. *Phys. Plasmas*, 15(5):058303–11, 2008.

[46] M. J. Rubel, J. P. Coad, P. Wienhold, G. Matthews, V. Philipps, M. Stamp, and T. Tanabe. Fuel inventory and co-deposition in grooves and gaps of divertor and limiter structures. *Phys. Scr.*, T111:112–117, 2004.

[47] F.C. Sze, L. Chousal, R.P. Doerner, and S. Luckhardt. Growth of redeposited carbon and its impact on isotope retention properties on tungsten in a high flux deuterium plasma. *J. Nucl. Mater.*, 266:1212–1218, 1999.

[48] J. P. Coad, D. E. Hole, M. Rubel, A. Widdowson, J. Vince, and JET-EFDA Contributors. Deposition results from rotating collector diagnostics in JET. *Phys. Scr.*, T138:014023 (4pp), 2009.

[49] A. Kirschner, K. Ohya, D. Borodin, R. Ding, D. Matveev, V. Philipps, and U. Samm. Prediction of long-term tritium retention in the divertor of ITER: Influence of modelling assumptions on retention rates. *Phys. Scr.*, T138:014011 (6pp), 2009.

[50] A. Kreter, M. J. Baldwin, R. P. Doerner, D. Nishijima, P. Petersson, A. Pospieszczyk, M. Rubel, and K. Umstadter. Fuel retention in carbon materials under ITER-relevant mixed species plasma conditions. *Phys. Scr.*, T138:014012 (5pp), 2009.

[51] K. Ohya and A. Kirschner. Modeling of erosion and deposition by the Monte Carlo codes EDDY and ERO. *Phys. Scr.*, T138:014010 (7pp), 2009.

[52] D. L. Rudakov, C. P. C. Wong, A. Litnovsky, W. R. Wampler, J. A. Boedo, N. H. Brooks, M. E. Fenstermacher, M. Groth, E. M. Hollmann, W. Jacob, S. I. Krasheninnikov, K. Krieger, C. J. Lasnier, A. W. Leonard, A. G. McLean, M. Marot, R. A. Moyer, T. W. Petrie, V. Philipps, R. D. Smirnov, P. C. Stangeby, J. G. Watkins, W. P. West, and J. H. Yu. Overview of the recent DiMES and MiMES experiments in DIII-D. *Phys. Scr.*, T138:014007 (6pp), 2009.

[53] B. Schweer, G. Beyene, S. Brezinsek, N. Gierse, A. Huber, F. Irrek, V. Kotov, V. Philipps, U. Samm, and M. Zlobinski. Laser techniques implementation for wall surface characterization and conditioning. *Phys. Scr.*, T138:014008 (7pp), 2009.

[54] J. Westerhout, D. Borodin, R. S. Al, S. Brezinsek, M. H. J. 't Hoen, A. Kirschner, S. Lisgo, H. J. van der Meiden, V. Philipps, M. J. van de Pol, A. E. Shumack, G. De Temmerman, W. A. J. Vijvers, G. M. Wright, N. J. Lopes Cardozo, J. Rapp, and G. J. van Rooij. Chemical erosion of different carbon composites under ITER-relevant plasma conditions. *Phys. Scr.*, T138:014017 (4pp), 2009.

[55] L. C. Alves, E. Alves, N. P. Barradas, R. Mateus, P. Carvalho, J. P. Coad, A. M. Widdowson, J. Likonen, and S. Koivuranta. Erosion and re-deposition processes in JET tiles studied with ion beams. *Nucl. Instrum. Methods Phys. Res., Sect. B*, 268(11-12):1991–1996, 2010.

[56] T. Dittmar, P. Roubin, E. Tsitrone, E. Gauthier, A. Hakola, J. Likonen, F. Linez, C. Martin, M. Mayer, C. Pardanaud, J. Y. Pascal, B. Pasquet, B. Pegourie, J. Roth, I. Roure, and R. Ruffe. Deuterium Inventory in Tore Supra: Status of post-mortem analyses. *Phys. Scr.*, T138:014027 (6pp), 2009.

[57] H. G. Esser, V. Philipps, P. Wienhold, K. Sugiyama, A. Kreter, J. P. Coad, T. Tanabe, and JET-EFDA Contributors. Post mortem analysis of a JET quartz microbalance system. *J. Nucl. Mater.*, 363:146–151, 2007.

[58] T. Tanabe, K. Masaki, K. Sugiyama, and M. Yoshida. An overview of recent erosion/deposition and hydrogen retention studies in JT-60U. *Phys. Scr.*, T138:014006 (9pp), 2009.

[59] L. Aho-Mantila, M. I. Airila, M. Wischmeier, K. Krieger, R. Pugno, D. P. Coster, A. V. Chankin, R. Neu, V. Rohde, and ASDEX Upgrade Team. Modelling of (CH4)-C-13 injection and local carbon deposition at the outer divertor of ASDEX Upgrade. *Phys. Scr.*, T138:014019 (4pp), 2009.

[60] V. Rohde, M. Balden, T. Lunt, and ASDEX Upgrade Team. Dust investigations at ASDEX Upgrade. *Phys. Scr.*, T138:014024 (4pp), 2009.

[61] W. Eckstein, C. Garcia-Rosales, J. Roth, and W. Ottenberger. Sputtering Data. Techn. Rep. IPP 9/82, Max-Planck-Institut für Plasmaphysik, Garching, 1993.

[62] J.W. Davis, A.A. Haasz, and P.C. Stangeby. Hydrocarbon formation due to combined H^+ ion and H^0 atom impact on pyrolytic graphite. *J. Nucl. Mater.*, 155(Part A):234–240, 1988.

[63] A.A. Haasz and J.W. Davis. Synergistic chemical erosion of graphite due to simultaneous bombardment by H+ and other low-Z ions using a dual-beam accelerator. *Nucl. Instrum. Methods Phys. Res., Sect. B*, 83(1-2):117–124, 1993.

[64] Y. et al. Hirooka. A new plasma-surface interactions research facility - pisces-B and 1st materials erosion experiments on bulk-boronized graphite. *J. Vac. Sci. Technol. A*, 8(3, Part 1):1790–1797, 1990.

[65] F.W. Meyer, L.I. Vergara, and H.F. Krause. Recent ORNL measurements of chemical sputtering of ATJ graphite by slow atomic and molecular D ions. *Phys. Scr.*, T124:44–49, 2006.

[66] K. Ohya. Dynamic simulation of erosion and redeposition on plasma-facing materials. *Phys. Scr.*, T124:70–75, 2006.

[67] A. Kirschner, V. Philipps, J. Winter, and U. Kogler. Simulation of the plasma-wall interaction in a Tokamak with the Monte Carlo code ERO-TEXTOR. *Nucl. Fusion*, 40(5):989–1001, 2000.

[68] C. Adelhelm. *Structure and Erosion Behavior of Metal-doped Carbon Films*. PhD thesis, Technical University of Munich, 2008.

[69] M. Mayer, M. Balden, and R. Behrisch. Deuterium retention in carbides and doped graphites. *J. Nucl. Mater.*, 252(1-2):55–62, 1998.

[70] J.W. Davis, A.A. Haasz, and D.S. Walsh. Flux and fluence dependence of H^+ trapping in graphite. *J. Nucl. Mater.*, 176:992–999, 1990.

[71] A.A. Haasz and J.W. Davis. Fluence dependence of deuterium trapping in graphite. *J. Nucl. Mater.*, 209(2):155–160, 1994.

[72] A.A. Haasz and J.W. Davis. Deuterium retention in doped graphites. *J. Nucl. Mater.*, 232(2-3):219–225, 1996.

[73] A.A. Haasz, P. Franzen, J.W. Davis, S. Chiu, and C.S. Pitcher. Two-region model for hydrogen trapping in and release from graphite. *J. Appl. Phys.*, 77(1):66–86, 1995.

[74] C. H. Skinner, A. A. Haasz, V. KH. Alimow, N. Bekris, R. A. Causey, R. E. H. Clark, J. P. Coad, J. W. Davis, R. P. Doerner, M. Mayer, A. Pisarev, J. Roth, and T. Tanabe. Recent advances on hydrogen retention in ITER's plasma-facing materials: Beryllium, carbon, and tungsten. *Fusion Sci. Technol.*, 54(4):891–945, 2008.

[75] M. Balden and C. Adelhelm. Characterization and erosion of metal-containing carbon films. *Phys. Scr.*, T128:121–126, 2007.

[76] W. Möller and B.M.U. Scherzer. Modeling of hydrogen implantation into graphite. *J. Appl. Phys.*, 64(10, Part 1):4860–4866, 1988.

[77] W. Jacob and J. Roth. Chemical Sputtering. In R. Behrisch and W. Eckstein, editors, *Sputtering by Particle Bombardment, Experiments and Computer Calculations from Threshold to MeV Energies*. Springer, Berlin, 2006.

[78] W. Eckstein. Reflection (Backscattering). Techn. Rep. IPP 17/12, Max-Planck-Institut für Plasmaphysik, Garching, 2009.

[79] Y.T. Pei, D. Galvan, and J.T.M. de Hosson. Nanostructure and properties of TiC/a-C : H composite coatings. *Acta Mater.* , 53(17):4505–4521, 2005.

[80] M. D. Abad, J. C. Sanchez-Lopez, N. Cusnir, and R. Sanjines. WC/a-C nanocomposite thin films: Optical and electrical properties. *J. Appl. Phys.*, 105(3):033510–6, 2009.

[81] E. Lewin, O. Wilhelmsson, and U. Jansson. Nanocomposite nc-TiC/a-C thin films for electrical contact applications. *J. Appl. Phys.*, 100(5):054303–10, 2006.

[82] W.J. Meng and B.A. Gillispie. Mechanical properties of Ti-containing and W-containing diamond-like carbon coatings. *J. Appl. Phys.*, 84(8):4314–4321, 1998.

[83] D. Nilsson, F. Svahn, U. Wiklund, and S. Hogmark. Low-friction carbon-rich carbide coatings deposited by co-sputtering. *WEAR*, 254(11):1084–1091, 2003.

[84] M. Stuber, H. Leiste, S. Ulrich, H. Holleck, and D. Schild. Microstructure and properties of low friction TiC-C nanocomposite coatings deposited by magnetron sputtering. *Surf. Coat. Technol.*, 150(2-3):218–226, 2002.

[85] C. Adelhelm. Investigation of metal distribution and carbide crystallite formation in metal-doped carbon films (a-C:Me, Me = Ti, V, Zr, W). *Surf. Coat. Technol.*, 205(19):4335–4342, 2011.

[86] J. Robertson and E.P. Oreilly. Electronic and atomic-structure of amorphous-carbon. *Phys. Rev. B*, 35(6):2946–2957, 1987.

[87] S.R.P. Silva. *Properties of amorphous carbon*. Volume 29 of EMIS Data Review Series, 2003.

[88] M. Bauer, T. Schwarz-Selinger, W. Jacob, and A. von Keudell. Growth precursors for a-C:H film deposition in pulsed inductively coupled methane plasmas. *J. Appl. Phys.*, 98(7):073302–11, 2005.

[89] B. Feng, D.M. Cao, W.J. Meng, J. Xu, R.C. Tittsworth, L.E. Rehn, P.M. Baldo, and G.L. Doll. Characterization of microstructure and mechanical behavior of sputter deposited Ti-containing amorphous carbon coatings. *Surf. Coat. Technol.*, 148(2-3):153–162, 2001.

[90] W.J. Meng, R.C. Tittsworth, J.C. Jiang, B. Feng, D.M. Cao, K. Winkler, and V. Palshin. Ti atomic bonding environment in Ti-containing hydrocarbon coatings. *J. Appl. Phys.*, 88(5):2415–2422, 2000.

[91] S.J. Park, K.R. Lee, D.H. Ko, and K.Y. Eun. Microstructure and mechanical properties of WC-C nanocomposite films. *Diamond Relat. Mater.*, 11(10):1747–1752, 2002.

[92] A.A. Voevodin, J.P. O'Neill, S.V. Prasad, and J.S. Zabinski. Nanocrystalline WC and WC/a-C composite coatings produced from intersected plasma fluxes at low deposition temperatures. *J. Vac. Sci. Technol. A*, 17(3):986–992, 1999.

[93] A.Y. Wang, K.R. Lee, J.P. Ahn, and J.H. Han. Structure and mechanical properties of W incorporated diamond-like carbon films prepared by a hybrid ion beam deposition technique. *CARBON*, 44(9):1826–1832, 2006.

[94] S. El Mrabet, M.D. Abad, C. Lopez-Cartes, D. Martinez-Martinez, and J.C. Sanchez-Lopez. Thermal evolution of WC/C nanostructured coatings by Raman and in situ XRD analysis. *Plasma Processes Polym.*, 6(Suppl. S):S444–S449, 2009.

[95] VDI-Richtlinie VDI 2840. Kohlenstoffschichten. Grundlagen, Schichttypen und Eigenschaften, 2005.

[96] R Behrisch and W. Eckstein. Ion Backscattering from Solid Surfaces. In D.E. Post and R. Behrisch, editors, *Physics of Plasma Wall Interaction in Controlled Fusion*. Plenum Publishing Corporation, 1986.

[97] L.G. Haggmark and J.P. Biersack. Monte-carlo studies of light-ion reflection from metal-surfaces. *J. Nucl. Mater.*, 85-6:1031–1035, 1979.

[98] R. Behrisch. Sputtering by Particle Bombardment I: Physical Sputtering of Single-Element Solids. In R. Behrisch, editor, *Topics in Applied Physics*, volume 47. Springer, Berlin, 1981.

[99] W. Eckstein. Calculated Sputtering, Reflection and Range Values. Techn. Rep. IPP 9/132, Max-Planck-Institut für Plasmaphysik, Garching, 2002.

[100] J. Bohdansky. A universal relation for the sputtering yield of monoatomic solids at normal ion incidence. *Nucl. Instrum. Methods Phys. Res., Sect. B*, 2(1-3):587–591, 1984.

[101] W. Eckstein, C. Garcia-Rosales, J. Roth, and J. Laszlo. Threshold energy for sputtering and its dependence on angle of incidence. *Nucl. Instrum. Methods Phys. Res., Sect. B* , 83(1-2):95–109, 1993.

[102] M. Balden and J. Roth. New weight-loss measurements of the chemical erosion yields of carbon materials under hydrogen ion bombardment. *J. Nucl. Mater.*, 280(1):39–44, 2000.

[103] A. Horn, A. Schenk, J. Biener, B. Winter, C. Lutterloh, M. Wittmann, and J. Küppers. H atom impact induced chemical erosion reaction at C:H film surfaces. *Chem. Phys. Lett.*, 231(2-3):193–198, 1994.

[104] H. Plank and W. Eckstein. Preferential sputtering of carbides under deuterium irradiation - A comparison between experiment and computer simulation. *Nucl. Instrum. Methods Phys. Res., Sect. B*, 124(1):23–30, 1997.

[105] W. Eckstein. *Computer Simulation of Ion-Solid Interactions*. Springer, Berlin, 1991.

[106] W. Möller, W. Eckstein, and J.P. Biersack. TRDYN - binary collision simulation of atomic-collisions and dynamic composition changes in solids. *Comput. Phys. Commun.*, 51(3):355–368, 1988.

[107] E. de Juan Pardo, M. Balden, B. Cieciwa, C. Garcia-Rosales, and J. Roth. Erosion processes of carbon materials under hydrogen bombardment and their mitigation by doping. *Phys. Scr.*, T111:62–67, 2004.

[108] P. Starke, C. Adelhelm, and M. Balden. Erosion behaviour of metal-doped carbon layers in deuterium low pressure plasmas and the determination by optical emission spectroscopy. *Contributions to Plasma Physics*, 47(7):530–536, 2007.

[109] V.K. Alimov, R. Schwörer, B.M.U. Scherzer, and J. Roth. Thermal-desorption of D2 and CD4 from bulk-boronized graphites. *J. Nucl. Mater.*, 187(3):191–196, 1992.

[110] J. Roth. Chemical erosion of carbon based materials in fusion devices. *J. Nucl. Mater.*, 266:51–57, 1999.

[111] R. Schwörer and J. Roth. Sputtering of boron-doped graphite USB15 - investigation of the origin of low chemical erosion. *J. Appl. Phys.*, 77(8):3812–3817, 1995.

[112] J. Roth, J. Bohdansky, and J.B. Roberto. On the influence of impurities on the high-temperature sputtering yield of graphite. *J. Nucl. Mater.*, 128:534–539, 1984.

[113] J. Roth, C. Garcia-Rosales, R. Behrisch, and W. Eckstein. Search for low-erosion carbon materials. *J. Nucl. Mater.*, 191(Part A):45–49, 1992.

[114] R. Schworer, H. Plank, and J. Roth. Reduction of the chemical erosion of doped graphite due to surface modification during low energy D+ bombardment. *J. Nucl. Mater.*, 241:1156–1159, 1997.

[115] M. Balden, C. Adelhelm, E. de Juan Pardo, and J. Roth. Chemical erosion by deuterium impact on carbon films doped with nanometer-sized carbide crystallites. *J. Nucl. Mater.*, 363:1173–1178, 2007.

[116] M. Balden, J. Roth, E. de Juan Pardo, and A. Wiltner. Chemical erosion of atomically dispersed doped hydrocarbon layers by deuterium. *J. Nucl. Mater.*, 313:348–353, 2003.

[117] M. Balden, C. Garcia-Rosales, R. Behrisch, J. Roth, P. Paz, and J. Etxeberria. Chemical erosion of carbon doped with different fine-grain carbides. *J. Nucl. Mater.*, 290:52–56, 2001.

[118] B.L. Doyle, W.R. Wampler, and D.K. Brice. Temperature-dependence of H saturation and isotope exchange. *J. Nucl. Mater.*, 103(1-3):513–517, 1982.

[119] P. Franzen. Reemission of Hydrogen from Graphite at high Temperatures. Rep. IPP 9/92, Max-Planck-Institut für Plasmaphysik, Garching, 1993.

[120] B.L. Doyle, D.K. Brice, and W.R. Wampler. A local mixing model for deuterium replacement in solids. *Rad. Eff. Lett.*, 57(3):81–87, 1980.

[121] B.L. Doyle, W.R. Wampler, D.K. Brice, and S.T. Picraux. Saturation and isotopic replacement of deuterium in low-Z materials. *J. Nucl. Mater.*, 93-4:551–557, 1980.

[122] W. Möller. Hydrogen trapping and transport in carbon. *J. Nucl. Mater.*, 162:138–150, 1989.

[123] G. Federici and CH. Wu. Modeling of plasma hydrogen isotope behavior in porous materials (graphites/carbon–carbon composites). *J. Nucl. Mater.*, 186(2):131–152, 1992.

[124] M. Balden, E. Oyarzabal, E. de Juan Pardo, K. Durocher, J. Roth, and C. Garcia-Rosales. Deuterium retention by implantation in carbide-doped graphites. *Phys. Scr.*, T103:38–42, 2003.

[125] M Mayer. SIMNRA, a simulation program for the analysis of NRA, RBS and ERDA. Proceedings of the 15th International Conference on the Application of Accelerators in Research and Industry, J. L. Duggan and I.L. Morgan (eds.), American Institute of Physics Conference Proceedings 475, p. 541 (1999).

[126] W.K. Chu. *Backscattering spectrometry*. Academic Press, New York, 1978.

[127] M. Mayer. SIMNRA user's guide. Report IPP 9/113, Max-Planck-Institut für Plasmaphysik, Garching, Germany, 1997.

[128] J.R. Tesmer and M. Nastasi, editors. *Handbook of modern ion-beam materials analyses*. Materials Research Society, Pittsburgh, Pennsylvania, 1995.

[129] W. Möller and F. Besenbacher. Note on the ^{3}He+D nuclear-reaction cross-section. *Nucl. Instrum. Methods*, 168(1-3):111–114, 1980.

[130] J.F. Ziegler, J.P. Biersack, and U. Littmark. The Stopping and Range of Ions in Solids. In *The Stopping and Ranges of Ions in Matter*, volume 1. Pergamon Press, New York, 1985.

[131] H.H. Anderson and J.F. Ziegler. Hydrogen - Stopping Powers and Ranges in All Elements. In *The Stopping and Ranges of Ions in Matter*, volume 3. Pergamon Press, New York, 1977.

[132] J.F. Ziegler. Helium - Stopping Powers and Ranges in All Elements. In *The Stopping and Ranges of Ions in Matter*, volume 4. Pergamon Press, New York, 1977.

[133] M. Mayer. RESOLNRA: A new program for optimizing the achievable depth resolution of ion beam analysis methods. *Nucl. Instrum. Methods Phys. Res., Sect. B*, 266(8):1852–1857, 2008.

[134] E. de Juan Pardo. *Characterisation and Mitigation of Chemical Erosion of Doped Carbon Materials*. PhD thesis, Technical University of Munich, 2004.

[135] T. Kimura and H. Kasugai. Properties of inductively coupled RF Ar/H2 plasmas: Experiment and global model. *J. Appl. Phys.*, 107(8), 2010.

[136] L. I. Vergara, F. W. Meyer, H. F. Krause, P. Traskelin, K. Nordlund, and E. Salonen. Methane production from ATJ graphite by slow atomic and molecular D ions: Evidence for projectile molecule-size-dependent yields at low energies. *J. Nucl. Mater.*, 357(1-3):9–18, 2006.

[137] High Voltage Engineering Europa. B.V. Manual for 3 MV Tandetron Accelerator, Brochure. 2010.

[138] High Voltage Engineering Europa. B.V. Tandetron Accelerator System, Brochure. 2010.

[139] J. Biener, A. Schenk, B. Winter, C. Lutterloh, U.A. Schubert, and J. Küppers. Spectroscopic identification of C-H species in C:H films using HREELS. *Surf. Sci.*, 291(1-2):L725–L729, 1993.

[140] A. Schenk, B. Winter, J. Biener, C. Lutterloh, U.A. Schubert, and J. Küuppers. Growth and thermal-decomposition of ultrathin ion-beam deposited C:H films. *J. Appl. Phys.* , 77(6):2462–2473, 1995.

[141] J. Biener, U.A. Schubert, A. Schenk, B. Winter, C. Lutterloh, and J. Küppers. A surface reaction with atoms: Hydrogenation of sp-hybridized and sp2-hybridized carbon by thermal H(D) atoms. *J. Chem. Phys.*, 99(4):3125–3128, 1993.

[142] K. Sugiyama. Personal communication. *Unpublished data*, 2011.

[143] J. Roth and C. Garcia-Rosales. Analytic description of the chemical erosion of graphite by hydrogen ions. *Nucl. Fusion*, 36(12):1647–1659, 1996.

[144] J. Luthin and Ch. Linsmeier. Carbon films and carbide formation on tungsten. *Surf. Sci.*, 454:78–82, 2000.

[145] J. Roth, H. Plank, and R. Schworer. Erosion of Si- and Ti-doped graphites due to deuterium irradiation. *Phys. Scr.*, T64:67–70, 1996.

[146] V. Kh. Alimov. Deuterium retention in chemically vapour deposited tungsten-carbides. *Alimov-AnnRep*, 2006.

[147] ITER Documentation 2001. *Generic Site Safety Report*, volumes III, ITER Document Ref. G 84 RI.

[148] C.H. *et al.* Skinner. Plasma wall interaction and tritium retention in TFTR. *J. Nucl. Mater.*, 241:214–226, 1997.

[149] C.H. Skinner, J.T. Hogan, J.N. Brooks, W. Blanchard, R.V. Budny, J. Hosea, D. Mueller, A. Nagy, and D.P. Stotler. Modeling of tritium retention in TFTR. *J. Nucl. Mater.*, 266:940–946, 1999.

[150] K. Schmid, M. Reinelt, and K. Krieger. An integrated model of impurity migration and wall composition dynamics for Tokamaks. *J. Nucl. Mater.*, 2011, doi:10.1016/j.jnucmat.2011.01.105.

[151] K. Schmid. Personal communication. *Unpublished data*, 2011.

[152] M. Balden. Characterization of nano-structured W-, Ti-, V-, and Zr-doped carbon films. *Thin Solid Films*, 519:4032–4036, 2011.

[153] OV. Ogorodnikova, J. Roth, and M. Mayer. Deuterium retention in tungsten in dependence of the surface conditions. *J. Nucl. Mater.*, 313:469–477, 2003. 15th International Conference on Plasma-Surface Interactions in Controlled Fusion Devices (PSI-15), GIFU, JAPAN, MAY 26-31, 2002.

[154] H.T. Lee. *Tungsten Material Erosion under Deuterium and Carbon Co-bombardment*. PhD thesis, Technical University of Munich, 2009.

[155] M. Reinelt. *Erosion behavior of ultra-thin carbon layers and hydrogen retention in beryllium*. PhD thesis, Technical University of Munich, 2008.

[156] A. Centeno, C. Blanco, R. Santamaria, M. Granda, R. Menendez, G. Pintsuk, and J. Linke. Behaviour of Ti-doped 3D carbon fibre composites under intense thermal shock tests. *Phys. Scr.*, 2009(T138):014055, 2009.

[157] C. Garcia-Rosales, G. Pintsuk, C. Gualco, N. Ordas, I. Lopez-Galilea, J.M. Ramos Fernandez, M. Martinez Escandell, A. Centeno, C. Blanco, J. Linke, M. Grattarola, and F. Mataloni. Manufacturing and high heat-flux testing of brazed actively cooled mock-ups with Ti-doped graphite and CFC as plasma-facing materials. *Phys. Scr.*, 2009(T138):014062, 2009.

[158] M. Balden, J. Roth, and C.H. Wu. Thermal stability and chemical erosion of the silicon doped CFC material NS31. *J. Nucl. Mater.*, 258(Part a):740–744, 1998.

[159] I. Lopez-Galilea, N. Ordas, C. Garcia-Rosales, and S. Lindig. Improvement of thermal shock resistance of isotropic graphite by Ti-doping. *J.Nucl.Mater.*, 386-388:805–808, 2009.

[160] O. Stenzel. *Das Dünnschichtspektrum*. Akademie Verlag, Berlin, 1996.

[161] U. v Toussaint, T. Schwarz-Selinger, and C. Hopf. Bayesian analysis of ellipsometry measurements. *AIP Conference Proceedings*, 872:272–279, 2006.

[162] E.S. Gadelmawla, M.M. Koura, T.M.A. Maksoud, I.M. Elewa, and H.H. Soliman. Roughness parameters. *J. Mater. Process. Technol.*, 123(1):133–145, 2002.

[163] http:// gwiddion.net. Gwyddion.

[164] *Joined committee for powder diffraction studies - International centre for diffraction data (JCPDS ICDD), Powder diffraction file, Release 2000.*

[165] M. Birkholz. Thin Film Analysis by X-Ray Scattering. Wiley-VCH, Weinheim, 2006.

Appendix A

Characterization of the D beam profile

Beam profile characterization

Since the D beam is focused by a complex ion optic, a lateral variation of the fluence across the D beam is to be expected. Since, for instance, the D inventory in a-C:W depends on fluence, a lateral variation of the fluence across the D beam must result in a lateral variation of the D inventory across the specimen surface. In order to relate each D inventory measured at a position on the specimen to the fluence at the same position, the lateral variation of the fluence across the D beam needs to be known. Such a lateral variation across the D beam is denoted as the beam profile in the following.

In order to investigate the profile of 200 eV D beam, hydrogenated amorphous C layers produced by plasma-enhanced chemical vapour deposition with CH_4 precursor gas were used. Figure A.1 shows an erosion spot on a a-C:H layer after the D beam exposure with an accumulated ion charge of 0.6 Cb. The erosion spot is clearly distinguishable by changes

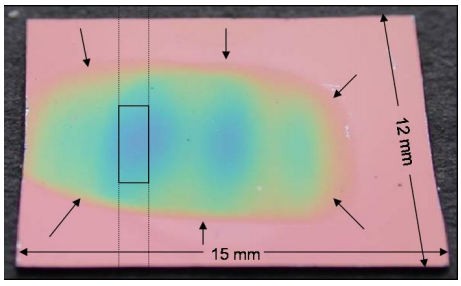

Figure A.1: Eroded a-C:H layer with a hydrogen content of 30% on Si plate of 12x15 mm^2 size is imaged on a dark background. The erosion spot covers a colour spectrum between yellow and near violet and is distinguishable from the outer, red areas of the specimen. The boundary of the erosion spot is marked by arrows and the area analysed by NRA by the dotted rectangle (1D scanned area of 1 mm width: dotted; reference area: solid). The reference zone is depicted by the solid rectangle.

of the interference colour of the transparent a-C:H layer. Here, the red colour from the original film changes to yellow and near violet. The wavelength difference between red and near violet is about 150-200 nm, corresponding to a maximal change of layer thickness of about 75-100 nm [160]. At the edge of the spot (marked by arrows in figure A.1) the sharp transition from yellow to red indicates a steep gradient. Inside the erosion spot inhomogeneities in thickness of about 25 nm are observable.

The erosion depth was determined by ellipsometry. A laser spot of 10x30 μm^2 size was scanned two dimensionally over the specimen area with a rectangular grid of 0.3 mm step width. The layer thickness of each pixel was calculated as described in [161].

In the framework of a test series, which was performed in order to check the reproducibility of the beam profile (figure A.1) over the measurement campaigns, five specimens were exposed to the same conditions up to the same fluence and analysed with ellipsometry. Two specimens were eroded on the same day, the third one after a week and a fourth one after two weeks. During this campaign the high current ion source was continuously running over two weeks at the same settings. The fifth one was eroded in a second campaign, two weeks after the first campaign. Between these two campaigns, the machine was running at different settings. By simple optical inspection only slight variations between the five erosion spots could be detected, mainly between the fifth specimen and the four other ones.

By comparing equivalent pixels with each other, the average thickness, the standard derivation and the relative error was calculated. This value gives a position dependent measure of the reproducibility of the beam profile. At areas exposed to high fluences in the central region of the erosion spot, according to colours between turquoise and violet, the relative error is not higher than 15%.

The area with a reproducible spot profile has a size of 30 mm^2, while the area surrounded by the steep gradient is about 70 mm^2. In three zones of the reproducible area a higher erosion depth is observable (erosion depths between 70 nm and 90 nm, corresponding to colours between blue and violet). Inside each of the three zones the lateral variation of the erosion depth is not bigger than 10%. The largest of these zones had an area of 6 mm^2. In each campaign, this zone was analysed and selected as a reference zone for data evaluation (figure A.1). In order to characterize the reference zone, the area and the position of the reference zone on the specimen as well as an averaged erosion depth over the reference zone were evaluated, valid for one campaign (under the assumption of a reproducible beam profile during one campaign). In this context, it should be mentioned here that the time span between the different campaigns was about two to three months. In between the high current ion source was running at different settings and the focusing of the ion optics was varied in some cases during maintenance, in order to vary the beam profile. It turned out that the averaged erosion depth over the reference zone did not change more than 9% over a period of two years. The position of the reference zone on the specimen and the area of the reference zone, however, changed in between different campaigns (the position changed by 2-4 mm along the 15 mm-edge and 1-3 mm along the 12 mm-edge; the area changed between 3 mm^2 and 25 mm^2).

In order to estimate the concentration of neutrals in the D beam, a thin W layer of 30 nm thickness, deposited on silicon substrate from W, evaporated by electron beam, was exposed to the D beam with an accumulated charge of 5.2 Cb. D_3^+ ions were accelerated with a bias of 3600 V. The target was biased with 3000 V. Since the sputtering threshold energy of W for D bombardment is 211.4 eV [100], the W layer is sputtered exclusively by the 1200 eV neutrals.

RBS with ^{4}He at 0.5 MeV was performed to obtain the amount of W atoms per unit area, both before and after the D beam exposure. The total amount of eroded W atoms was obtained from the difference between these two values.

Before the D beam exposure, the RBS analysing beam was scanned along both diagonals

of the specimen. With the obtained data, the initial thickness values were calculated over the whole specimen area. After the D beam exposure, the thickness values were measured over the whole specimen area, by applying a two dimensional scan with a rectangular grid of 1 mm step width.

Figure A.2 shows the 1200 eV erosion spot. The spot is extended over the whole specimen

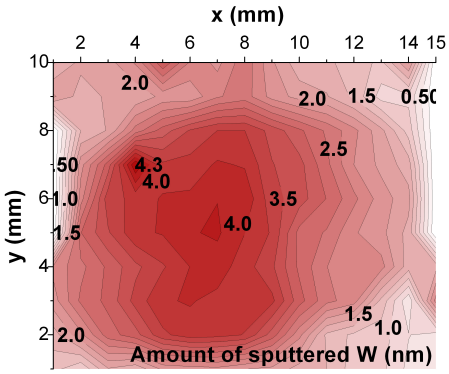

Figure A.2: Two dimensional plot of the amount of sputtered W in nm, sputtered by D neutrals in D ion beam with an accumulated charge of 5.2 Cb, obtained from the RBS analysis with ^{4}He at 0.5 MeV. The spot is extended over the whole analysed area of the specimen of 14 x 9 mm^2. The eroded thickness values show a low gradient from 0.5 nm to 4 nm.

area and shows a low gradient: The eroded thickness values at zones near the edge (0.5 nm) increase slightly towards the centre of the specimen (4 nm).

The fluence of neutrals at a unit area is the product of the sputter yield of W (about $6.4 \cdot 10^3$ at 1 keV/D and normal incidence [61]) and the averaged amount of sputtered W atoms per unit area. The concentration of neutrals at a unit area was obtained out of the ratio between the fluence of neutrals and the total fluence at this unit area. The concentration of neutrals was about 10%, averaged over the entire specimen area, and about 5% over the reference zone. However, at zones near the edge of the specimen, which are not affected by the D_3^+ ion beam, the concentration of neutrals was 100%.

Similar investigations were performed in [102] (about 10 years ago), by measuring the weight loss of a gold target at 60 eV D impact energy (180 eV D_3^+ ion beam). The concentration of neutrals over the specimen area was about 3%. The corresponding concentration of neutrals in this study (600 eV D_3^+ ion beam) is about 10%. Comparing these two results shows that the concentration of neutrals in the D beam changes with time.

Fluence distribution

By using the following considerations, the lateral fluence distribution can be derived from the erosion depth of the 200 eV beam spot on a-C:H.

Erosion processes lead to a decreased film thickness, since C atoms are removed by the incident D particles [143]. The decrease in film thickness is proportional to the number of removed C atoms. The number of removed C atoms depends on the number of incident particles and the erosion yield. Under the assumption of a constant erosion yield (D fluxes in the range of $(1\text{-}8) \cdot 10^{15}$ D/cm^{2}s [102], homogeneous a-C:H layer and incident angle), the

number of removed C atoms per unit area is directly proportional to the number of incident particles per unit area, namely the fluence.

For the accumulated charge of 0.6 Cb, by averaging the erosion depth over the reference zone, an average fluence of $2{\cdot}10^{19}$ D/cm^2 was determined with an accuracy of 8%. This leads to a calibration factor of $3.3{\cdot}10^{19}$ D$\cdot$cm$^{-2}\cdot$Cb^{-1} for the accumulated charge in the D retention experiment of a-C and a-C:W:

$$\Phi = 3.3 \cdot 10^{19} \frac{D}{cm^2 \cdot Cb} \cdot Q. \tag{A.1}$$

For instance, for a fluence of 10^{20} D/cm^2 a charge of 3.0 Cb needs to be accumulated. For a D_3^+ ion current of 35 μA a D beam exposure of $\sim$24 h is necessary. Comparison of equation (A.1) and equation (3.1) results in an effective area of 0.57 cm^2 for the erosion spot.

In each campaign, the calibration factor of the accumulated charge was evaluated anew. The variation of the calibration factor among the different campaigns is in convolution with the variation of the averaged erosion depth over the reference zone, which was 9% over a period of two years.

Appendix B

Generation of IBA data

Since the beam profile is reproducible during a campaign and specimens were adjusted well during the D beam exposure and the D beam exposure was performed at a fixed position, the reference zone can be allocated on each specimen exposed to the D beam. This is illustrated in figure B.1 (a). The erosion spot is visible as a dark area on a-C:W, exposed to a D beam with an accumulated ion charge of $\sim$3 Cb. The right edge of the specimen is in line with the right edge of the specimen holder. Furthermore, the position of each specimen was controlled by aligning the same edge of the specimens in the erosion experiment and in the analysing facility. Therefore, it was possible to hit the reference zone with the analysing beam. This is illustrated in figure B.1 (b). A photo of two specimens is depicted, eroded a-C:W and eroded a-C:H, mounted on the specimen holder of the tandem accelerator. In order to adjust the eroded a-C:W on the specimen holder of the tandem accelerator, first the eroded a-C:H was positioned over the specimen holder in such a way that the analysing beam, which runs along the middle of the specimen holder with a tread width of 1 mm, would cross the reference zone while scanning along the 12 mm edge of the specimen. a-C:W, which was the specimen destined for the analyses by the ion beam, was positioned on the specimen holder next to a-C:H, in such a way that the right edge of both specimens was aligned to the right edge of the specimen holder by the same distance.

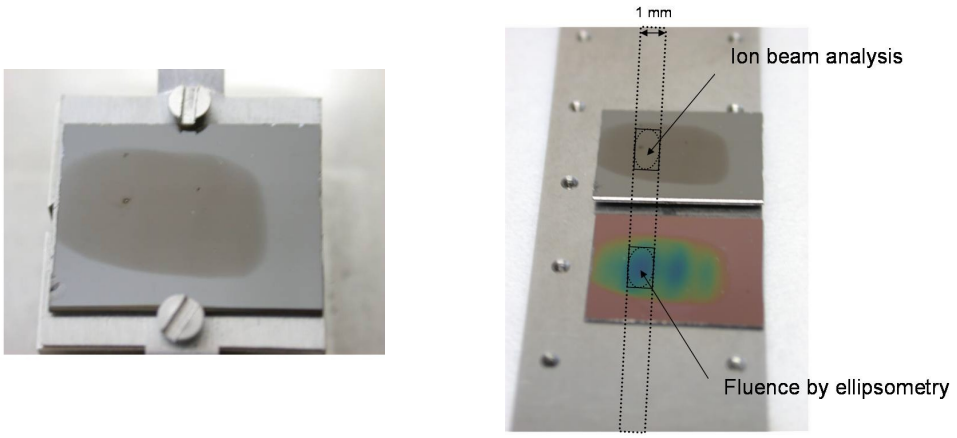

Figure B.1: Photos illustrating the positioning of specimens (eroded a-C:W and a-C:H on Si plate of 12 x 15 mm^2 size) on the specimen holder, (a) of the high current ion source, (b) of the tandem accelerator. Specimens were aligned with their right edge to the right edge of both specimen holders.

The positioning of the analysing area in the IBA experiment directly influences the error of the fluence value. Using the known distribution of the fluence (see subsection *Fluence distribution*) and assuming a half millimetre positioning error, the error of the fluence value increases from 8% to 16%.

In this context, it should be mentioned here that shape, area and position of the 200 eV beam spot and of the reference zone varied among the different measurement campaigns as already listed afore. Hence performing data evaluation over the 200 eV spot irrespective of the area and of the position of the reference zone the data will likely be obtained outside the reference zone. Despite the fact that the beam profile is not reproducible outside the reference zone, this must result in the wrong relation between the data, e.g. the D inventory, and the fluence. This means, the fluence at the position, at which data were obtained, must be different to the fluence obtained at the reference zone from the calibration factor of the accumulated charge given in equation (A.1); the positioning error increases above a half millimetre (2-4 mm along the 15 mm-edge and 1-3 mm along the 12 mm-edge) leading to a larger error of the fluence value. This is illustrated in figure B.2. The calibration value of the accumulated charge was calculated for different positions along the 15 mm-edge. The calculation of the calibration value was performed in the same manner as described in the subsection *Fluence distribution* (the calibration value is obtained from an averaged erosion depth), irrespective of the fact that the beam profile is not reproducible outside the reference zone. The averaged erosion depth for different positions along the 15 mm-edge was obtained by averaging those erosion depths along the 12 mm-edge, which were obtained at a rectangular area inside the 200 eV spot. This rectangular area is 1 mm in width and matches the extent of the 200 eV spot along the 12 mm-edge in length. This kind of averaging of the erosion depth takes the positioning error along the 12 mm-edge into account. The error of the fluence value at a position along the 15 mm-edge was estimated by comparing the calibration value of the accumulated charge at this position with the calibration value of the accumulated charge obtained at the reference zone. These estimations were performed for one specimen from the test series (see figure B.2 (a); photo depicted in figure A.1) and for another specimen exposed to the D beam one year later (see figure B.2 (b)). In figure B.2 (a) the reference zone is at 9.5-10.5 mm and the error of the fluence value obtained at the reference zone is 16%. Even at the position 9.5 mm the positioning error along the 12 mm-edge increases the error of the fluence value to 0.25. A similar error would be obtained at the second maximum of the calibration value, which is at 7 mm. Between these two maximums the error even increases to 0.3. In figure B.2 (b) the reference zone is at 7-9.5 mm. The error of the fluence value obtained at the reference zone is decreased to 3%. In this case, the effect of the positioning error along the 12 mm-edge is pronounced more strongly, e.g. at the position 9.5 mm the error is increased to 0.22. Between 4.5 mm and 9.5 mm, however, the calibration value is nearly constant and the error of the fluence value does not increase above 0.25. This means, a positioning error inside this range would be tolerable so that the effect of the positioning error along the 15 mm-edge on the error of the fluence value is milder, in contrast to the specimen mentioned afore.

Concluding, while the effect of the positioning error along the 15 mm-edge on the error of the fluence value is decreased for the specimen depicted in figure B.2 (b), the effect of the positioning error along the 12 mm-edge is considerable for both specimens depicted in figure B.2. Therefore, the knowledge of the area and of the position of the reference zone is a necessary condition, in order to calculate the fluence at the reference zone using the

calibration factor of the accumulated charge given in equation (A.1). Further to this, it needs to be mentioned that an averaging of the erosion depth over the entire area of the 200 eV spot - as it is performed relating the D inventory obtained by TDS to a fluence - reduces the calibration factor of the accumulated charge to 2/3. This results in an error for the fluence value of ∼0.3.

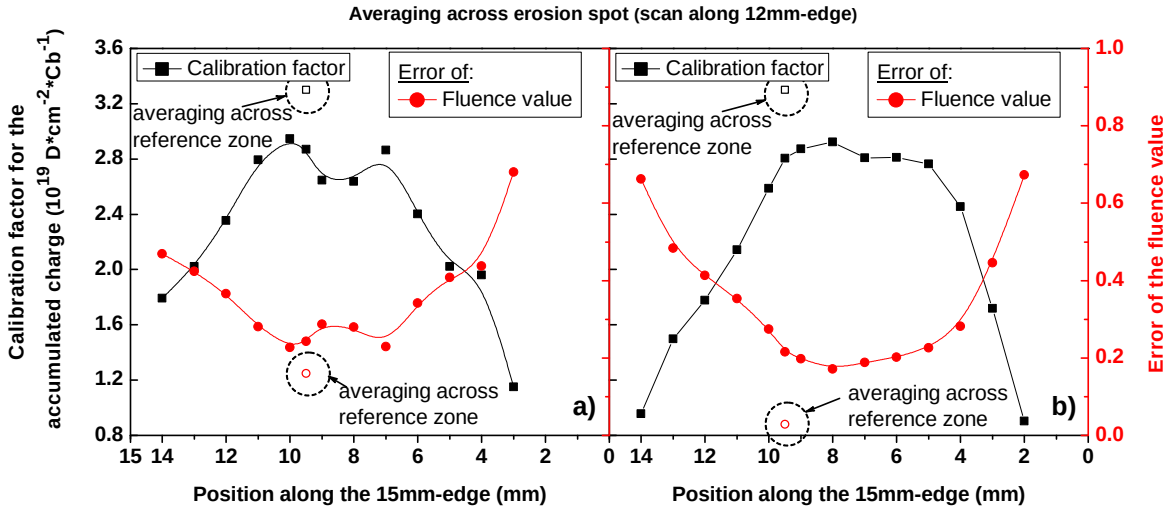

Figure B.2: Illustration of the dependence of the calibration factor of the accumulated charge (see equation A.1) and of the error of the fluence value on the position along the 15 mm-edge of the specimen, in (a) for the same a-C:H film as depicted in figure A.1 (the orientation of the 15 mm-edge matches in both figures; zero position is in line with the right edge of the specimen holders as depicted in figure B.1), in (b) for another a-C:H film exposed to the D beam one year later. Curves are a guide to the eye.

Appendix C

Evaluation of RBS and NRA spectra

Influence of target composition on peak fitting

SIMNRA converts energy spectra into depth profiles by means of a given stopping power (for the used projectile species at the incident energy) in each layer of a target. For a projectile species at an energy the stopping power depends on the composition of a target layer. The target, which shall describe a depth profile of D and a depth profile of W, consists of layers, containing W, C and D. Consequently, the shape of the RBS spectrum not only depends on the W depth profile but also on the D depth profile. This means, not only the concentration of W and of C need to be adapted in each target layer, so that it is possible to find a fitting curve for the RBS spectrum, but also for the D concentration. In a RBS spectrum, however, no peak exists, which originates from D. Therefore, it is not possible to adapt D concentrations. The shape of a NRA spectrum, on the other hand, not only depends on the D depth profile but also on the W depth profile. This means, not only the concentration of D needs to be adapted in each target layer, so that it is possible to find a fitting curve for the NRA spectrum, but also the W concentration. In a NRA spectrum, however, the peak originating from W is not resolvable. Therefore, the W concentration can not be adapted. Consequently, it needs to be determined whether it is possible to neglect the W depth profile converting a NRA spectrum into a D depth profile and vice versa. It is supposed that the influence of the W depth profile on the shape of the NRA spectrum can be neglected, if changes of the stopping power due to changes of the W concentration can be neglected in each target layer. It is also supposed that the influence of the D depth profile on the shape of the RBS spectrum can be neglected, if changes of the stopping power due to changes of the D concentration can be neglected in each target layer. Note, a maximal difference in the stopping power leads to a maximal difference in the energetic loss and, neglecting differences in energetic loss straggling, to a maximal change for the thickness of a target layer. The change of stopping power of ^{4}He (projectile in W(^{4}He,^{4}He)W, ejectile in D(^{3}He,^{4}He)p) was estimated for different compositions of a target layer, containing W, C and D. These estimations were carried out with the help of data bases of elemental stopping powers given in literature, e.g. Ziegler-Biersack stopping [130]. Elemental stopping powers can be used to describe stopping in compounds. In "Bragg′s rule" elemental stopping powers are weighted with the atomic concentration of each component before superposition [126]. For the RBS spectrum stopping powers were evaluated for the enrichment zone, containing 70% W and by varying the D concentrations (0.5%-30%), in an energy range between 0.5 MeV and 1 MeV. For the NRA spectrum the D concentration was

fixed at 30% and the W concentration was varied between 10% and 70%, in an energy range between 2 MeV and 3 MeV. Note, energy ranges mentioned match that energy ranges of a RBS and a NRA spectrum, respectively, which contains the peak to be fitted.

Results are illustrated in figure C.1. The stopping power in different C-W-D compounds

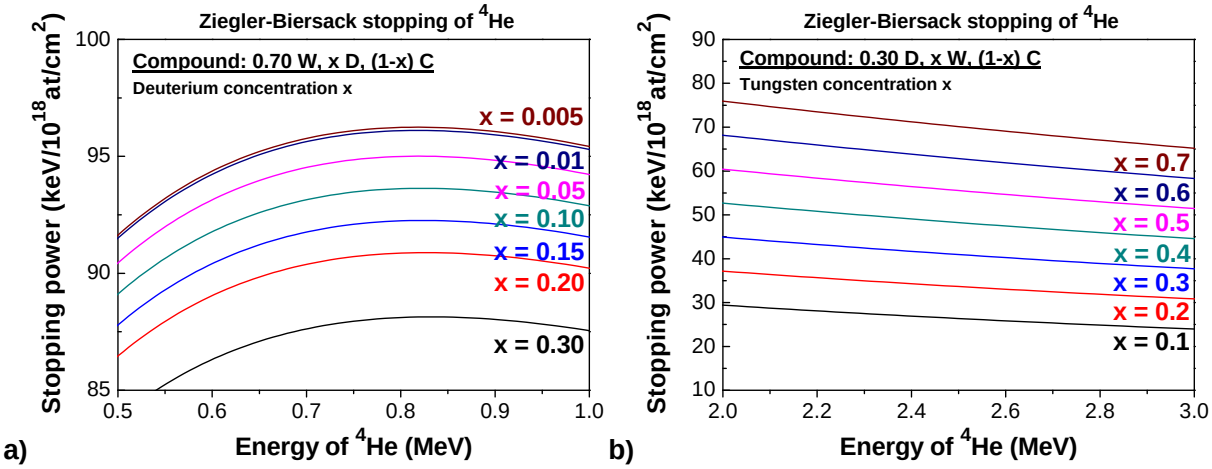

Figure C.1: Ziegler-Biersack stopping of ^{4}He in a C-W-D compound [130]; elemental stopping powers were weighted with the atomic concentration of each component before superposition. In (a) the W concentration is fixed at 70% and the D concentration is varied against C, between 0.5% and 30%. In (b) the D concentration is fixed at 30% and the W concentration was varied against C, between 10% and 70%.

is plotted over the energy of the alpha particles. Energy ranges and compositions are different among the two graphs. Figure C.1 (a) shows stopping powers for a W enrichment zone (70% W), containing different D concentrations (0.5%-30%), for a projectile energy between 0.5 MeV and 1 MeV. A series of curves is visible; the stopping power decreases with increasing D concentration, since C has a higher stopping power than D. Each of these curves has a maximum between 0.8 MeV and 0.85 MeV. The largest difference between the curves is found in this energy range. Increasing the D concentration from 0.5% to 30% decreases the stopping power by about 8 keV/10^{18} at/cm^2, from 96 keV/10^{18}at/cm^2 to 88 keV/10^{18}at/cm^2. This means, the relative derivation of the stopping power among different compounds is not larger than 4.5%. Consequently, it can be assumed that for D concentrations below 30% the D depth profile has no significant effect on the shape of the RBS spectrum, i.e. C and D can be removed against each other without changing the shape of the calculated RBS spectrum significantly. A RBS spectrum can be fitted without the addition of D to any target layer. In the case of a NRA spectrum, however, the situation is quite different. Figure C.1 (b) shows stopping powers in a W enrichment zone with varying W concentrations (10%-70% W), containing a fixed D concentration of 30%, for an ejectile energy between 2 MeV and 3 MeV. For the series of curves the stopping power slightly decreases with increasing ejectile energy. Among the curves of the series the stopping power clearly increases with increasing W concentration, i.e. W dominates the stopping power in the C-W-D compound. The lowest difference between the curves is at 3 MeV. Increasing the W concentration from 10% to 70% increases the stopping power by about 42 keV/10^{18}at/cm^2, from 24 keV/10^{18}at/cm^2 to 66 keV/10^{18}at/cm^2. By comparing the stopping power in an initial specimen without a W enrichment zone (W content of 10%) and a specimen with an enrichment zone, containing pure W (W content of 70%), the relative derivation of the stopping power is at least 46%. Conse-

quently, the shape of the NRA spectrum is significantly influenced by the W concentration in the enrichment zone. It is not possible to convert a NRA spectum into a depth profile of D without the knowledge of the depth profile of W. Consequently, in order to investigate the diffusion depths of D, W depth profiles need to be investigated first.

Influence of target composition on depth resolution

In order to convert an energy spectrum of alpha particles into a depth profile, the depth resolution needs to be known. This is the smallest distance, which enables two depths to be distinguished. The depth resolution, which depends on target composition and experimental setup, can be estimated by using RESOLNRA software [133]. This software calculates the depth resolution versus the depth for the same target composition and a given experimental setup, which were used to fit the NRA and the RBS spectra by SIMNRA software. Therefore, the uncertainty for a depth is given by the depth resolution at depth. Note that RESOLNRA gives depth resolution and depth in the unit 10^{18} at/cm^2. The unit 10^{18} at/cm^2 can be converted into the unit nanometre, by using the literature data of atomic densities given in [127] ($1{\cdot}10^{18}$ at/cm^2 equals 88 nm for C and 158.3 nm for W; assuming a dense material).

In order to distinguish the depth from the surface, for instance, a detected particle must have emerged from a depth, which is larger than the depth resolution at depth. The depth, which is just larger than the depth resolution at depth, is be denoted as the resolvable depth in the following. The resolvable depth can just be distinguished from the surface and significant signals emerge from depths larger than the resolvable depth.

Depth resolution for NRA on hard a-C:D

For the first step, the resolvable depth was estimated for a NRA spectrum of a target, which has a composition similar to a-C:D (C target, containing 40% D). The result obtained from RESOLNRA was compared to another method (see description below). This comparison leads to a range of values, which gives an overall estimation concerning magnitudes.

For the NRA spectrum of a-C:D (C target, containing 40% D) the resolvable depth was estimated to be $\sim$100 nm ($\sim 0.9{\cdot}10^{18}$ at/cm^2). This is illustrated in figure C.2. The depth resolution is plotted versus the depth. Additionally, a line through the origin is inserted, which has a slope of one (dashed line). The resolvable depth can be read off from the intersection between the dashed line and the depth resolution.

For comparison, three specimens of hard a-C:D of different thickness (16 nm, 78 nm, 151 nm) were produced and analysed by applying the 800 keV D(^{3}He,^{4}He)p nuclear reaction. In a-C:D, D is distributed homogeneously [88] and the content can be adapted quite well by the parameter choice of the PECVD process [88]. The ratio between D and C in so called hard a-C:D is $\sim$0.4. The density of C atoms per unit volume is $\sim 9{\cdot}10^{22}$ at/cm^3. Cross-checks of the D amount and the film thickness can be obtained by the D(^{3}He,p)^{4}He reaction and profilometry, with an accuracy of 25% and $\pm$5 nm (= $0.045{\cdot}10^{18}$ at/cm^2, under the assumption of a constant number density of $\sim 9{\cdot}10^{22}$ at/cm^3 for C in a-C:D), respectively.

For each film it was tested whether it is possible to fit the energy spectra of the alpha particles by applying SIMNRA software. The D amount and the film thickness were chosen as input parameters. Figure C.3 depicts SIMNRA fits on the experimental data for each film. For the dashed curves, data were fitted with the input parameters. For each film the

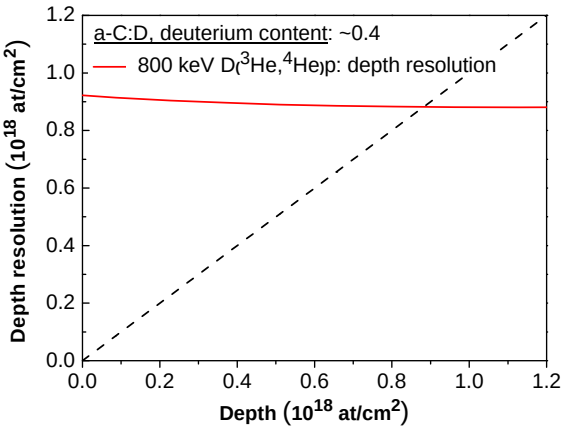

Figure C.2: Depth resolution versus the depth, of the 800 keV D(^{3}He,^{4}He)p nuclear reaction at 102° on a C target, containing 40% D, obtained from RESOLNRA [133]. The resolvable depth can be read off from the intersection between the dashed line and the depth resolution (solid curve) ($\sim 0.9 \cdot 10^{18}$ at/cm^2).

simulated NRA spectrum shows a peak with a lower width and a larger maximum compared to the experimental NRA spectrum. For the dash-dotted curves, input parameters were changed, in order to find the best fit. Therefore, the thickness values were increased and the D content was decreased. The NRA spectrum of a film of 151 nm thickness (D amount of $6.0 \cdot 10^{17}$ D/cm^2) was fitted successfully, increasing the thickness by 5 nm and decreasing the D content by 10%. This is within the framework of accuracies for the D amount and the film thickness mentioned above. The NRA spectrum of a film of 78 nm thickness (D amount of $3.1 \cdot 10^{17}$ D/cm^2) was fitted successfully, increasing the thickness by 5 nm and decreasing the D content by $\sim$20%. This is just within the framework of accuracies mentioned above. The NRA spectrum of a film of 16 nm thickness (D amount of $6.4 \cdot 10^{16}$ D/cm^2) was not fitted successfully. For the fit curve in figure C.3 (c) the film thickness was increased by 5 nm and the D content was decreased by 37%. This exceeds the framework of accuracies mentioned above. This means, the measured spectrum of the film of 16 nm thickness is smeared out compared to the fit curve, even for the best fit within the framework of accuracies for thickness and D content.

Concluding, the NRA spectrum of the a-C:D of 151 nm thickness and of the a-C:D of 78 nm thickness is resolvable, while the thickness of the latter film seems to be just resolvable. For the film of 16 nm thickness the NRA spectrum is smeared out and thus not resolvable. Therefore, the resolvable depth is between 78 nm and 151 nm. This result is in the same range as obtained from RESOLNRA ($\sim$100 nm), and thus RESOLNRA gives reasonable results for the depth resolution.

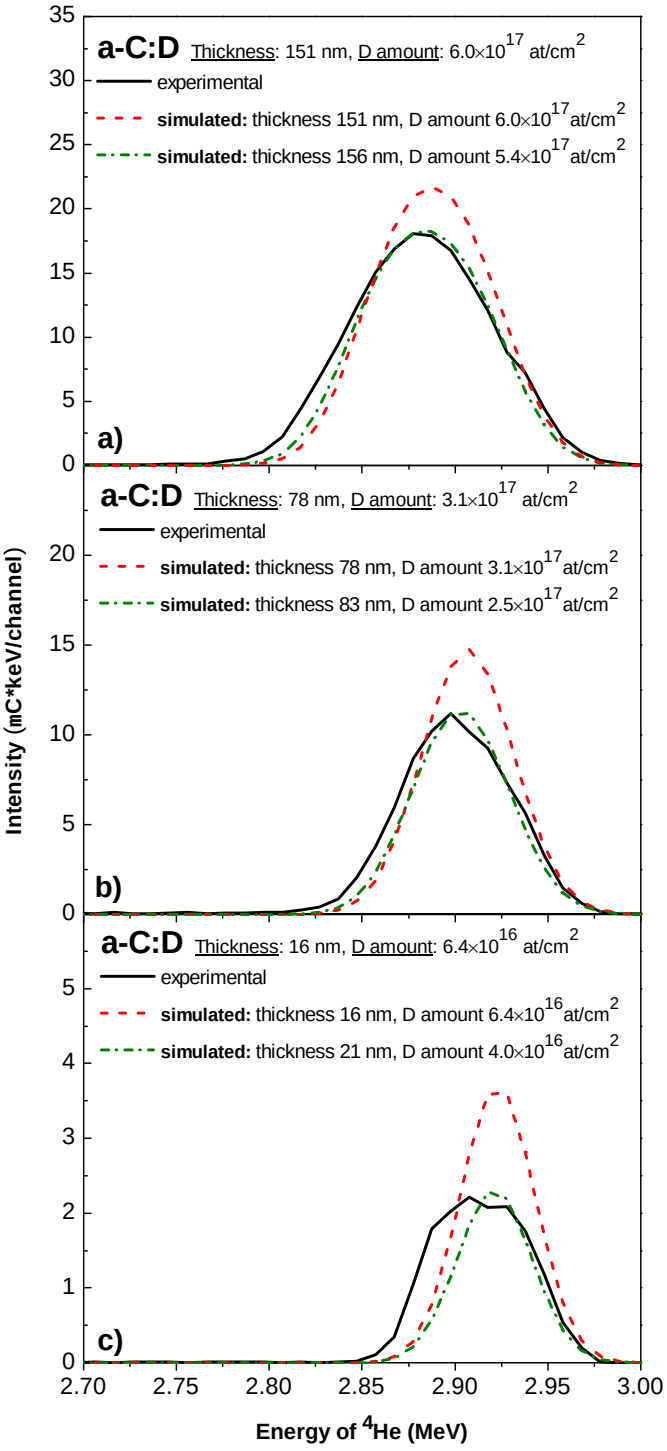

Figure C.3: SIMNRA fits on the energy spectrum of alphas out of the 800 keV D(^{3}He,^{4}He)p nuclear reaction on three a-C:D specimens of different thickness and D content. (a): 151 nm, $6.0 \cdot 10^{17}$ D/cm^2; (b): 78 nm, $3.1 \cdot 10^{17}$ D/cm^2; (c): 16 nm, $6.4 \cdot 10^{16}$ D/cm^2. For the dashed curves data were fitted with the input parameters. For the dash-dotted curves input parameters were changed, in order to find the best fit.

Depth resolution for RBS and NRA on enriched a-C:W

In the second step, the resolvable depths for the NRA and the RBS spectra were estimated, by varying the target composition (the W and the D concentration) in a range, which is of relevance for the depth profiles of W and D in a-C:W. This gives an overview over the influence of target composition and layer thicknesses in a-C:W on the depth resolution of NRA and RBS spectra, on one hand, and results in an estimation regarding ranges of resolvable depths in a-C:W, enriched with W, on the other hand. Values resulting from these estimations were used, in order to find a start parameter for the thickness of the enrichment zone and for the diffusion depth, in fitting the RBS and the NRA spectra with SIMNRA (see subsection *Peak fitting*). For these estimations the influence of surface roughness was neglected.

Figure C.4 plots the depth resolution of the RBS spectra versus the depth, inside a W enrichment zone, containing different W and D concentrations. The resolvable depth can be read off from the intersection between the dashed line and the depth resolution. A set of curves is visible, which has a small increase versus the depth. Curves of this set clearly shift with the W concentration, so that the resolvable depths are clearly distinguishable.

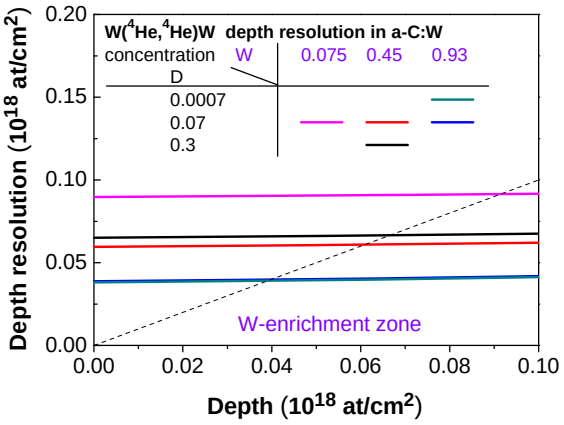

Figure C.4: Depth resolution of the 1 MeV W(^{4}He,^{4}He)W RBS process at 165° on a-C:W for different W and D concentrations, obtained from RESOLNRA [133]. The resolvable depth can be read off from the intersection between the dashed line and the depth resolution (solid curve).

The resolvable depth of the RBS spectra decreases with increasing W concentration, from $\sim 0.09 \cdot 10^{18}$ at/cm^2 (8 nm) to finally $\sim 0.04 \cdot 10^{18}$ at/cm^2 (6 nm). The latter value is just below the width of the ion range of a 200 eV D beam in W ($\sim$6.3 nm [99]). Variations in the D concentration below 30% change the resolvable depth less than $\sim$5%. The resolvable depth inside the enrichment zone is dominated by the W content. Since the width of the W enrichment zone is expected to be close to the width of the ion range, it is not possible to evaluate a depth profile of the W concentrations inside the enrichment zone. Consequently, a maximal extent into depth and an average W concentration can be found for the W enrichment zone.

Figure C.5 plots the depth resolution of the NRA spectra versus the depth for a W enrichment zone of a thickness of $1 \cdot 10^{18}$ at/cm^2, containing different W and D concentrations. In figure C.5 (a) the depth resolution inside the W enrichment zone is plotted and in figure C.5 (b) the depth resolution is plotted for depths extending beyond the W enrichment zone. Regarding the NRA spectra, the resolvable depth is larger. The resolvable depth

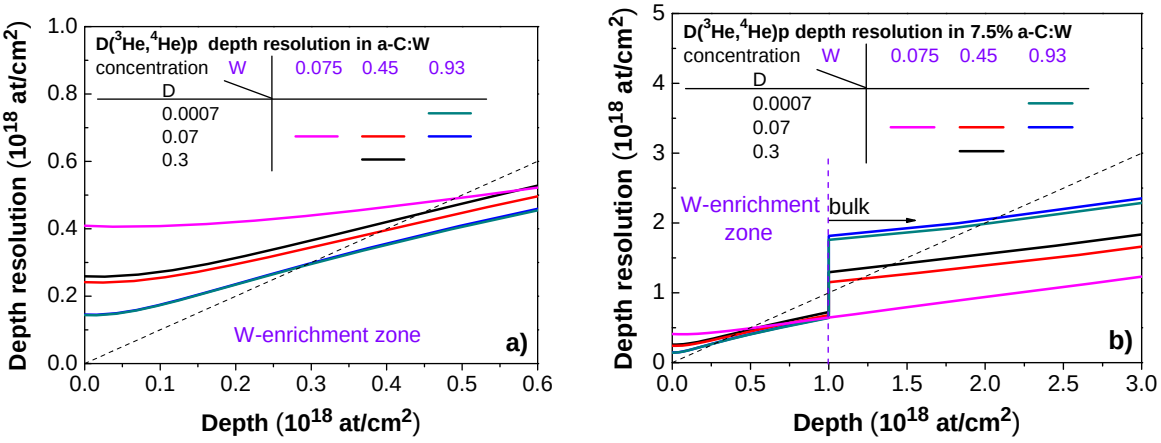

Figure C.5: Depth resolution of the 800 keV D(^{3}He,^{4}He)p nuclear reaction at 102° on 7.5% a-C:W for different D concentrations and for a W enrichment zone, containing different W concentrations, obtained from RESOLNRA [133]. The thickness of the W enrichment zone is $1{\cdot}10^{18}$ at/cm^2. In (a) a the W enrichment zone is magnified. The resolvable depth can be read off from the intersection between the dashed line and the depth resolution (solid curve).

of the NRA spectra inside the W enrichment zone decreases with increasing W concentration, from $\sim 0.49{\cdot}10^{18}$ at/cm^2 (46 nm) to finally $\sim 0.29{\cdot}10^{18}$ at/cm^2 (27 nm). Variations of the D concentration below 30% change the resolvable depth less than ~5%. The resolvable depth inside the enrichment zone is dominated by the W content. Each value is clearly above the width of the ion range of a 200 eV as well as of a 1.2 keV D beam in W. Therefore, it can not be distinguished between D trapped in the implantation zone and D diffused into depths, which are just below the resolvable depth. In contrast to the case mentioned, the resolvable depth for depths beyond the enrichment zone increases above $\sim 0.49{\cdot}10^{18}$ at/cm^2 (46 nm) with increasing W concentration, to finally $\sim 2.08{\cdot}10^{18}$ at/cm^2 (320 nm). Beyond the W enrichment zone the influence of the D concentration on the resolvable depth is more strongly pronounced. Therefore, the depth resolution of the NRA spectra is dominated by the W content inside the enrichment zone and by the overall D content. In this case, it can not be distinguished between D trapped in the W enrichment zone and D diffused into depths, which are just below the resolvable depth. Consequently, a maximal diffusion depth and an average D concentration can be found for D trapped in depths below the resolvable depth.

Since the width of the W enrichment zone is expected to be close to the width of the ion range, the resolvable depths of the NRA spectra were evaluated for a thickness of the W enrichment zone, which is lower than the resolvable depths inside the W enrichment zone, e.g. $0.2{\cdot}10^{18}$ at/cm^2. Figure C.6 plots the depth resolution of the NRA spectra versus the depth for different W concentrations in the enrichment zone and for different D concentrations. In contrast to the case mentioned, the NRA spectrum is not resolvable inside the W enrichment zone. The resolvable depths are larger than the width of the W enrichment zone. The resolvable depth increases above $\sim 0.49{\cdot}10^{18}$ at/cm^2 (46 nm) with increasing W concentration, to finally $\sim 0.87{\cdot}10^{18}$ at/cm^2 (130 nm). These values are between the values found for the W enrichment zone of a thickness of $1{\cdot}10^{18}$ at/cm^2. The influence of the D concentration on the resolvable depth is pronounced in this case as well. This means, the resolvable depths, which are larger than the width of the W enrichment zone, are also affected by the D content; the depth resolution of the NRA spectra is dominated

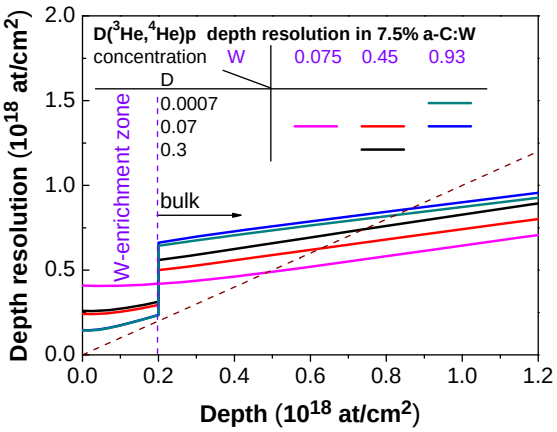

Figure C.6: Depth resolution of the 800 keV D(^{3}He,^{4}He)p nuclear reaction at 102° on 7.5% a-C:W for different D concentrations and for a W enrichment zone, containing different W concentrations, obtained from RESOLNRA [133]. The thickness of the W enrichment zone is $0.2{\cdot}10^{18}$ at/cm^2. The resolvable depth can be read off from the intersection between the dashed line and the depth resolution (solid curve).

by the W content inside the enrichment zone and by the D content. In general, it can not be distinguished between D trapped in the W enrichment zone and D diffused into depths, which are just below the resolvable depth. Again, a maximal diffusion depth and an average D concentration can be found for D trapped in depths below the resolvable depth. This maximal diffusion depth is larger than the width of the ion range and the width of the W enrichment zone. Note, the resolvable depths evaluated for this case are in the range of the values obtained for a-C:D (∼100 nm).

In conclusion, the resolvable depth of an RBS spectrum just depends on the composition of the W enrichment zone and obtains its minimum for a W enrichment zone, containing 100% of W. Therefore, in converting a RBS spectrum into a depth profile of W, a W concentration of 100% was chosen as start parameter for the composition of the W enrichment zone; the start parameter for the thickness of the enrichment zone is given by the resolvable depth for a W enrichment zone, containing 100% of W (∼5 nm; see figure D.1).

A comparison of the results obtained for the $0.2{\cdot}10^{18}$ at/cm^2 thick and the $1{\cdot}10^{18}$ at/cm^2 thick enrichment zone shows that the thickness of the enrichment zone has the strongest influence on the depth resolution of a NRA spectrum, besides the influence of the W concentration; the influence of the D concentration can be neglected, for D concentrations below 30%. Therefore, the resolvable depth may exceed values obtained for a-C:D with increasing thickness of the W enrichment zone. In converting a NRA spectrum into a depth profile of D, the start parameter for the diffusion depth is given by the resolvable depth of the NRA spectrum, which depends on thickness and composition of the W enrichment zone. The resolvable depth can be estimated by the resuts given in figures C.5 and C.6.

The resolvable depth of a NRA spectrum always obtains larger values than that of a RBS spectrum for the same target layer. Generally it is not possible to distinguish between D trapped within the width of the ion range and D trapped in the depth. Further to this, if the width of the W enrichment zone is smaller than the resolvable depth of a NRA spectrum, it is not possible to distinguish between D trapped inside the enrichment zone and D trapped in the depth. Nevertheless, D diffused into depths larger than 200 - 300 nm can always be

distinguished from D trapped within the enrichment zone.

In the third step, the resolvable depth was estimated for the NRA and the RBS spectra of those a-C:W, which were implanted at different temperatures (300 K - 1300 K) and analysed with regard to the depth profiles of W and D (see sections 4.1 *Enrichment of W: Depth profiles* and 5.1 *Diffusion of D: Depth profiles*). For each of these specimens the depth profiles of W and D will be discussed by taking the respective value of their resolvable depth into account.

Peak fitting

The RBS and the NRA spectra were converted into the depth profiles of W and D using SIMNRA software [125]. The following procedure was performed finding one target, which describes the NRA spectrum and the RBS spectrum of a specimen:

Layer composition of the target

In the previous subsection, it was shown that for a W and for a D depth profile only a maximal extent into depth and an average W and an average D concentration can be found, respectively. Therefore, the target, which describes a W and a D depth profile, was composed of three layers, covering the silicon substrate. This is illustrated in figure C.7. The silicon

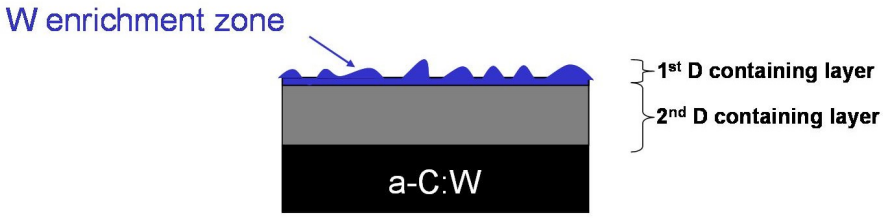

Figure C.7: Sketch illustrating the layer composition of the target used to fit the RBS and the NRA spectra.

substrate is covered by an a-C:W layer which is not affected and thus exhibits its initial film composition. The unaffected a-C:W layer is covered by a D-containing layer which describes the D depth profile by means of a thickness and an average D concentration. It can be divided into two sub-layers, containing equal D concentrations. Among these sub-layers, the surface near layer (1^{st} D-containing layer) describes the W enrichment zone by means of a thickness and an average W concentration. In case of D trapped in depths beyond the resolvable depth, the 2^{nd} D-containing layer was divided into further sub-layers with a different D concentration.

In taking the influence of surface roughness for the case of an eroded a-C:W into account, the specimen is supposed to consist of a rough surface layer, the W enrichment zone, on a smooth substrate, the second D-containing sub-layer. In this case, SIMNRA approximates the spectrum of a rough film by a superposition of N spectra with different layer thicknesses (thickness distribution) [127]. The calculation is performed by a distribution function for the layer thickness, e.g. the Gaussian distribution or the Gamma distribution, which is characterized by a mean thickness value and a full width at half maximum (FWHM; in the

following called FWHM of the surface roughness). The mean thickness corresponds to the thickness of the W enrichment zone and the FWHM of the surface roughness is an additional fit parameter. The start value of the FWHM of the surface roughness was obtained from AFM measurements. For a rough surface portions of the enrichment zone may exhibit lower widths than the resolvable depth. At those portions of the enrichment zone W at depth can not be distinguished from W at the surface. In order to compare the resolvable depth with the width of the enrichment zone, the FWHM of the surface roughness was taken into account. A RBS spectrum was supposed to be resolvable if the difference between the width of the enrichment zone and the half value of the FWHM of the surface roughness is larger than the resolvable depth of the RBS spectrum.

Fit procedure

The conversion of spectra into depth profiles was performed in two steps. For the first step, the RBS spectrum was converted into a depth profile of W without adding D to the target (as mentioned above, the influence of D on the peak shape can be neglected). In the second step, the same target was used converting the NRA spectrum into a depth profile of D. Therefore, a portion of the C atoms was removed by the D atoms and the concentration of W atoms was held constant in each layer.

For each of these two steps, the depth resolution was taken into account. This is illustrated in figure C.8 for the case of the RBS spectra; the procedure described in the following was also performed in fitting a NRA spectrum by means of a diffusion depth and a D concentration. The Simulated and the measured RBS spectra are plotted as intensity

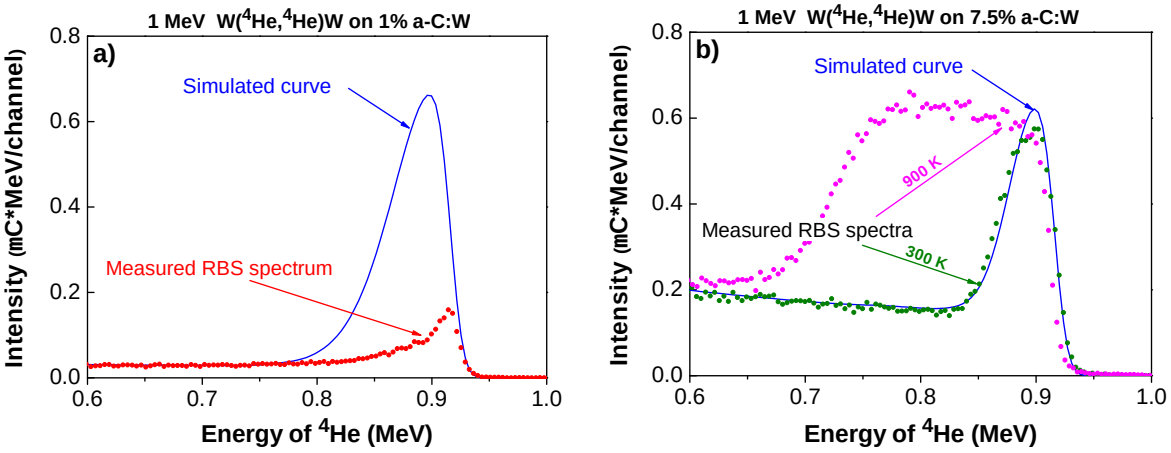

Figure C.8: Illustration of the depth resolution of the 1 MeV W(^{4}He,^{4}He)W RBS process at 165° on a-C:W. The simulated and the measured RBS spectra are plotted over the energy of backscattered alpha particles. Simulated curves were calculated for a certain W enrichment zone (93% W, 7% D; the thickness matches the sum of the resolvable depth for this composition ($0.04 \cdot 10^{18}$ at/cm^2; see previous subsection) and the half of the the FWHM of the surface roughness ($0.05 \cdot 10^{18}$ at/cm^2 in (a), $0.025 \cdot 10^{18}$ at/cm^2 in (b); obtained from AFM)). The RBS spectra were obtained from (a) 1% a-C:W (implanted at 300 K), (b) 7.5% a-C:W (implanted at 300 K and 900 K).

(counts normalized on the accumulated charge and the channel width) over the energy of backscattered alpha particles, in a range between 0.6 MeV and 1.0 MeV. The simulated

curves were calculated for a W enrichment zone, containing 93% W and 7% D, i.e. a pure W enrichment zone implanted with D; the thickness matches the sum of the resolvable depth for this composition ($0.04 \cdot 10^{18}$ at/cm^2; see previous subsection) and the half of the FWHM of the surface roughness ($0.05 \cdot 10^{18}$ at/cm^2 in (a), $0.025 \cdot 10^{18}$ at/cm^2 in (b); obtained from AFM). The RBS spectrum in figure C.8 (a) was obtained from 1% a-C:W. The RBS spectra in figure C.8 (b) were obtained from two specimens of 7.5% a-C:W. Each specimen was implanted at a fluence of 10^{20} D/cm^2. One 7.5% a-C:W was implanted at 900 K and the other 7.5% a-C:W was implanted at 300 K. A spectrum is supposed to be resolvable, if the resolvable depth is smaller than the difference between the thickness of the W enrichment zone and the half of the FWHM of the surface roughness. This criterion can be applied in this graph, by comparing peak width of a measured spectrum with the peak width of the calculated curve. In figure C.8 (a) the RBS spectrum has a lower peak width than the calculated curve. This means, in fitting the RBS peak of the 1% a-C:W, one must choose a lower thickness of the W enrichment zone as the thickness of the calculated peak. In this case, arbitrary combinations of thickness and composition of the W enrichment zone are possible. Therefore, the RBS spectrum of the 1% a-C:W is obviously not resolvable. In figure C.8 (b) the peak with the largest width belongs to the RBS spectrum of the 7.5% a-C:W implanted at 900 K. This means, in fitting the RBS peak of the 7.5% a-C:W implanted at 900 K one must choose a larger thickness of the W enrichment zone as the thickness of the calculated peak. Therefore, the RBS spectrum of the 7.5% a-C:W implanted at 900 K is expected to be resolvable. The thicknesses of the peak of the calculated curve and of the 7.5% a-C:W implanted at 300 K are close together. For the 7.5% a-C:W implanted at 300 K the thickness of the enrichment zone is close above the thickness of the calculated curve, i.e. the RBS spectrum is expected to be just resolvable.

However, the depth resolution is changed slightly after adapting the peak intensity by means of the composition of the enrichment zone. For instance, a decrease of the W concentration in the enrichment zone from 100% to 15% results in an increase of the depth resolution from $\sim$5 nm to $\sim$8 nm. In case of a W enrichment zone, which contains a lower W concentration as 100% and which obtains a width between $\sim$5 nm and $\sim$8 nm, the W peak in the RBS spectrum is not resolvable. In general, care should be taken for a layer thickness, which matches the resolvable depth. In this case, it can not be distinguished between a RBS spectrum, which is just resolvable, and a RBS spectrum, which is just unresolvable. In order to ensure that a RBS spectrum is still resolvable after the fitting of the W peak, the resolvable depth was evaluated again for that composition of the W enrichment zone, which was obtained from the fitting of the W peak. This value was finally compared to the final thickness of the W enrichment zone. In this context, this resolvable depth must again obtain a lower value than the final thickness of the W enrichment zone minus the half of the FWHM of the surface roughness.

Note that the latter step is not necessary for the conversion of a NRA spectrum into a depth profile of D, since the effect of the D concentration on the resolvable depth of a NRA spectrum can be neglected (see previous subsection). For the conversion of a NRA spectrum into a depth profile of D the diffusion depth needs to be larger than the resolvable depth for the D peak as well. For that value an average D content can be found.

For the W enrichment zone a maximal extent into depth and an average W content can be found. In many cases, it is not possible to find a distribution of the D content inside

the W enrichment zone. Analogous, an average D content and a maximal extent into depth can be found, which is always larger than the thickness of the W enrichment zone.

Summary

As already explained afore (see subsection *Influence of target composition on peak fitting*), while the D depth profile has no significant effect on the shape of the RBS spectrum, for D concentrations of 30% and below, the shape of the NRA spectrum is significantly influenced by the W concentration in the enrichment zone. Therefore, the RBS spectrum was converted into a depth profile of W, first, and then the NRA spectrum was converted into a depth profile of D.

The evaluation of the depth profiles of W and D was performed in two steps: For the first step, surface roughness was investigated for each specimen from the temperature series (see appendix E *Surface morphology: Roughening*), in order to study the influence of roughness on the shape of the energy spectra and the influence of roughness on depth resolution. In the second step, a RBS/NRA spectrum was converted into a depth profile of W/D in that manner, which is described in subsection *Peak fitting*, if it was supposed to be resolvable and if the influence of roughness on its shape was supposed to be negligible. In order to get a comparison for the widths of the enrichment zone obtained from the RBS spectra, a cross section SEM was performed once at the surface of a specimen. In cross section SEMs the enrichment zone is visible as a bright area on top of a dark area (film).

Appendix D

Depth resolution of RBS and NRA spectra

Depth resolution of RBS spectra

The depth resolution of the 1 MeV W(^{4}He,^{4}He)W RBS process at 165° on a-C:W was evaluated applying RESOLNRA [133] for the W concentrations given in the inlet of figure 4.1. Figure D.1 plots the depth resolution of the temperature series versus the depth for a thickness of the W enrichment zone of $0.1 \cdot 10^{18}$ at/cm^2 (each W concentration is assigned to a temperature, given in the inlet). The resolvable depth can be read off from the intersection between the dashed line and the depth resolution. The deuterium (D) content was neglected; surface roughness is not taken into account in the routines of RESOLNRA [133]. A set of curves is visible, which has a small increase over the thickness of the W enrichment zone. Curves in this set clearly shift with the W concentration, so that the resolvable depths are clearly distinguishable. The resolvable depth increases with decreasing W concentration from $0.031 \cdot 10^{18}$ at/cm^2 (4.8 nm) to $0.055 \cdot 10^{18}$ at/cm^2 (6.1 nm). These values are just below the width of the ion range of a 200 eV D beam in pure W (6.3 nm). Since the increase of the curves with thickness is low, the uncertainty for the thickness of the W enrichment zone is about equal the resolvable depth (∼5 - 6 nm). Neglecting surface roughness, W at the depth can be distinguished from W at the surface for each RBS spectrum of the temperature series, since the thickness of the enrichment zone is expected to be equal or larger than the width of the ion range of a 200 eV D beam.

Depth resolution of NRA spectra

The depth resolution of the 800 keV D(^{3}He,^{4}He)p nuclear reaction at 102° on a-C:W was evaluated applying RESOLNRA [133] for the D concentrations given in the inlet of figure 5.2 and the corresponding thickness and composition of the W enrichment zone (see figure 4.2). Since for the thickness of the W enrichment zone only a range can be given at 300 K and at 700 K (6.3 nm - 16 nm), the depth resolution was calculated once for a thickness of ∼6 nm (300 K) and once for a thickness of ∼16 nm (700 K). Figure D.2 plots the depth resolution of the temperature series versus the depth, in a range between $0.4 \cdot 10^{18}$ at/cm^2 and $1.4 \cdot 10^{18}$ at/cm^2, beyond the W enrichment zone. A set of curves is visible, which clearly shifts with thickness

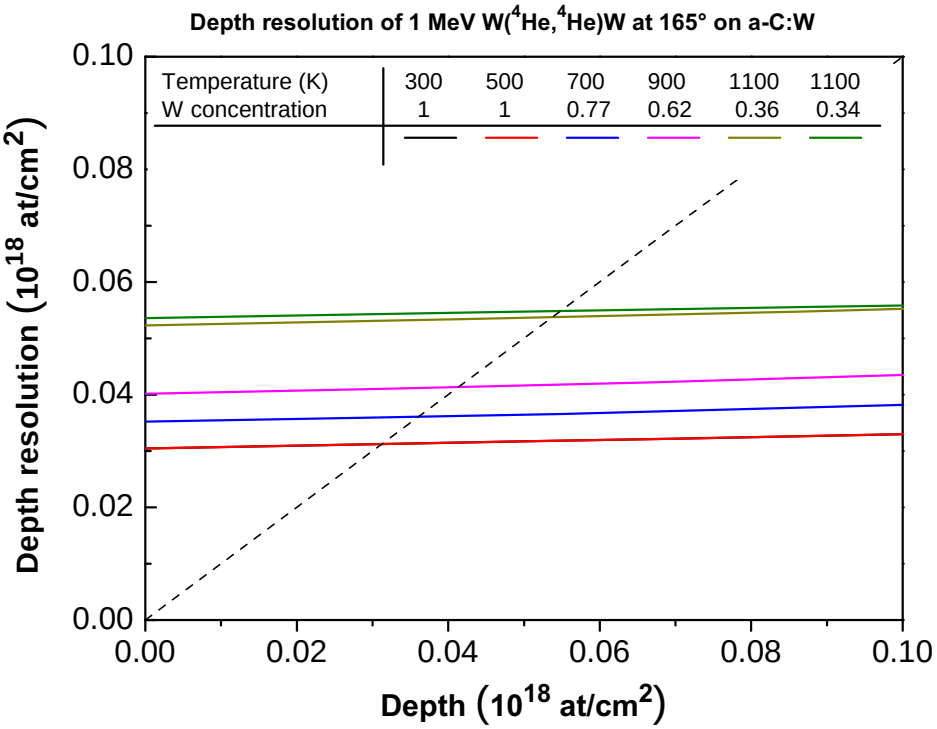

Figure D.1: Depth resolution of the 1 MeV W(^{4}He,^{4}He)W RBS process at 165° on a-C:W with different W concentrations, according to the W concentrations at different temperatures given in figure 4.1, obtained from RESOLNRA [133]. The resolvable depth can be read off from the intersection between the dashed line and the depth resolution (solid curve).

of the W enrichment zone, so that the resolvable depths are clearly distinguishable. Between 300 K and 700 K the resolvable depth is between 50 nm and 60 nm. At 900 K the resolvable depth is at 95 nm. These values are larger than the width of the ion range of a 200 eV and a 1.2 keV D beam in pure W (6.3 and 16 nm, respectively), i.e. the width of the implantation zone is not resolvable for any specimen from the temperature series.

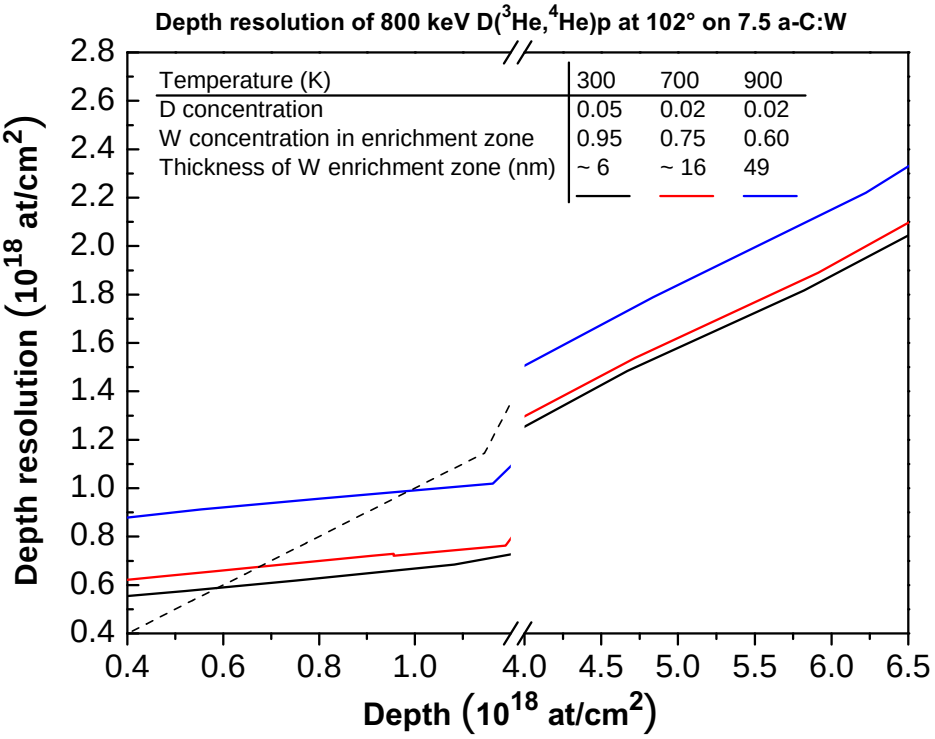

Figure D.2: Depth resolution of the 800 keV D(^{3}He,^{4}He)p nuclear reaction at 102° on a-C:W with different D concentrations (figure 5.2) and the corresponding thickness and composition of W enrichment zone (figure 4.2), obtained from RESOLNRA [133]. The resolvable depth can be read off from the intersection between the dashed line and the depth resolution (solid curve).

Appendix E

Surface morphology: Roughening

Surface roughness is difficult to quantify, since this term includes a couple of features (e.g. distribution of the local tilt angles and heights, presence of fine and thick featured structures), which are in convolution with each other and describe the surface morphology as a whole. In literature, a wide variety of roughness parameters exists [162]. Roughness parameters have informative value only in combination with a plot of a lateral distribution of heights over the scanned area. AFM was applied, in order to analyse surface roughness. Data processing was performed using the open-source software Gwyddion [163].

Surface roughness is changed during deuterium (D) beam exposure and thus differs from the roughness of the initial specimens. The characteristics of these changes depend on a variety of parameters, e.g. the initial tungsten (W) concentration, the implantation temperature and the fluence of incident D. A correlation between the evolution of roughness and these parameters, however, is not known. Analysis of surface roughness performed on the individual specimens, which were exposed to the D beam in the frame of the studies presented in this thesis, did not aim to find a correlation between the evolution of surface roughness and the parameters mentioned. In fact, roughness was analysed, in order to find explanations for the retention behaviour of the individual specimens of interest. On a rough surface, segments are shaped in such a way that portions of the incoming D beam are reflected from one hump to a neighbouring hump, where further portions can be implanted. Therefore, the reflection coefficient is reduced in the net and the implantation volume is enhanced (due to an incidence closer to the normal of a surface segment; increased width of implantation zone). Larger portions of the incoming D beam are trapped inside the implantation zone. In this context, roughening was observed changing one of the parameters mentioned.

Another important aspect of roughness lies in its influence on the depth resolution and the shaping of the RBS and the NRA spectra. Comparing the resolvable depth of the RBS and the NRA spectra with the width of the enrichment zone and with the diffusion depth, respectively, the FWHM of the surface roughness was taken into account. Surface roughness may cause problems with depth resolution. A rough surface may be identified as a superposition of different film thicknesses, i.e. as a thickness distribution with a FWHM (FWHM of the surface roughness). A portion of these thickness values may be lower than the resolvable depth. A RBS (or NRA) spectrum was supposed to be resolvable if the difference between the width of the enrichment zone (or the diffusion depth) and the half value of the FWHM of the surface roughness is larger than the resolvable depth of the RBS (or NRA) spectrum. For this problem it is not important whether structures are fine or thick featured.

Regarding the shaping of the RBS and the NRA spectra, it was checked whether multiple surface crossings need to be taken into account by means of the distribution of the local tilt angles of the surface segments. Multiple surface crossings may smear out the peak in the RBS and the NRA spectra, so that the width of the W enrichment zone and the diffusion depth appear to reach larger values, respectively. In this case it was assumed that multiple surface crossings do not have to be taken into account in the RBS and the NRA spectra, if the half value of the FWHM of the distribution of the local tilt angles of surface segments is smaller than 20° and 12°, respectively (i.e. the angular distribution of surface tangents is larger than 70° and 78°, respectively). This means that in both experiments, RBS (angle of incidence 70°, exit angle 70.71°) and NRA (angle of incidence 0°, exit angle 78°), incident and exit angle are lower than the half value of the FWHM of the angular distribution of surface tangents. In this case, multiple surface crossings are not possible. Note, for very thick featured structures it may be possible to neglect multiple surface crossings for even larger tilt angles. So the criterion mentioned is an upper limit for the influence of multiple surface crossings. Furthermore, it needs to be mentioned that AFM is only a suitable tool estimating the influence of multiple surface crossings, if it is possible to neglect the presence of narrow channels at the surface, which exhibit a lower diameter than the AFM tip and reach large depths. These channels are not probed by AFM and smear out the energy of alpha particles. For instance, an alpha particle from the D(^{3}He,^{4}He)p nuclear reaction (exit angle 78°) at a depth of 500 nm has a travelling distance of $\sim$2.5 μm towards the surface and an alpha particle from the W(^{4}He,^{4}He)W Rutherford backscattering process (incident and exit angle $\sim$70°) at a depth of 50 nm has a total travelling distance of (adding incident and exit path length) $\sim$300 nm. Consequently, the presence of narrow channels can be neglected for the NRA and for the RBS spectrum, if only few channels cross the path of the alpha particles along a travelling distance of $\sim$2.5 μm and $\sim$300 nm, respectively. In principle, the frequency of such a kind of channels can be estimated by cross-section SEMs. For the study presented in this thesis, however, no statistics exist, but spot checks (see figures F.3 (a) and F.4 (a)). The channels present in the specimen depicted in figure F.3 (a), for instance, have a lateral distance of $\sim$2.5 μm, in depths not larger than 0.5 μm. The distance of these channels is even larger for an alpha particle, which is ejected under 78°. Therefore, an alpha particle from the D(^{3}He,^{4}He)p nuclear reaction, which originates from depths $\leq$0.5 μm, will not cross such a channel more than one time during the travel towards the surface. For an alpha particle from the W(^{4}He,^{4}He)W Rutherford backscattering process (incident and exit angle $\sim$70°), which was scattered at depths $\leq$50 nm, such a channel will not be crossed during the travel towards the surface.

Roughening at 300 K

For the specimens exposed to the D beam at 300 K the roughening with increasing fluence was observed, e.g. by increasing the fluence from 10^{19} D/cm^2 to 10^{20} D/cm^2. Thereby, the pure carbon film (a-C) was compared to the 2.5% and to the 7.5% tungsten-containing carbon film (a-C:W), by means of the root mean square value (RMS value) [162] and the surface area.

Roughening with increasing fluence at 300 K is illustrated in figure E.1. The RMS value of surface roughness and the surface area are inserted in each part of figure E.1. On the left hand column the specimens implanted at a fluence of 10^{19} D/cm^2 are shown and on the

right hand column the specimens implanted at a fluence of 10^{20} D/cm^2 are shown. For a-C the RMS value and the surface area increase with increasing fluence to the 3.3-fold and to the 1.01-fold, respectively. For 2.5% a-C:W the RMS value shows a strong increase with increasing fluence to the 10-fold. The surface area also increases strongly with increasing fluence to the 1.17-fold. For 7.5% a-C:W the RMS value and the surface area decrease with increasing fluence to the 0.65-fold and to the 0.98-fold, respectively. Note, at a fluence of 10^{19} D/cm^2 the RMS value and the surface area increase monotonically with increasing W concentration to the 3.4-fold and to the 1.03-fold, respectively. This is in the same order as the increase of surface roughness with fluence of a-C. Consequently, if a-C shows an increase of the D inventory with fluence only caused by roughening (increase of the width of the implantation zone), the magnitude of this increase will not be larger than the difference between the D inventory of a-C, implanted at a fluence of 10^{19} D/cm^2, and the D inventory of 7.5% a-C:W, implanted at a fluence of 10^{19} D/cm^2. This conclusion will be discussed in the frame of the discussion of the influence of W and pre-heating on accumulation of D (see section 5.2) and the increase of the D inventory with fluence.

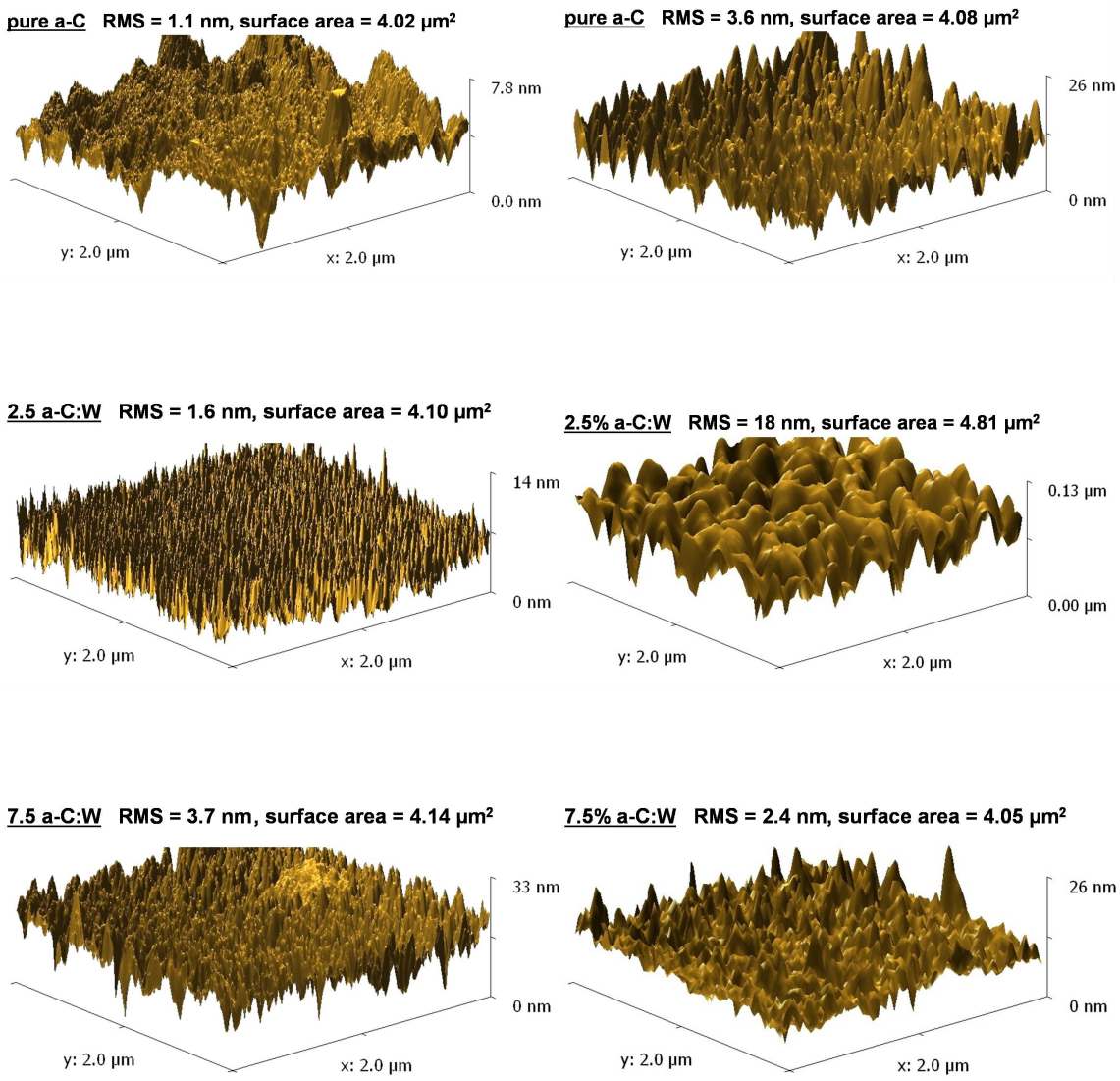

Figure E.1: Surface morphology (AFM scan area of 2x2 μm^2) of a-C, 2.5% a-C:W and 7.5% a-C:W, exposed to a 200 eV D beam at 300 K and at different fluences (left column: 10^{19} D/cm^2; right column: 10^{20} D/cm^2). The RMS value and the surface area are inserted.

Roughening between 300 K and 1300 K

For the specimens implanted at elevated temperatures the roughening with implantation temperature was observed. AFM measurements on the temperature series did not aim to investigate changes in surface roughness with temperature comprehensively. In fact, only special features of surface roughness are of interest (the FWHM of the surface roughness, the distribution of the local tilt angles of surface segments), which are supposed to be important in the context of resolvable depths, on one hand, and in the context of multiple surface crossings, on the other hand.

For the temperature series 3D-plots are illustrated in figure E.2 first. The value of the FWHM of the surface roughness is inserted in each part of figure E.2. Surface roughness clearly changes with temperature. This is demonstrated in figure E.2 for the temperature series of a-C:W. For each temperature fine structured features are visible in a scan area of $2\text{x}2\,\mu\text{m}^2$. Above 900 K the FWHM of the surface roughness increases to 20 nm, from a nearly constant level between 300 K and 900 K (5 nm - 7 nm). At 1100 K one of the two specimens has a larger FWHM of 27 nm; thick structured features are superposed by fine structured features. These results, however, are discussed in the frame of the discussion of resolvable depths (see subsection *Temperature series of RBS spectra* in section 4.1 *Enrichment of W: Depth profiles*).

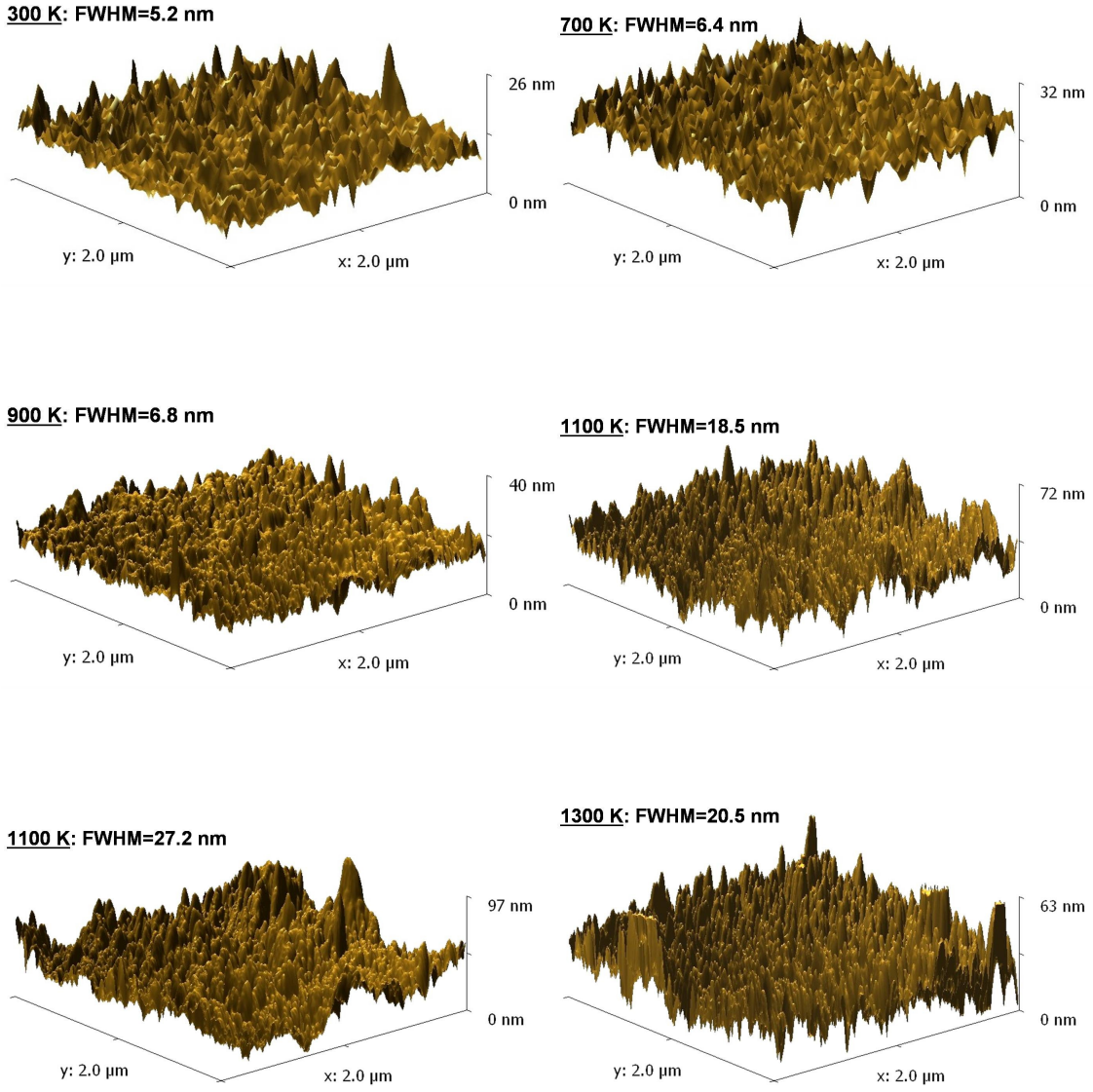

Figure E.2: Surface morphology of 7.5% a-C:W, exposed to a 200 eV D beam between 300 K and 1300 K and at 10^{20} D/cm^2, measured by AFM over a scan area of 2x2 μm^2. The FWHM of the surface roughness is inserted.

In the next step, the influence of multiple surface crossings is evaluated for each specimen from the temperature series, by taking the distribution of the local tilt angles into account. Local tilt angles are given in polar direction and the azimuth direction (scanning direction) was chosen in such a way so that the plane, which is spanned by the scanning direction and the AFM tip, falls together with the plane, which is spanned by the incoming and the outgoing beam in the ion beam analysis experiments. Thus, the distribution of the local tilt angles can be compared with incident and exit angle in ion beam analysis. Figure E.3 depicts the distribution of the local tilt angles of the temperature series of a-C:W by means of a relative frequency (each distribution was normalized to its maximum) plotted over tilt angles, between -40° and 40°. The horizontal line at 0.5 (dotted line) marks the half maximum.

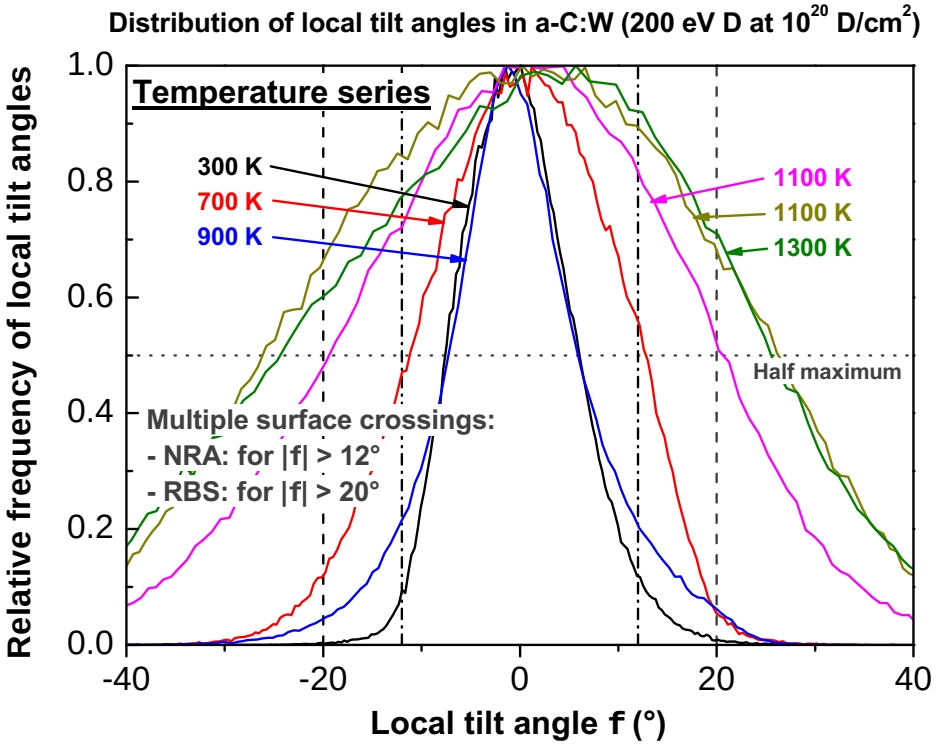

Figure E.3: Distribution of the local tilt angles of surface segments of 7.5% a-C:W, exposed to a 200 eV D beam between 300 K and 1300 K and at 10^{20} D/cm^2, measured by AFM over a scan area of 2x2 μm^2. If the FWHM is larger than $|12|°$ and $|20|°$ multiple surface crossings need to be taken into account in the NRA and in the RBS spectrum, respectively.

Thus, the FWHM can be easily read off from the two intersections of the horizontal line and the distribution. Four vertical lines are inserted, two at an angle of $\pm 12°$ (dash-dotted lines) and two at an angle of $\pm 20°$ (dashed lines), respectively. If the FWHM is larger than the region, which is spanned by the vertical lines at $\pm 12°$ and at $\pm 20°$, multiple surface crossings need to be taken into account in the NRA and in the RBS experiment, respectively. From the peak integrals it can be shown that, in this case, more than 10% among the local tilt angles are larger than $|12|°$ and $|20|°$, respectively. At 900 K and below, less than 10% among the local tilt angles are larger than $|12|°$ (at 700 K about 10% among the local tilt angles are larger than $|12|°$). Consequently, multiple surface crossings do not have to be taken into account for the specimens implanted at 900 K and below, neither in the RBS nor in the NRA spectra. Above 900 K the situation is critical. For each of the specimens implanted at 1100 K

and at 1300 K more than 10% among the local tilt angles are larger than $|12|^\circ$. At 1100 K, 27% among the local tilt angles of a specimen are larger than $|12|^\circ$ and 30% of another specimen. At 1300 K, 32% among the local tilt angles are larger than $|12|^\circ$. Consequently, multiple surface crossings need to be taken into account in each NRA spectrum. At 1100 K and above, the NRA spectra are spread, due to multiple surface crossings. It is not possible to distinguish between the influence of surface roughness and the influence on the D depth profile on the shape of the NRA spectra, so that it is not possible to quantify the extent of diffusion of D into depth for specimen implanted at 1100 K and above. The situation for the RBS spectra, however, is different at 1100 K. At 1100 K, 10% among the local tilt angles of a specimen are larger than $|20|^\circ$ and 20% of another specimen. Consequently, multiple surface crossings can only be neglected for the first specimen. At 1100 K, the RBS spectrum of the first specimen is not significantly spread due to multiple surface crossings, so that it is possible to quantify the width of the enrichment zone. Note, the first specimen has a FWHM of the surface roughness of 27 nm and the latter one has a FWHM of the surface roughness of 20 nm (see figure E.2). This shows that a large FWHM of the surface roughness is not necessarily in convolution with a large FWHM of the distribution of the local tilt angles and vice versa. At 1300 K, 20% among the local tilt angles are larger than $|20|^\circ$, so that it is not possible to quantify the width of the enrichment zone.

Appendix F

Analysis of carbide phases

The retention and erosion behavior of a-C:W was investigated for different temperatures up to 1300 K. With increasing temperatures up to 1300 K, a trend was observed concerning the formation of carbide phases in a-C:W [85]. While in the as-deposited specimen W is atomically dispersed inside the C matrix, crystallite growth occurs with increasing temperature, so that it is possible to observe the W_2C phase at 1300 K [85].

In order to follow up this trend, further investigations were performed within the framework of the study presented in this thesis, with regard to carbide formation in a-C:W by annealing. Thereby, annealing temperatures were increased up to 2800 K. Furthermore, higher W concentrations (up to 22 at%) were investigated, regarding their carbide formation by annealing. Applying X-ray diffraction (XRD) studies, W carbide phases were analysed in a-C:W, containing less than 25% of W. They were produced by magnetron sputter deposition and annealed to different temperatures up to 2800 K.

Analysis of phase transformations in the a-C:W system: XRD and STEM

The crystallographic phase in a-C:W was determined by XRD using a Seifert XRD 3003 PTS diffractometer operated with Cu K_α radiation. The experimental setup was optimized to measure thin films. Details are described elsewhere [68]. The most diffractograms were acquired as theta-scans at a gracing incidence angle of 5°. Phases were identified by comparing the peak position in the X-ray diffractogram with peak positions of W carbide standards, tabulated in the ICDD data base as powder diffraction files (PDF) [164]. The Scherrer formula with a pre-factor of 1 was used for an estimation of the carbide crystallite size D [165]

$$D = \frac{\lambda}{B_{2\theta} \cdot cos\theta_B}, \tag{F.1}$$

with $B_{2\theta}$ the peak FWHM, θ_B the peak position and λ the radiation wavelength (0.154 nm). Peak broadening is assumed to be dominated by the small crystallite size. It was taken care that the broadening by the experimental set-up contributes less than the half line width.

The surface morphology as well as film growth and the depth distribution of crystallite sizes was investigated in a scanning electron microscope (SEM) with focused ion beam (FIB) column (Helios Nanolab 600, FEI). Another FIB microscope from Warsaw University of Technology (FB 2100, Hitachi) was used for the preparation of electron transparent lamella.

Argon ion milling in a Gentle Mill device was applied for final thinning and elimination of damage introduced into the material by FIB preparation. Bright field and Z contrast imaging and nano diffraction was carried out on a 200 kV C_s corrected scanning transmission electron microscope (STEM) (HD-2700, Hitachi). Therefore it was possible to probe the structure of nano particles and to identify their phase.

W carbide phases

A special focus was put on the attempt to observe the phase transformation from W_2C to WC, in the temperature range between 1450 K and 2800 K, for 9.5% a-C:W (W_2C was proposed already at 1300 K and WC was observed at 1700 K [68]). Phases, textures and crystallite sizes were analysed by XRD. For comparison, nano diffraction was performed on 9% a-C:W samples, annealed to 1450 K and to 2800 K.

X-ray diffraction

The X-ray diffractograms for an annealing series of 9% a-C:W are shown in figure F.1 (a). For the as-deposited sample and samples annealed to temperatures below 2000 K carbide phases are clearly allocatable, since broad peaks observed in the diffractograms were probably caused by WC_{1-x} and W_2C. No significant texture could be measured. Annealing to 2200 K leads to occurrence of peaks which can be attributed to the WC_{1-x} phase. At 35° a small shoulder appears at the peak position of the W_2C standard. The WC_{1-x} peak around 37° shows a steep descent that levels out with unexpected strength at 39°, i.e. at another peak position of the W_2C standard. This is a hint on the W_2C phase. At 2800 K clearly a mixture of WC and WC_{1-x} is present in the film. The peak at 34° can be identified as WO_3. A WO_3 surface layer is supposed to be build up (see subsection *Nano diffraction at individual crystallites*). This may be caused by a leak at the furnace during the heating run at 2800 K.

Annealing the 6% and the 7% W-containing specimens to 2200 K leads to an analogue carbide formation with WC_{1-x} as a dominant phase (the diffractogram is not shown). Figure F.1 (b) shows the evolution of the diffraction patterns of 18% a-C:W. A broad bump around 35° and around 70° only occurs in the as-deposited sample. Already after annealing to 1450 K both the WC and the W_2C phase exists. With increasing the annealing temperature the intensity for the WC peaks increases while for the W_2C peaks decreases. After annealing at 2800 K the dominant phase is WC. The W_2C peaks disappeared. At 34° again the WO_3 peak is present, as already mentioned for the case of lower W concentrations. The diffraction patterns of 22% a-C:W are depicted in figure F.1 (c) for temperatures up to 2200 K. At 1450 K the WC phase is clearly identified and no indication for W_2C and WC_{1-x} exists. With increasing temperature an overall increase in peak intensity and a peak narrowing is observed. This is due to growth in crystallite size (above 50 nm) with increasing annealing temperature. For instance, the FWHM of the peak at 48° decreases from 0.61° at 1450 K to 0.19° at 2200 K. Crystallite sizes that are smaller than 20 nm at 1450 K increase to values larger than 50 nm at 2200 K.

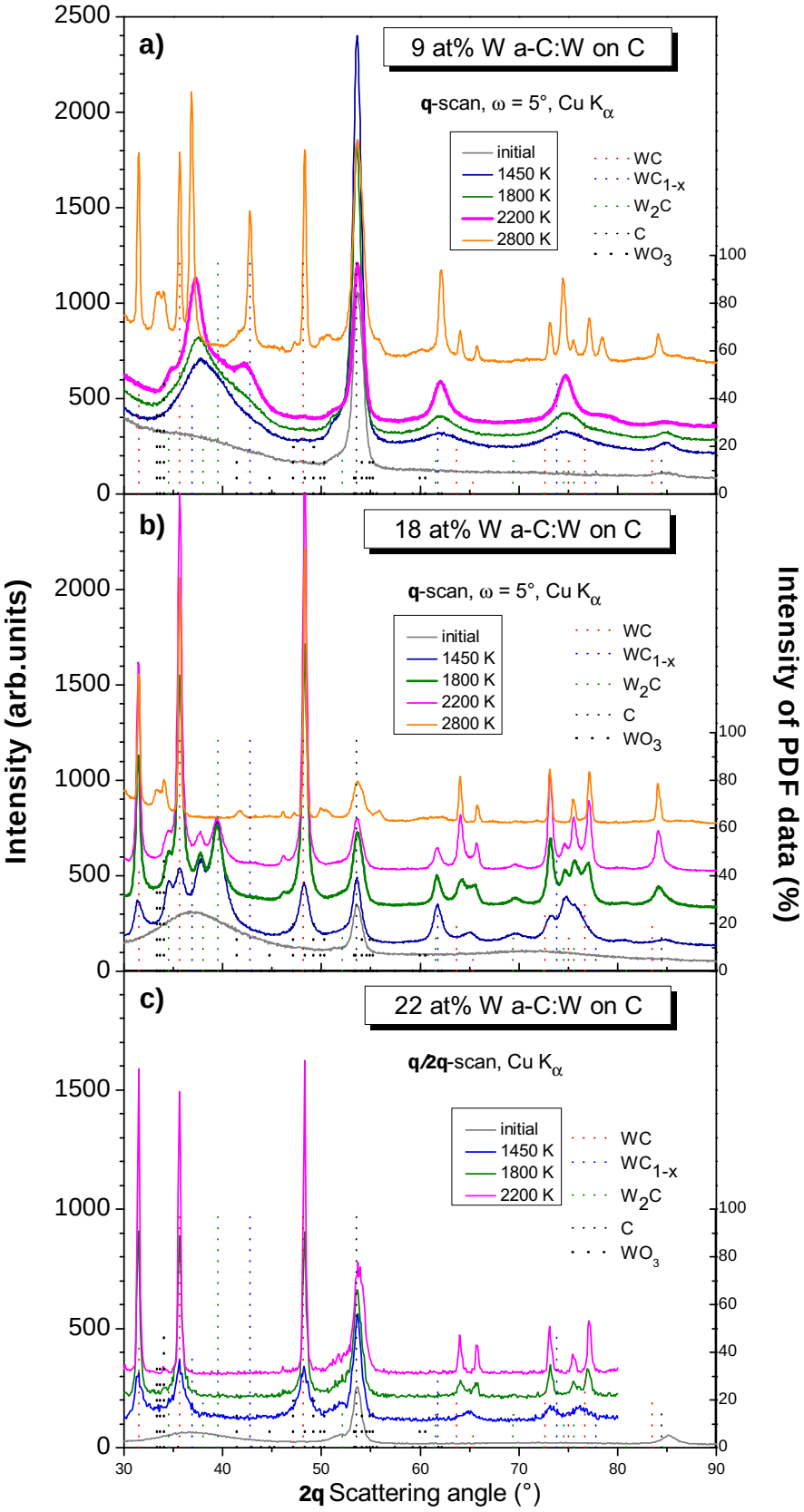

Figure F.1: X-ray diffractograms of annealing series of a-C:W. W concentration: (a) 9%, (b) 18%, (c) 22%. Diffraction peaks for the carbide phases WC, W_2C, WC_{1-x} (PDF card 25-1047, 35-776, 20-1316), for WO_3 (PDF card 20-1324) and for pure graphite (substrate) are indicated (right axes show the intensity in % of the PDF data). All films are deposited on graphite substrate.

Nano diffraction at individual crystallites

For the 9% a-C:W sample WC and WC_{1-x} were clearly observed by XRD after annealing to 2800 K. For comparison, nano diffraction was performed. Figure F.2 (a) shows a SEM image of a cross-section of a 9% a-C:W sample annealed to 2800 K. Two size types particles are

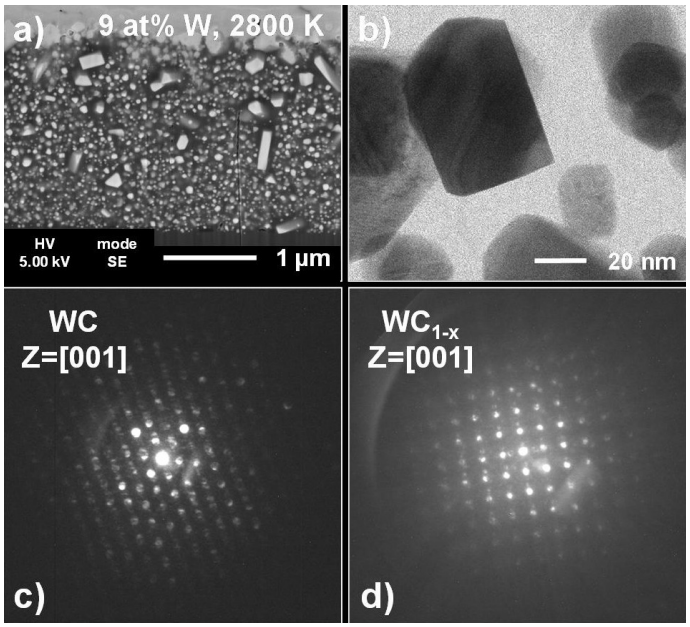

Figure F.2: (a) SEM micrograph of a cross-section of a 9% a-C:W sample, annealed up to 2800 K. (b) STEM bright field of a single crystallite (dark area). (c) and (d) Nano diffraction of single particles revealed the WC phase and the WC_{1-x} phase, respectively. Note (d) is made on the crystallite in the central of (b).

visible (large crystallites: up to several hundred nm in size, small crystallites: 10-100 nm in size). Figure F.2 (b) shows a STEM bright field image of a small crystallite, chosen for nano diffraction. The diffraction pattern of this crystallite (figure F.2 (d)) corresponds to the WC_{1-x} phase. Some of the small crystallites, however, are present in the WC phase as well (figure F.2 (c)). By performing nano diffraction at the large particles the WC phase was found. Note the oxide layer at the surface (oxidised W carbide grains are irregularly shaped and light grey in figure F.2 (a).

For the as-deposited sample and for samples annealed to temperatures below 2000 K no carbide phases are allocatable in the diffractograms, since broad peaks were observed. Nano diffraction on a 9% a-C:W sample annealed to 1450 K was performed in order to learn, weather peak broadening is due to atomically dispersed W inclusions, phase mixtures or small distorted W carbide particles. Figure F.3 (a) shows a STEM image of a cross-section of a 9% a-C:W sample annealed to 1450 K. The film is built up in a columnar structure. Figure F.3 (b) shows STEM image in bright field mode, with a part of this image (upper right corner) obtained in Z-contrast mode. Atomic lattice fringes structure, which are visible on this figure, allows to estimate that the crystallites size are in the range 1-5 nm. Nano diffraction on single crystallites (figure F.3 c and F.3 (d) clearly reveals the presence of two W carbide phases (W_2C and WC_{1-x}).

Figures F.4 (a) and F.4 (b) show SEM images of cross-sections of a-C:W samples annealed to 2200 K, with the W concentrations of 9% and 18%, respectively. The 9% W-containing

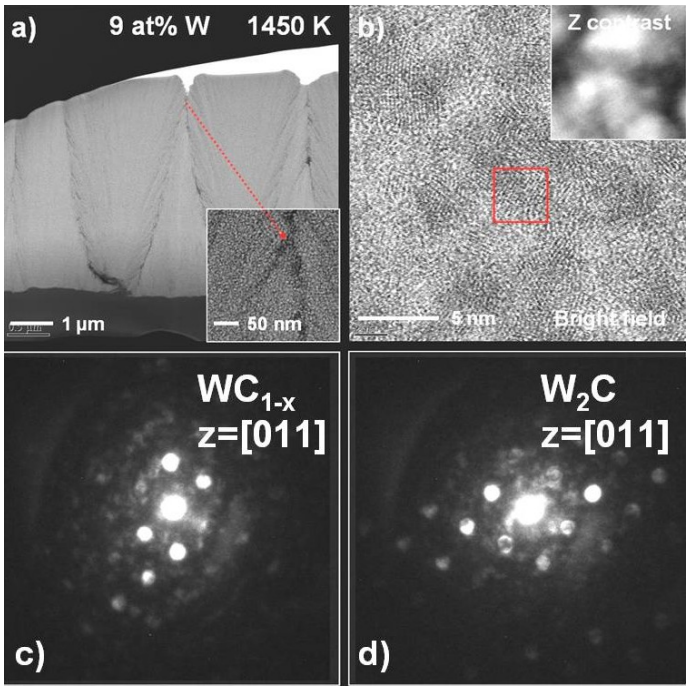

Figure F.3: (a) STEM bright field micrograph of a 9% a-C:W sample, annealed up to 1450 K. (b) Magnification to nm-scale (overlayer in the upper right corner: correlated STEM Z contrast micrograph). Nano diffraction of single particles revealed (c) the WC_{1-x} phase and (d) the W_2C phase (area of diffraction: in diameter $\sim$3 nm^2).

sample contains small crystallites (5-10 nm), homogeneously distributed. In the 18% W-containing sample a broad distribution of crystallite sizes is observed (10-200 nm), with decreasing average size with increasing distance to the surface. However, no explanation for this effect has yet been found. By comparing figures F.4 (a) and F.4 (b), the crystallite size increases with the W concentration. Comparing crystallite sizes in figure F.4 (a) with crystallite sizes in figure F.2 (a) also shows that crystallite size coarsen strongly with temperature.

Performing nano diffraction on a 9% W-containing sample annealed to 2800 K showed that results are comparable to XRD measurements. Nano diffraction allows phase identification of single crystallites on a nm-scale. The analysis of 9% a-C:W annealed to 1450 K showed that phase analysis is possible even for very small particles using nano diffraction, where XRD fails. Furthermore, phase mixtures could be identified at 1450 K, which also lead to broad peaks in the X-ray diffractograms.

Carbide formation and enrichment

With increasing W concentration, the temperature range, in which carbide formation is observable, decreases to lower temperatures. Crystallite sizes increase with increasing W concentration. Crystallite sizes in the order of 100 nm are already observable in a medium temperature range (around 2200 K), for the high W concentrations (22% of W), while for the low W concentrations (9% of W) higher temperatures up to 2800 K are necessary. Nevertheless, for all as-deposited specimens, even for those specimens, containing 22% W, no carbide phases are allocatable; crystallite sizes are small.

Since in the enrichment zone of a-C:W exposed to the D beam the W concentrations are

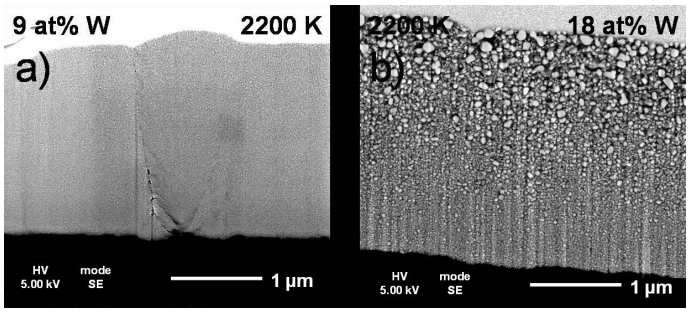

Figure F.4: Cross-section SEM of a-C:W samples annealed to 2200 K. (a) 9% W-content, small crystallite sizes. (b) 18% W-content, bimodal distribution of crystallite sizes (sizes increasing towards the surface).

larger than 22%, in a temperature range between 300 K and 1100 K, a formation of carbide phases inside the enrichment zone already appears to be possible at temperatures below 1300 K. This kind of carbide formation may influence the retention and erosion behaviour. Furthermore, for the unaffected C matrix, i.e. in depths not affected by enrichment, a significant formation of carbide phases in the temperature range between 300 K and 1300 K can be excluded from the results presented above. Therefore, the influence of carbide formation inside the unaffected C matrix on the retention and erosion behaviour can be neglected for all experimental conditions used within the framework of the study presented in this thesis.

Appendix G

List of publications and poster presentations

Publications

1. P. A. Sauter and M. Balden. Deuterium retention in tungsten-doped carbon films. *Phys. Scr.*, T138:014044 (4pp), 2009.

2. P. A. Sauter, M. Balden. Temperature dependence of the erosion behavior of deuterium beam exposed tungsten-doped carbon films (a-C:W). *J. Nucl. Mater.* (2010), doi:10.1016/j.jnucmat.2010.08.021

3. M. Balden, P. A. Sauter, S. Jong, C. Adelhelm, S. Lindig, M. Rasinski, and T. Plocinski. Carbide formation in tungsten-containing amorphous carbon films by annealing. *Thin Solid Films*, 519:4049 - 4053, 2011.

Poster presentations

1. Sauter, P. A. and M. Balden: Deuterium retention of tungsten-doped carbon films. (12th International Workshop on Plasma-Facing Materials and Components for Fusion Applications (PFMC-12), 2009-05-11 to 2009-05-14, Jülich).

2. Sauter, P. A. and M. Balden: Temperature Dependence of the Deuterium Retention in Tungsten-doped Carbon Films. (19th Conference on Plasma Surface Interactions in Controlled Fusion Devices (PSI 19), 2010-05-24 to 2010-05-28, San Diego, CA).

3. Sauter, P. A. and M. Balden: Deuterium retention in tungsten-doped carbon films at elevated temperatures. (E-MRS 2010 Spring Meeting, Symposium N: Nuclear Materials IV, 2010-06-07 to 2010-06-11, Strasbourg).

4. Balden, M., P. A. Sauter, S. Jong, C. Adelhelm, S. Lindig, M. Rasinski and T. Plocinski: Carbide formation in amorphous tungsten-containing carbon films by annealing. (E-MRS 2010 Spring Meeting, Symposium L: Carbon- or nitrogen-containing nanostructured composite films, 2010-06-07 to 2010-06-11, Strasbourg).

5. Adelhelm, C., M. Balden, P. A. Sauter and P. Starke: Deuterium plasma and ion beam erosion experiments on metal-doped amorphous carbon films. (18th International Conference on Plasma Surface Interactions in Controlled Fusion Devices (PSI 18), 2008-05-26 to 2008-05-30, Toledo).

6. Balden, M., I. Segues Guridi, C. Adelhelm and P. A. Sauter: Oxidative Behaviour of Metal-Doped Carbon Films. (E-MRS 2010 Spring Meeting, Symposium N: Nuclear Materials IV, 2010-06-07 to 2010-06-11, Strasbourg).

7. Lopez-Galilea, I., C. Garcia-Rosales, C. Adelhelm, P.A. Sauter, M. Balden and P. Starke: Chemical erosion behaviour of Ti-doped isotropic graphite for plasma facing components. (18th International Conference on Plasma Surface Interactions in Controlled Fusion Devices (PSI 18), 2008-05-26 to 2008-05-30, Toledo).

8. Balden, M., P. Starke, C. Adelhelm, P. A. Sauter, I. Lopez-Galilea, N. Ordas, C. Garcia-Rosales, J. M. Ramos Fernandez, M. Martinez Escandell, A. Centeno and C. Blanco: Chemical sputtering of metal-doped carbon-based materials by deuterium bombardment from ion beam and plasma. (12th International Workshop on Plasma-Facing Materials and Components for Fusion Applications (PFMC-12), 2009-05-11 to 2009-05-14, Jülich).

9. Balden, M., P. Starke, C. Garcia-Rosales, C. Adelhelm, P. A. Sauter, I. Lopez-Galilea, N. Ordas, A. Centeno, C. Blanco, J. M. Ramos Fernandez and M. Martinez Escandell: Compilation of erosion yields of metal-doped carbon materials by deuterium impact. (14th International Conference on Fusion Reactor Materials (ICFRM-14), 2009-09-06 to 2009-09-11, Sapporo). Starke, P., M. Balden, D. Filimonov, C. Adelhelm, P. A. Sauter and ExtreMat Partners: Erosionsverhalten dotierter Kohlenstoffmaterialien in Deuterium-Niederdruckplasmen. (DPG Frühjahrstagung, 2009-03-30 to 2009-04-02, Greifswald).

10. Sinclair, L., J. W. Davis, B. W. N. Fitzpatrick, A. A. Haasz, C. Adelhelm, P. A. Sauter and M. Balden: Thermo-Oxidation of Carbon films with Tungsten Impurities. (10th International Workshop on Hydrogen Isotopes in Fusion Reactor Materials, 2010-05-31 to 2010-06-01, Pleasanton, CA).

Appendix H

Acknowledgements

Zum Gelingen dieser Arbeit haben eine Vielzahl an Personen beigetragen, denen ich hiermit danken möchte.

Mein erster Dank gilt meinem Doktorvater **Prof. Dr. Dr. Harald Bolt**, der es mir ermöglichte, diese Arbeit am IPP durchzuführen. Für sein Vertrauen, seine Unterstützung und sein Interesse an meiner Arbeit möchte ich mich sehr herzlich bedanken.

Bei **Prof. Dr. E. Werner** möchte ich mich für die Bereitschaft bedanken, sich als Zweitgutachter zur Verfügung zu stellen.

Prof. Dr. H. Baier danke ich für die freundliche Unterstützung, meine Promotion an der Fakultät für Maschinenwesen durchführen zu können.

Meinem Betreuer **Dr. Martin Balden** gilt mein größter Dank für 4 Jahre tolle Zusammenarbeit, bei der ich sehr viel lernen konnte. Sein Vertrauen in mich, sein großer persönlicher Einsatz, seine Expertise und Unterstützung bei Experimenten sowie die vielen hilfreichen Diskussionen sind mir unvergessen. Danke!

Ein großer Dank geht an **Dr. habil. Christian Linsmeier**, der mir stets als kompetenter und motivierender Ratgeber zur Seite stand. Vielen Dank auch für die Leitung und Organisation des hilfreichen Doktorandenseminars.

Besonders danken möchte ich meinem Vorgängerdoktoranden **Dr. Christoph Adelhelm** für das offene Ohr, die fachliche, vor allem aber die persönliche Unterstützung der letzten Jahre. **Dr. Matej Mayer** danke ich für die Diskussionsbereitschaft in allen Fragen zur Auswertung von Messergebnissen aus der Ionenstrahlanalytik. **Dr. Klaus Schmid** bin ich für die Überlassung der Ergebnisse aus seinen Modellrechnungen bezüglich der zeitlichen Redistribution von Be, C und W in ITER dankbar, sowie für seinen kompetenten Rat aus dem weiten Feld der Physik, v.a. über Aufbau und Funktion der Hochstromionenquelle, den ich mir jederzeit einholen konnte. **Thomas Dürbeck** danke ich für die Durchführung der TDS Messungen und seine Diskussionsbereitschaft bei der Auswertung der Messdaten. Des weiteren danke ich ihm und **Dr. Thomas Schwarz-Selinger** für die Herstellung und Charakterisierung von a-C:H und a-C:D Filmen, sowie für die praktischen Tips im Umgang

mit dem Ellipsometer. **Dr. Martin Balden** und **Stefan Lindig** danke ich für die äußerst professionellen SEM und cross-section SEM Aufnahmen am Helios Nanolab 600, FEI, sowie für die äußerst professionellen XRD Aufnahmen am Seifert XRD 3003 PTS Diffraktometer und die damit verbundenen vielseitigen Diskussionen. **Marcin Rasinski** und **Thomasz Plocinski** von der Warsaw University of Technology danke ich für die Phasenanalysen an unseren a-C:W Filmen mittels STEM und nano-diffraction.

Für das angenehme Arbeitsklima und die Unterstützung bei kleinen Problemen aller Art geht ein ganz großes Dankeschön an die Kollegen des Bereichs E2M (v.a. ehemals MF), speziell an die Arbeitsgruppen PFMC (ehemals MSC) und PMI (ehemals RPP). Ohne das viele Know-How und die Hilfe, die ich jederzeit von Euch erhalten habe, wäre ich oftmals auf dem Schlauch gestanden. Besonders viel lernen konnte ich in Diskussionen mit: **Dr. Thomas Schwarz-Selinger** und **Dr. Hans Maier**, aber auch mit **Dr. Udo von Toussaint**, **Dr. habil. Wolfgang Jacob** und **Dr. Peng Wang**. Besonderen Dank schulde ich **Freimut Koch** für die Sputter-Unterstützung, den Ofen-Meistern **Till Höschen**, **Thomas Dürbeck**; **Armin Manhard** danke ich für die Unterstützung bei Wartung und Bedienung des Hochtemperaturofens HORST. **Arno Weghorn** ("Mr. Hochstromquelle") sowie dem Beschleuniger-Team mit **Dr. Karl Ertl** danke ich für gute Zusammenarbeit und die stets herausragenden Instandhaltungsarbeiten. Danken möchte ich auch meinen beiden Praktikanten **Stefan Jong** und **Laura Sinclair** für die Unterstützung bei der Probenherstellung und der elektronischen Datenverarbeitung von Ellipsometerdaten. **Dr. Wolfgang Eckstein** danke ich für die freundliche Überlassung der elektronischen Datenbanken zu "W. Eckstein. Calculated Sputtering, Reflection and Range Values. Techn. Rep. IPP 9/132, Max-Planck-Institut für Plasmaphysik, Garching, 2002." und die damit verbundenen Diskussionen. **Kazuyoshi Sugiyama** danke ich für die freundliche Überlassung der Messdaten seiner NRA Analysen an den Wolfram beschichteten Graphiten und den damit verbundenen Diskussionen.

Leonie Krieger danke ich für Korrekturen und Ratschläge bei englischen Formulierungen.

Für die schöne gemeinsame Zeit danke ich vor allem: Christoph Adelhelm, Martin Balden, Karola Bald-Solimann, Bernd Böswirth, Thomas Dürbeck, Anne Eggeling, Karl Ertl, Henri Greuner, Till Höschen, Stefan Jong, Freimut Koch, Martin Köppen, Stefan Lindig, Armin Manhard, Gabriele Matern, Monika Mezger, Martin Oberkofler, Mathias Reinelt, Johann Riesch, Gilbert de Saint-Aubin, Michael Schlüter, Thoms Schwarz-Selinger, Beata Tyburska, Peng Wang, Alessandro Zivelonghi,

Meinen Eltern, meinem Bruder Gabriel, meinem Opa, meinem Onkel Manfred und meinem Götti Robert danke ich für ihre mentale bzw. finanzielle Unterstützung.

Garching bei München, im November 2011
Philipp-André Sauter